



**HAL**  
open science

# Observations of the tropical atmospheric water cycle and its variations with sea surface temperature using a constellation of satellites

Erik Höjgård-Olsen

► **To cite this version:**

Erik Höjgård-Olsen. Observations of the tropical atmospheric water cycle and its variations with sea surface temperature using a constellation of satellites. Ocean, Atmosphere. Université Paris-Saclay, 2020. English. NNT: 2020UPASJ007 . tel-03215903

**HAL Id: tel-03215903**

**<https://theses.hal.science/tel-03215903>**

Submitted on 3 May 2021

**HAL** is a multi-disciplinary open access archive for the deposit and dissemination of scientific research documents, whether they are published or not. The documents may come from teaching and research institutions in France or abroad, or from public or private research centers.

L'archive ouverte pluridisciplinaire **HAL**, est destinée au dépôt et à la diffusion de documents scientifiques de niveau recherche, publiés ou non, émanant des établissements d'enseignement et de recherche français ou étrangers, des laboratoires publics ou privés.

Observations du cycle de l'eau atmosphérique  
tropicale et de ses variations avec la  
température de surface de la mer,  
à l'aide d'une constellation de satellites  
*Observations of the Tropical Atmospheric Water Cycle,  
Using a Constellation of Satellites*

**Thèse de doctorat de l'université Paris-Saclay**

École doctorale n°129, sciences de l'environnement d'Île-de-France (SEIF)  
Spécialité de doctorat: Océan, atmosphère, climat et observations spatiales  
Unité de recherche : Université Paris-Saclay, UVSQ, CNRS, LATMOS, 78280, Guyancourt, France.  
Réfèrent : Université de Versailles Saint-Quentin-en-Yvelines

**Thèse présentée et soutenue à Paris-Saclay,  
le 27/11/2020, par**

**Erik HÖJGÅRD-OLSEN**

**Composition du Jury**

<b>Philippe BOUSQUET</b> Professeur des universités, UVSQ/LSCE	Président
<b>Jean-Pierre CHABOUREAU</b> Physicien, HDR, UPS/LA	Rapporteur & Examinateur
<b>Céline CORNET</b> Professeure, UDL/LOA	Rapporteuse & Examinatrice
<b>Dominique BOUNIOL</b> Chargée de Recherche, UPS/CNRS	Examinatrice

**Direction de la thèse**

<b>Hélène BROGNIEZ</b> Maîtresse de Conférence, UVSQ/LATMOS	Directrice de thèse
<b>Hélène CHEPFER</b> Professeure, UPMC/LMD	Co-directrice de thèse
<b>Laurence PICON</b> Professeure, UPMC/LMD	Invitée



## *Acknowledgements*

First, I would like to direct a most sincere thank you to my thesis supervisors, H  l  ne Brogniez and H  l  ne Chepfer, for three years of pedagogic guidance and dedication to my work.

I would also like to thank the directors of my hosting laboratories Philippe Keckhut and Fran  ois Ravetta (LATMOS) and Philippe Drobinski (LMD), as well as the administrative offices for managing the labs – especially during the exceptional circumstances of 2020.

I want to thank all the members of the jury for accepting to examine my thesis. Thanks to Philippe Bousquet for having accepted to chair the jury, and thank you Jean-Pierre Chaboureau and C  line Cornet for agreeing to be the reporters of my manuscript.

Thank you to Dominique Bouniol and Tristan L’Ecuyer for following my progress as members of my thesis committee and for fruitful discussions during our meetings.

At LATMOS and LMD, I want to thank the *SPACE* team and *Cloud* teams. I want to especially thank the people whose help made my thesis possible: H  l  ne Brogniez, H  l  ne Chepfer, Christophe Dufour, Rodrigo Guzman, Patrick Raberanto, and Artem Feofilov.

I want to direct a special thanks to Rodrigo Guzman for the time he took to help me get settled with the software and administrative issues during the first months of my PhD.

I want to thank the social groups at LMD and LATMOS for many pleasant and relaxed social engagements. I especially want to thank Melissa, Oscar, Pragya and Minh with whom I have shared countless enjoyable moments and hilarious conversations. Thank you also to Eivind, L  o, Bastien, Nicolas, Artemis, Aurelie, Fuxing, Felipe, Antonin, Olivier, Assia, Navi, Thibault, Alexis, Stavros, Fausto, Sakina, Cyprien, Chlo  e...

A final and most sincere thank you to my family and friends back in Scandinavia, for their love, support and encouragements during my adventure.

# Table of Content

Introduction .....	1
1 Context .....	6
1.1 Complexity Facets of the Atmospheric Water Cycle .....	7
1.2 Radiation and the Water Cycle.....	12
1.3 Principal Hypotheses About the Tropical Atmospheric Water Cycle’s Response to Surface Warming.....	19
1.4 Present Day Limitations with Observations and Models.....	23
1.5 Principal Science Questions.....	26
2 The Synergistic Dataset.....	29
2.1 Introduction to the Dataset.....	30
2.2 Relative Humidity from SAPHIR .....	32
2.3 Cloud Characteristics from GOCCP.....	40
2.4 Near-Surface Precipitation from the CloudSat 2C-PRECIP-COLUMN Product .....	47
2.5 Surface Temperature and Vertical Pressure Velocity from ERA5 .....	54
2.6 Satellite Collocations .....	57
3 Variations on the Instantaneous Timescale Under Large-Scale Circulation Constraints .....	62
<i>Summary of the Paper and Its Main Outcomes</i> .....	63
3.1 Introduction.....	69
3.2 Data .....	70
3.3 Methods .....	72
3.4 Analyses of the Tropical Atmospheric Water Cycle’s Variation with SST in Different Regimes.....	78
3.5 Discussion.....	87
3.6 Conclusion .....	91
4 Covariations on Different Temporal and Spatial Scales.....	94
4.1 Introduction.....	95
4.2 Method.....	98
4.3 Analysis of Observed Water Cycle Variable Covariations on Different Timescales .....	104
4.4 Discussion of These Results.....	119
4.5 Summary and Conclusions.....	125
Conclusions and Perspectives.....	129

Appendices .....	135
A Basic Radiative Transfer Equations .....	136
B Supporting Data Information .....	138
C Supplementary Figures of Höjgård-Olsen et al. (2020).....	140
D Supplementary Figures of Chapter 4.....	155
E Résumé de thèse en français .....	159
List of Abbreviations and Notations .....	161
Abbreviations .....	161
Notations .....	163
Bibliography.....	164



## Introduction

Perhaps are the global cloud systems the most striking features in a satellite image? On an otherwise blue background, only interrupted by the continents' earthy colors, clouds are manifested as shiny and bright tracers of atmospheric motion (Fig. I-1).

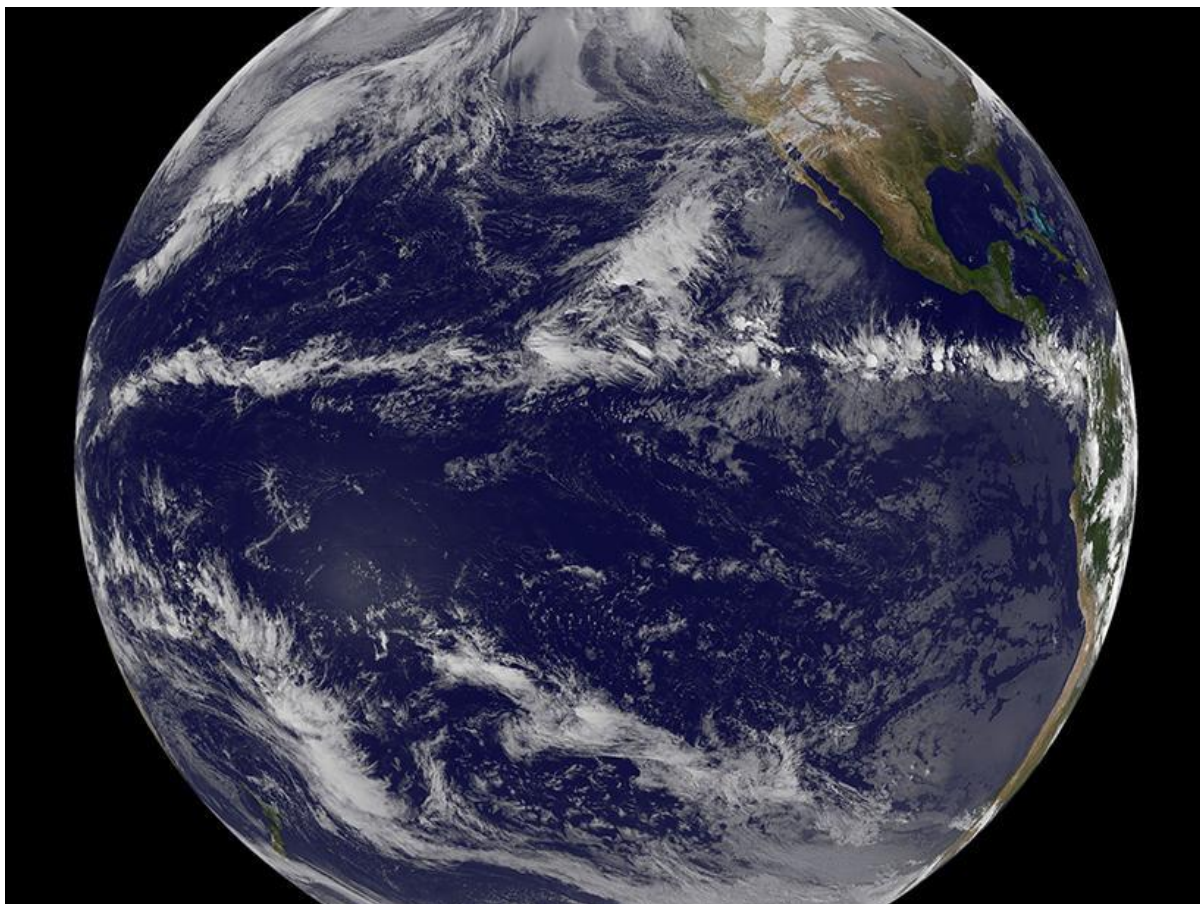


**FIGURE I-1:** This image is a combination of cloud data from NOAA's Geostationary Operational Environmental Satellite (GOES-11) and color land cover classification data from November 24, 2010. Accessed: September 8, 2020 from: <https://eos.org/research-spotlights/tropical-rainfall-intensifies-while-the-doldrums-narrow>

And life is pretty exciting for atmospheric water. Only 0.25 % of Earth's water is found in the atmosphere, out of which 99.5 % is in the vapor phase (Wallace and Hobbs 2006). Water vapor is the principal atmospheric greenhouse gas, and the only one that is sufficiently short-lived and abundant in the atmosphere to be considered under natural control. It has a unique quality to be the only substance on Earth that can exist naturally in its vapor, liquid and solid states for temperatures possible in the atmosphere. Despite the small concentration of water in the atmosphere, water vapor, clouds, and precipitation make the planet hospitable and are essential components of human life. Their variations thus transcend topics like everyday small talk and choice of clothing, for impacts on the seasonal harvests, climate change and the future of our planet.

Through uneven solar heating, an equatorial energy surplus and polar deficit give rise to a poleward heat transfer within the Earth system, carried by atmospheric winds and ocean currents, referred to as the general circulation. In the tropics, energy is transported from the surface to the upper troposphere via deep convective clouds. As the atmospheric water transitions from vapor, to liquid, to ice, it releases massive amounts of latent and sensible heat. Through its phase transitions, atmospheric water is the principal method of energy transport in the atmosphere (Wallace and Hobbs 2006, Holton 2013), and a driver of the atmospheric general circulation.

In the complex system of dynamic and thermodynamic processes that is the Earth system, the interactions between temperature, water vapor, clouds, precipitation, and radiation occur under the influence of the large-scale atmospheric circulation, which is influenced by them in return. These interactions are difficult to understand and untangle as, for example, cloud formation and vertical deployment involve mixed thermodynamic processes of the cloudy and clear-sky atmosphere, radiative exchanges and atmospheric dynamics.

Superimposed on these complexities is a radiative forcing due to anthropogenically emitted greenhouse gases over the industrial era and a warming of the global mean surface temperature (IPCC AR5 2013). Before a new equilibrium climate state is reached, all components (atmosphere, ocean, cryosphere, etc.) and variables (water vapor, clouds, precipitation, sea ice, vegetation, etc.) of the Earth system must adjust to this change.

What will the future climate be like? This is the ultimate question that our community has asked for decades. The equilibrium climate sensitivity is the response of the global mean surface temperature to a doubling of carbon dioxide concentration, relative to the preindustrial state (e.g. Charney et al. 1979). It is typically estimated assuming that changes in radiative flux are proportional to changes in surface temperature. However, these estimates are based on partial derivatives of parameters that cannot be rigorously translated into observations, and where intensities of non-independent feedback mechanisms are intertwined (Stephens 2005, Klein and Hall 2015). Most uncertain are the responses of the atmospheric water cycle to surface warming. Figure I-2 shows an illustration of a selected number of these uncertainties to be investigated in this work.

Atmospheric water vapor is most important for weather in the lower troposphere, whilst for climate in the upper troposphere (Kiemle et al. 2012). In the absence of clouds (clear-sky regions), the outgoing longwave radiation (OLR) emitted to space at the top of the atmosphere (TOA) is determined by water vapor (and other greenhouse gases). The atmospheric specific humidity increases by 6 to 7 % for every degree warming according to the Clausius-Clapeyron equation under constant RH. The greater atmospheric moisture traps more heat and lowers the OLR. This is the strongest warming effect referred to as the *water vapor feedback* (Hansen et al. 1984, Held and Soden 2000, Soden and Held 2006). But the RH profile may also change. The OLR increases logarithmically with RH (Allan et al. 1999, Roca et al. 2000), meaning that the change in OLR with RH is greatest at low relative humidities, e.g. in the dry upper troposphere. If the upper troposphere warms more than the lower troposphere, the lapse rate decreases and the emission to space moves closer to the emission from Earth's surface, making the greenhouse effect less efficient.

These radiative effects due to changes in atmospheric moisture explain the net radiative flux at TOA in the absence of clouds. But when clouds are present, they simultaneously induce a cooling and warming effect on the Earth system. By reflecting incoming shortwave (SW) radiation, clouds prevent it from being absorbed. At the same time, they absorb LW radiation emitted from below at their bases, only to emit it to space from their tops at colder temperatures, thereby reducing the OLR and warming the system. So how will cloud characteristics change with surface warming? Will the cover widen and reflect more SW radiation? Will their altitudes rise and warm the Earth system by emitting LW radiation at even colder temperatures?

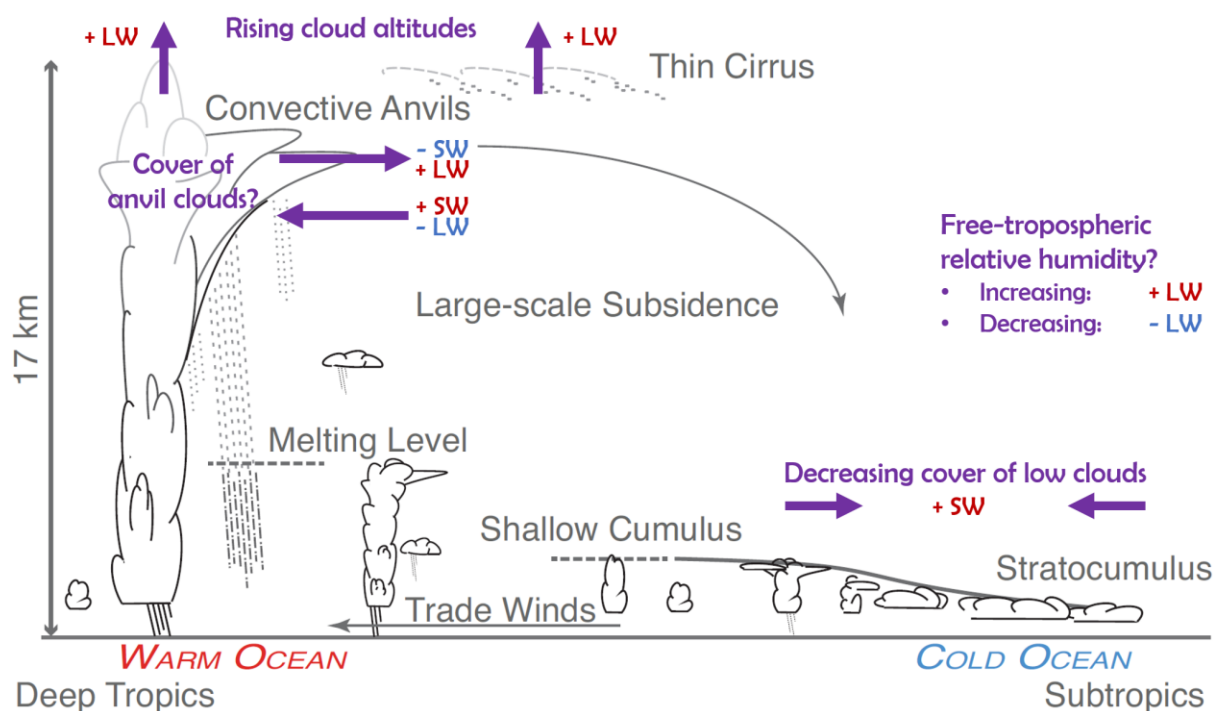


**FIGURE I-2:** Schematic illustration of the tropical water cycle (gray illustrations and text) and selected responses of tropical water cycle variables to warming investigated in this work (purple arrows and text). Expected effects on the TOA radiative flux due to shortwave (longwave) radiation are indicated by “SW” (“LW”). Warming effects are indicated by a positive sign and dark red text, whilst cooling effects by a negative sign and blue text. The background schematic (i.e. text and illustrations in gray) is extracted from IPCC AR5 (2013).

Understanding the changes in water cycle variables with surface warming are hence of apparent importance to make realistic projections of the future climate. These analyses require intense use of numerical climate models, whose description of processes do not converge towards a single behavior but currently propose a wide range of projections (e.g. Vial et al. 2013). Cloud responses to climate change are highlighted by the Global Energy and Water cycle Exchanges (GEWEX) as one of the grand challenges and a major uncertainty for climate sensitivity estimates and modelled circulation, and the need to improve the understanding of processes linking clouds, circulation of atmospheric water and climate is a key issue for the numerical models built to anticipate climate changes (Bony et al. 2015).

In my PhD thesis I aim at progressing on our understanding of the covariability of surface temperature, water vapor, clouds and precipitation in the tropical belt by analyzing satellite observations of these key water cycle variables. This general introduction gives a brief overview of our interest in the tropical atmospheric water cycle. The rest of the manuscript investigates these aspects in more detail, starting with Chapter 1 (next) that introduces our knowns and unknowns of the tropical atmospheric water cycle in a changing climate and why it is important to improve on its uncertainties. It ends by stating the principal science questions asked in my thesis, and with an outline for the rest of the manuscript.



# Chapter 1

## 1 Context

1	Context .....	6
1.1	Complexity Facets of the Atmospheric Water Cycle .....	7
1.1.1	Earth's Radiative Equilibrium .....	7
1.1.2	Water Microphysics .....	9
1.1.3	The Tropical Large-Scale Circulation.....	10
1.2	Radiation and the Water Cycle.....	12
1.2.1	Radiative Forcing and Climate Feedbacks .....	12
1.2.2	Clear-Sky Feedbacks .....	14
1.2.3	Cloud Feedbacks and Radiative Effects.....	16
1.3	Principal Hypotheses About the Tropical Atmospheric Water Cycle's Response to Surface Warming.....	19
1.4	Present Day Limitations with Observations and Models.....	23
1.4.1	Observational Limitations .....	23
1.4.2	Model Limitations.....	25
1.5	Principal Science Questions.....	26
1.5.1	Focus on the Instantaneous Timescale and Large-Scale Regimes.....	26
1.5.2	Focus on Different Temporal and Spatial Scales.....	26
1.5.3	Dataset Objective.....	27
1.5.4	Manuscript Structure.....	27

This first chapter presents our current knowns and unknowns of the tropical atmospheric water cycle in a changing climate and why it is important to improve on its uncertainties. Sect. 1.1 introduces some basic concepts of Earth's radiative equilibrium, the tropical large-scale circulation and the role of atmospheric water in these. Sect. 1.2 explains the concept of radiative forcing and climate feedbacks. Better understanding of covariations of the tropical atmospheric water cycle variables under surface warming is motivated by these terms being associated with the most uncertainty in the feedback equation. Sect. 1.3 explains some of the most discussed hypotheses concerning the tropical atmospheric water cycle's response to surface warming. Sect. 1.4 discusses the usage of observations and models and in Sect. 1.5, I have summarized the specific science questions that I ask in my PhD, which shapes the manuscript outline and the upcoming chapters.

## 1.1 Complexity Facets of the Atmospheric Water Cycle

### 1.1.1 Earth's Radiative Equilibrium

In radiative equilibrium, there is a balance between incoming and outgoing radiation at the top of the atmosphere (TOA). The Earth system (atmosphere and surface) is heated by absorption of solar radiation (*shortwave*, SW wavelengths  $\lambda < 4 \mu\text{m}$ ) and cools by emitting *longwave* radiation (LW,  $\lambda > 4 \mu\text{m}$ ) to space. The emission of LW radiation to space (*outgoing longwave radiation*, OLR) does however not take place at the Earth's surface ( $T \approx 288 \text{ K}$ ), but at an altitude higher up in the atmosphere of colder emission temperature ( $T \approx 255 \text{ K}$ ). The reason is numerous selective absorbers in the Earth's atmosphere (*greenhouse gases*, GHGs) that are active in Earth's LW spectrum. Figure 1-1 shows the absorption spectrum of some of Earth's most important atmospheric GHGs.

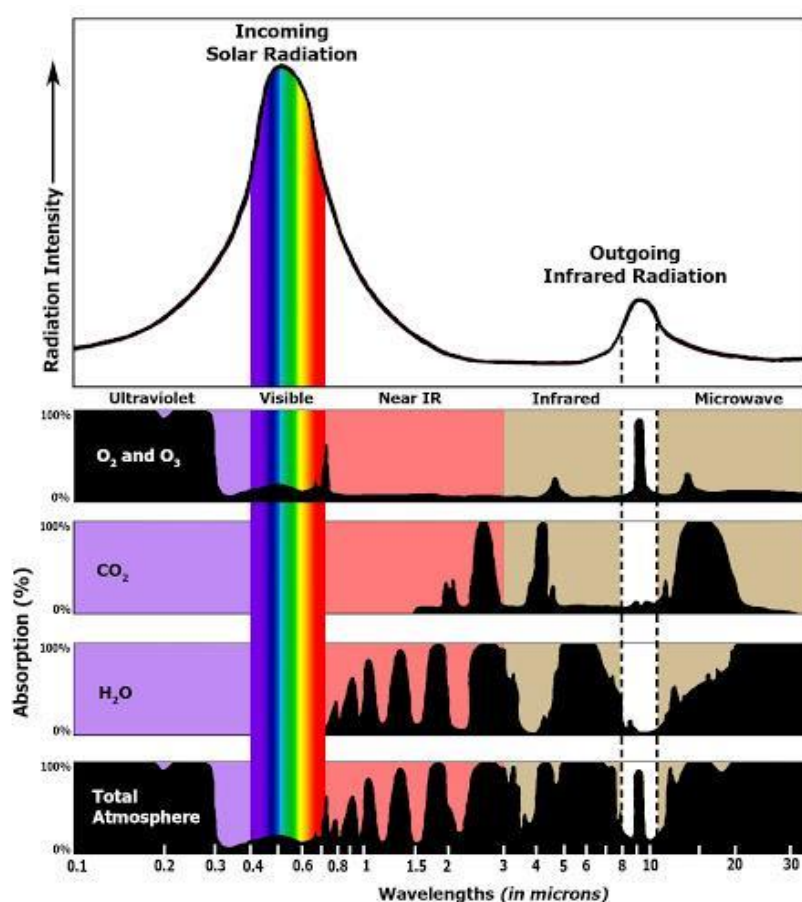


**FIGURE 1-1:** Absorption spectra of the primary greenhouse gases in Earth's atmosphere. The figure is extracted from NASA's Climate Science Investigations (see link). Accessed May 31, 2020.

<http://www.ces.fau.edu/nasa/module-2/how-greenhouse-effect-works.php>

Water vapor is the principal GHG and atmospheric absorber of IR radiation. It is active over almost the full range of wavelengths radiated by the Earth, apart from the *atmospheric window* between 8 and 12  $\mu\text{m}$  (Ahrens 2013). Additionally, the bent orientation of the water molecule gives it a permanent dipole moment, which makes it an effective absorber of all wavelengths longer than 20  $\mu\text{m}$  (at the right edge of Fig. 1-1). Due to the redundancy of water vapor, IR wavelengths are predominantly emitted to space at the atmospheric altitude level where water vapor remains in enough quantities to render even thin atmospheric layers opaque

to this radiation, which is the altitude of unit optical depth<sup>1</sup> of water vapor for these wavelengths (Wallace and Hobbs 2006). The warming effect due to GHGs (the *greenhouse effect*, GHE) is effectively the difference between the energy emitted by the Earth's surface and the energy emitted to space at the top of the atmosphere (TOA) (e.g. Ramanathan and Collins 1991).

The total instantaneous solar irradiance is  $1360.8 \text{ Wm}^{-2}$ , or  $340 \text{ Wm}^{-2}$  averaged over the global sphere. Out of the  $340 \text{ Wm}^{-2}$  received from the sun, about  $100 \text{ Wm}^{-2}$  is reflected by clouds and atmospheric aerosols (e.g. sulfates, nitrates), leaving  $240 \text{ Wm}^{-2}$  to be absorbed by Earth's atmosphere ( $79 \text{ Wm}^{-2}$ ) and surface ( $161 \text{ Wm}^{-2}$ ), as illustrated in Fig. 1-2 (Wild et al. 2013). The planetary *albedo* (the fraction of SW radiation scattered back to space by the Earth system) is thus 0.29 (Stephens et al. 2015).

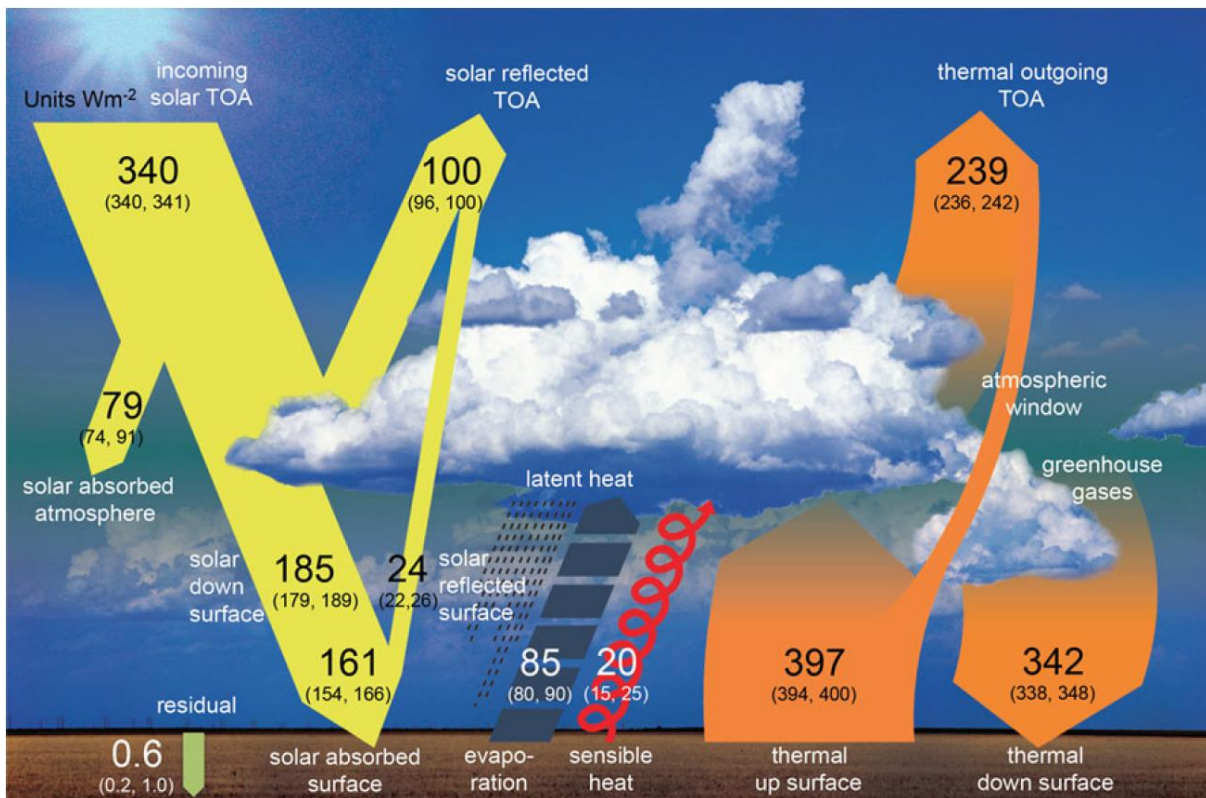


**FIGURE 1-2:** Schematic diagram of the Earth's global mean energy balance at the beginning of the 21st century. Large numbers indicate the best estimates and numbers in parentheses the uncertainty range. The figure is extracted from Wild et al. (2013).

In global radiative equilibrium, there is a balance between incoming and outgoing radiation at TOA. This is almost true, as  $239 \text{ Wm}^{-2}$  of LW radiation is emitted from the Earth system at TOA (Fig. 1-2). The globally averaged TOA net imbalance<sup>2</sup> (the net downward heat flux) is  $0.6 \text{ Wm}^{-2}$  (Stephens et al. 2012, IPCC AR5 2013). This is how much the Earth system accumulates heat excess. About 93 % of this excess heat is stored in the ocean, whilst only 1 % in the atmosphere (Loeb et al. 2018).

<sup>1</sup> Above the level of unit optical depth, absorption and emission are negligible. Far below this level, the transmissivity of the overlying layer is so small that very little radiation passes through, meaning that most of the radiation has already been absorbed (Wallace and Hobbs 2006).

<sup>2</sup>A more recent value of  $0.7 \text{ Wm}^{-2}$  was computed in Loeb et al. (2018).

### 1.1.2 Water Microphysics

The basic concepts of water microphysics presented in this subsection are typically found in basic textbooks on atmospheric science (e.g. Wallace and Hobbs 2006, Ahrens 2013).

#### Humidity

The *relative humidity* (RH) of a parcel of air is measured as the ratio of vapor pressure to the saturation vapor pressure (multiplied by 100 for the percentage). The *vapor pressure* is the pressure exerted by all the water vapor molecules bouncing off the parcel's interior and the *saturation vapor pressure* the pressure exerted by them in a saturated parcel. The saturation vapor pressure increases with temperature (Clausius-Clapeyron equation, Eq. A1-11), which means that the mass of water vapor to the total mass of all the parcel's molecules (the *specific humidity*) increases with temperature under constant RH.

#### Thermodynamics of Phase Changes of Atmospheric Water

The strong hydrogen bondings between water molecules require much energy to break apart. In order to melt ice into liquid water, the ice must absorb energy from its surroundings to energize the water molecules and weaken the attractive forces between them. The amount of energy required for this phase transition (the *heat of fusion*) from solid ice to liquid water is  $3.34 \times 10^5 \text{ J kg}^{-1}$ . Evaporation of liquid water to water vapor then happens in two steps: First, we must add heat to raise the temperature of the liquid water to  $100^\circ\text{C}$  ( $4.19 \times 10^5 \text{ J kg}^{-1}$ ). Second, we must apply additional heat in order for the phase transition from liquid to vapor ( $2.25 \times 10^6 \text{ J kg}^{-1}$ ), referred to as the *heat of vaporization*. These numbers are taken from Wallace and Hobbs (2006).

What we just described were *endothermic* processes in which energy is removed (absorbed) from the surrounding environment. The process can however occur in the other direction as well (i.e. from the gaseous vapor phase to the solid ice phase), in which case the heat of vaporization and heat of fusion are released in the *exothermic* processes of *condensation* and *freezing*, respectively. The process occurs in both directions in the atmosphere.

These latter exothermic processes are key elements for the process of convection (which is an essential process for tropical heat distribution). When the air becomes supersaturated, atmospheric water vapor condenses onto cloud condensation nuclei and forms clouds. As the vapor condenses it releases its heat of vaporization that has been stored (*latent heat*) to its surroundings. The warmer surrounding air rises due to increased atmospheric instability and condenses at a higher altitude, thereby raising the cloud height. For temperatures below the  $0^\circ\text{C}$  isotherm, ice particles may begin to form on ice condensation nuclei. Because the saturation vapor pressure with respect to ice is less than that of liquid, ice particles grow at the expense of its neighbouring supercooled liquid droplets, when water molecules diffuse from the latter to the former (Wegener 1911, Bergeron 1935, Findeisen 1938). Again, latent heat is released, when less energy is required to keep ice particles in an equilibrium state compared to liquid particles.

Deep convective clouds and systems (e.g. thunderstorms, tropical cyclones) are fueled by the latent heat released when cloud droplets and ice crystals form. Latent heat is the principal energy transport from the surface to the atmosphere in the tropics and responsible for driving the tropical circulation (Sect. 3.1.1.3).

Additionally, liquid and ice phase clouds have important implications on the Earth's radiative balance (as discussed in Sect. 3.1.2.3) by reflecting incoming SW radiation (primarily thick optically clouds) and trapping OLR (primarily high ice clouds).

### 1.1.3 The Tropical Large-Scale Circulation

This subsection introduces atmospheric circulations in the tropical belt. The information can be found in standard textbooks on atmospheric circulation, like Ahrens 2013 or Holton 2013, which I consulted for details to this description.

The radiative energy balance at TOA is maintained for the closed Earth system, but not for individual regions. The equatorial belt receives the most solar radiation (more than the IR it emits), whilst the poles emit more IR radiation than it receives by the sun. The equatorial energy surplus and polar deficit give rise to a poleward heat transfer within the Earth system, carried by atmospheric winds and ocean currents.

Figure 1-3 illustrates the large-scale circulation in the tropical belt (referred to here as between 30°S to 30°N). From a zonal (latitudinal) perspective, the excessive heating of the equatorial belt forces the surface air to rise, causing surface low pressure there (1-3a). As the warm air rises, it expands and cools. The water vapor it carries condenses into clouds and precipitation, and releases massive amounts of latent heat stored in the water that fuels the ascent by making the air more buoyant.

At the tropopause inversion, the flow is deflected laterally towards the poles. The air grows denser as the air travels poleward due to IR cooling and converging longitudes. Around 30° latitude surface pressure has increased so much that the dense air sinks. As the air descends it is heated by compression, causing a band of semi-permanent high pressure systems in the subtropical region, characterized by clear skies and warm surface temperatures. At the surface level, the air is again deflected laterally. A part of it returns to the equatorial surface low pressure, deflected by the Coriolis force, causing an easterly equatorward return flow, also known as the *trade winds*. Trade winds in the Northern and Southern hemispheres converge at the equator along a boundary referred to as the *Intertropical Convergence Zone (ITCZ)*, characterized by strong ascent and vigorous convection. This atmospheric cell between the equator and 30° latitude is referred to as the *Hadley cell*<sup>3</sup> (Fig. 1-3a).

Superimposed on the zonally distributed Hadley cell, are zonally asymmetric atmospheric circulations (1-3b), caused by longitudinal variations in sea surface temperature. The easterly trade winds drag the equatorial surface water westward, concentrating the warm surface waters off the east coasts of tropical land masses and raising the sea level there, whilst lowering the sea level off the west coast of tropical continents and promoting upwelling of cooler ocean waters there. This is best seen in the tropical Pacific (Fig. 1-3c), with the *Pacific Warm Pool* region in the west (covering Oceania and usually extending into the Indian Ocean) and cold waters off the west coast of Peru.

---

<sup>3</sup> The Hadley cell is named after the English meteorologist George Hadley. For more information about the atmospheric general circulation (e.g. the Ferrel cell between 30° and 60° or the Polar cell between 60° and 90°), the reader is referred to standard textbooks on atmospheric physics (e.g. Wallace and Hobbs 2006, Ahrens 2013, Holton 2013)

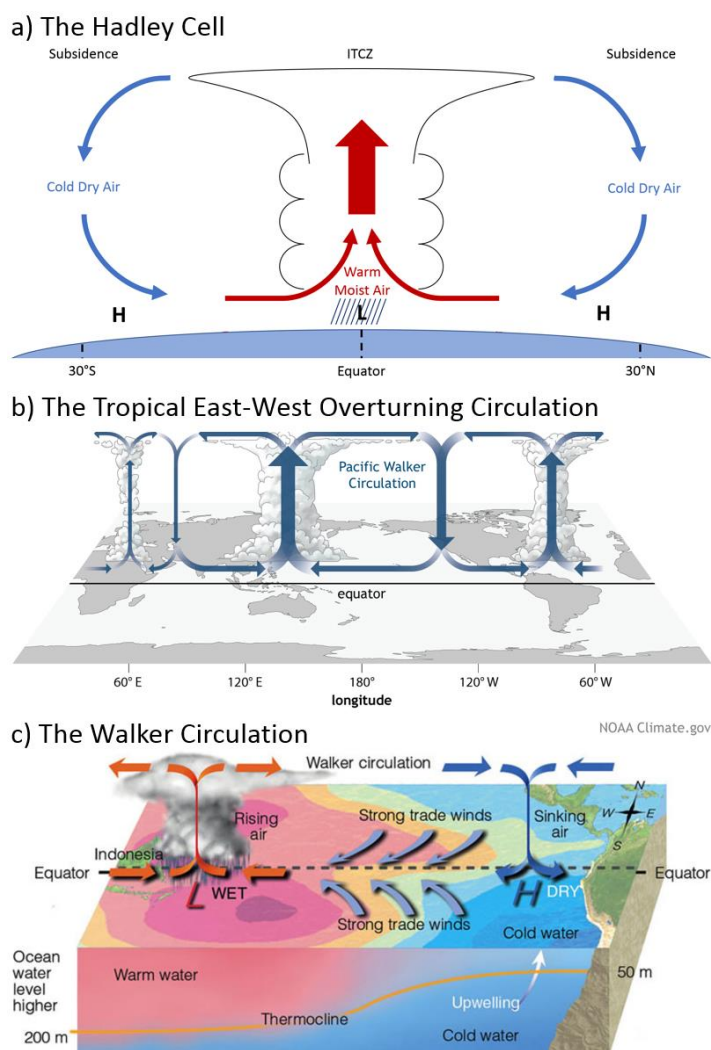


**FIGURE 1-3:** Illustration of the tropical large-scale circulation. a) The Hadley cell, the meridional tropical circulation. b) The zonal tropical large-scale circulation. c) The Pacific Walker circulation (as also located in b). Notations “H” and “L” stand for surface high and low pressures respectively. Subplot c is extracted from Ahrens 2013 (reprinted from Cengage Learning) and subplot b from NOAA Climate.gov. (accessed on May 27, 2020): <https://www.climate.gov/news-features/blogs/ens0/walker-circulation-ensos-atmospheric-buddy>

Thus, tropical atmospheric processes are subject to both dynamic (linked to atmospheric circulation) and thermodynamic (linked to temperature) (Sect. 1.1.2) influences, where cloud formation is sensitive to both albeit predominantly to the former (Bony et al. 2004). The large-scale circulation (dynamical) can be observed by measures of vertical velocity. The most common proxy for large-scale circulation is perhaps the vertical pressure velocity at the 500 hPa level (e.g. Su et al. 2011, Konsta et al. 2012, Vaillant de Guélis et al. 2017, Chepfer et al. 2019), which is the parameter that I employ in Ch. 3 as a proxy for the tropical large-scale circulation.

## 1.2 Radiation and the Water Cycle

This section discusses current knowns and unknowns of the interactions of radiation and the water cycle. Sect. 1.2.1 introduces the concept of radiative forcing and climate feedbacks. It is with respect to the current principal uncertainties for solving the feedback equation that my work is motivated, i.e. the rate of change of water cycle variables with surface temperature. The principal climate feedbacks are separated into clear-sky feedbacks (Sect. 1.2.2) and cloud feedbacks (Sect. 1.2.3) and explained in more detail in these sections.

### 1.2.1 Radiative Forcing and Climate Feedbacks

The radiative balance at TOA has been perturbed by a *radiative forcing*  $F$ , induced by an anthropogenic increase in greenhouse gas concentrations (IPCC AR5, 2013), which gives rise to a net downward radiation at TOA ( $\Delta R$ ) and an accumulation of energy in the Earth system that will ultimately force the climate to change and establish a new equilibrium surface temperature  $T_s$  (Rose and Rayborn 2016). The climate feedback formalism assumes that changes in radiative flux are proportional to changes in surface temperature. Then, the global energy imbalance at TOA can be written

$$\Delta R = F + \lambda \Delta T_s \quad (\text{E1-1})$$

where the constant of proportionality  $\lambda$  is the total climate feedback parameter (Charney et al. 1979), assumed to be timescale-invariant (Gregory et al. 2004). Eventually, the Earth system will adjust to this imbalance, as  $\Delta R$  goes to zero when the warmer planet emits more energy to space (Rose and Rayborn 2016, Goosse et al. 2018). The adjustment time differs however between the Earth system's components (atmosphere, ocean, continent, cryosphere, etc.), and a new equilibrium temperature is not achieved until all components have adjusted to the forcing. With  $\Delta R = 0$ , the ultimate change in global surface temperature  $\Delta T_s$  due to the radiative forcing is characterized by:

$$F = -\lambda \Delta T_s \quad (\text{E1-2})$$

The assumption of linear dependence on  $\Delta T_s$  implies that the total climate feedback parameter can be decomposed into individual additive components, each one representative of a different radiative process internal to the Earth system (Wallace and Hobbs 2006):

$$\lambda = \sum_j \lambda_j \quad (\text{E1-3})$$

If we insert E1-3 in E1-2 and divide by  $\Delta T_s$ , we can expand the expression and see that the change in radiative flux with surface temperature is both sensitive to atmospheric water cycle variables  $Y_j$  and their responses to changes in surface temperature:

$$\frac{dF}{dT_s} = \frac{\partial F}{\partial T_s} + \sum_j \frac{\partial F}{\partial Y_j} \frac{dY_j}{dT_s} \quad (\text{E1-4})$$

where the last term can be expanded to

$$\frac{dY_j}{dT_s} = \frac{\partial Y_j}{\partial T_s} + \sum_k \frac{\partial Y_j}{\partial Y_k} \frac{dY_k}{dT_s} \quad (\text{E1-5})$$

on account of many of the atmospheric water cycle variables  $Y$  being dependent on each other (e.g. the dependence of clouds  $Y_j$  on humidity  $Y_k$ ). From these expansions we can think of a feedback factor as the sensitivity of a variable to some meteorological predictor, scaled by the change of the control predictor's response to climate change.

Of these terms, the sensitivities of the TOA radiative fluxes to changes in humidity and clouds ( $dF/dY$ ) are fairly well known as they can be reliably estimated from radiative transfer computations (e.g. Liou 2002). In contrast, responses of the water cycle variables to climate warming ( $dY/dT_s$ ) are more uncertain. First order uncertainties are related to how the individual water cycle variables vary with surface temperature ( $dY_j/dT_s$ , E1-4), and second order uncertainties to how the water cycle variables vary with each other ( $dY_j/dY_k$ , E1-5).

The total climate feedback parameter  $\lambda$  is usually decomposed into a sum of five terms: 1) the Planck feedback, 2) the water vapor feedback, 3) the lapse rate feedback, 4) the cloud feedback, and 5) the albedo feedback (Dufresne and Bony 2008):

$$\lambda = \lambda_P + \lambda_{WV} + \lambda_{LR} + \lambda_C + \lambda_\alpha \quad (\text{E1-6})$$

Feedbacks 1 to 4<sup>4</sup> will be described next in sections 1.2.2 and 1.2.3. Figure 1-4 below shows the ensemble mean global radiative feedback estimates from CMIP5 and CMIP6 models. Evidently, the largest intermodel spread is seen for the cloud feedbacks. In fact, cloud responses to climate change are highlighted by the Global Energy and Water cycle Exchanges (GEWEX<sup>5</sup>) as one of the grand challenges and a major uncertainty for climate sensitivity estimates and modelled circulation (Bony et al. 2015).

---

<sup>4</sup> The albedo feedback (5), also called the ice-albedo feedback, is not relevant for the tropical region.

<sup>5</sup> GEWEX is one of the core projects under the World Climate Research Programme (WCRP) dedicated to understanding Earth's water cycle and energy fluxes at and below the surface and in the atmosphere: <https://www.gewex.org/about/>

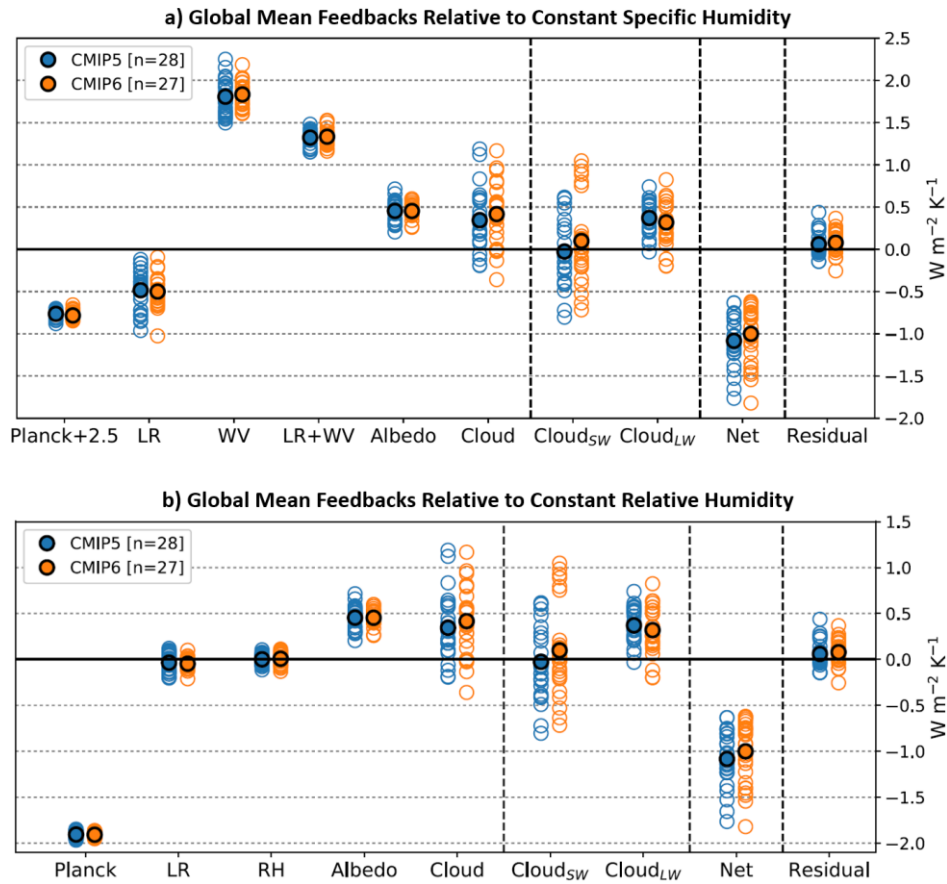


**FIGURE 1-4:** Estimates of global radiative feedbacks from abrupt-4xCO<sub>2</sub> experiments in CMIP5 (blue) and CMIP6 (orange), **a)** relative to constant specific humidity and **b)** relative to constant relative humidity. The subplots are extracted from Zelinka et al. (2020).

### 1.2.2 Clear-Sky Feedbacks

The *Planck feedback* (e.g. Hansen et al. 1984) is the strongest negative climate feedback and results from the Planck function (Eq. A1-1), where the blackbody radiation of an object is a function of its temperature. This is the most fundamental climate feedback, simply stating that the warmer the Earth, the more it radiates.

Following the Clausius-Clapeyron equation (EA-11), specific humidity increases approximately exponentially with temperature (at a rate of about 6 to 7 %  $K^{-1}$ ), under the assumption of constant relative humidity (e.g. Raval and Ramanathan 1989, Allan 2012, Dewey and Goldblatt<sup>6</sup> 2018). The higher concentrations of water vapor increase the greenhouse effect and accelerates the warming. This *water vapor feedback* (Held and Soden 2000) is the strongest warming climate feedback (e.g. Soden and Held 2006, Dessler 2013, Ingram 2013).

The *lapse rate feedback* is due to vertically non-uniform atmospheric heating. If the upper troposphere warms more than the lower troposphere, the lapse rate decreases and the emission to space moves closer to the emission from Earth's surface. Thus, the greenhouse effect is less efficient, and the sign of this feedback is negative. The lapse rate feedback is robustly negative in the tropics where the temperature profile follows the moist adiabatic lapse rate, but can be

<sup>6</sup> Dewey and Goldblatt 2018 observed decreasing OLR for surface temperatures in excess of  $\sim 298$  K, whilst a continued nonlinear increase in column integrated water vapor.

positive in high latitudes in the presence of stable stratification that suppresses vertical mixing, thereby confining the warming to a thin near-surface layer (Soden and Held 2006, Pithan and Mauritsen 2013, Goosse et al. 2018).

But the lapse rate is a function of RH as well, where the non-uniform tropospheric heating can change as a result of non-uniform change in RH with warming. Because the radiative effect (IR absorption) of water vapor is roughly proportional to the logarithm of its relative humidity (Allan et al. 1999, Roca et al. 2000), the radiative impact of a change in water vapor concentration is greatest (smallest) at initially low (high) relative humidities as illustrated in Fig. 1-5 below. A change in the lapse rate can thus result from only a small increase in initial upper tropospheric relative humidity (which is significantly drier than the lower troposphere).

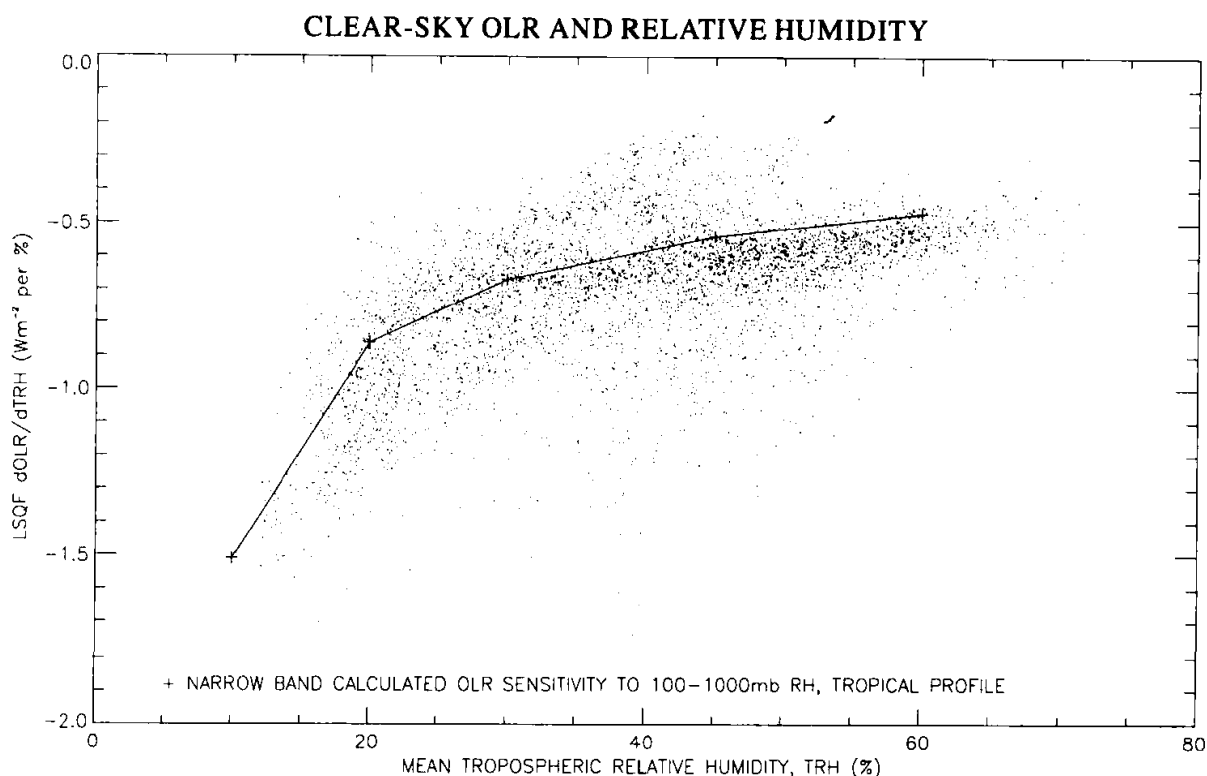


**FIGURE 1-5:** Sensitivity of the change in clear-sky OLR with tropospheric RH ( $dOLR/dTRH$ ) to the mean tropospheric RH from the European Centre for Medium-Range Weather Forecasts ReAnalysis project over the time period 1979 to 1993. The figure is extracted from Allan et al. (1999).

Because these clear-sky feedbacks (Planck, lapse rate, water vapor) are not independent of each other, the effects of them are often combined assuming constant relative humidity, as advocated by Held and Shell (2012). An example of this is seen in Fig. 1-4 above, where the ensemble mean values of these feedbacks are reduced from about  $-3.2 \text{ W m}^{-2} \text{ K}^{-1}$ ,  $-0.5 \text{ W m}^{-2} \text{ K}^{-1}$  and  $+1.8 \text{ W m}^{-2} \text{ K}^{-1}$  respectively, to about  $-1.8$ ,  $-0.1$  and  $+0.05 \text{ W m}^{-2} \text{ K}^{-1}$  (Caldwell et al. 2016, Zelinka et al. 2020). This repartitioning limits the spread in general circulation model (GCM) projections around the ensemble mean (Ingram 2013), reduces the covariance between the lapse rate and water vapor feedbacks (Caldwell et al. 2016), and avoids dealing with feedback computations relative to unrealistic supersaturated base states (Held and Shell 2012).

### 1.2.3 Cloud Feedbacks and Radiative Effects

In cloudy scenes, two competing radiative effects stand against each other; the SW and the LW. At TOA, the cloud radiative effect (CRE) is defined as the difference between the downwelling and upwelling radiative fluxes in all-sky situations minus the difference in clear-sky situations (Matus and L'Ecuyer 2017):

$$CRE = (F^\downarrow - F^\uparrow)_{all\ sky} - (F^\downarrow - F^\uparrow)_{clear\ sky} \quad (E1-7)$$

The shortwave cloud radiative effect (SWCRE) is due to the high albedo of clouds (Stephens et al. 2015). The SWCRE therefore has a cooling effect on the Earth system as it prevents solar radiation from being absorbed. The SWCRE is sensitive to the size of the reflective droplets (liquid cloud droplets are smaller and closer than ice crystals to SW wavelengths), and the condensed water amount (optically thick clouds reflect more than optically thin clouds) (Stephens and Tsay 1990, Hogan et al. 2003, Henderson et al. 2012).

Clouds also absorb LW radiation. Effectively so in the 8 and 11  $\mu\text{m}$  range, thereby closing the atmospheric window (Wallace and Hobbs 2006, Ahrens 2013). The longwave cloud radiative effect (LWCRE) is due to clouds' ability to decrease the OLR, by absorbing surface emitted IR radiation at their bases and emitting OLR from their tops. Because temperature decreases with altitude in the troposphere, the temperature at the cloud top is colder than the surface temperature, so OLR emitted from clouds is less than OLR emitted from Earth's surface. Hence, the LWCRE has a warming effect and the higher the cloud altitude, the colder the emission temperature, and the greater the difference between OLR emitted at cloud top and Earth's surface.

The SWCRE and LWCRE always compete where clouds are present. Because warm low liquid clouds have higher albedo than cold high ice clouds, and because their cloud tops are not much colder than the surface ( $\sim 10$  degrees), the net CRE is dominated by the stronger SWCRE. However, for high ice clouds, the warming LWCRE is considerably more important for the net CRE.

The SW and LW cloud feedbacks are then the changes in SWCRE and LWCRE at TOA with surface warming (Vaillant de Guélis et al. 2018). In the tropics, the principal regions of interest for the SW cloud feedback are tropical subsidence regions off the west coast of continents characterized by low clouds (often referred to as the stratocumulus regions), whilst the LW cloud feedback is interesting for convective regions. Figure 1-6 below shows global mean cloud feedbacks in CFMIP1 and CFMIP2 models. It shows that the LW cloud feedback (red) is dominated by changes in cloud cover ("Amount" in Fig. 1-6), altitude and optical depth, whilst the SW cloud feedback (blue) is only sensitive to cloud cover and optical depth.

The LW cloud feedback is positive in models (e.g. Zelinka et al. 2013, 2016, 2020, Ceppi and Gregory 2017) primarily due to rising cloud altitudes of high clouds with surface warming (Fig. 1-6a,b). The positive sign is only partly offset by decreasing high cloud cover (Fig. 1-6a,b). Rising cloud altitudes and dropping cloud temperatures have also been reported in process-oriented observational studies. For example, Igel et al. (2014), observed rising anvil bases and decreasing cloud-top temperatures measured by CloudSat with warmer surface

temperature. However Vaillant de Guélis et al.<sup>7</sup> (2018) showed that the LW cloud feedback is negative in observations by CALIPSO and CERES, due to decreasing opaque cloud cover with surface temperature. The decreasing opaque cloud cover induces a negative LW cloud feedback whose magnitude is more than twice the positive LW cloud feedback induced by rising opaque cloud altitudes. This is an important result as it shifts (i) the sign of the total observed LW cloud feedback from positive to negative and (ii) the principal determining variable from opaque altitude to cover. How the anvil width changes with surface warming is diverging in previous observational studies (e.g. Lindzen et al. 2001, Rapp et al. 2005, Su et al. 2008, Igel et al. 2014), likely due to different study regions, evaluation methods and observational instruments (Hartmann and Michelsen 2002).

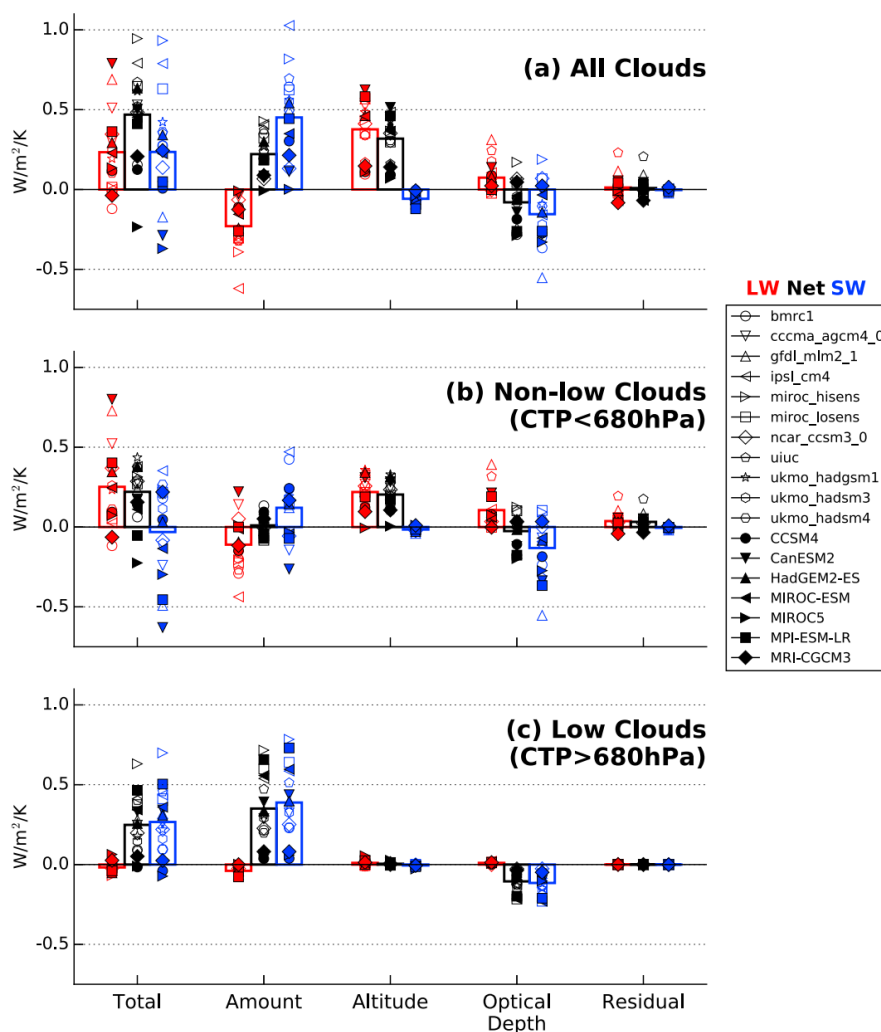


**FIGURE 1-6:** Global mean (red) LW, (blue) SW, and (black) net cloud feedbacks decomposed into amount, altitude, optical depth, and residual components for (a) all clouds, (b) non-low clouds only, and (c) low clouds only. Open symbols are for CFMIP1 models and filled symbols are for CFMIP2 models. Multimodel mean feedbacks are shown as bars. The figure is extracted from Zelinka et al. (2016).

<sup>7</sup> Vaillant de Guélis et al. (2018): CALIPSO, CERES EBAF, monthly global means over ocean surfaces, 2008-2014

Like the LW cloud feedback, the SW cloud feedback is also positive in models (Fig. 1-4, 1-6a). The positive sign is explained by decreasing tropical marine boundary layer cloud cover with SST, which induces a warming due to more SW absorption (1-6c) (Ceppi and Gregory 2017, Zelinka et al. 2012, 2020). The total SW cloud feedback is only partly off-set by increasing cloud optical depth with surface warming, which poses a range of negative SW feedbacks (Fig. 1-6, Zelinka et al. 2016). There seems to be a general consensus on the sign of the rate of change of marine boundary layer cloud cover and SST between model and observational studies (as observed in e.g. Zhai et al. 2015), but the exact rate of change of this decrease is not known and is the principal reason for intermodel spreads (Figs. 1-4, 1-6). The sensitivity of the marine boundary layer cloud cover to SST is identified as an *emergent constraint* (Focus Box 1) and a key uncertainty for climate models (Bony and Dufresne 2005, Ceppi et al. 2017).

### FOCUS BOX 1: EMERGENT CONSTRAINTS

Is there a way to decide which quantities of the current climate are relevant for climate change? *Emergent constraints* (Klein and Hall 2015) answer this question by examining the collective behavior that emerges unexpectedly in climate model ensembles. They are physically explainable empirical relationships between characteristics of the current climate and long-term climate prediction that emerge in collections of climate model simulations (Klein and Hall 2015).

Klein and Hall (2015) identifies the following three potential emergent constraints for cloud feedbacks: (1) low-level cloud optical depth, (2) subtropical marine low-level cloud cover, and (3) lower tropospheric mixing. These are listed in the inserted table below:

Reference	Current climate predictor	Future climate predictand	Primary missing factor
Promising emergent constraints			
Gordon and Klein	The sensitivity of extra-tropical low-level cloud optical depth to temperature	Extra-tropical low-level cloud optical depth response to greenhouse gas-induced warming	Clarification as to which candidate physical mechanisms are dominant
Qu et al.	The sensitivity of subtropical marine low-level cloud cover to sea surface temperature	The twenty-first century change in subtropical marine low-level cloud cover	Demonstration of how the candidate physical explanation accounts for predictor variations
Sherwood et al.	The strength of cloud-scale and large-scale lower tropospheric mixing over oceans	Equilibrium climate sensitivity	Demonstration that the predictor explains variations in low-level clouds better than equilibrium climate sensitivity

The Primary missing factor column contains a subjective quality remark identifying what we see as the leading deficiency preventing classification as a confirmed emergent constraint

Gordon and Klein (2014); Qu et al. (2014); Sherwood et al. (2014)

A key feature for the overall decrease in marine boundary layer cloud cover with SST seems to be a greater moisture contrast between the boundary layer (BL) and the free troposphere (FT) with warmer surface temperatures that can arise either due to enhanced surface latent heat flux, or through greater surface evaporation (Kamae et al. 2016). Regardless, the moisture contrast between the BL and FT means a greater vertical gradient of moist static energy that causes enhanced vertical mixing and drying at the capping inversion, and an effectively deeper BL with horizontally smaller clouds (Brient and Bony 2013, Myers and Norris 2013, Wood and Bretherton 2016).

The study of low cloud cover with SST is motivated by recent work in e.g. Klein et al. (2017) and Zelinka et al.<sup>8</sup> (2020). They found that the sensitivity of low cloud cover to SST was small compared to other cloud controlling factors (estimated inversion strength, RH, pressure velocity), but that the change in SST with unit global warming was about 10 times greater than the change in any of the other cloud controlling factors, making the predicted change in low cloud cover per unit global warming most sensitive to SST.

On the global scale, the Earth system can be thought of as a closed system, but on shorter timescales, local and regional states are dominated by e.g. seasonal or diurnal scale processes. Knowing that different components of the Earth system adjust to a climate forcing on different timescales, and that different atmospheric processes and mechanisms are important on different timescales, how can we assume that the individual feedback terms are timescale-invariant? Klein et al. (2017) assumed sensitivities of the low cloud cover to various cloud controlling factors to be constant in time, but ended their work with a thorough discussion on the validity of the assumption of timescale invariant feedback terms.

### 1.3 Principal Hypotheses About the Tropical Atmospheric Water Cycle's Response to Surface Warming

The previous section discussed changes in clear-sky and cloudy-sky feedbacks separately. This section discusses the collective response of the atmospheric water cycle to SST over the full tropical belt, including both clear-sky and cloud feedbacks. Here I also explain the most discussed hypotheses concerning the tropical atmospheric water cycle's response to surface warming, with special emphasis on the *iris* and *Fixed-Anvil Temperature (FAT)* hypotheses that are investigated in this work.

The hydrological cycle is expected to intensify, with increasing surface evaporation following the warming, making more atmospheric water available for precipitation. Globally, already wet regions (precipitation rate > evaporation rate) grow wetter, whilst dry regions (evaporation > precipitation) become even drier in a nonuniform response of the global water cycle referred to as “wet-get-wetter” and “dry-get-drier” trend (IPCC AR5, 2013). It is illustrated in Fig. 1-7 by observed trends in surface specific humidity over oceans (a) and predicted precipitation changes in the RCP4.5 scenario (c-f).

Hypotheses regarding the responses of the tropical region to surface warming discuss an intensified hydrological cycle, characterized by a narrowing of the ascending branch of the Hadley circulation with stronger updrafts in moist convective regions and horizontally broader clear-sky subsidence regions, as illustrated in the conceptual schematic from Su et al. (2017) based on ensemble means of climate model simulations under global warming (Fig. 1-8).

---

<sup>8</sup> Zelinka et al. (2020) compared results of climate sensitivity and radiative feedbacks in CMIP5 and CMIP6 models.

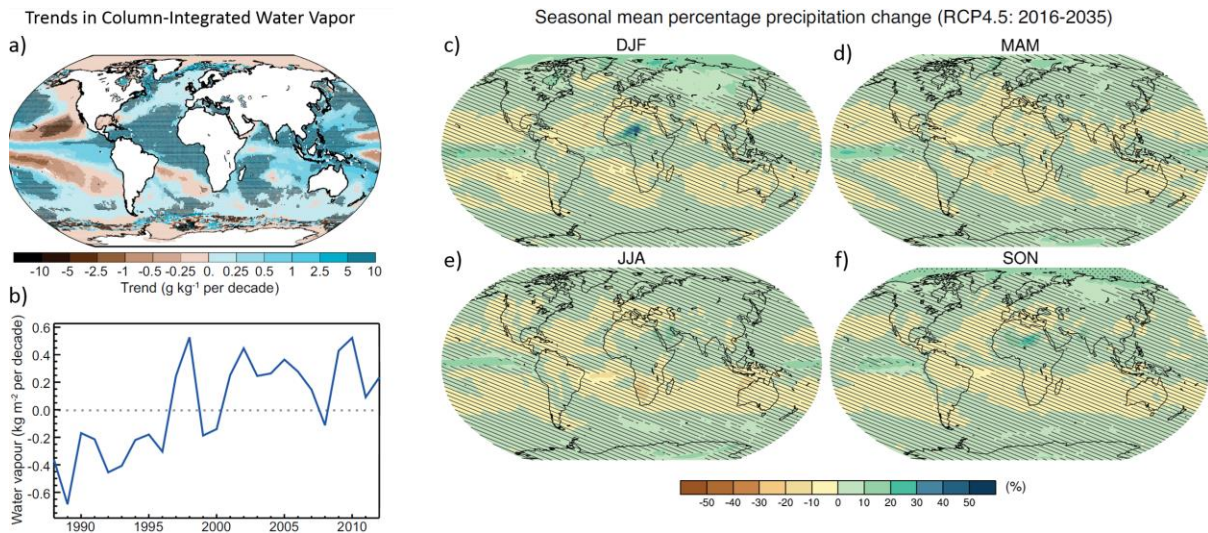


**FIGURE 1-7:** **a)** Trends in column-integrated water vapor observed by the Special Sensor Imager over ocean surfaces over the period 1988 to 2012. **b)** Global annual average column-integrated water vapor over ocean surfaces relative to the 1988 to 2007 average. **c-f)** Seasonal multi-model ensemble mean of 42 CMIP5 models for projected changes in precipitation (%) over the period 2016 to 2035 relative to 1986 to 2005 under RCP4.5. The figures are extracted from IPCC AR5 (2013).

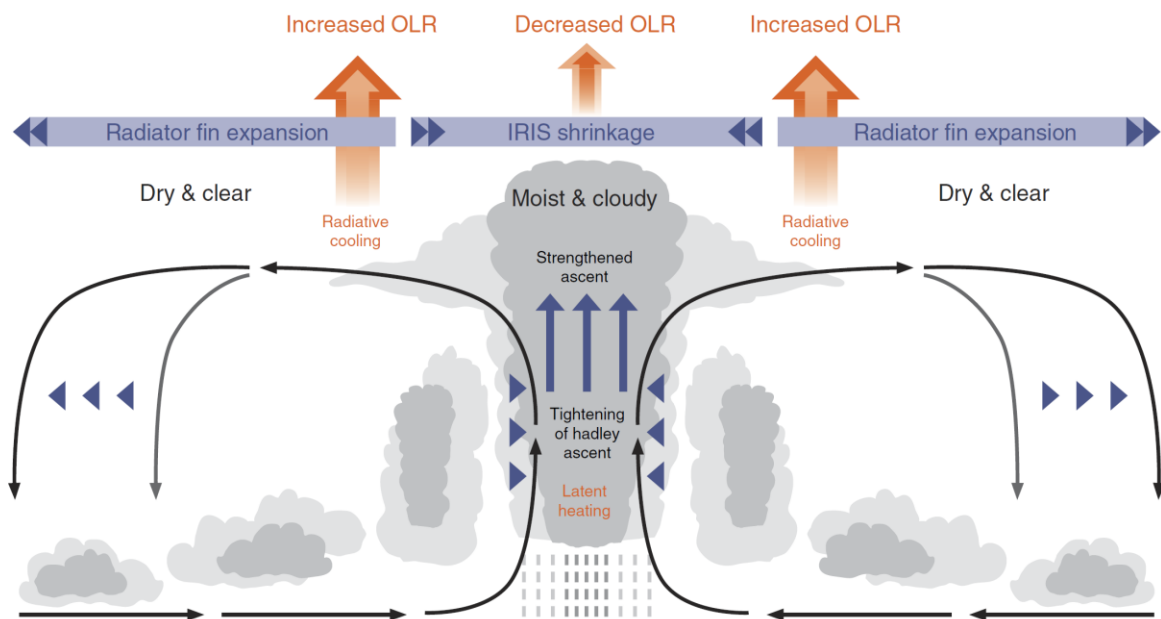


**FIGURE 1-8:** Schematic of the tightening of the Hadley circulation in a warmer climate. Light colors represent the current climate and dark colors a warmer climate. The figure is extracted from Su et al. (2017).

The intensified tropical hydrological cycle is fueled by greater moisture supply from enhanced surface evaporation and horizontal moisture convergence that enable greater latent heat release in the updraft. The stronger updrafts cause convective anvils to rise, but also greater precipitation efficiency, leaving fewer hydrometeors to build up the anvil cloud, effectively shrinking the horizontal extent of the anvil and allowing more OLR to be emitted to space in the clear skies outside of the convective clouds (Su et al. 2017).

This reasoning is the basic theory for the *iris hypothesis* (first postulated by Lindzen<sup>9</sup> et al. 2001, and subsequently revised in e.g. Fu et al. 2002, Hartmann and Michelsen 2002, Lin et al. 2002, 2004, 2006, Su et al. 2008, Mauritsen and Stevens<sup>10</sup> 2015.) in which precipitation efficiency increases with SST, leading to smaller convective anvils and effectively more OLR as fewer hydrometeors are left to build these (Fig. 1-8). Radiatively, the increase in OLR is balanced by an increase in latent heat release due to greater convective precipitation efficiency.

To a first approximation, the iris hypothesis compares the extent of the tropical moist and dry regions. It received its name from the adaptive behavior of the system to open (close) to allow for more (less) OLR to be emitted to space with warmer (colder) surface temperature, in much the same way as the eye's iris opens/closes to light changes (Lindzen et al. 2001). This thinking is in line with Pierrehumbert (1995) who suggested a regulation by the area of large-scale subsidence regions (radiator fins), in which the clear-sky GHE is determined by the water vapor feedback. Such radiator fins (illustrated in Fig. 1-8) are consistent with broader clear-sky subsidence regions with surface warming.

Within a stronger updraft, it is possible that SW reflection increases, which could explain the *thermostat hypothesis*, proposed by Ramanathan and Collins<sup>11</sup> (1991), where thicker cirrus anvils act like a thermostat regulating the amount of SW radiation that can be absorbed by the surface. Observational support for this hypothesis was found in e.g. Lebsack et al.<sup>12</sup> (2010) and Igel et al.<sup>13</sup> (2014).

In the *Fixed-Anvil Temperature hypothesis* (FAT), first presented by Hartmann and Larson (2002) (and subsequently assessed in a number of papers, e.g. Zelinka and Hartmann 2010, 2011, Seeley et al. 2019), cloud altitudes rise in response to surface temperature increase. They rise in such a way that they stay at the same temperatures as before the warming, which means that the temperature at the anvil detrainment level remains constant, making the anvil emission temperatures and the OLR independent of surface temperature. The altitude of anvil detrainment (convective outflow) occurs at the altitude where radiative cooling decreases most rapidly with height, which is where the saturation vapor pressure of water vapor becomes so low that water vapor no longer has a significant effect on the emitted radiation.

---

<sup>9</sup> Lindzen et al. (2001) used cloud observations from the Japanese Geostationary Meteorological Satellite-5 over the western Pacific (30°S to 30°N and 130°E to 170°W).

<sup>10</sup> Mauritsen and Stevens (2015) found that inclusion of an iris effect in the ECHAM6 GCM brought simulated equilibrium climate sensitivity closer to observed values.

<sup>11</sup> Ramanathan and Collins (1991) used radiation data from the Earth Radiation Budget Experiment and sea surface temperature from weather satellites and ships over the time period 1985 to 1989, including the El Niño event in 1987. They found that cirrus anvils were thicker and their SW reflectivity anomaly higher over the warmest sea surface temperatures during the 1987 El Niño event.

<sup>12</sup> Lebsack et al. (2010) found positive correlations between precipitation rate (AMSR-E) and high-cloud reflectivity (CERES-EBAF) in the tropics.

<sup>13</sup> Igel et al. (2014) observed physically thicker cloud anvils and increasing ice water path in convective systems derived from CloudSat observations.

## FOCUS BOX 2: SUPER-GREENHOUSE EFFECT

The super-greenhouse effect (SGE, e.g. Hallberg and Inamdar 1993, Raval and Ramanathan 1989) refers to those tropical locations where the Planck function fails to stabilize the climate (Stephens et al. 2016), which is effectively where OLR decreases with SST. Following the equations outlined in Valero et al. (1997), the greenhouse effect  $G$  can be expressed as:

$$G = \varepsilon\sigma(SST^4) - OLR$$

Where  $\varepsilon$  is the emissivity of the Earth's surface and  $\sigma$  the Stefan-Boltzmann constant. The SGE is thus present when:

$$\frac{dG}{dSST} > 4\varepsilon\sigma(SST^3)$$

Dewey and Goldblatt (2018) find that the decrease in OLR with SST occurs for SSTs  $> 298$  K (Fig. Ba). Column moistening by deep convection in cloudy regions and advection of moisture in clear-sky regions, increases the proportion of OLR that originates from the cold high troposphere rather than the warm surface.

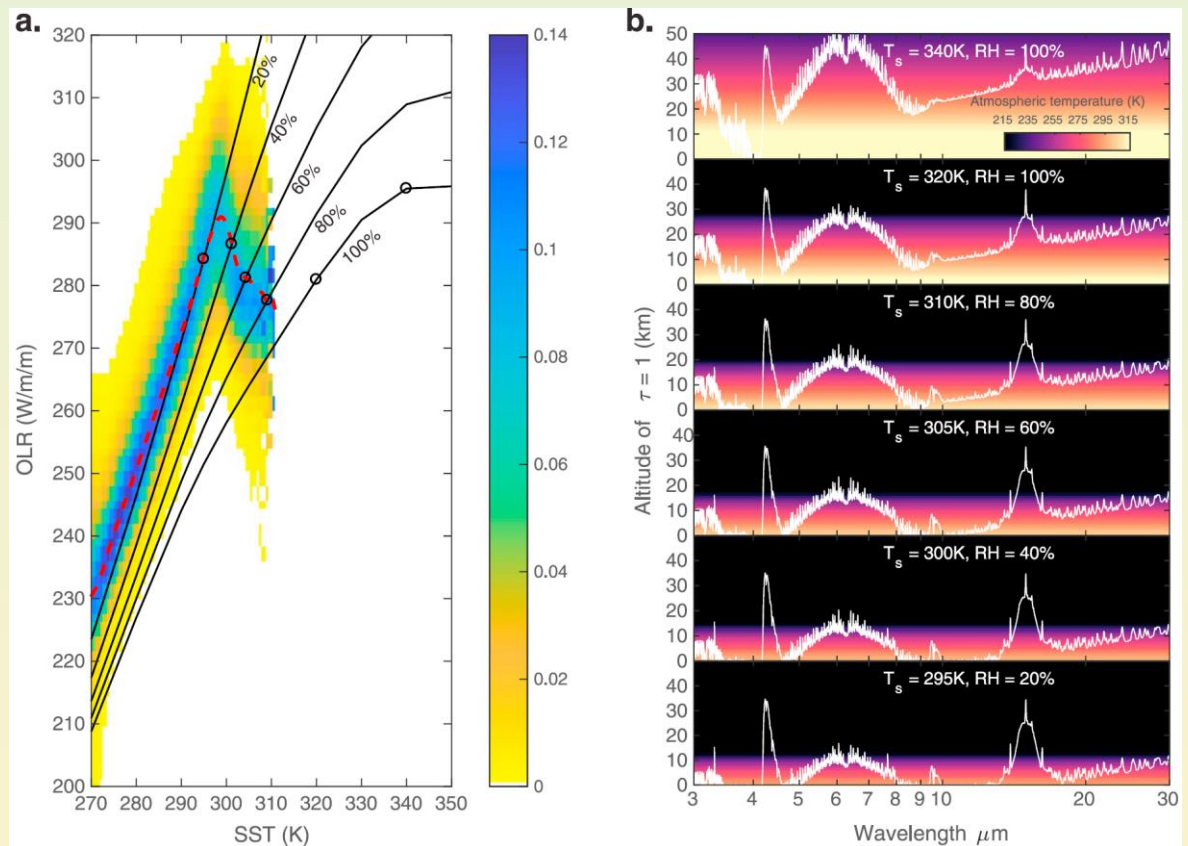


**FIGURE B:** (a) Observational OLR dependence on SST, and OLR output for various humidity values. The red dashed line is the mean, and the black circles correspond to the panels in (b). (b) Spectra of thermal emission altitude. The bottom four panels are the surface temperatures and RH where the observational OLR intersects model curves, and the top two panels are at higher surface temperatures, both with 100 % RH. The background color indicates the atmospheric temperature, and the white line is the altitude at which optical depth is unity. The figure is extracted from Dewey and Goldblatt (2018).

Bony et al.<sup>14</sup> (2016) revisited both the iris and the FAT hypotheses using three GCMs and proposed the idea of a “stability iris mechanism” that links the two, where the detrainment is controlled by stability (the ratio of the radiative cooling to vertical velocity). Tropical stability ( $\sigma$ ) is balanced by radiative cooling ( $Q$ ) and radiatively driven subsidence rate ( $\omega$ ):  $\sigma = Q / \omega$  (Allan 2012). Greater atmospheric moisture associated with warmer temperatures moves the environmental lapse rate closer to the moist adiabatic lapse rate, thus increasing the atmospheric stability and diminishing the radiative cooling and the subsidence rate needed to balance it, resulting in less convective outflow.

## 1.4 Present Day Limitations with Observations and Models

### 1.4.1 Observational Limitations

Issues that deal with circulation, cloud and climate relations require analyses of observations to test for theories and hypotheses. These must be able to accurately sample the key water cycle variables with high temporal and spatial resolution over the full tropical belt, and must cover a long enough time period to account for natural and interannual variability – with the dominant tropical interannual variability being the El Niño-Southern Oscillation.

That said, observations are snapshots of reality that require analysis and theories to explain what they show. The reason is that all variables change together in observations, and they can therefore not be used to study causality. Nor can they be used to study isolated physical processes or mechanisms that require all other aspects of the atmosphere to be held fixed.

For a long time, the observational coverage was limited to land stations or ship tracks at sea. For that reason the observational coverage is much denser and continuous records extend much further back in time over land than over oceans. Fig. 1-9 shows the number of observations made in oceanic  $1^\circ \times 1^\circ$  grid boxes following ship tracks over the first decade in the 19th, 20th and 21st centuries. The top figure shows that the tropical Pacific Ocean was completely unobserved during the 19th and early 20th century. It took until the dawn of the satellite era and the launch of the first weather satellites Vanguard 2, Explorer-6, Explorer-7 and TIROS 1 (Television InfraRed Observational Satellite) in the late 1950s and early 1960s (Capderou 2014) for atmospheric observations to be possible over ocean surfaces outside of ship tracks and unpopulated land surfaces. These satellite observations provided the first global views of the atmospheric water cycle and TOA radiative fluxes. Fig. 1-10 below shows the first image of the Earth taken by a weather satellite. This image was taken by the TIROS 1 satellite, whose objective was to test experimental television techniques designed to develop a worldwide meteorological satellite information system ([https://airandspace.si.edu/collection-objects/tiros-meteorological-satellite/nasm\\_A19650289000](https://airandspace.si.edu/collection-objects/tiros-meteorological-satellite/nasm_A19650289000), accessed September 8, 2020). The satellite carried two television cameras, one of low and a second of high resolution.

---

<sup>14</sup> Bony et al. (2016) conducted their simulations with the GCMs from MPI, IPSL and NCAR.

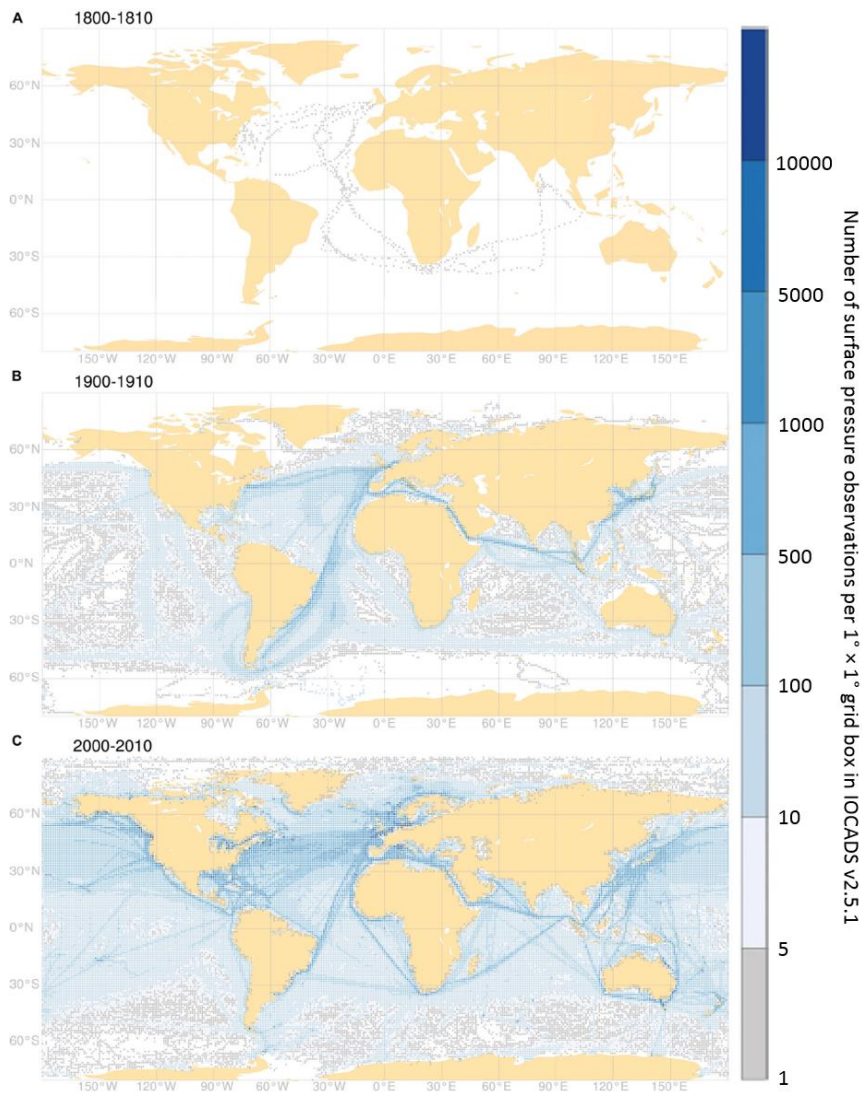


**FIGURE 1-9:** Data counts per  $1^\circ \times 1^\circ$  latitude, longitude of surface pressure observations by ships in the International Comprehensive Ocean-Atmosphere Data Set, used by the National Oceanic and Atmospheric Administration and European Centre for Medium-Range Weather Forecasts 20th century reanalyses, for three selected time periods: (A) 1800–1810, (B) 1900–1910, and (C) 2000–2010. The figure is extracted from Smith et al. (2019).

Back then, satellites were equipped with passive sensors that could not observe the detailed vertical structure of the atmosphere, which is perhaps why previous work only studied one vertical range (e.g. Ross et al. 2002, Gettleman et al. 2006, Läderch and Raible 2013). Detailed observations could be made in field campaigns with radiosondes or aircraft measurements, but as these only observed a local restricted region, they under sampled the tropics and missed the large-scale context. It was not until the turn of the millennium that active sensors (e.g. lidars and radars) were mounted onboard satellites, providing means of detailed observations of global coverage. By now, these instruments have been in use long enough to account for natural variability and detect significant trends.

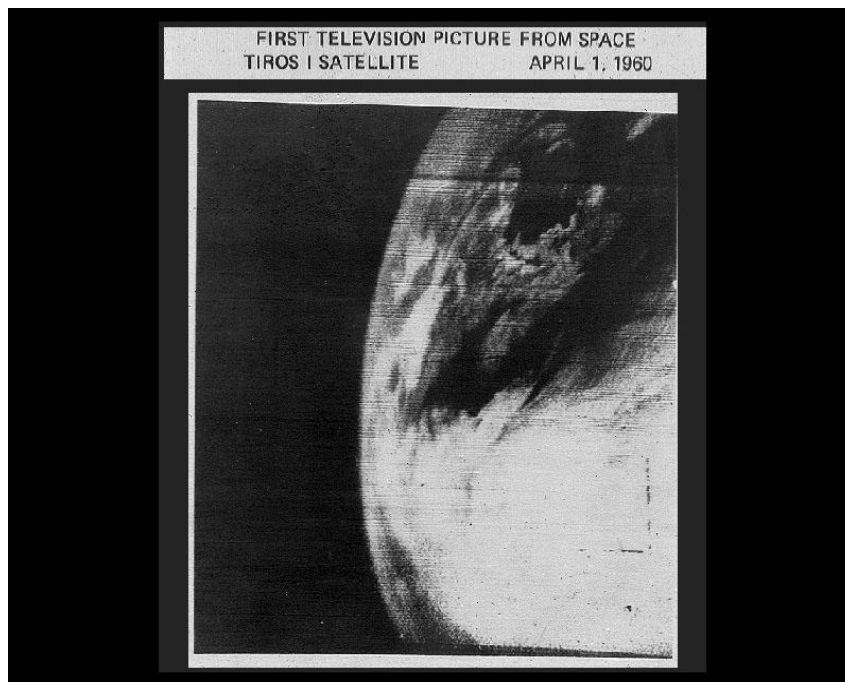


**FIGURE 1-10:** The figure shows the first image taken of the Earth by a weather satellite, the TIROS 1 satellite. It is extracted from NASA (accessed September 8, 2020): [https://www.nasa.gov/vision/earth/features/bm\\_gallery\\_3.html](https://www.nasa.gov/vision/earth/features/bm_gallery_3.html)

## 1.4.2 Model Limitations

In contrast to observations, climate models are very useful for tracking processes as well as for projections of historical and future climate scenarios. They are rooted to their best ability in physical laws, but all equations cannot be solved analytically, which is why the models must rely on numerical estimations and parameterizations.

However, not all processes are described equally in all models, nor do they all make the same assumptions. This leads to significant intermodel spreads of key results with a wide range of projections (as illustrated in Figs. 1-4 and 1-6) when the models do not converge towards a single behavior (e.g. Andrews et al. 2012, Vial et al. 2013, Po-Chedley et al. 2018, Zelinka et al. 2016, 2020). This is particularly concerning for feedback mechanisms and climate sensitivity that must be computed by numerical models.

Still, as computer power increases and more data storage is made available, climate model performance is constantly advancing, with more accurate predictions of higher resolutions and longer records.

## 1.5 Principal Science Questions

Given that the primary feedback uncertainties are derived to uncertainties in how moisture and clouds vary with surface warming, this work aims to improve on our understanding of the relationships between the RH profile and cloud characteristics with SST.

### 1.5.1 Focus on the Instantaneous Timescale and Large-Scale Regimes

Short and local scales are where we come the closest to observing covariations of variables of interest. Instantaneous observations of one or two of the key water cycle variables (moisture, clouds, precipitation) have been made in the past, but the study in Chapter 3 observes instantaneous covariations of the RH profile and cloud cover with SST over the full tropical belt and under the influence of the large-scale circulation. The principal questions asked are:

- Do RH and cloud cover vary differently with SST under large-scale ascent and descent?
- Do RH and cloud cover vary differently with SST in the presence and absence of precipitation?
- Do low liquid and high ice cloud covers vary differently with SST?
- Does the RH profile vary differently with SST in the vicinity of low liquid clouds and high ice clouds?

### 1.5.2 Focus on Different Temporal and Spatial Scales

Chapter 3 studies covariations of some of the key components of the tropical atmospheric water cycle on the instantaneous grid box scale. It is thus restricted to one temporal scale and one spatial scale. In contrast, the study in Chapter 4 assesses the dependence of the water cycle variables' covariations and responses to SST warming on the choice of temporal and spatial scale by observing them on four different timescales (daily, monthly, seasonal, annual), as well as in both spatially global values and more process-oriented grid box values.

Spatial and temporal scales are not independent of each other, as the larger the atmospheric system/phenomenon, the longer its expected lifespan or the adjustment time to changes for the components and variables it interacts with (e.g. Orlanski 1975, Steyn et al. 1981). Process-oriented studies are best executed on small and short spatial and temporal scales, whilst climatological long-term trends are most relevant on the global scale, as climate change is constrained by the global energy budget and the net radiative flux at TOA. Time-varying climate predictions have previously been made with models (e.g. Armour et al. 2013, Gregory and Andrews 2016), but I am unaware of observational studies that deal with the sensitivity of the atmospheric water cycle to surface temperature across timescales.

The principal questions asked in this study are:

- How do RH and cloud cover, altitude, temperature vary with SST on different timescales? This question targets the principal uncertain terms in the feedback equation.
- How does the low cloud cover vary with SST on different timescales? This question is central to the SW cloud feedback.
- How do high ice cloud characteristics (cover, altitude, temperature) vary with SST over the warmest waters? This question is central to the LW cloud feedback and relates to both the iris and FAT hypotheses.
- How do cloud characteristics covary and how do they vary with the RH profile? These are the second order uncertain terms in the feedback equation.

Secondary questions ask if the signs and magnitudes of these rates of changes are robust across timescales? These are novel questions from an observational perspective.

### 1.5.3 Dataset Objective

Answers to the science questions listed above require a comprehensive observational dataset. In Chapter 2, I build a dataset of observational diagnostics on a regular grid of  $1^\circ \times 1^\circ$  spatial resolution that can be directly relatable to climate studies. This resolution is a common standard today, which roughly translates into  $100 \text{ km} \times 100 \text{ km}$  in the tropics.

### 1.5.4 Manuscript Structure

To answer these questions, I have built a synergistic dataset of collocated instantaneous observations of the tropical atmospheric water cycle. Chapter 2 presents these observational products and the instrument payloads from which they are retrieved. In Chapter 3, I assess how the RH profile and cloud cover varies with SST on the instantaneous timescale under the influence of the tropical large-scale circulation (i.e. the questions asked in Sect. 1.5.1). In Chapter 4, I assess the dependence of the water cycle variables' covariations and responses to surface warming on the choice of temporal and spatial scale by observing them on four different timescales (daily, monthly, seasonal, annual), as well as in both spatially global values and more process-oriented grid box values (the questions asked in Sect. 1.5.2). I end this manuscript by a concluding chapter, where I have summarized the answers to the principal science questions and put the results in perspective.



## Chapter 2

### 2 The Synergistic Dataset

2	The Synergistic Dataset.....	29
2.1	Introduction to the Dataset.....	30
2.2	Relative Humidity from SAPHIR .....	32
2.2.1	The Megha-Tropiques Mission.....	32
2.2.2	The SAPHIR Microwave Radiometer .....	34
2.2.2.1	Microwave Sounding of Water Vapor .....	34
2.2.2.2	The SAPHIR Sounder .....	35
2.2.3	RH Profile Retrievals from SAPHIR.....	36
2.2.4	The Gridded RH Product.....	37
2.2.5	Advantages and Limitations with SAPHIR.....	38
2.2.5.1	Advantages .....	38
2.2.5.2	Limitations.....	39
2.3	Cloud Characteristics from GOCCP.....	40
2.3.1	The A-Train Constellation.....	40
2.3.2	The Lidar CALIOP .....	41
2.3.2.1	Lidar.....	41
2.3.2.2	CALIOP .....	42
2.3.3	Single Profile GOCCP-OPAQ.....	42
2.3.4	The Gridded Cloud Product.....	45
2.3.5	Advantages and Limitations with GOCCP.....	47
2.3.5.1	Advantages .....	47
2.3.5.2	Limitations.....	47
2.4	Near-Surface Precipitation from the CloudSat 2C-PRECIP-COLUMN Product .....	47
2.4.1	CloudSat's Cloud Profiling Radar .....	47
2.4.1.1	Radar .....	47
2.4.1.2	The Cloud Profiling Radar .....	49
2.4.2	Single Column: Retrievals from the 2C-PRECIP-COLUMN Product .....	49
2.4.3	The Gridded Precipitation Product .....	51
2.4.4	Advantages and Limitations with CloudSat 2C-PRECIP-COLUMN.....	53
2.4.4.1	Advantages .....	53
2.4.4.2	Limitations.....	53

2.5	Surface Temperature and Vertical Pressure Velocity from ERA5 .....	54
2.5.1	ERA5 Reanalysis .....	54
2.5.2	The ERA5 Variables Used in This Work .....	54
2.5.2.1	Skin Surface Temperature .....	54
2.5.2.2	Atmospheric Vertical Pressure Velocity .....	55
2.5.3	Advantages and Limitations with ERA5 .....	56
2.5.3.1	Advantages .....	56
2.5.3.2	Limitations .....	57
2.6	Satellite Collocations .....	57

## 2.1 Introduction to the Dataset

Better understanding of how the key tropical atmospheric water cycle variables (temperature, moisture, clouds, precipitation, radiation) covary under climate warming lacks a comprehensive observational view. As discussed in Ch. 1, previous observational work typically did not observe the detailed vertical structure of the tropical atmospheric water cycle and the instantaneous covariations between its key variables (moisture, clouds, precipitation). Or if they did, they under sampled the tropical region and therefore missed the large-scale context.

To answer the science questions asked in Ch.1, I have built a synergistic dataset of collocated instantaneous observational products, encompassing the atmospheric water cycle over the tropical belt (30°N to 30°S) on a  $1^\circ \times 1^\circ$  spatial grid. This chapter presents these observational products and the instrument payloads from which they are retrieved, as well as their principal advantages and limitations. Each instrument payload and the variables retrieved from it, is the focus of one section.

The dataset includes:

- the relative humidity profile, observed by the passive microwave radiometer SAPHIR (Sounder for Atmospheric Profiling of Humidity in the Intertropics by Radiometry) onboard the Megha-Tropiques satellite (presented in Sect. 2.2)
- cloud characteristics, observed by the lidar CALIOP (Cloud-Aerosol Lidar with Orthogonal Polarization) onboard the CALIPSO (Cloud-Aerosol Lidar and Infrared Pathfinder Satellite Observations) satellite (presented in Sect. 2.3)
- near-surface precipitation, observed by the cloud profiling radar (CPR) onboard the CloudSat satellite (presented in Sect. 2.4)
- reanalyses of skin surface temperature and vertical pressure velocity from the 5<sup>th</sup> generation of the European Centre for Medium-Range Weather Forecast's (ECMWF) reanalyses (ERA5: ECMWF ReAnalysis) (presented in Sect. 2.5)

This dataset is illustrated in Figure 2-1. It is meant to enable statistical representations of the tropical atmospheric water cycle variables at selected moments in time.

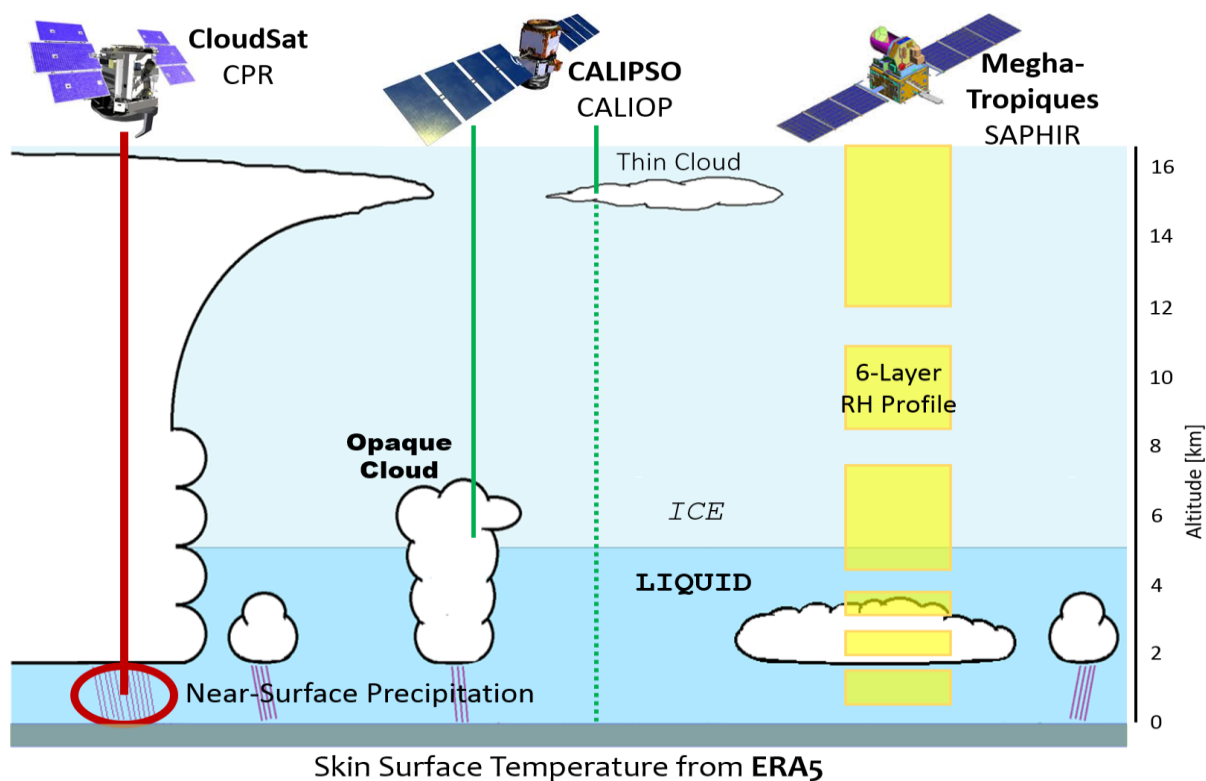


**FIGURE 2-1** Schematic of the satellites, payloads and observed variables from which the data products used in the present work to build the dataset of instantaneous observations on a  $1^\circ \times 1^\circ$  grid are retrieved. Satellite names are given in bold and their payload in normal font on the line below.

One of the objectives of this thesis work is to build diagnostics from observations that can be directly relatable to climate studies in general. A regular grid enables direct comparisons with general circulation models (GCMs), and the  $1^\circ \times 1^\circ$  spatial resolution (roughly  $100 \text{ km} \times 100 \text{ km}$  in the tropics), is enough to observe global and synoptic scale processes (e.g. atmospheric waves, air masses, weather systems, Madden-Julian Oscillation, large-scale circulation, etc.), as well as the largest mesoscale processes (e.g. tropical cyclones, mesoscale convective systems). Some examples of unresolved subgrid processes are microphysical processes, small-scale turbulence and convection, and individual clouds (up to the size of about single thunderstorms).

The trajectories and narrow observations made by the polar orbiting CALIPSO and CloudSat satellites, lead to wider euclidian distance between their tracks in the longitudinal direction the closer they are to the equator. When observations following these tracks are reprojected onto a  $1^\circ \times 1^\circ$  spatial resolution, the vast majority of all tropical  $1^\circ \times 1^\circ$  grid boxes are covered, but a few are never sampled (top panel in Fig. 2-2, and also seen in Figs. 2-16 and 2-19, in Sect. 2.3 CALIPSO and 2.4 CloudSat). Figure 2-2 shows that the climatology is the same for observations reprojected onto  $1^\circ \times 1^\circ$  (top panel) and  $2^\circ \times 2^\circ$  (bottom panel) resolutions.

Because the number of unobserved grid boxes increases with the resolution, going towards even higher resolutions was not a priority for this work. With a  $2^\circ \times 2^\circ$  resolution, there would be no grid boxes that were never observed, but this work accepts a few uncovered grid boxes with the  $1^\circ \times 1^\circ$  grid in favor of the four times higher resolution.

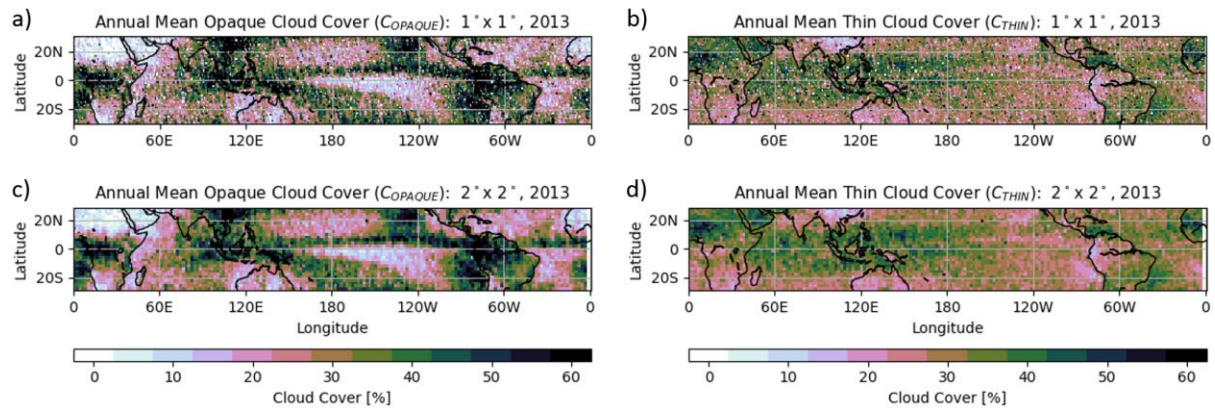


**FIGURE 2-2:** Illustration of annual mean opaque (left column) and thin (right) cloud cover with  $1^\circ \times 1^\circ$  (top panel) and  $2^\circ \times 2^\circ$  (bottom panel) resolution from GOCCP (Sect. 2.3).

## 2.2 Relative Humidity from SAPHIR

Throughout this manuscript, instantaneous vertical relative humidity (RH) profiles are taken from the  $1^\circ \times 1^\circ$  gridded SAPHIR L2B product. These RH profiles are retrieved over six tropospheric pressure layers from brightness temperatures measured by the cross-track scanning, passive microwave radiometer SAPHIR. A more detailed description of SAPHIR and a brief presentation of the RH retrieval are given in this section.

### 2.2.1 The Megha-Tropiques Mission

The Megha-Tropiques satellite was launched on October 12, 2011. It is an Indo-French mission, built by the Indian Space Research Organization (ISRO) and the French space agency CNES (Centre National d'Etudes Spatiales) to monitor the tropical water cycle and energy budget. The following details on the Megha-Tropiques satellite are retrieved from Roca et al. (2015):

Megha-Tropiques flies in a circular low inclination orbit ( $20^\circ$  at the equator) over the tropical belt at an altitude of 866 km. This high altitude and low inclination orbit enables greater sampling of the tropical region compared to other previous lower observing platforms (e.g. the Tropical Rainfall Measuring Mission, TRMM).

The precession cycle of Megha-Tropiques is 51.3 days. The satellite orbits the tropical belt within 100 minutes, yielding around 14 orbits per day with a high revisiting frequency of 3 to 5 observations per day in the same location. For 14 consecutive days, all payloads onboard Megha-Tropiques observe the same part of the tropics at about the same local time.

The swath of SAPHIR (Fig. 2-3) is 1700 km around nadir where each scan line consists of 130 non-overlapping footprints. The footprint size is  $10 \text{ km} \times 10 \text{ km}$  at nadir but deformed to elliptic shapes along the swath ( $14.5 \text{ km} \times 22.7 \text{ km}$  at the edge) due to the scanning of the antenna beam in the cross-track direction (Megha-Tropiques Level 1 Products Handbook 2015). The deformation of the footprints is illustrated in Fig. 2-3.

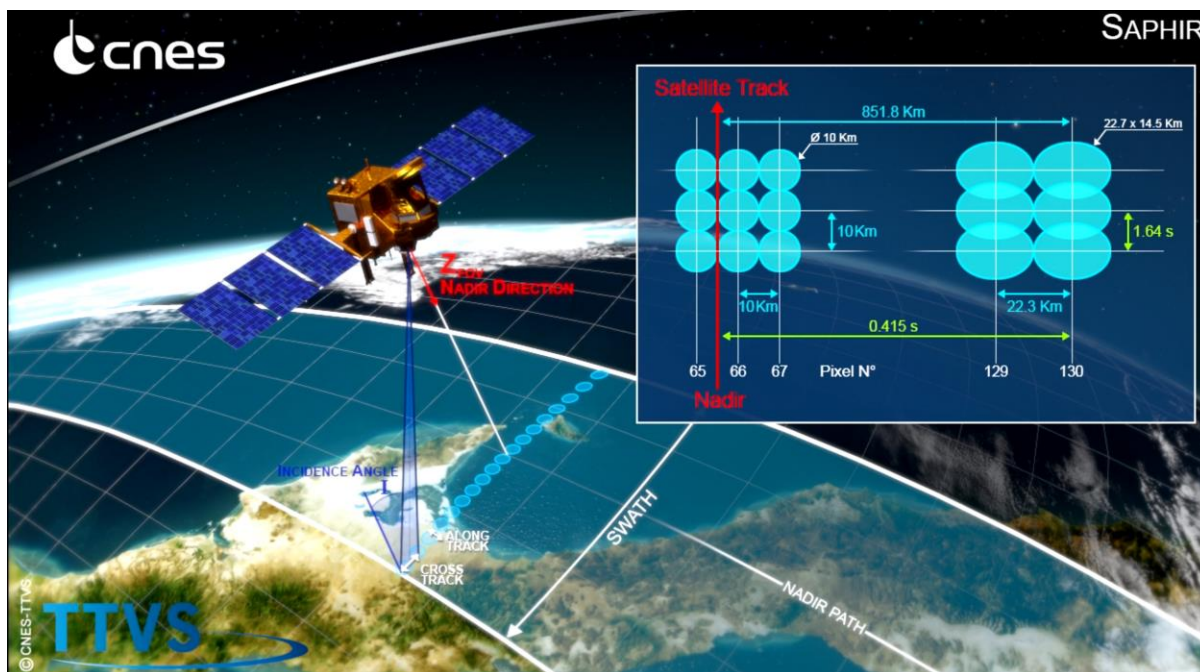


**FIGURE 2-3** Swaths and footprints of the SAPHIR payload carried by the Megha-Tropiques satellite. The figure is extracted from CNES. Accessed September 8, 2020: [https://megha-tropiques.cnes.fr/sites/default/files/migration/smsc/megha-tropiques/icons/films/C05-A10\\_Copyright-WEB.mp4](https://megha-tropiques.cnes.fr/sites/default/files/migration/smsc/megha-tropiques/icons/films/C05-A10_Copyright-WEB.mp4)

Figure 2-4a shows the Megha-Tropiques orbits on an example date (January 1, 2013). During the course of one day, the orbits cover the whole tropical belt spatially, but as mentioned above, observations are made at different local times in different locations. Fig. 2-4b shows the average daily number of overpasses in a given longitude for SAPHIR. The average sampling rate of SAPHIR is 3.5 times per day in the equatorial region (7°S to 7°N) and peaks with 5.5 observations per day around 13°S/N, but falls off towards zero observations poleward of 28°S/N.

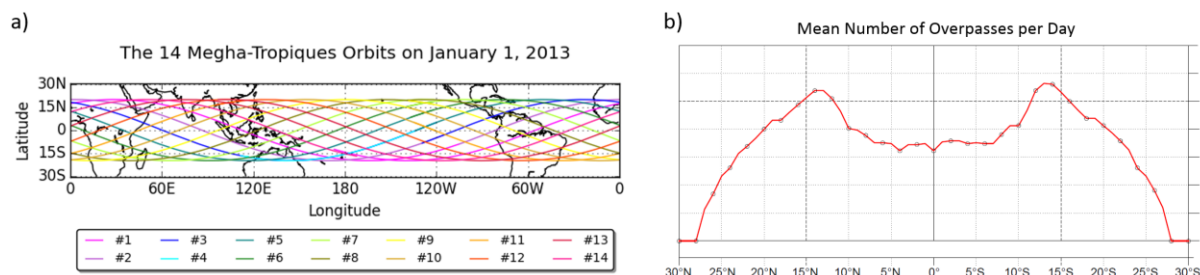


**FIGURE 2-4 a)** All Megha-Tropiques orbits on January 1, 2013. **b)** Average number of daily observations in a given longitude for the SAPHIR payload onboard Megha-Tropiques. Fig. b is extracted from Capderou (2009).

## 2.2.2 The SAPHIR Microwave Radiometer

### 2.2.2.1 Microwave Sounding of Water Vapor

Wavelengths of microwave frequencies are much larger than the size of a typical cloud droplet, meaning that microwave measurements can penetrate non-precipitating clouds (transparent at frequencies  $\lesssim 100$  GHz) with little to no scattering (Liou 2002). Hence, with microwave frequencies, observations can be made under both clear and cloudy conditions, as long as the clouds do not produce large hydrometeors or ice crystals, characterized as deep convection or convective overshoots (Burns et al. 1997, Greenwald and Christopher 2002). Microwave sensors are thus preferred over infrared (IR) sensors that are limited to cloud-free situations, due to the comparable sizes of cloud droplets and IR wavelengths that make clouds effective absorbers of IR. For more details about basic radiative transfer and the interactions about atmospheric gases and electromagnetic waves, the reader is referred to textbooks about radiative transfer (e.g. Liou 2002).

The water molecule has a permanent dipole moment on account of its bent orientation, which makes it an efficient absorber of rotational energies ( $\geq 20$  micrometer) characteristic of temperatures in Earth's atmosphere. Figure 2-5 below shows the atmospheric transmittance spectra of H<sub>2</sub>O and O<sub>2</sub>, where the 183.31 GHz purely rotational transition line of water vapor is well suited for measuring the vertical relative humidity profile. The 183.31GHz line is preferred over the weaker 22.235 GHz rotational transition line which is widely used for remote measures of total column atmospheric water vapor (Schaerer and Wilheit 1979, Liou 2002).

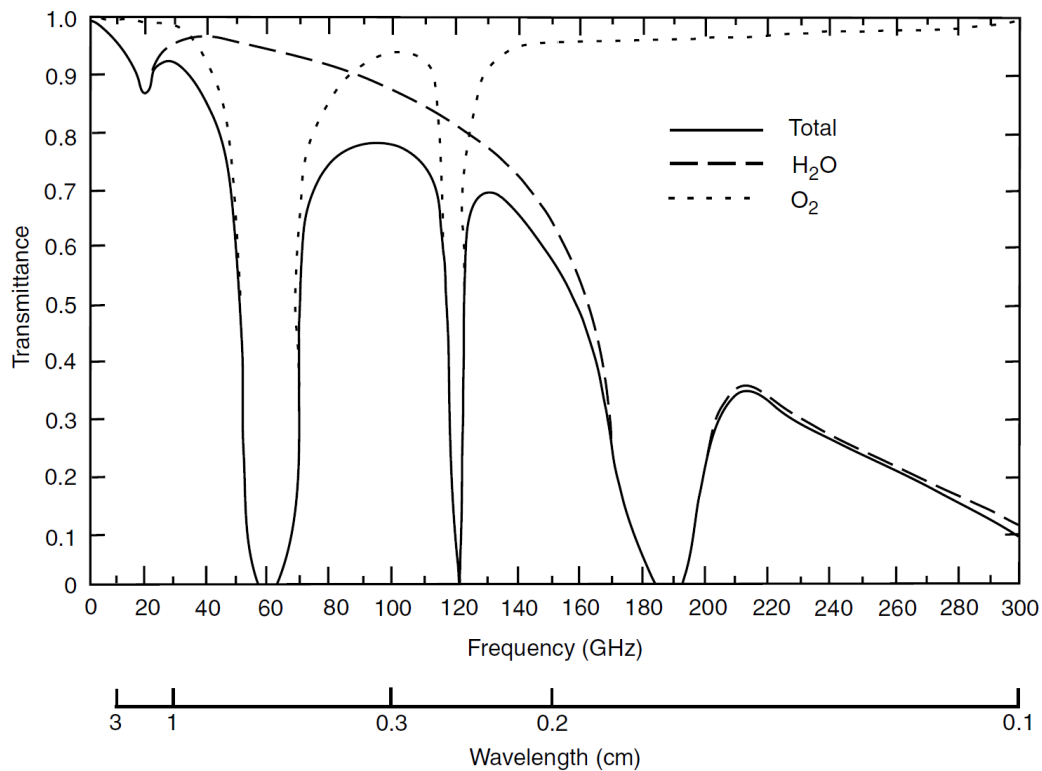


**FIGURE 2-5** Atmospheric transmittances (total, H<sub>2</sub>O, O<sub>2</sub>) as a function of frequency and wavelength in the microwave region. The figure is extracted from Liou (2002).

### 2.2.2.2 The SAPHIR Sounder

SAPHIR measures the upwelling radiation emitted by water vapor (interpreted as brightness temperature, BT) in six channels around this 183.31 GHz line. The locations of these channels with respect to the central frequency are illustrated and listed in Figure 2-6 and Table 2-1 respectively. The reader is referred to Eymard et al. (2002) for more technical details.

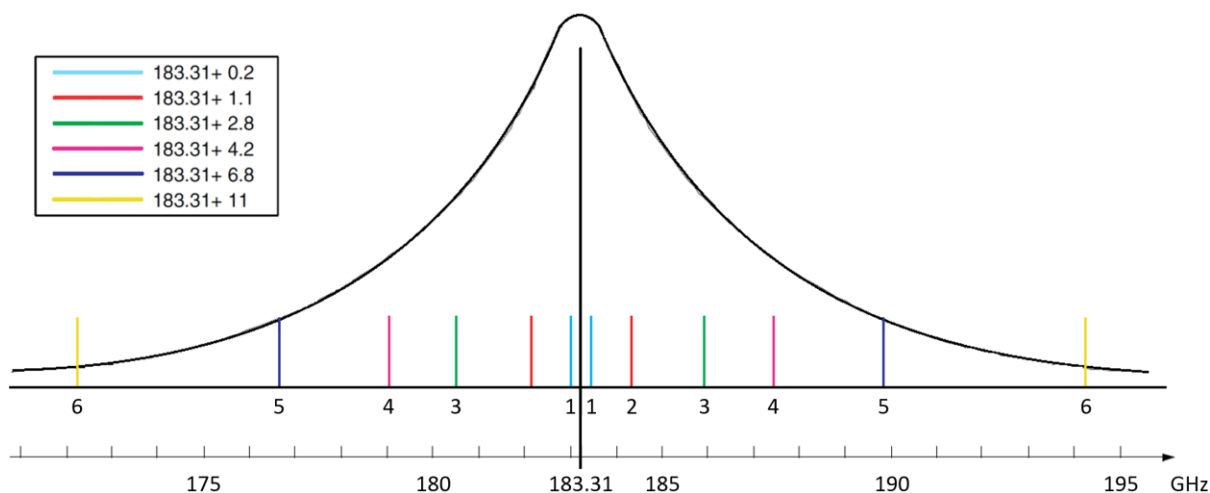


**FIGURE 2-6** Locations of the six double-sideband channels of SAPHIR with respect to the center of the absorption line at 183.31 GHz. The figure is extracted from Eymard et al. (2002), but color enhanced for this work.

**TABLE 2-1:** SAPHIR channel frequencies and bandwidths.

Channel	Central Frequency	Bandwidth
1	$183.31 \pm 0.2$ GHz	200
2	$183.31 \pm 1.1$ GHz	350
3	$183.31 \pm 2.8$ GHz	500
4	$183.31 \pm 4.2$ GHz	700
5	$183.31 \pm 6.8$ GHz	1200
6	$183.31 \pm 11$ GHz	2000

The upwelling radiation transmitted to TOA, is a function of water vapor and temperature. The perturbation of transmission with pressure (or optical depth) is given by its *weighting function* (Fig. 2-7). The narrower the channel bandwidth, the narrower the weighting function and the higher the vertical resolution. Figure 2-7 illustrates the water vapor weighting functions for the six SAPHIR channels, computed in Aires et al. (2013) for a standard tropical atmosphere. The greater the atmospheric moisture, the higher the atmospheric opacity and the higher the altitude where the weighting function peaks.

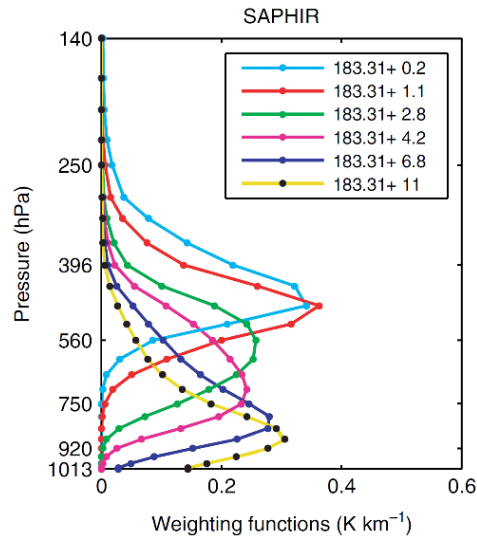


**FIGURE 2-7** The water vapor weighting functions of the six SAPHIR channels computed for a standard tropical atmosphere. Values are expressed as change of relative humidity and normalized to one kilometer of altitude of atmosphere (i.e.  $\text{K km}^{-1}$  per unit change of RH). The figure is extracted from Aires et al. (2013).

As shown in Fig 2.7, the first channel of SAPHIR, at the center of the 183.31 GHz channel ( $183.31 \pm 0.2$  GHz, light blue), is the most sensitive to the upwelling radiation transmitted to TOA near 300 hPa, whilst the wide bandwidth of the sixth channel ( $183.31 \pm 11$  GHz, yellow), located on the wings of this absorption line (see Fig 2.6) is the most sensitive near 600 hPa (Eymard et al. 2002, Brogniez et al. 2013, Roca et al. 2015).

There is a considerable overlap of the weighting functions of the six SAPHIR channels in Fig. 2-7, meaning that their information is not independent (Aires et al. 2013, Brogniez et al. 2013, 2015, Sivira et al. 2015). Stevens et al. (2017) showed that in the vicinity of a strong humidity gradient in the lower troposphere, the width and the overlap of the weighting functions lead to a misinterpretation of the origin of the emission, as moisture from lower layers are interpreted as having arisen higher up. This behavior is more discussed in subsection 2.2.5.2.

### 2.2.3 RH Profile Retrievals from SAPHIR

From the BT measured by the six channels of SAPHIR and knowledge of their weighting functions, the *RH profile* in a SAPHIR footprint is computed with a retrieval technique called ARPIA (Atmospheric Relative humidity Profiles Including Analysis of confidence intervals, described in detail in Sivira et al. 2015, Brogniez et al. 2016). ARPIA is based on a general additive model (GAM, Sivira et al. 2015, Brogniez et al. 2013, 2016), built from a statistical learning technique that takes training examples of paired BT-RH values to infer RH as a function of BT (Sivira et al. 2015).

The ARPIA retrieval generates a deep sounding of the troposphere with RH profile estimations from the upper troposphere (upper limit at 100 hPa) down to the boundary layer (lower limit at 950 hPa) under both clear and cloudy conditions. Because of the scatter produced by large hydrometeors or ice crystals, only BT-RH pairs of non-precipitating footprints are processed by ARPIA. For each estimation by ARPIA, i.e. for each footprint, the expectation of a full RH profile is provided together with its retrieval uncertainty and standard error in six atmospheric pressure layers:  $\text{RH} + \varepsilon$  (in %). The RH is defined with respect to liquid water only (Sivira et al. 2015).

Fig. 2-8 shows an illustration of the RH profile retrieved from SAPHIR in the six layers, following the first orbit of Megha-Tropiques on January 1, 2013. The left figure (2-8a), shows maps of the layer-mean RH over the full swath of SAPHIR. Following this orbit, SAPHIR observed the convective systems characteristic of the intertropical convergence zone (ITCZ, sampled between 30°E and 120°E by this orbit) represented by greater free-tropospheric RH (FTRH) and the subtropical subsidence region (150°E to 120°W) of a characteristically dry free troposphere (here FTRH < 25 %)

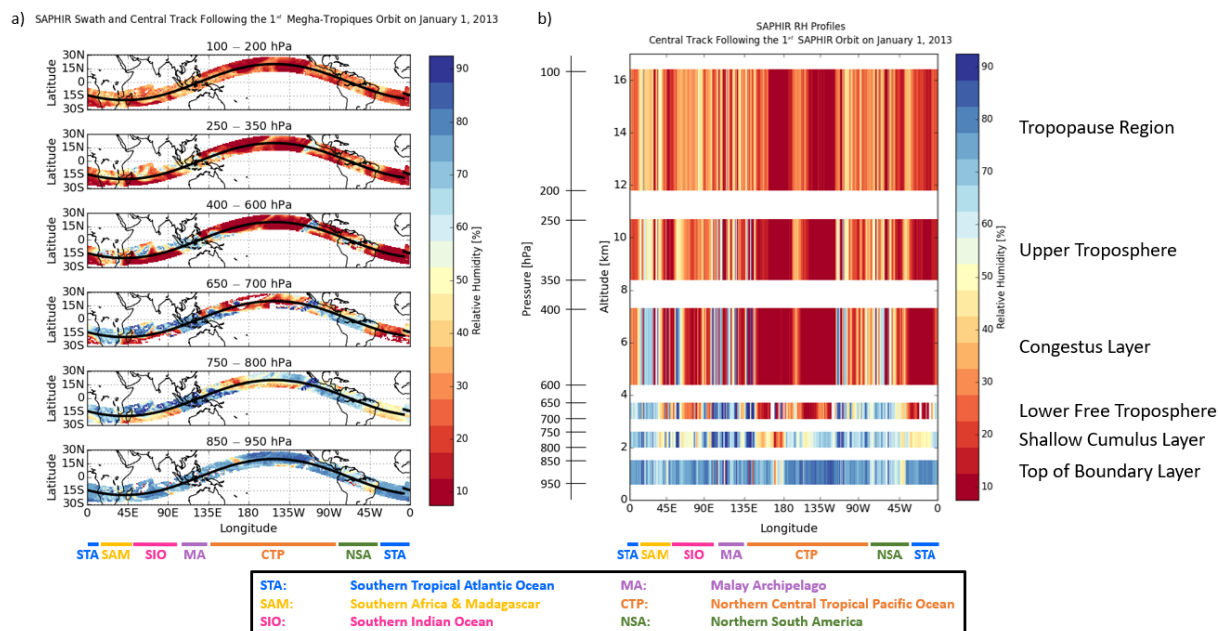


**FIGURE 2-8** Layer-mean RH retrieved from SAPHIR following the first orbit of Megha-Tropiques on January 1, 2013. **a)** Maps of layer-mean RH over the full SAPHIR swath. **b)** Layer-mean RH following the central track of Megha-Tropiques (black line in the maps) An interpretation of the six SAPHIR layers are given to the far right in the figure. The interpretations are extracted from Stevens et al. (2017).

The right figure (2-8b) shows the layer-mean RH profile following the central track of Megha-Tropiques (black line in subplot a). In accordance with the left figure, the typical RH profiles of the ITCZ and subsidence regions are captured in the ranges 30°E to 120°E and 150°E to 120°W respectively, but at the same time, the figure shows that there is some variability between the profiles on the footprint resolution within these ranges. The vertical distortion of the layers seen in Fig. 2-8b is due to the conversion from pressure to kilometers for easier direct comparisons between RH and cloud altitude. The pressure levels of the six atmospheric layers are marked for reference. The figure also adapted the atmospheric description of the atmospheric layers from Stevens et al. (2017), seen to the far right in the figure.

## 2.2.4 The Gridded RH Product

In the SAPHIR L2B product used in the present work, footprints containing RH profiles retrieved by ARPIA are reprocessed from the nominal grid (10 km at nadir) onto a 1° × 1° grid. All footprints that fall within a 1° × 1° grid box, are averaged and weighted by their uncertainty  $\varepsilon$  that is computed by the ARPIA retrieval scheme (Sivira et al. 2017). Moreover, only 1° × 1° grid boxes filled to more than 75 % by footprints processed by ARPIA (i.e. non-precipitating footprints with valid BTs) are considered. In addition, RH estimations are removed and considered erroneous if the associated beta function distributions are too flat or truncated, i.e. if the cumulative distribution function is less than 0.5.

Figure 2-9 below shows an illustration of the interannual mean six-layer RH profile for two seasons December, January, February (DJF) and June, July, August (JJA) from the  $1^\circ \times 1^\circ$  gridded SAPHIR L2B product. The mean states derived to the large-scale circulation are clearly visible on these maps, where regions of large-scale ascent (e.g. the Pacific warm-pool region or the ITCZ) are marked by drier conditions in the lowest layer and greater RH values in the layers above. In contrast, oceanic subsidence regions are marked by the greatest RH closest to the surface and dry conditions (RH < 30 %) in the top four layers. The seasonal cycle is manifested by northward shifts of the ascending regions going from DJF (left) to JJA (right), in accordance with the northward shift in peak solar insolation from DJF to JJA.

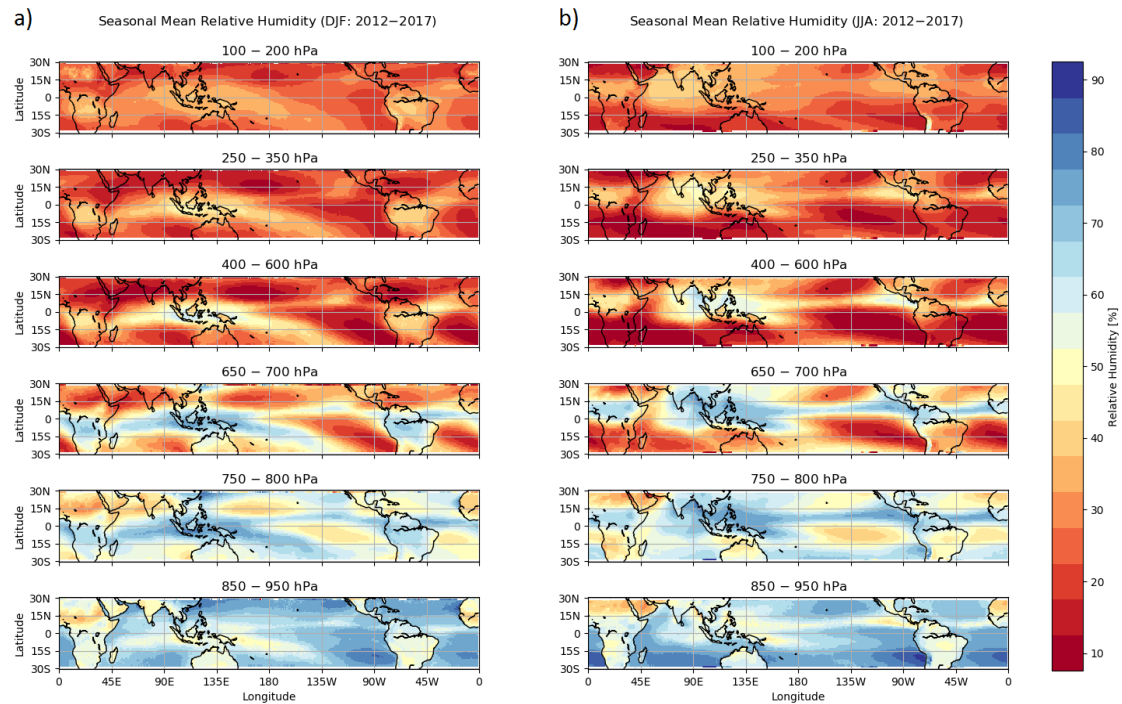


**FIGURE 2-9** Seasonal layer-mean relative humidity in the six atmospheric layers of SAPHIR during 2012-2017. Interannual mean over **a)** December, January, February (DJF) and **b)** June, July, August (JJA). The data was taken from the  $1^\circ \times 1^\circ$  SAPHIR product L2B.

## 2.2.5 Advantages and Limitations with SAPHIR

### 2.2.5.1 Advantages

SAPHIR is the first microwave sounder to provide direct observations of the moisture profile with six observing channels. Previous satellites like AMSU-B (Advanced Microwave Sounding Unit-B), MHS (Microwave Humidity Sounder) or ATMS (Advanced Technology Microwave Sounder), observed the moisture profile with three (AMSU-B, MHS:  $\pm 1.0$ ,  $\pm 3.0$ ,  $\pm 7.0$ ) or five (ATMS:  $\pm 1.0$ ,  $\pm 1.8$ ,  $\pm 3.0$ ,  $\pm 4.5$ ,  $\pm 7.0$ ) channels around 183.31 GHz, respectively. Brogniez et al. (2013) showed that thanks to its three additional channels located closer to the center and the wings, RH estimates derived from SAPHIR have higher accuracy in the upper and lower troposphere than MHS and AMSU-B (Brogniez et al. 2013).

Even so, SAPHIR was designed to focus on the free troposphere with little information at the tropopause and in the boundary layer. Consistently, Sivira et al. (2015) showed that the GAM performs the best in layers 2, 3 and 4, where the scatter is the smallest, standard deviations between 3.79 to 6.02 % RH, and the Pearson's correlation coefficients between the estimated and reference RH values are within 0.91 to 0.95.

### 2.2.5.2 Limitations

As mentioned above, the effect of non-precipitating particles is well represented by Rayleigh scattering so microwave radiometers like SAPHIR can observe the atmospheric humidity close to convective cores (Brogniez et al. 2013, 2015, Sivira et al. 2015). Still, because the retrieval algorithm ARPIA only processes non-precipitating footprints, precipitating footprints are excluded from the computation of the average RH value in a grid box. This exclusion naturally introduces a dry bias to the RH value when non-precipitating and precipitating situations are aggregated together.

Stevens et al. (2017) found that SAPHIR, like other passive remote sensors, has problems to retrieve RH in the lower troposphere when there is a strong humidity gradient present there. As an example, Fig. 2-10 below shows a humidity gradient between layer 5 (about 60 % RH) and layer 4 (about 10 % RH) during the NARVAL-1 (Next-Generation Airborne Remote Sensing Research for Validation studies) campaign that took place in the downstream winter trades on December 12, 2013. On the right side of the dashed vertical line, the SAPHIR retrieval (in blue) fails to capture the amplitudes of the lidar fluctuations (in red) in layer 5, and overestimates RH by 5 to 15 % (absolute values) compared to the lidar in layer 4 above. Stevens et al. (2017) conclude that in cases like this, the width and overlap of the sensitivity functions (as was seen in Fig. 2-7 above) likely causes a misinterpretation of what level the upwelling radiation was emitted from.

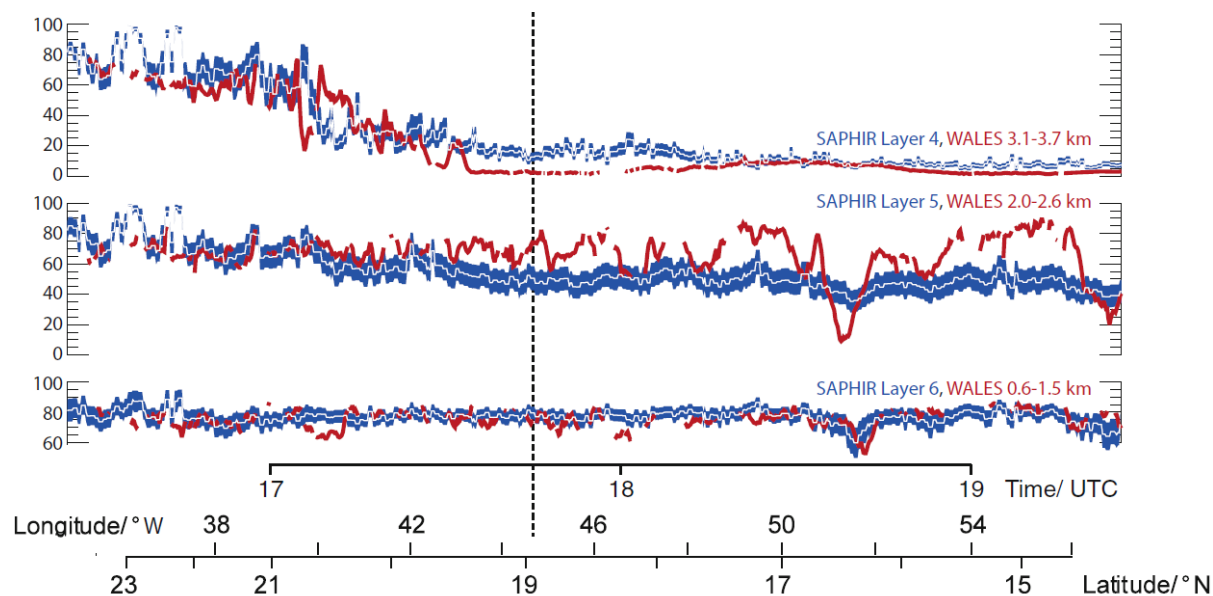


**FIGURE 2-10** Comparison of relative humidity profiles on December 12, 2013. Shown are measurements from the WALEs (Water vapor Lidar Experiment in Space) lidar instrument aboard HALO as part of NARVAL-1 and the Megha-Tropiques profiles along the same track. The time of the Megha-Tropiques overpass is indicated by the vertical dashed line. SAPHIR retrievals are shown in blue bounded by the first and third interquartile uncertainty, and WALEs estimates are shown in red. The figure is extracted from Stevens et al. (2017).

## 2.3 Cloud Characteristics from GOCCP

Cloud characteristics are collected from the  $1^\circ \times 1^\circ$  spatially gridded version of the General Circulation Model-Oriented CALIPSO Cloud Product (GOCCP, Chepfer et al. 2010, 2013, Cesana and Chepfer 2012, Cesana et al. 2016) v.3.1.2 product (Guzman et al. 2017), which consists of diagnosed cloud properties from observations collected with the spaceborne lidar CALIOP onboard the CALIPSO satellite.

### 2.3.1 The A-Train Constellation

CALIPSO flies as part of the Afternoon train constellation (more commonly referred to as the *A-train* constellation) at an altitude of 705 km. The A-train constellation (Fig. 2-11) is a suite of Earth-observing satellites, flying in a near-sun synchronous polar orbit and operated by various space agencies. The satellites follow each other closely within minutes, yielding nearly simultaneous observations of the Earth from all payloads. The constellation makes 15 orbits per day, each one crossing the equator twice daily at 01:30 am and 01:30 pm local time (LT) with a 16-day repeat cycle (Winker et al. 2009). The A-train satellites of interest for this work are CALIPSO and CloudSat which fly only 15 seconds apart.

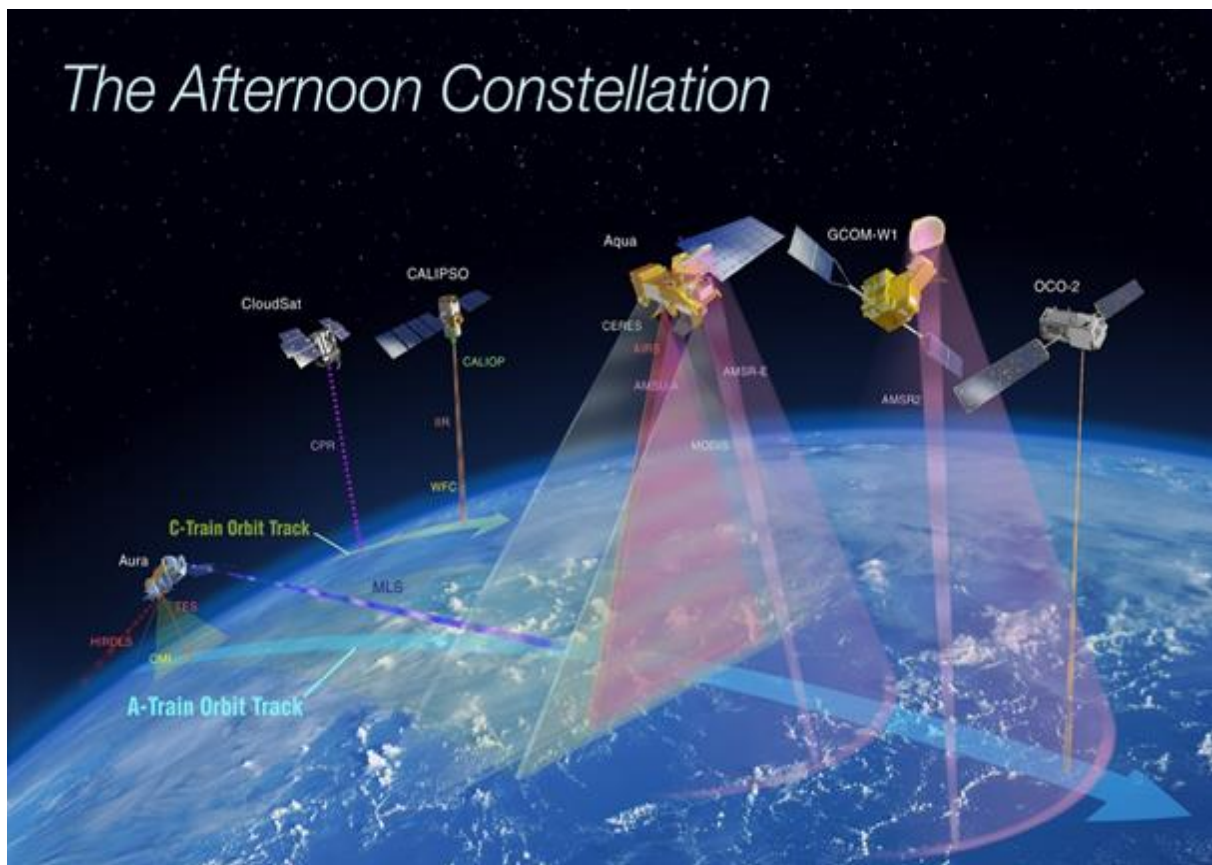


**FIGURE 2-11** The international Afternoon Constellation includes the A-Train satellites (OCO-2, GCOM-W1, Aqua, and Aura) as well as the C-Train satellites (CALIPSO and CloudSat). Active instruments aboard CALIPSO (CALIOP) and CloudSat (CPR) are indicated with dashed lines. This illustration color-codes instrument swaths based on observed wavelength ranges. Microwaves are represented in shades of purple, solar wavelengths in yellow; gray represents solar and infrared wavelengths, and red represents other infrared wavelengths. The figure is extracted from NASA on April 24, 2020: <https://atrain.nasa.gov/>

CALIPSO and CloudSat have provided simultaneous and complementing observations of the atmosphere since their launches in April 2006. That is, CALIOP lidar observes aerosols and hydrometeors too small for the sensitivity of the CloudSat radar (CRP), whilst the radar penetrates through even the thickest clouds and measures hydrometeors from thick clouds and light precipitation all the way down to the surface. In February 2018, CloudSat left the A-train constellation following a technical issue with its maneuvering capabilities. Due to the much-appreciated complementing observations that CALIPSO and CloudSat provide, CALIPSO also left the A-train in September that same year to follow in the new orbit of CloudSat – forming the *C-train* constellation (Fig. 2-11) of these two satellites.

Figure 2-11 above shows an illustration of the satellite tracks in the current A-train and C-train constellations and the payloads they carry. Active and passive measurements are shown as dashed lines or swaths and color-coded after wavelength as described in the figure caption.

Figure 2-12 below, shows an example representation of all A-train orbits in one day (January 1, 2013), represented here by the CALIPSO orbits separated into local daytime and nighttime orbits.

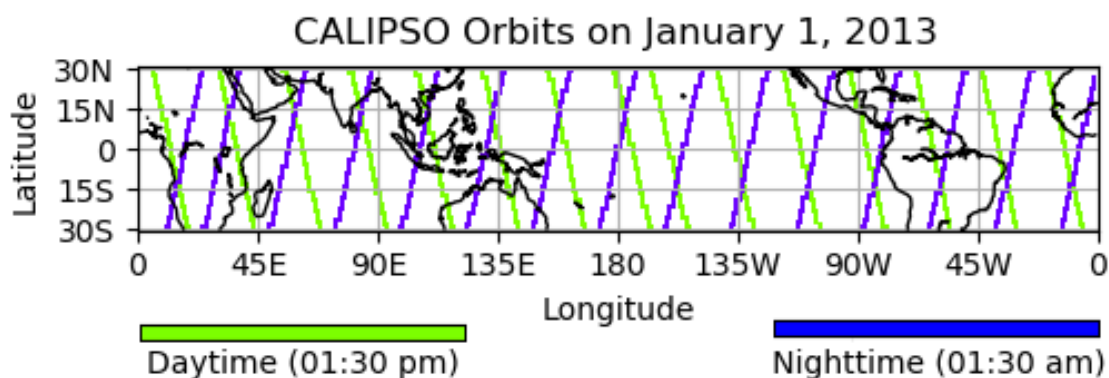


**FIGURE 2-12** All CALIPSO (A-train) orbits in the tropical belt during one day. Daytime orbits crossing the equator around 01:30 pm LT, are shown in green, and nighttime orbits crossing the equator around 01:30 am LT are shown in blue. The example date is January 1, 2013.

## 2.3.2 The Lidar CALIOP

### 2.3.2.1 Lidar

In contrast to passive remote sensors (e.g. the microwave radiometer SAPHIR described above) that measure scattered radiation emitted from natural sources, active remote sensors, such as *lidars* (light detection and ranging) and *radars* (radio detection and ranging) measure the return signal from artificial radiation sources.

Lidars emit laser pulses in specific wavelengths. The laser pulse is scattered by atmospheric molecules, aerosols and cloud particles. As it is scattered in all directions, the lidar pulse undergoes attenuation. The light scattered in the backwards direction (*backscatter*,  $\Theta = \pi$  radians) is collected by a detector on the telescope. We measure the Attenuated Backscatter signal (ATB).

### 2.3.2.2 CALIOP

CALIPSO carries the lidar CALIOP that emits simultaneous laser pulses of 532 and 1064 nm. This work only uses measurements (ATB signal) at the 532 nm wavelength, which is scattered but not absorbed by cloud particles and gas molecules (Chepfer et al. 2008).

Table 2-2 below lists the fundamental sampling resolutions of the 532 nm ATB signal (Winker et al. 2009). It is 30 m vertically and 333 m horizontally from the surface up to 8.2 km, and 60 m vertically and 1 km horizontally from 8.2 to 20.2 km, with a receiver footprint diameter of 90 m at ground level. Only signals measured below 40 km altitude are kept as profile data. In total, the nominal profiles consist of 583 unevenly distributed vertical levels.

**TABLE 2-2:** Spatial resolution of the nominal (level 1) 532 nm CALIOP data. The table is extracted from Winker et al. (2009).

Altitude Range [km]	Horizontal Resolution [km]	Vertical Resolution [m]
30.1 to 40.0	5.0	300
20.2 to 30.1	1.67	180
8.2 to 20.2	1.0	60
-0.5 to 8.2	0.33	30
-2.0 to -0.5	0.33	300

### 2.3.3 Single Profile GOCCP-OPAQ

Cloud diagnostics are performed in GOCCP by applying thresholds of *scattering ratio* (SR, unitless variable) (Chepfer et al. 2008, 2010), which are computed from CALIOP ATB profiles as follows:

First, profiles of molecular ATB ( $ATB_{mol}$ ) are computed using pressure and temperature profiles provided by NASA's Global Modelling and Assimilation Office (GMAO).  $ATB_{mol}$  is the profile that would be measured if the atmosphere contained only molecules, no particles (no aerosols, no clouds). This profile is then scaled to match the ATB profile in the reference range between 27 and 29 km altitude, where the atmosphere is free of particles (Chepfer et al. 2008, 2010). Second, in the GOCCP product, these profiles are then independently reprojected onto a vertical grid of 40 equidistant levels from the surface up to 19 km altitude (each bin is 480 m thick) (Chepfer et al. 2010). Ultimately, the SR profile is computed by dividing ATB by  $ATB_{mol}$ :

$$SR(z) = \frac{ATB(z)}{ATB_{mol}(z)} \quad (E2-1)$$

Given the SR profile, atmospheric layers are classified using SR thresholds. These are (i) *cloudy* for  $SR > 5$ , (ii) *clear* for  $0.01 < SR < 1.2$ , (iii) *fully attenuated* for  $SR < 0.01$  and (iv) *uncertain* for  $1.2 < SR < 5$  (Chepfer et al. 2008, 2010). Fig. 2-13 below illustrates one nighttime orbit of CALIPSO, from a) the nominal CALIOP ATB profiles in the 583 unevenly distributed vertical levels to b) the SR profiles onto the vertical grid of 40 equally distributed levels of 480 m thick bins and c) the GOCCP cloud diagnostics, given the SR thresholds. The 8.2 km altitude (at which the nominal vertical resolution shifts from 30 to 60 m) is clearly marked in the ATB profile (2-13a). This feature is then naturally removed in Fig. 2-13b when the SR profile is plotted with the vertical resolution of 40 equidistant levels.

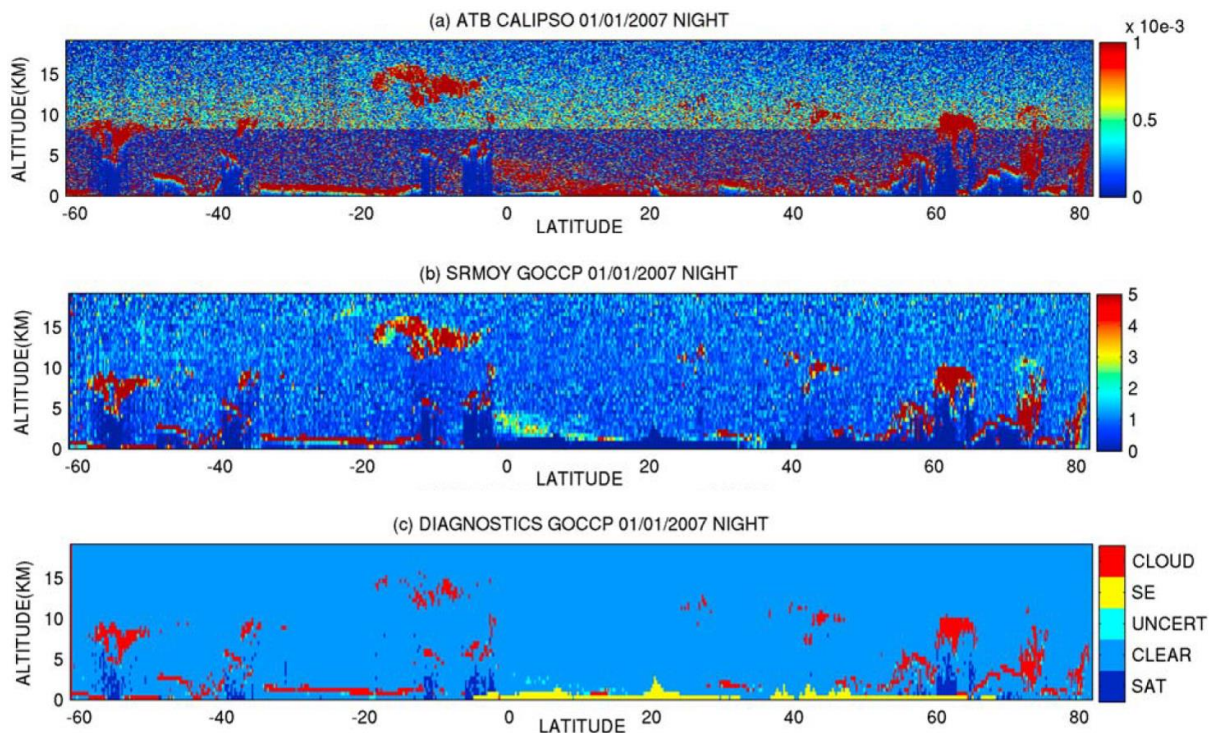


**FIGURE 2-13** Example of one nighttime orbit: a) CALIOP ATB signal in its nominal unevenly distributed vertical levels, b) Lidar scattering ratios over the 40 vertical equidistant levels (480 m grid), c) GOCCP diagnostics: cloudy, clear, uncertain, fully attenuated (SAT), below the surface elevation (SE). The figure is extracted from Chepfer et al. (2010).

Figure 2-14a illustrates the more advanced GOCCP-OPAQ cloud mask (Guzman et al. 2017) developed from the one shown in Fig. 2-13, and employed in this work. The GOCCP-OPAQ algorithm distinguishes between clear-sky, thin and opaque cloud profiles. It takes individual profiles of total ATB from CALIOP and seeks a “surface echo” near the surface elevation (dashed horizontal lines in Fig. 2-14b,c). A profile will have a surface echo if a fraction of the lidar pulse reached the surface before it was reflected to its source on the satellite telescope (the “echo”). The *surface detection threshold* ( $SDT = 0.001 \text{ km}^{-1} \text{ sr}^{-1}$ , Fig. 2-14bc) represents the minimum ATB value that can be attributed to a surface echo and thus separates opaque cloud profiles (defined by  $ATB < SDT$ ) from thin/clear-sky profiles (defined by  $ATB > SDT$ ) (Guzman et al. 2017). An additional illustration of the distinction between opaque and thin clouds, as seen by the lidar, are shown in Fig. 2-15.

**Opaque Clouds:** A profile containing an opaque cloud (visible optical depth  $> 3$  to 5) will not contain a surface echo (Fig. 2-14b), for the lidar beam is completely scattered at some altitude before it reaches the surface (Fig. 2-15, left). The level just below this altitude of full attenuation is referred to as  $Z_{OPAQUE}$  (Guzman et al., 2017). It corresponds to the green flags in Fig. 2-14a.

$Z_{OPAQUE}$  is a radiatively interesting altitude that can be derived with high accuracy from a spaceborne lidar. LW radiation emitted upward at altitudes below  $Z_{OPAQUE}$  has negligible impact on the OLR in an opaque cloud column. Thus, Vaillant de Guélis et al. (2017) showed that a good approximation for the radiative temperature for an atmospheric column containing opaque clouds is the average temperature of the cloud temperatures at cloud top and at  $Z_{OPAQUE}$ .

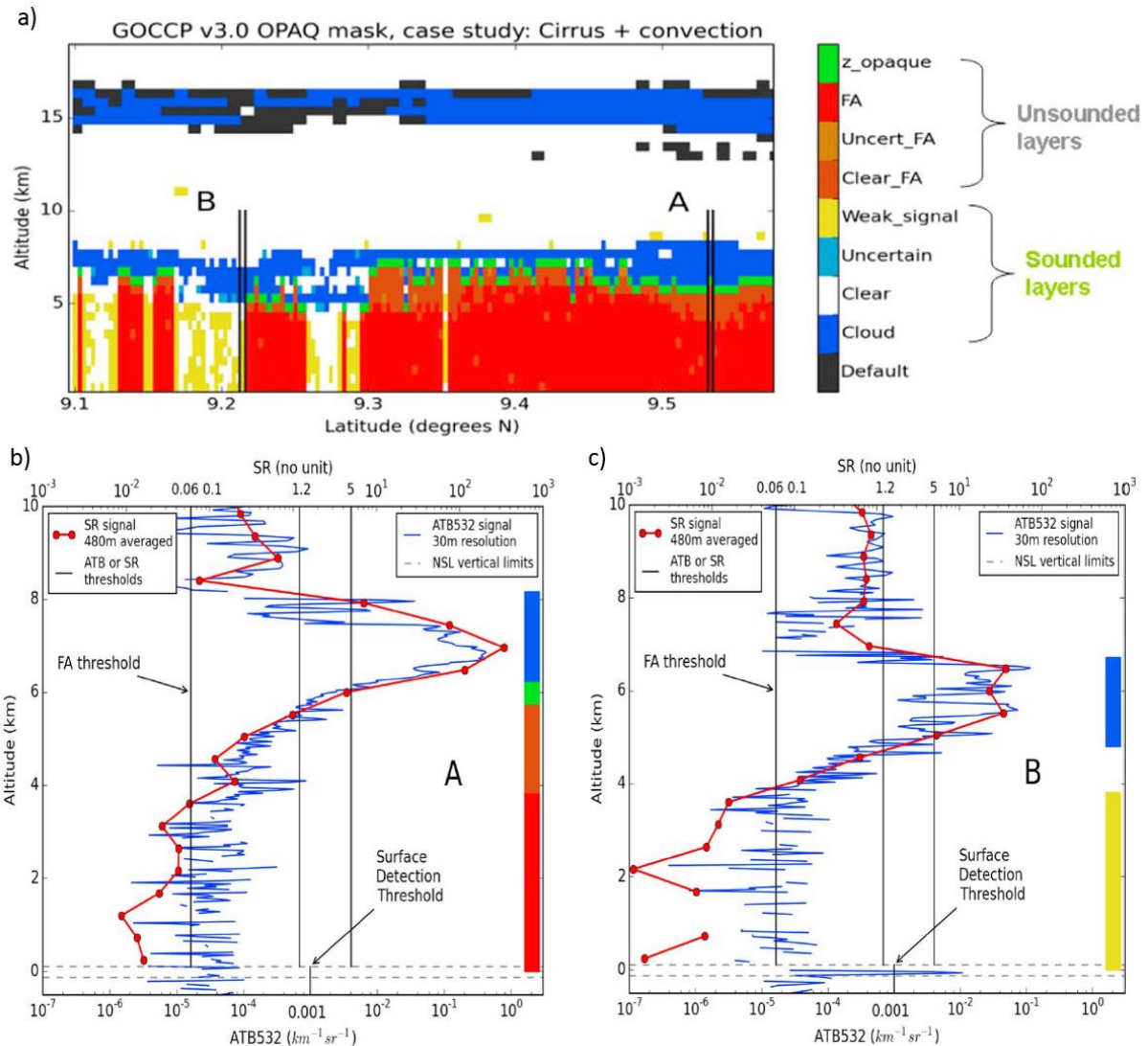


**FIGURE 2-14** GOCCP v.3 cloud masks for a segment of a CALIPSO orbit in the Indian Ocean on June 15, 2007. **a)** GOCCP v.3.0 instant\_OPAQ mask. **b)** ATB and SR profiles for profile “A”. **c)** ATB and SR profiles for profile “B”. ATB profiles of the 532 nm lidar beam at 30 m vertical resolution are shown in blue together with the SR profiles of 480 m vertical resolution in red. The figure is extracted from Guzman et al. (2017).

**Thin Clouds:** In contrast, a profile containing a thin cloud (visible optical depth  $< 3$  to 5) or no clouds at all (clear sky) will contain a surface echo, as is illustrated by the surface echo spike in the near-surface layer for the thin cloud profile in Fig. 2-14c. As both thin cloud profiles and clear-sky profiles contain a surface echo, these are distinguished by their scattering ratios. In GOCCP, none of the 40 vertical levels are flagged as *cloudy* in a clear-sky profile, whilst in thin cloud profiles at least one level is flagged as *cloudy* (although the lidar beam is never fully attenuated).

Thin clouds are partly transparent to the upward emitted LW radiation so that some of it passes through them unabsorbed. Vaillant de Guélis et al. (2017) defined the radiative temperature of a thin cloud ( $T_{THIN}$ ) as the average temperature of the temperatures at thin cloud top and thin cloud bottom, and accordingly the thin cloud altitude  $Z_{THIN}$  as the altitude from which  $T_{THIN}$  is emitted.

The cloud altitudes  $Z_{OPAQUE}$  and  $Z_{THIN}$  are schematically illustrated in Fig. 2-15 below, together with the cloud emission temperatures at these respective altitudes, referred to in this work as  $T_{OPAQUE}$  and  $T_{THIN}$ . They are thoroughly described in Vaillant de Guélis et al. (2017). The altitudes  $Z_{OPAQUE}$  and  $Z_{THIN}$  are used here because they are radiatively relevant, and the study in Ch. 4 discusses LW cloud feedback (as well as other tropical key water cycle feedbacks) and the impact on OLR due to changes of these altitudes with surface temperature.

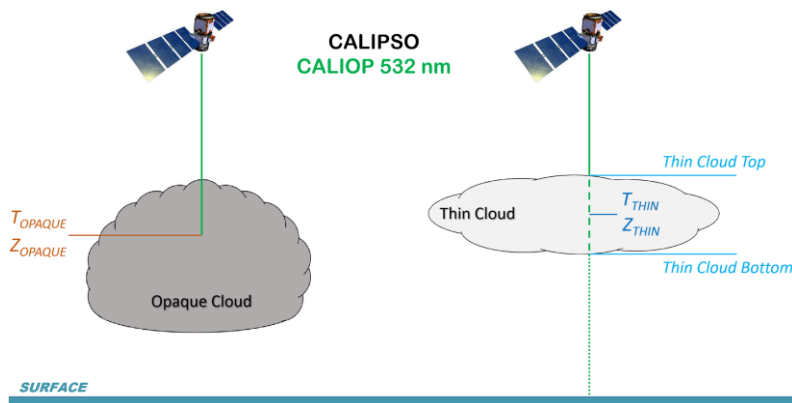


**FIGURE 2-15** Illustration of the opaque and thin cloud altitudes  $Z_{OPAQUE}$  and  $Z_{THIN}$ , and cloud temperatures  $T_{OPAQUE}$  and  $T_{THIN}$ .

### 2.3.4 The Gridded Cloud Product

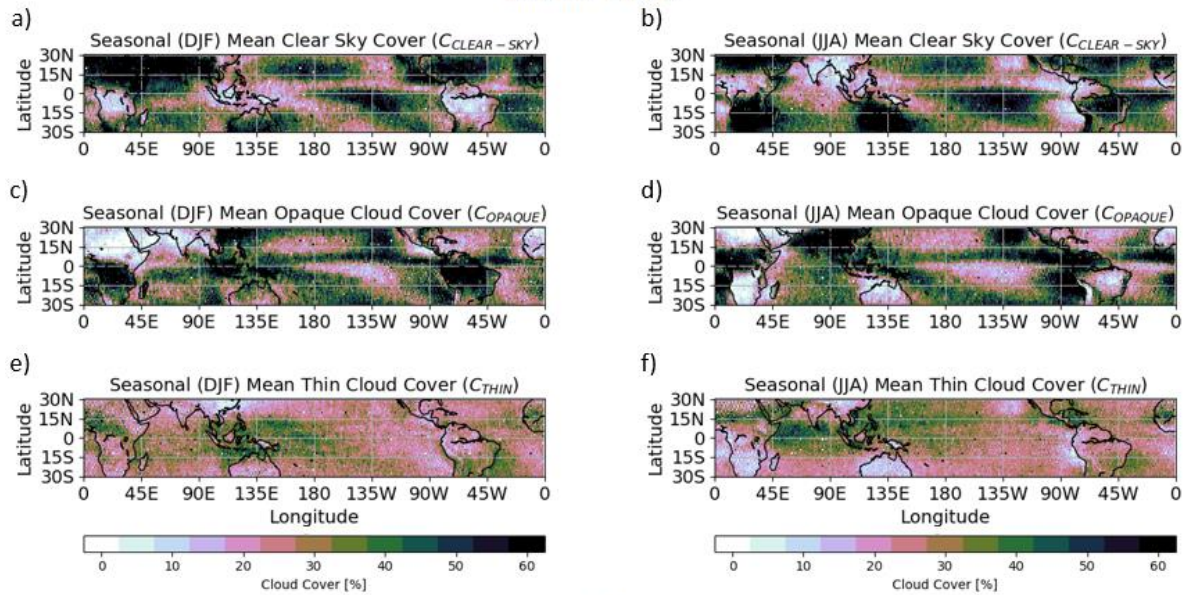
The  $1^\circ \times 1^\circ$  spatially gridded GOCCP product is built by aggregating profile information within a  $1^\circ \times 1^\circ$  spatial grid (Guzman et al. 2017). Each grid box contains one value each of the clear-sky cover, the opaque cloud cover and the thin cloud cover (the sum of which equals 100 %), as well as the opaque and thin cloud altitudes ( $Z_{OPAQUE}$ ,  $Z_{THIN}$ ) and cloud emission temperatures ( $T_{OPAQUE}$ ,  $T_{THIN}$ ). These are computed as follows:

The clear-sky, opaque and thin cloud cover values within a grid box are taken as the number of profiles identified as clear-sky, opaque or thin, divided by the total number of profiles measured within said grid box. In contrast, the altitude  $Z_{OPAQUE}$  ( $Z_{THIN}$ ) is the average value of  $Z_{OPAQUE}$  ( $Z_{THIN}$ ) in all opaque (thin) profiles within the grid box, and the corresponding cloud temperature at that altitude  $T_{OPAQUE}$  ( $T_{THIN}$ ) the average value of  $T_{OPAQUE}$  ( $T_{THIN}$ ) in all opaque (thin) profiles within the grid box. These cloud variables are illustrated by their seasonal mean states (interannual mean DJF and JJA states over the time period 2012 to 2017) in Fig. 2-16 below.

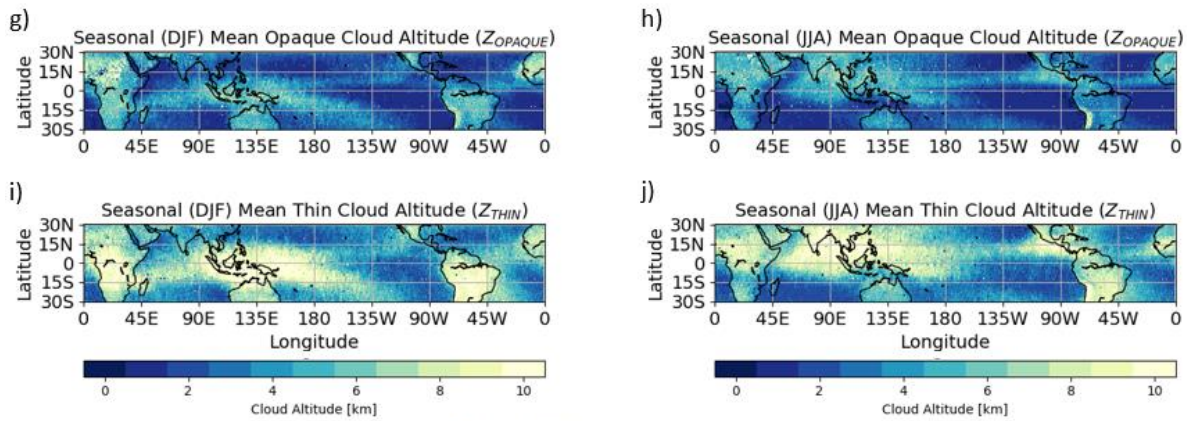
The figure shows clear features of the large-scale circulation, with greater cloud cover (c-f), higher cloud altitudes (g-j) and hence lower cloud temperatures (k-n) in the ascending regions (ITCZ and Pacific warm pool). There are also marked differences between the cloud types (opaque vs. thin). The opaque cloud cover is greater (c, d) than the thin (e,f), but  $Z_{OPAQUE}$  is lower than  $Z_{THIN}$ . That  $Z_{OPAQUE}$  is lower than  $Z_{THIN}$  is explained by their different definitions.

Similar seasonal shifts following the peak solar insolation as in Fig. 2-9 (RH) are also visible in Fig. 2-16, where the ascending regions move northward from DJF to JJA. The speckled/grainy appearance of Fig. 2-16 is due to some  $1^\circ \times 1^\circ$  grid boxes never observed, as mentioned in Sect. 2.1.

## Cloud Cover



## Cloud Altitude



## Cloud Temperature

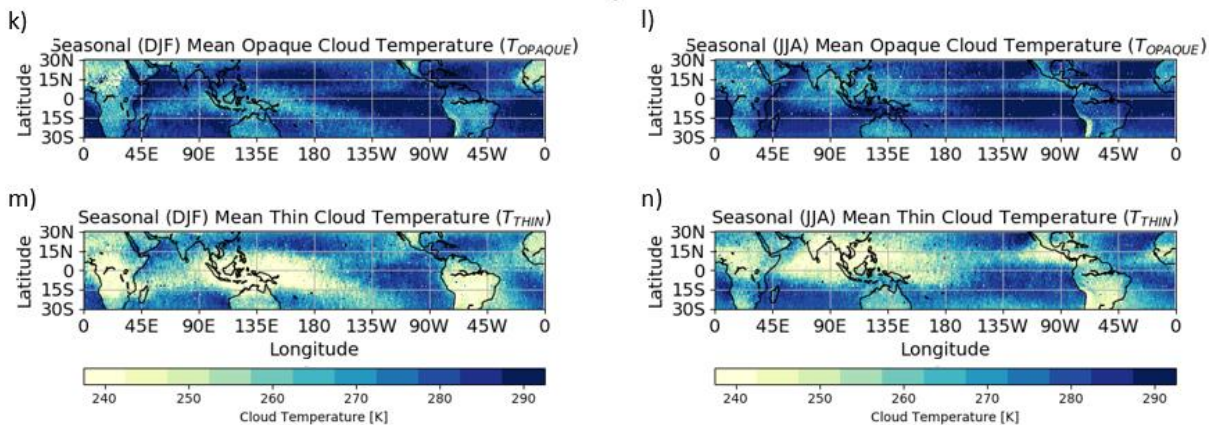


**FIGURE 2-16** Seasonal mean states of cloud characteristics from the GOCCP product computed over the years 2012-2017 **a, b**) clear-sky cover, **c, d**) opaque cloud cover, **e, f**) thin cloud cover, **g, h**) opaque cloud altitude, **i, j**) thin cloud altitude, **k, l**) opaque cloud temperature and **m, n**) thin cloud temperature. Maps in the left column are interannual means for the season December, January, February (DJF) and the right column interannual means for the season June, July, August (JJA).

## 2.3.5 Advantages and Limitations with GOCCP

### 2.3.5.1 Advantages

By the time of the launch of CALIPSO (April 2006), the resolution and accuracy of CALIOP was unprecedented by previous satellite-borne cloud instruments, as prior to the present millennium, clouds were observed from space by passive satellite sensors that can only observe single atmospheric layers, and have troubles with observations of thin and semi-transparent clouds (Winker et al. 2009). In addition, they rarely retrieve more than one cloud layer, which is a problem when about half of all cloud systems are multilayered (e.g. Hahn et al. 1990, Hang et al. 2019).

### 2.3.5.2 Limitations

Despite the high accuracy and vertical resolutions of the CALIOP, flying in the A-train or C-train orbits means significant temporal undersamplings of the atmosphere by their payloads. Over the course of the 24 hours in a day, observations made by the A-train and C-train satellite instruments only sample two instantaneous moments (01:30 am/pm). Previous studies have however shown that this does not impact climatological mean values (e.g. Konsta et al. 2012). Thus, for the purpose of this work it is more a problem of a limited number of situations where the A-train satellites and Megha-Tropiques can be collocated on the instantaneous timescale.

In opaque cloud columns, no additional information is provided for altitudes below  $Z_{OPAQUE}$ , where the lidar beam has become completely attenuated, which leaves CALIOP blind to atmospheric layers below this altitude. This undersampling of vertical information is most problematic when  $Z_{OPAQUE}$  occurs at high altitudes (e.g. deep convective anvils), as low liquid water clouds likely coexist with these in many cases (e.g. Matus and L'Ecuyer 2017), although not observed by CALIOP.

Finally, no threshold of minimum number of profiles is considered when the gridding is performed. Meaning that, if a grid box only contains one profile, the cloud characteristics derived from that single profile will represent the whole  $1^\circ \times 1^\circ$  grid box.

## 2.4 Near-Surface Precipitation from the CloudSat 2C-PRECIP-COLUMN Product

This work makes use of a  $1^\circ \times 1^\circ$  gridded version of the CloudSat Data Processing Center's 2C-PRECIP-COLUMN product (v. P\_R05, Haynes et al. 2013) for detection of near-surface precipitation over tropical oceans (480-960 m above ground level over oceans, Kay et al. 2018).

### 2.4.1 CloudSat's Cloud Profiling Radar

#### 2.4.1.1 Radar

Radars employ the same backscatter theory as lidars. As such they emit an electromagnetic pulse in a straight line referred to as the radar beam. Objects in the path of the radar beam scatter the signal. If the size of the object is much smaller than the wavelength of the beam  $\lambda$ , we can assume *Rayleigh scattering*, in which the amount of energy scattered in the backward and forward directions are symmetrical (Liou 2002, Seinfeld and Pandis 2006). In this case, the

energy scattered in the backward direction, towards the emitter, can be measured by a receiver. Microwave and centimeter wavelengths are preferred for observing larger hydrometeors like large cloud droplets or rain drops. Figure 2-17 shows an illustration of the emitted and reflected radar signal in clear and cloudy columns assuming Rayleigh approximation.

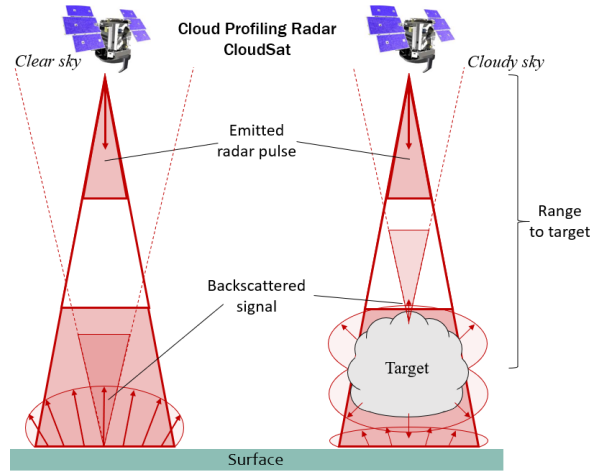


**FIGURE 2-17:** Illustration of the emitted and scattered radar beam assuming Rayleigh approximation in (left) clear-sky and (right) cloudy columns. Red shaded areas indicate a pulse, and arrows the travelling direction.

When travelling through the atmosphere, the power density decreases due to being inversely proportional to the square of the range to the target, and extinction by particles in its path. Only backscatter from hydrometeors that fill the whole radar beam are detected by the radar. However, since the width of the beam widens with distance (Fig. 2-17), small objects at large distances away from the radar are difficult to detect (Liou 2002).

The *backscattering cross-section*  $\sigma$  (unit: dB) is defined as the area of an imagined perfect isotropically radiating reflector, which corresponds to the same amount of energy that the actual target scatters in the backward direction (Stout and Mueller 1968). The reflectivity  $\eta$  of a unit volume is the volume integral over all backscattering cross-sections in the target volume  $V$  (L'Ecuyer and Stephens 2002):

$$\eta = \int_V \sigma dV = \frac{\pi^5}{\lambda^4} |K|^2 Z \quad (\text{E2-2})$$

where  $K$  is the dielectric factor of the scattering target, and the *Rayleigh reflectivity factor*  $Z$  is the integral over the number of hydrometeors of different diameters  $D$  (E2-3). Assuming a drop size distribution given by the Marshall and Palmer (1948) relation,  $Z$  can be associated to rain rate  $R$  (unit:  $\text{mm hr}^{-1}$ ) (Haynes et al. 2009):

$$Z = \int_0^{D_{max}} N_0 e^{A_\lambda R^{B_\lambda D}} D^6 dD \quad (\text{E2-3})$$

Here  $N_0 = 8 \times 10^6 \text{ m}^{-4}$ , and  $A_\lambda$  and  $B_\lambda$  the Marshall and Palmer (1948) parameters;  $A_\lambda = 4100 \text{ m}^{-1} (\text{mm h}^{-1})^{0.21}$ ,  $B_\lambda = -0.21$  in Haynes et al. (2009). As such,  $Z$  is a function of the number and diameter of the reflecting hydrometeors. The radar reflectivity is measured in the dimensionless logarithmic unit  $dBZ$ , which stands for decibel relative to  $Z$ . It measures the reflectivity factor of the target object to the reflectivity factor of a rain drop of 1 mm. The higher the  $dBZ$ , the more likely it is for precipitation to occur (Haynes et al. 2013).

### 2.4.1.2 The Cloud Profiling Radar

CloudSat flies as part of the A-train constellation and carries a near-nadir-looking cloud profiling radar (CPR,  $0.16^\circ$  off geodetic nadir) in the W-band (94 GHz), designed by NASA, JPL (Jet Propulsion Laboratory) and the Canadian Space Agency to profile atmospheric hydrometeors (Im et al. 2000, Haynes et al., 2009). It measures the power backscattered by clouds as a function of distance from the radar (Im et al. 2000, 2005). The nominal profiles range over 30 km and consist of 125 vertical bins, 240 m thick. The footprint is 1.4 km in diameter at the surface with an along-track resolution of 2.5 km and a minimum detection signal of  $-28$  dBZ (Im et al. 2000, Smalley et al. 2014). The CPR is the first millimeter wavelength radar to observe atmospheric hydrometeors from space (Haynes et al. 2009).

### 2.4.2 Single Column: Retrievals from the 2C-PRECIP-COLUMN Product

The 2C-PRECIP-COLUMN (Haynes et al. 2009, 2013) assesses the likelihood of near-surface precipitation over ocean surfaces by applying reflectivity thresholds. This subsection briefly describes the steps of this assessment following Haynes et al. (2009, 2013). A more detailed retrieval can be found in these publications, but I describe here its main part.

As outlined in Haynes et al. (2009, 2013), in the 2C-PRECIP-COLUMN product, precipitation detection is based on increasing values of non-attenuated near-surface CPR reflectivity, associated with increasing likelihood of precipitation.

The *path-integrated attenuation* (PIA, unit: dB) is the two-way integrated extinction due to hydrometeors integrated from the surface to the height of interest  $H$  (left-hand side of E2-4) Haynes et al. (2009). In E2-4,  $\psi$  is the conversion factor ( $10/\ln(10)$ ), and the extinction coefficient  $k_{ext}$  (unit:  $\text{m}^{-1}$ ) is a function of distance  $s$  and precipitation rate, given the knowledge of raindrop size distributions (Haynes et al. 2009). But the PIA in a raining column can also be expressed as the normalized backscattering cross-section at the surface  $\sigma_0$  relative to the clear-sky non-attenuated value  $\sigma_{clr}$ , accounting for gaseous attenuation  $G$  (right-hand side of E2-4):

$$2\psi \int_0^H k_{ext}(s) ds = PIA = \sigma_{clr} - (\sigma_0 + G) \quad (\text{E2-4})$$

Clear-sky columns are easily discernible as the surface scatter of the radar beam is orders of magnitude larger than the scatter from any atmospheric hydrometeor. In contrast, in columns where atmospheric hydrometeors are present, this signal of surface backscatter is masked by hydrometeor attenuation (Haynes et al. 2009), as illustrated to the right in Fig. 2-17.

The contribution of gaseous attenuation to the surface backscatter  $G$  (unit: dB) is calculated from the atmospheric moisture and temperature profiles at the time of measurement taken from the ECMWF auxiliary data and matched with observations. The normalized ocean surface backscatter is calculated knowing viewing angle, wind speed and sea surface temperature, also retrieved from ECMWF (see Haynes et al. 2009, 2013 for more details on how  $G$  is calculated).

In the 2C-PRECIP-COLUMN product employed in this work, CPR power returns in the lowest bins are discarded due to surface contamination (Tanelli et al. 2008). Instead, it considers the reflectivity in the fourth bin ( $Z_n$ , 600 and 840 m altitude) (Haynes et al. 2009). The non-attenuated radar reflectivity  $Z_u$  (E2-5) is the sum of the measured near-surface reflectivity  $Z_{ns}$  there, and the contributions from gaseous attenuation and the path-integrated attenuation. The

PIA is modified by a factor  $\chi$  that removes attenuations at levels lower than the near-surface bin (Haynes et al. 2009, 2013):

$$Z_u = Z_{ns} + PIA \cdot \chi + G \quad (\text{E2-5})$$

Figure 2-18 illustrates the CPR radar reflectivity profile (top) following a portion of a CloudSat orbit. The middle panel shows the anticorrelation between the ocean surface backscatter ( $\sigma_0$ ) and the PIA calculated to the fourth bin in green dots and to the surface in black dots.

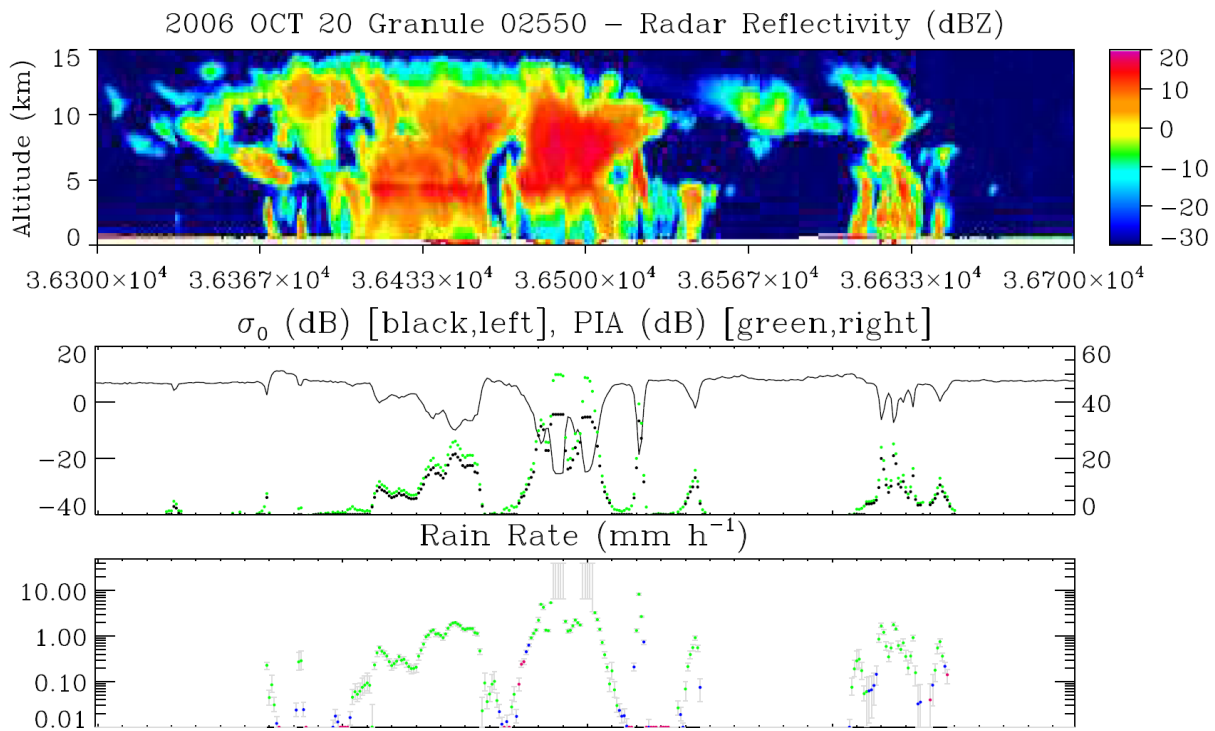


**FIGURE 2-18:** The figure shows a portion of a CloudSat orbit on October 20, 2006. **(top)** The radar reflectivity profile as observed by the CPR. **(middle)** The measured surface reflectivity (solid black line, left y scale) as well as the PIA to the surface (green dots, right y scale) and the PIA to the fourth bin above the surface (black dots, right y scale). **(bottom)** Retrieved rain rate (colored dots) and uncertainties (bars). Green dots: “rain certain”; blue dots: “rain probable”; red dots: “rain possible.” The figure is extracted from Haynes et al. (2013).

This retrieval described so far considers only single scattering, but multiple scattering effects may occur when photons are scattered more than once between the transmitter and the receiver antenna due to the presence of raindrops or snowflakes in that range. These effects are significant for precipitation more intense than approximately  $3 \text{ mm h}^{-1}$  and most pronounced in heavy precipitation, where the photons are scattered several times and the resulting time delay translates into an increase in the apparent range of the source of the scatter. Hence, multiple scattering effects manifest themselves as increases in return power, and radar reflectivity, at range gates farther from the radar than the source of the initial scattering event. Multiple scattering effects are corrected for in the 2C-PRECIP-COLUMN by applying a backward Monte Carlo model of the radiative transfer equation (Haynes et al. 2009).

Melting particle effects may also be important when precipitating ice is present. The presence of a melting layer tends to produce more PIA (through the enhancement just below the melting level) than would result if only warm rain were considered (Haynes et al. 2009). To account for this bias, a model that simulates the effect of the melting layer was developed for the 2C-PRECIP-COLUMN that follows a snowflake as it makes the transition to raindrop (Haynes et al. 2009).

Ultimately, precipitation flags (precip\_flag, Haynes et al. 2009, 2013) are assigned based on the near-surface non-attenuated reflectivity. This study relies on some of these precipitation flags for detection of rain over tropical oceans. These precipitation flags are listed in Table 2-3 below and illustrated in the rain rates in the bottom panel in Fig. 2-18. Because this work is conducted in the tropical belt, near-surface precipitation flags related to snow are ignored.

**TABLE 2-3:** Near-surface precipitation types and names of the 2C-PRECIP-COLUMN precip\_flags used in this work. The table is a merger of information extracted from Table 2 in Haynes et al. (2009), Table 5 in Haynes et al. (2013) and Table 2 in Kay et al. (2018).

Type of Rain	Precip_flag	Non-Attenuated Reflectivity Threshold
No Rain	<i>No precip detected</i>	$Z_u < -15$ dBZ
Drizzle	<i>Rain possible</i> <i>Rain probable</i>	$-15 < Z_u < -7.5$ dBZ $-7.5 < Z_u < 0$ dBZ
Rain	<i>Rain certain</i>	$Z_u > 0$ dBZ
Heavy Rain	<i>Rain certain</i>	$Z_u > 40$ dBZ

### 2.4.3 The Gridded Precipitation Product

In the gridded product, local solar daytime and nighttime observations are gridded separately using a uniform  $1^\circ \times 1^\circ$  grid and filtered with respect to the 2C-PRECIP-COLUMN quality flags (Status\_flag). Only retrievals with no error (Status\_flag < 8, Haynes et al. 2013) and from daytime observations (01:30 local time at the equator) are used in this work.

In Ch. 3, cloudy grid boxes are partitioned by the presence or absence of near-surface precipitation. *Precipitating grid boxes* are defined as grid boxes containing at least one of the three rainy near-surface precipitation flags in Table 2-3 and therefore include all near-surface rain rates observed by the CPR, from drizzle and higher. In contrast, *non-precipitating grid boxes* only contain near-surface levels flagged as non-raining.

Additionally, the study in Ch. 3 defines the *near-surface precipitation cover within a precipitating grid box* as the accumulated number of near-surface precipitating profiles, divided by the total number of profiles in that grid box (Fig. 2-19 c,d). Fig. 2-19 shows such cover within a grid box separately for each of the precipitation flags in Table 2-3. The figure shows seasonal means of each precipitation flag cover for December, January, February (DJF, left column) and June, July, August (JJA, right column).

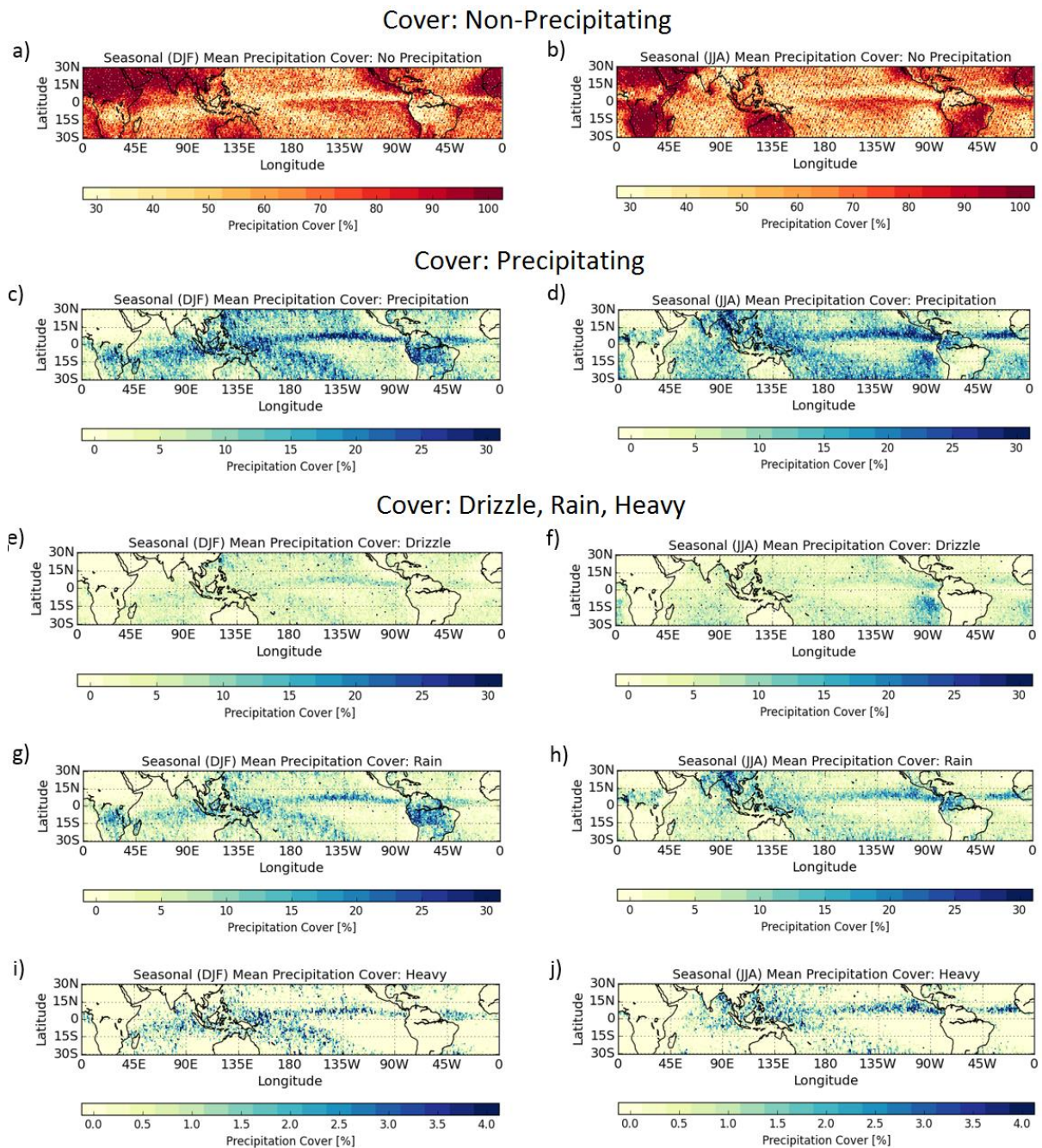


**FIGURE 2-19** Seasonal mean states of daytime `precip_flag` cover within a  $1^\circ \times 1^\circ$  grid box retrieved from the 2C-PRECIP-COLUMN product over the period May 2012 - April 2016. **a, b**) non-precipitating cover, **c,d**) precipitating cover, **e,f**) cover of drizzle, **g,h**) cover of rain, and **i,j**) cover of heavy rain. Maps in the left column are interannual means for DJF and the right column interannual means for JJA. The seasonal precipitation cover in subplot c (d) is the sum of the covers in subplots e, g (f, h), and the heavy rain in i,j is a part of the rain in g,h.

As expected, over oceans, the precipitation cover is the greatest in the ascending regions (ITCZ and Pacific warm pool) and the smallest in the subsidence regions off the west coast of continents. This feature is seen in all maps, i.e. for all precipitation flags. The dominating precipitation type is rain (maps g and h), which includes all rain rates observed by CloudSat that are greater than drizzle. When heavy rain is extracted from the rain category (in maps i and j) it is seen to cover up to 4 % of grid boxes along the ITCZ. Drizzle can occur over almost any part of the tropical oceans (e,f), but where it occurs, the grid box cover is less than 5 % (the exception is off the west coast of Peru during JJA where it covers about 20 % of the grid boxes).

In contrast to the seasonal mean RH and cloud characteristics (Figs. 2-9 and 2-16), there is a much less pronounced northward seasonal shift of the precipitation cover going from DJF to JJA over the oceans. Rather, this northward shift is seen in precipitation over land. The spatial patterns of seasonal near-surface precipitation observations in Fig. 2-19 are consistent with results in e.g. Haynes et al. (2009) and Liu (2015). Haynes et al. (2009) notice a dual peak of zonal mean liquid precipitation during DJF observed by the CPR, AMSR-E, GPCP, PR and TMI between 20°S and 5°N, consistent with the spatial patterns in subplots g and i.

## 2.4.4 Advantages and Limitations with CloudSat 2C-PRECIP-COLUMN

### 2.4.4.1 Advantages

First, as CloudSat and CALIPSO have flown in formation since their launches, their observations are collocated by design, which makes simultaneous instantaneous observations of cloud characteristics and near-surface precipitation easy to work with.

Second, as the CPR was designed to profile the atmosphere and observe both clouds and precipitation, the high frequency and sensitivity of the CPR makes it an excellent spaceborne detector of light precipitation and sensitive to even the small water droplets in the incipient stages of precipitation formation (Haynes et al. 2009). It is therefore well suited for discrimination of precipitating and non-precipitating clouds. This sensitivity is a welcome complement to previous satellite borne precipitation-observing Ku-band (12 to 18 GHz) radars (e.g. the 13.8 GHz precipitation radar onboard TRMM) and passive microwave sensors (Behrangi et al. 2012, Smalley et al. 2014). Because of different science objectives however, the CPR should not be considered an enhancement of the precipitation radar onboard TRMM, but rather as a complementary observational platform for lighter rain rates (Berg et al. 2010). A brief comparison of precipitation retrievals from CPR and TRMM are given in Appendix B.

### 2.4.4.2 Limitations

As the radar signal was chosen to be sensitive to both cloud droplets and raindrops, the surface return may be completely attenuated in heavy precipitation (Berg et al. 2010, Stephens et al. 2010). In which case, an estimate of the surface cross-section is impossible (Lebsock 2018).

The sensitivity of the CPR is however lower than e.g. the CALIOP lidar, which means that CloudSat cannot observe optically thin clouds. For observations of thin clouds, this work employs CALIOP (Sect. 2.3).

Despite being sensitive to light precipitation, shallow light precipitation risks being missed as the layer closest to the surface is discarded to remove reflectivity contamination due to surface returns (Tanelli et al. 2008, Behrangi and Richardson 2018). Discarding the layer closest to the surface also means that there are no observations of shallow boundary layer clouds due to the surface echo.

Due to a battery failure on CloudSat in April 2011, only daytime observations (01:30 pm LT) have been available since then, as the satellite must rely on solar power. Therefore, in order to have the longest possible homogeneous time series that I can collocate with SAPHIR observations (launched October 2011), I make use of only daytime observations of precipitation.

## 2.5 Surface Temperature and Vertical Pressure Velocity from ERA5

In this work, skin surface temperature (SKT) and vertical pressure velocity at the 500 hPa level ( $\omega_{500}$ ) are taken from the 5<sup>th</sup> generation of the European Centre for Medium-Range Weather Forecast's (ECMWF) reanalyses (ERA5: ECMWF ReAnalysis).

### 2.5.1 ERA5 Reanalysis

A climate reanalysis (e.g. ERA5) is a numerical climate description, built from a combination of models and observations. The reanalysis uses historical observational data from satellites and in-situ measurements (land-based stations, drifting buoys, ships, aircrafts, radiosondes, etc.) as inputs in a modern weather model and computes a recent historical climate going back decades in time (Hersbach and Dee 2016).

ERA5<sup>15</sup> is the latest four-dimensional (longitude, latitude, altitude, time) reanalysis dataset from ECMWF. It is produced from 4D-Var data assimilations of the ECMWF Integrated Forecast System Cycle 41r2 and is given in hourly values with a horizontal resolution of  $\sim 31$  km ( $0.3^\circ \times 0.3^\circ$ ) in 137 vertical pressure levels (Hoffmann et al. 2018).

The reanalysis builds on a sequential data assimilation scheme that advances forward in time in 12-hourly analysis cycles (Dee et al. 2011). Each cycle combines observations with information computed by the forecast model in the previous cycle. This result is then used to initialize a short-range forecast model which in turn, provides the prior state estimates of the next analysis cycle (Dee et al. 2011). Hence, the forecast model allows for information from local observers to be extrapolated and forwarded in time.

### 2.5.2 The ERA5 Variables Used in This Work

The present work takes hourly reanalysis values of the  $0.3^\circ \times 0.3^\circ$  skin surface temperature (Fig. 2-20) and atmospheric vertical pressure velocity  $\omega_{500}$  (Fig. 2-21) from ERA5 and reprojects them onto a  $1^\circ \times 1^\circ$  spatial grid.

#### 2.5.2.1 Skin Surface Temperature

The skin surface temperature in ERA5 is the theoretical temperature of the Earth's uppermost surface layer that is required to satisfy the surface energy balance. This layer has no heat capacity so it can respond instantaneously to changes in surface fluxes. The mean of the 01:00 am/pm and 02:00 am/pm SKT values are taken as the 01:30 am/pm value when the A-train crosses the equator.

---

<sup>15</sup> For more details about ERA5, the reader is referred to the ERA5 online documentation (see link), which collects all aspects of the observations, data assimilations and modelling used to produce the reanalysis. Accessed May 16, 2020: <https://confluence.ecmwf.int/display/CKB/ERA5%3A+data+documentation>

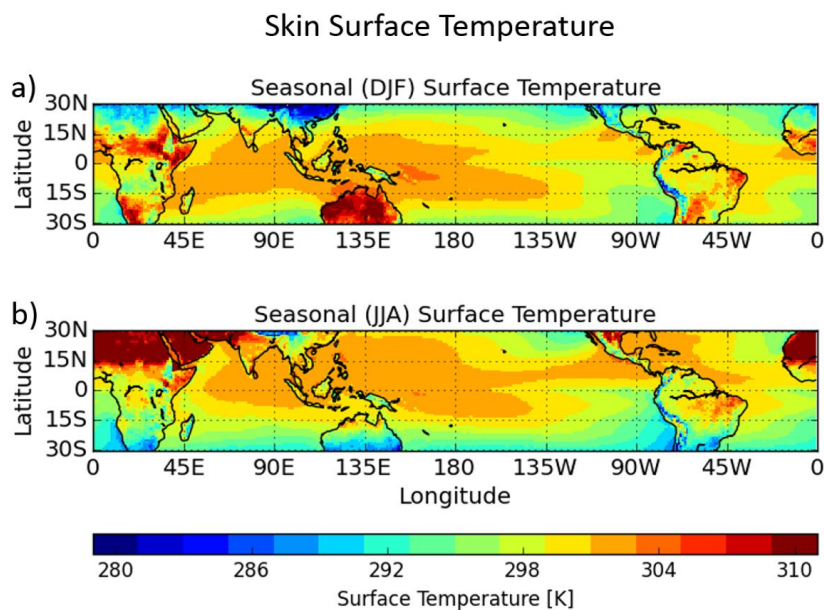


**FIGURE 2-20:** Interannual seasonal mean skin surface temperature from ERA5 over the years 2012-2017 **a)** DJF and **b)** JJA.

This work only considers tropical oceanic surfaces. I refer to *sea surface temperature* (SST) as SKT over ocean surfaces and thus discard SKT over land masses. Interannual mean values of SST typically stay within 291 to 305 K, with the highest values in the ascending regions along the ITCZ and in the Pacific warm pool region. The coldest temperatures are seen off the west coast of continents, where upwelling cold water replaces the surface water transported westward with the ITCZ. Following the seasonal cycle of peak solar insolation, the warmest SSTs are shifted northward going from DJF to JJA.

This northward shift is more pronounced over continents, where the most extreme (coldest and warmest) SKTs are located. In DJF (2-20a), the warmest tropical land surface temperatures are found over Australia, South Africa and Africa's Horn, whilst the coldest over Sahara and southeast China. In contrast, during JJA (2-20b) when the northern hemisphere faces the sun, North Africa (Sahara and Sahel) and the Arabian Peninsula are some of the warmest places in the world, with seasonal mean temperatures in excess of 310 K. That said, there is an apparent northward shift in the SSTs as well, where the warmest SSTs (> 302 K) that are concentrated to the equatorial (15°N to 15°S) Indian and western tropical Pacific oceans in DJF (a), expand northward to 30°N in JJA (b) as well as into the Caribbean and Mexican Gulf.

#### 2.5.2.2 Atmospheric Vertical Pressure Velocity

The vertical pressure velocity at the 500 hPa level ( $\omega_{500}$ ) has been used extensively in the past as a proxy for the large-scale circulation (e.g. Su et al. 2011, Konsta et al. 2012, Vaillant de Guéllis et al. 2017, Chepfer et al. 2019). This variable is however sensitive to local dynamics and subject to significant biases at the instantaneous scale (Trenberth et al. 2000), which is why this work computes monthly mean values of  $\omega_{500}$  from the hourly values provided by ERA5 and employs these as a proxy for the large-scale circulation. Monthly mean values do however naturally smooth out all processes that occur on timescales shorter than a month. Such values are therefore ambiguous, as for example a single value of weak ascent could both represent (1) a month including days of strong ascent and moderate descent, and (2) more constant weak ascending motion.

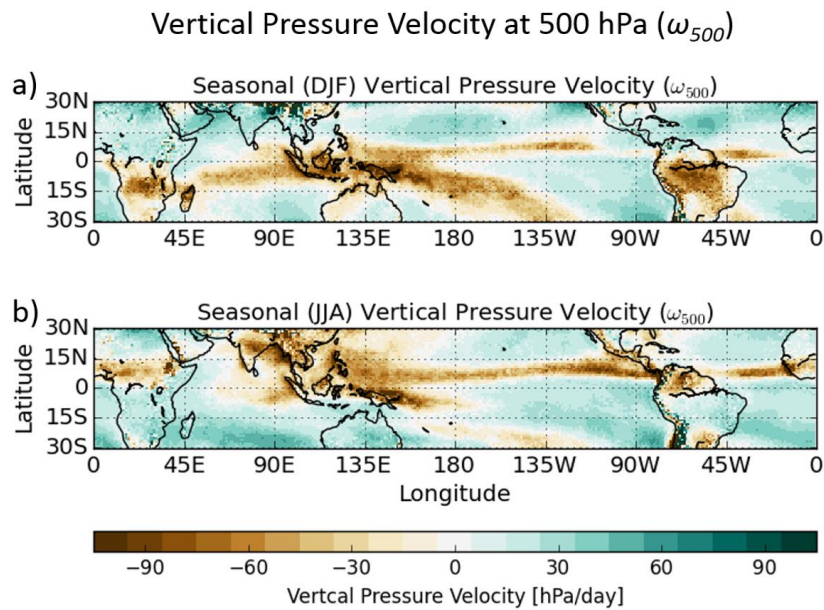


**FIGURE 2-21:** Interannual seasonal mean vertical pressure velocity at the 500 hPa level from ERA5 over the years 2012-2017 **a)** December, January, February and **b)** June, July, August. Negative (positive) values indicate rising (sinking) vertical motion.

The ascending regions (ITCZ and Pacific warm pool region) referred to when discussing all previous seasonal maps, are clearly marked in brown colors in Fig. 2-21. The spatial patterns of ascending and descending vertical motion closely resemble the patterns of the presence and absence of near-surface precipitation in Fig. 2-19, respectively. During JJA (2-21b) the Pacific warm pool region reaches its northernmost locations, covering all of southeast Asia and its coastlines. A permanent branch of the ITCZ is located between  $0^{\circ}\text{N}$  and  $15^{\circ}\text{N}$ , though most pronounced during JJA when it almost completely encircles the globe in that latitudinal band (2-21b). The mean position of the ITCZ north of the equator is due to more landmasses in the northern hemisphere compared to the southern (e.g. McGee et al. 2014, Byrne et al. 2018). As land surfaces heat up more quickly than ocean surfaces, air converges more strongly towards northern hemisphere land masses during JJA than towards southern hemisphere land masses during DJF, resulting in a mean location just north of the equator. During DJF (2-21a), a very pronounced second branch of the ITCZ stretches out southeastward from the Pacific warm pool region. Also during this season, when the southern hemisphere faces the sun, rising motion prevails over southern Africa and the central parts of South America.

## 2.5.3 Advantages and Limitations with ERA5

### 2.5.3.1 Advantages

ERA5 followed in the footsteps of its predecessor ERA-Interim that stopped its production in August 2019. Both reanalyses are produced from 4D-Var, but ERA5 includes significant improvements due to higher spatial and temporal resolution (Hoffmann et al. 2018). The horizontal resolution has been updated from  $\sim 79$  km ( $0.75^{\circ} \times 0.75^{\circ}$  in ERA-Interim) to  $\sim 31$  km ( $0.3^{\circ} \times 0.3^{\circ}$  in ERA5), and the vertical resolution updated from 60 vertical levels (up to 0.1 hPa in ERA-Interim) to 137 vertical pressure levels (up to 0.01 hPa in ERA5). The temporal resolution of ERA5 is also improved; 1-hourly values compared to 6-hourly values (00, 06, 12, 18 UTC) in ERA-Interim (Dee et al. 2011, Hoffmann et al. 2018).

In addition, compared to ERA-Interim, ERA5 includes better representation of the troposphere, including such processes as tropical cyclones, global precipitation and evaporation balance, tropical land precipitation, soil moisture as well as more consistent SST and sea ice (Hoffmann et al. 2018).

### 2.5.3.2 Limitations

In this work I build a collocated dataset of satellite observations of the tropical atmospheric water cycle, and reanalyses of surface temperature and vertical velocity. Alternatively, all water cycle variables could have been retrieved from ERA5, thus avoiding such additional work as collocations of the satellite observations. In the end however, as discussed in Dee et al. (2011), all reanalysis variables not directly observed are constrained by the observations used to initialize the forecast, so the accuracy of these model-generated estimates comes down to the quality of the model physics and the analysis.

Then, the reanalysis is a model fed at some places by observations, which are sorely lacking over oceans where my studies were performed. Some observations are rejected in the assimilation process if they are too far from the previous model step. The most robust observations of water vapor are made with radiosondes, but there are no radiosondes launched over oceans (outside of ship tracks). Reanalyses of clouds and precipitation are fed by observations from ground-based radar networks (again with negligible cover over oceans), or passive IR or microwave radiometers whose vertical resolutions are inferior to the active measurements provided by the lidar and radar carried onboard CALIPSO and CloudSat. Sea surface temperature can however be constrained by a global network of buoy observations, and satellite observations. For these reasons, except for sea surface temperature, the reanalysis is a numerical model fed at some selected places with observations.

## 2.6 Satellite Collocations

When building the dataset of  $1^\circ \times 1^\circ$  gridded instantaneous observations of the water cycle variables, collocation of the CALIPSO and CloudSat satellite observations is straight forward as these satellites fly in formation. Collocations with ERA5 skin surface temperature is also easy as the reanalysis is given in hourly values for each location. The mean of the 01:00 am/pm and 02:00 am/pm SKT values are taken as the 01:30 pm value when the A-train crosses the equator.

Collocating these datasets with RH from SAPHIR (Megha-Tropiques) requires more consideration. Still, the high return frequency of a zonally (eastward) progressing satellite like Megha-Tropiques, carrying an instrument with a cross-track swath like SAPHIR, makes it possible to collocate its measurements with observations made by instruments carried by polar orbiting satellites such as the A-train and/or C-train.

The collocation of the  $1^\circ \times 1^\circ$  gridded products of these in space and time is performed under the requirement that the following two conditions are met:

1. The same  $1^\circ \times 1^\circ$  grid boxes must be sampled by all products that day.
2. SAPHIR must sample said grid boxes within a 2-hour time window around 01:30 pm LT. It is assumed that the atmosphere does not undergo significant change within this time frame.

An example of these collocation requirements is seen in Figure 2-22 below, which illustrates the  $1^\circ \times 1^\circ$  grid boxes that meet these two collocation requirements (in red) for the combination of one specific SAPHIR orbit and all GOCCP nighttime tracks.

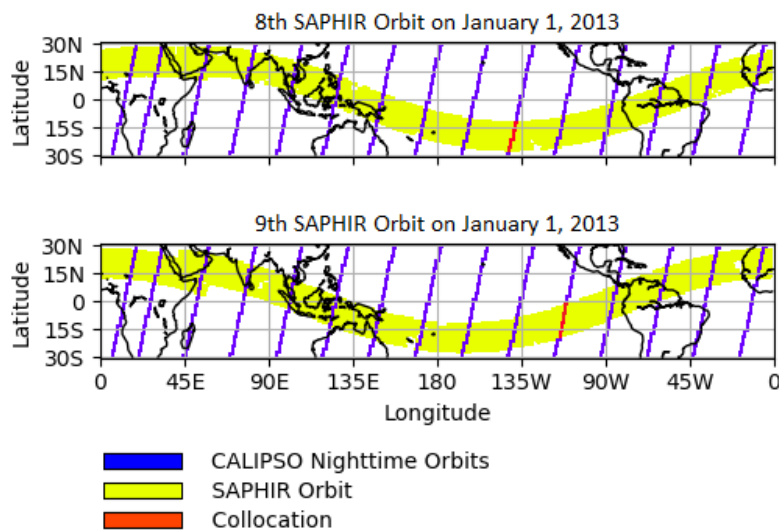


**FIGURE 2-22** Illustration of the collocation between the  $1^\circ \times 1^\circ$  gridded SAPHIR and GOCCP products. The blue lines show all nighttime CALIPSO orbits on January 1, 2013, whilst the broad yellow tracks show the SAPHIR sampling following the 8th (top) and 9th (bottom) Megha-Tropiques orbits on the same day. The red segments show the few  $1^\circ \times 1^\circ$  grid boxes that meet the two collocation requirements.

Lastly, Table 2-4 below summarizes the variables used to build the collocated dataset of the present work. It covers the tropical oceanic region ( $30^\circ\text{S}$  to  $30^\circ\text{N}$ ) with a spatial resolution of  $1^\circ \times 1^\circ$  and consists of instantaneous observations of the RH profile, cloud cover, altitude and temperature, and near-surface precipitation, as well as skin surface temperature and monthly mean vertical pressure velocity.

**TABLE 2-4:** The table summarizes the variables of the synergistic data set used in the present study (left) built from the initial variables (right). Shown here is the first half of the table. The second half follows on the next page.

Source	Variables in the Study						Initial Variables					
	Variable	Unit	Horizontal Resolution	Temporal Resolution	Abbreviation or Definition	Variable	Unit	Horizontal Resolution	Vertical Resolution	Temporal Resolution	Data Availability	
Megha-Tropiques (SAPHIR L2B)  Sivira et al. (2015) Brogniez et al. (2016)	Relative Humidity	%	$1^\circ \times 1^\circ$	01:30 am/pm	RH	Relative Humidity	%	10 km <sup>2</sup> at nadir	6 pressure layers	3 to 5 observations per day in the same location.	October 2011 – December 2019	
	Opaque Cloud Cover	%	$1^\circ \times 1^\circ$	01:30 am/pm	$Z_{OPAQUE}$	Opaque Cloud Cover	fraction: 0 – 1	333 m		01:30 am/pm	Jun. 2006 – December 2019	
Guzman et al. (2017)	Thin Cloud Cover	%	$1^\circ \times 1^\circ$	01:30 am/pm	$Z_{THIN}$	Thin Cloud Cover	fraction: 0 – 1	333 m		01:30 am/pm	June 2006 – December 2019	
	Opaque Cloud Altitude	km	$1^\circ \times 1^\circ$	01:30 am/pm	$Z_{OPAQUE}$	Opaque Cloud Altitude	km	333 m	480 m	01:30 am/pm	June 2006 – December 2019	
	Thin Cloud Altitude	km	$1^\circ \times 1^\circ$	01:30 am/pm	$Z_{THIN}$	Thin Cloud Altitude	km	333 m	480 m	01:30 am/pm	June 2006 – December 2019	
	Opaque Cloud Temperature	K	$1^\circ \times 1^\circ$	01:30 am/pm	$T_{OPAQUE}$	Opaque Cloud Temperature	K	333 m	480 m	01:30 am/pm	June 2006 – December 2019	
	Thin Cloud Temperature	K	$1^\circ \times 1^\circ$	01:30 am/pm	$T_{THIN}$	Thin Cloud Temperature	K	333 m	480 m	01:30 am/pm	June 2006 – December 2019	

Source	Variable	Unit	Horizontal Resolution	Temporal Resolution	Abbreviation or Definition	Variable	Unit	Horizontal Resolution	Vertical Resolution	Temporal Resolution	Data Availability
CloudSat (2C-PRECIP-COLUMN) Haynes et al. (2009, 2013) Kay et al. (2018)	No Near-Surface Precipitation	<i>Unitless</i> Precipitation not present.	$1^\circ \times 1^\circ$	Once Daily (01:30 pm)	dBZ < -15 at 480-960 m	Reflectivity	dBZ	1.4 km	480 m	Once Daily (01:30 pm)	June 2006 – August 2016
	Near-Surface Precipitation <u>Includes:</u> Drizzle, Rain, Heavy Rain	<i>Unitless</i> Precipitation is present.	$1^\circ \times 1^\circ$	Once Daily (01:30 pm)	dBZ > -15 at 480-960 m	Reflectivity	dBZ	1.4 km	480 m	Once Daily (01:30 pm)	June 2006 – August 2016
	Heavy Near-Surface Precipitation	<i>Unitless</i> Heavy precipitation is present.	$1^\circ \times 1^\circ$	Once Daily (01:30 pm)	dBZ > 40 at 480-960 m	Reflectivity	dBZ	1.4 km	480 m	Once Daily (01:30 pm)	June 2006 – August 2016
ERA5 Dee et al. (2011) Hoffmann et al. (2018)	Skin Surface Temperature	K	$1^\circ \times 1^\circ$	01:30 am/pm	SKT	Skin Surface Temperature	K	$0.3^\circ \times 0.3^\circ$	Surface Level	Hourly	January 2000 – December 2019
	Ascending Regime	hPa/day	$1^\circ \times 1^\circ$	Monthly Means	$\omega_{500} < -20$ hPa/day	Vertical Pressure Velocity	Pa/s	$0.3^\circ \times 0.3^\circ$	137 sigma pressure levels	Hourly	January 2000 – December 2019
	Intermediate Regime	hPa/day	$1^\circ \times 1^\circ$	Monthly Means	$-20 < \omega_{500} < 20$ hPa/day	Vertical Pressure Velocity	Pa/s	$0.3^\circ \times 0.3^\circ$	137 sigma pressure levels	Hourly	January 2000 – December 2019
	Descending Regime	hPa/day	$1^\circ \times 1^\circ$	Monthly Means	$\omega_{500} > 20$ hPa/day	Vertical Pressure Velocity	Pa/s	$0.3^\circ \times 0.3^\circ$	137 sigma pressure levels	Hourly	January 2000 – December 2019



## Chapter 3

# 3 Variations on the Instantaneous Timescale Under Large-Scale Circulation Constraints

Chapter 3 is based on my first published paper (Höjgård-Olsen et al. 2020), for which I first provide an extended summary (“*Summary of the Paper and Its Main Outcomes*”).

Höjgård-Olsen, E., Brogniez, H., Chepfer, H. (2020). Observed Evolution of the Tropical Atmospheric Water Cycle with Sea Surface Temperature. *Journal of Climate*, 33, pp. 3449-3470, DOI: [10.1175/JCLI-D-19-0468.1](https://doi.org/10.1175/JCLI-D-19-0468.1)

This analysis constitutes a comprehensive observational view of how the water cycle responds to sea surface temperature (SST) on the instantaneous timescale by characterizing fundamental relationships between aspects of the water cycle and SST. The structure of the paper is the following:

3	Variations on the Instantaneous Timescale Under Large-Scale Circulation Constraints .....	62
	<i>Summary of the Paper and Its Main Outcomes</i> .....	63
3.1	Introduction.....	69
3.2	Data .....	70
3.2.1	Relative Humidity from SAPHIR.....	70
3.2.2	Cloud Properties from GOCCP .....	71
3.2.3	Near-Surface Precipitation from CloudSat.....	71
3.2.4	Sea Surface Temperature and Vertical Pressure Velocity from ERA5.....	72
3.3	Methods .....	72
3.3.1	Collocation .....	72
3.3.2	Atmospheric Circulation Regimes.....	73
3.3.3	Summary of the Synergistic Dataset .....	74
3.3.4	Statistical Representation of the Collocated Instantaneous Dataset .....	77
3.4	Analyses of the Tropical Atmospheric Water Cycle’s Variation with SST in Different Regimes.....	78
3.4.1	Cloud Cover Variations with SST .....	78
3.4.2	Co-Variation of RH, Clouds and Near-Surface Precipitation with SST in the Descending Regime .....	80
3.4.3	Co-Variation of RH, Clouds and Near-Surface Precipitation with SST in the Ascending Regime	83

3.5	Discussion.....	87
3.5.1	Sensitivity of the Results to the Natural Climate Variability .....	87
3.5.2	About the Intermediate Circulation Regime.....	88
3.5.3	Limits of the Study .....	89
3.5.4	The Super Greenhouse Effect.....	89
3.5.5	Implications of the Study .....	90
3.6	Conclusion .....	91

## *Summary of the Paper and Its Main Outcomes*

Chapter 1 discusses the principal uncertainties in the feedback equation, and how previous observational work typically did not observe the detailed vertical structure of the tropical atmospheric water cycle and the instantaneous covariations between these, or if they did, they under sampled the tropical region and therefore missed the large-scale context.

All variables change together in observations. Thus, they cannot be used to study isolated causality or physical processes that require all other aspects of the atmosphere to be held fixed. Short and local scales are however where we come the closest to isolating our variables of interest, meaning that observations of instantaneous covariations are desirable to understand direct relationships between the water cycle variables. Instantaneous observations of one or two of the key water cycle variables (moisture, clouds, precipitation) have been made in the past, but this work builds a dataset of instantaneous satellite observations of the relative humidity (RH) profile, cloud characteristics and near-surface precipitation.

The study aims to improve on our knowledge of covariations of the tropical RH profile and cloud cover with SST on the instantaneous timescale, within different dynamical regimes and in the absence or presence of near-surface precipitation. The principal question is “*Do RH and cloud cover vary differently with SST on the instantaneous grid box scale under large-scale ascent and descent?*”, and secondary questions asked within each large-scale regime are:

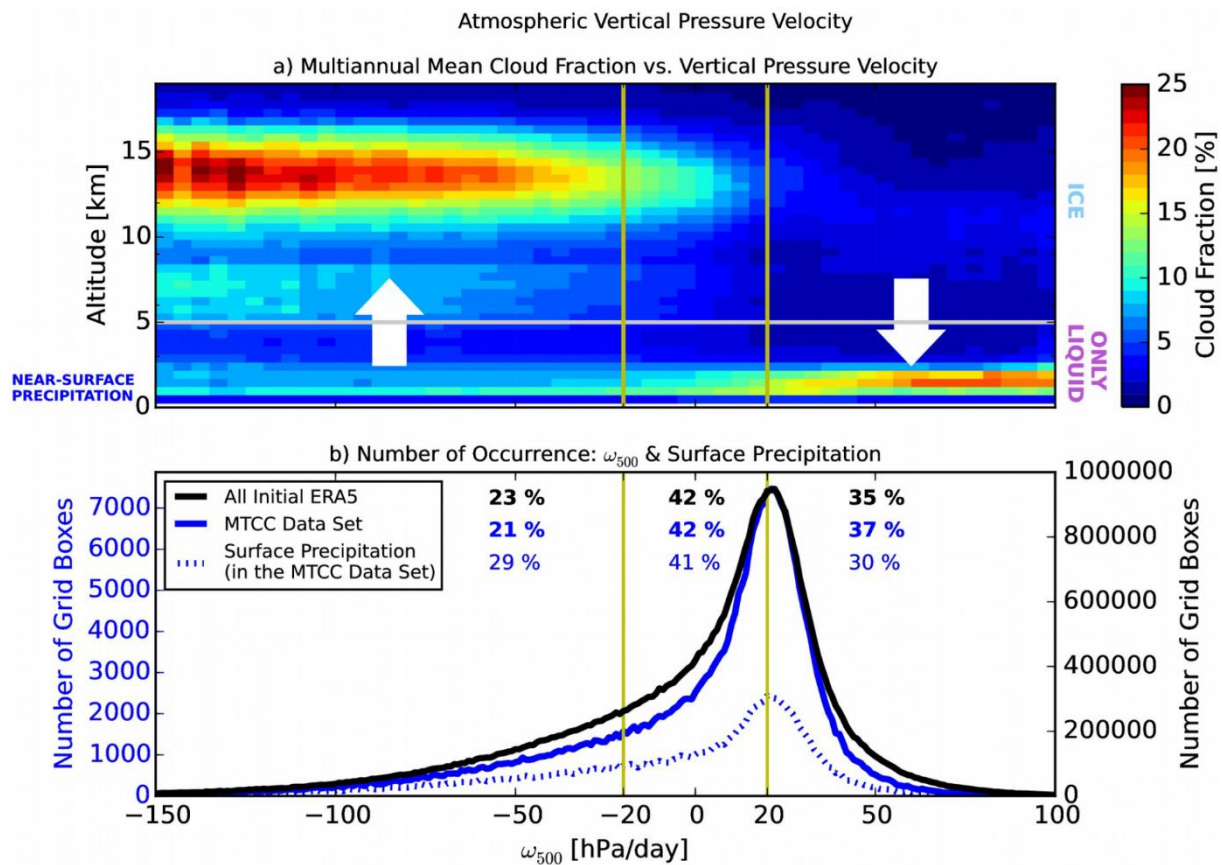
- Do RH and cloud cover vary differently with SST on this scale in the presence and absence of near-surface precipitation?
- Do low liquid and high ice cloud covers vary differently with SST on this scale?
- Does the RH profile vary differently with SST on this scale in the vicinity of low liquid clouds and high ice clouds?

This study builds, for the first time, a synergistic dataset of the RH profile, cloud characteristics and near-surface precipitation from instantaneous observations retrieved from the SAPHIR, CALIOP and CPR instruments described in Chapter 2. As cloud formation is known to be most sensitive to dynamic motions, the tropical atmosphere is partitioned into three large-scale vertical velocity regimes (ascending, intermediate, descending) based on monthly mean reanalysis of the vertical pressure velocity at the 500 hPa level ( $\omega_{500}$ , from ERA5). Additionally, cloudy scenes are separated by cloud phase (ice or liquid), opacity (opaque or thin) and the presence of near-surface precipitation. The collocated dataset of observations from SAPHIR, CALIPSO, and CloudSat with reanalysis from ERA5 is referred to as the *MTCC dataset*.

The study assesses the typical rates of change of RH and cloud cover with SST once daily at 01:30 pm within fully oceanic  $1^\circ \times 1^\circ$  grid boxes in the tropical belt ( $30^\circ\text{S}$  to  $30^\circ\text{N}$ ) and considers four years of observations (May 2012 to April 2016) to account for natural variability.

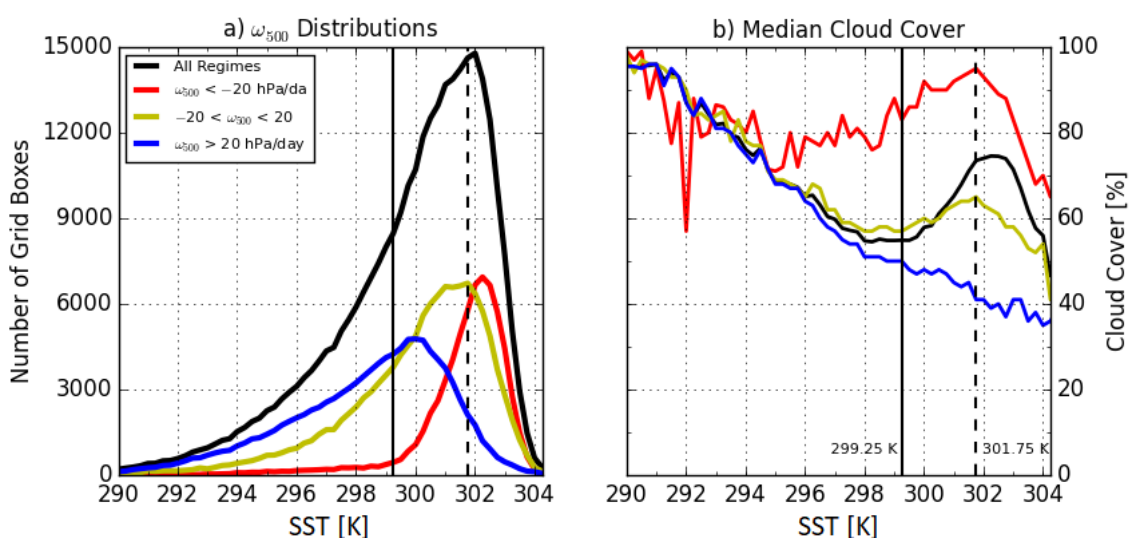
### Statistical Characteristics of the Large-Scale Regimes

Figure S3-1 shows defining features of the three large scale regimes. The sensitivity of cloud formation to dynamical regime is clearly seen in Fig. S3-1a, where two distinctive cloud populations stand out; 1) high ice clouds in the ascending regime ( $\omega_{500} < -20 \text{ hPa day}^{-1}$ ) and 2) low liquid water clouds in the descending regime ( $\omega_{500} > 20 \text{ hPa day}^{-1}$ ). Figure S3-1b shows that in the collocated MTCC dataset, 21 % of the grid boxes are sampled in the ascending regime, 37 % in the descending regime, and 42 % in the intermediate regime. The dataset is dominated by non-precipitating scenes, but when near-surface precipitation occurs, it is most frequent in the intermediate regime (41 %), and about equally frequent in the ascending (29 %) and descending regimes (30 %).



**FIGURE S3-1:** (a) Multiannual mean cloud fraction profiles as a function of vertical pressure velocity. The horizontal line represents the  $Z = 5$ -km level, which separates ice and only liquid phase clouds in the present study. The altitude at which “near-surface precipitation” is referred to (480-960 m) is also highlighted. (b) Distributions of grid boxes sorted by monthly mean  $\omega_{500}$  for ERA5 data sampled over the tropical oceans from May 2012 to April 2016 (black), the remaining  $\omega_{500}$  data in the collocated MTCC dataset (solid blue), and the subset of the collocated MTCC data containing near-surface precipitation (dashed blue). Percentages show the contribution of each regime to the total number of grid boxes in the respective distributions. The right y axis belongs to the black curve, while the left y axis belongs to the two blue curves.

Figure S3-2b shows the cloud cover evolution with SST in the individual regimes. Within grid boxes in the descending regime, cloud cover decreases monotonically with SST. However, in the intermediate regime the cloud cover evolution is nonlinear, defined by two transitions: a local minimum at SST = 299.25 K and a local maximum at SST = 301.75 K. Cloud cover in the ascending regime also peaks at SST = 301.75 K. The two transitions are referred to as the cold and warm SST thresholds in this work, and they are consistent with the SST ranges over which previous work have identified the onset of deep convection and the peak occurrence of deep convective clouds, respectively. Over the warm SST range (SST > 301.75 K), total cloudiness decreases with further SST warming in all regimes.



**FIGURE S3-2:** (a) Number distribution (gridbox sampling) with SST of the full MTCC dataset (black) as well as within the three  $\omega_{500}$  regimes. (b) Median cloud cover for the individual  $\omega_{500}$  regimes as well as without regime consideration (black).

### **How Do RH and Cloud Cover Vary with SST Under Large-Scale Descent?**

The descending regime ( $\omega_{500} > 20$  hPa/day) is the dominant regime over the cold SST range (SSTs < 299 K, S3-2a). It is characterized by low liquid water clouds (Fig. S3-1a) and a dry free troposphere. Fig. S3-3 below (top panel), shows a summarizing schematic of the changes in RH and cloud cover with SST in the descending regime with clouds in the liquid phase.

Over the cold SST range, opaque liquid cloud cover decreases with SST in this regime by  $-8\% \text{ K}^{-1}$  in the absence of near-surface precipitation and by  $-4\% \text{ K}^{-1}$  in the presence of near-surface precipitation. In contrast, the thin liquid cloud cover stays largely constant at  $\sim 20\%$  for all SSTs. Relative humidity increases slightly with SST in these scenes (up to  $+1.8\% \text{ K}^{-1}$ ). The *precipitation cover* (the number of precipitating cloud profiles divided by the total number of profiles) within these grid boxes decreases with warming, and the magnitude of the decrease increases going from the cold SST range ( $-0.4\% \text{ K}^{-1}$ ), to the moderate ( $-0.7\% \text{ K}^{-1}$ ), and warm SST range ( $-1.6\% \text{ K}^{-1}$ ).

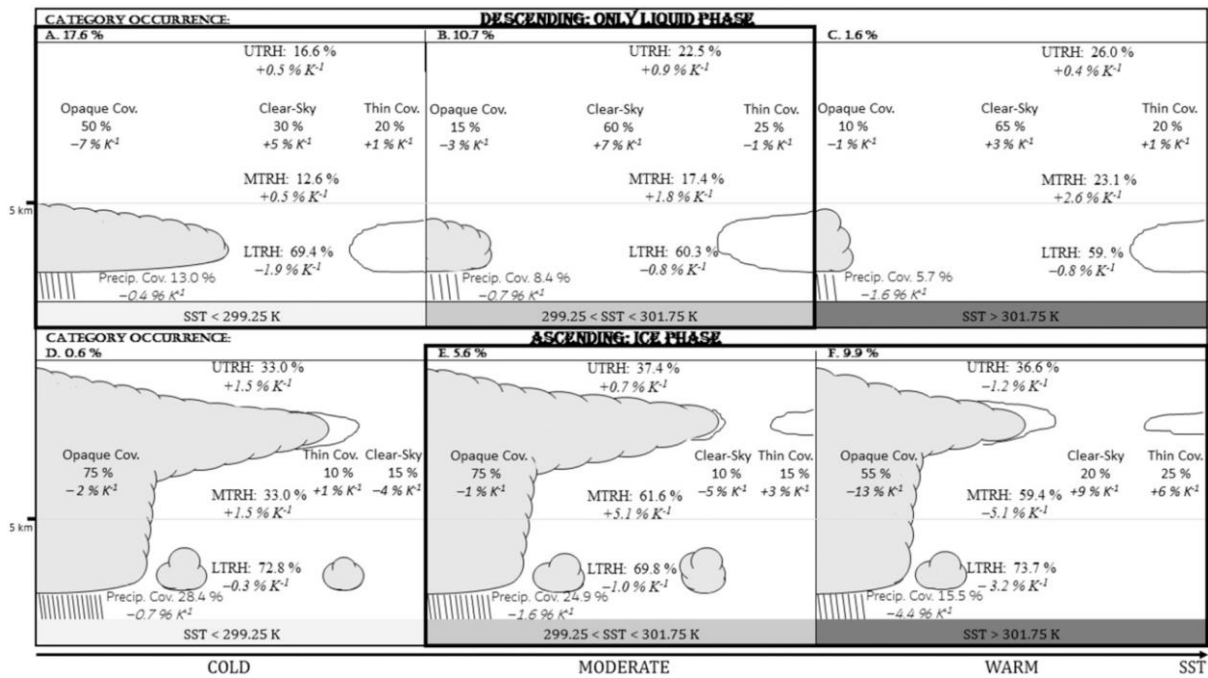


**FIGURE S3-3:** Schematic illustrating the tropical atmospheric water cycle's evolution with SST. (**top**) Low liquid clouds in the descending regime ( $\omega_{500} > 20 \text{ hPa day}^{-1}$ ). (**bottom**) High ice clouds in the ascending regime ( $\omega_{500} < -20 \text{ hPa day}^{-1}$ ). Mean values are given in normal font and the rate of change of each parameter with 1-K warming is given in italics. Values of category occurrence indicate how much of the tropical ocean is covered by that category and SST range in the MTCC dataset. Abbreviations: UTRH, MTRH, and LTRH stand for upper-, middle-, and lower-tropospheric RH, respectively; "Precip." stands for near-surface precipitation and "Cov." for cover within a grid box. The thick frames around subplots A,B and E,F highlight the SST ranges that are most important for the descending and ascending regimes, respectively.

### How Do RH and Cloud Cover Vary with SST Under Large-Scale Ascent?

The ascending regime ( $\omega_{500} < -20 \text{ hPa/day}$ ) is dominated by clouds in the ice phase (Fig. S3-1a) and is not important for SSTs  $< 299.25 \text{ K}$  (Fig. S3-2a). This cold threshold marks the onset of deep convection. Fig. S3-3 (bottom panel), summarizes the changes in RH and cloud cover with SST in the ascending regime with clouds in the ice phase.

In this regime, the moderate SST range ( $299.25 < \text{SST} < 301.75 \text{ K}$ ) is characterized by increasing thin ice cloud cover ( $+3 \text{ % K}^{-1}$ ) and middle-tropospheric RH with SST ( $+5 \text{ % K}^{-1}$ ). Over the warm SST range ( $> 301.75 \text{ K}$ ), the middle-tropospheric RH decreases again at a similar rate (MTRH:  $-5 \text{ % K}^{-1}$ ) and precipitating opaque high ice cloud cover decreases with SST by  $-13 \text{ % K}^{-1}$ . In contrast, thin high ice cloud cover (averaged over all grid boxes containing thin clouds) simultaneously increases by  $+6 \text{ % K}^{-1}$  over the warm SST range. As in the descending regime, the precipitation cover also decreases with warming in the ascending regime, and the magnitude of the decrease increases moving through the SST ranges (cold:  $-0.7 \text{ % K}^{-1}$ , moderate:  $-1.6 \text{ % K}^{-1}$ , warm:  $-4.4 \text{ % K}^{-1}$ ).

The collective observations made in the ascending regime over SSTs  $> 301.75 \text{ K}$  have implications for the theory surrounding the iris hypothesis, as they suggest that the previously observed decreasing opaque ice cloud cover with SST warming ( $-13 \text{ % K}^{-1}$ ), is not accompanied by increasing precipitation ( $-4.4 \text{ % K}^{-1}$ ), but rather by wider thin ice cloud cover ( $+6 \text{ % K}^{-1}$ ).

Additionally, if only grid boxes guaranteed to contain opaque high ice clouds and near-surface precipitation are considered, in the ascending regime over the warmest SSTs, the decrease in opaque high ice cloud cover in these grid boxes is accompanied by an equal increase in thin high ice cloud cover ( $+13\% \text{ K}^{-1}$ ) that keeps the total ice cloud cover at 100 %. This observation suggests a thinning of the anvil cloud cover (opaque ice cover) with SST over the warm SST range, under a constant total ice cloud cover of 100 %.

The observation that increasing thin ice cloud cover precisely compensates for the decrease in opaque ice cloud cover is possibly a previously undocumented observation and highlights the significance of observational tools that can distinguish clouds by their opacity.

### **What are the Expected Implications of These Observations on TOA Radiative Fluxes?**

The observed changes in RH and cloud cover with SST described above will affect the TOA radiative fluxes. Here I explain what effects I expect from these observations.

Based on the observations made in Fig. S3-3A, in the descending regime, and over the cold SST range, the outgoing longwave radiation (OLR) at the top of the atmosphere (TOA) should increase in accordance with decreasing cloudiness and thus induce a cooling effect there. Simultaneously, there should be a warming effect induced by slightly greater free-tropospheric RH and a decrease in opaque liquid cloud cover that allows for more SW absorption.

In the ascending regime, decreasing clear-sky cover over the moderate SST range (Fig. S3-3E), due to increasing thin ice cloud cover and constant opaque ice cloud cover with SST, together with increasing RH in the middle and upper troposphere, should induce an increase in atmospheric opacity and less OLR emitted at TOA over this SST range.

Over the warm SST range, in the ascending regime (Fig. S3-3F), free-tropospheric RH decreases with warming and the opaque ice cloud cover decreases substantially, suggesting an increase in OLR whilst a simultaneous increase in absorbed shortwave (SW) radiation. In opaque grid boxes, the thin ice cloud cover matches the decreasing opaque ice cloud cover which causes a significant reduction of OLR and a smaller reduction of absorbed SW radiation compared to clear-sky situations. In heavily precipitating scenes, RH is greater than 65 % in the middle troposphere, the total ice cloud cover is always 100 % (where opaque high ice cloud cover is 100% over the cold and moderate SST ranges and  $\geq 80\%$  over the warm). In these situations, OLR must be substantially reduced, whilst simultaneously little SW radiation is absorbed.

The net TOA radiative flux therefore varies between the large-scale regimes. The mean SST value is 299 K, with the interquartile range of tropical SSTs between 297 and 301 K. The tropical climate is thus centered around the cold SST threshold, and can be approximately represented by the dynamics over cold and moderate SST ranges. Being outside of the interquartile range of tropical SSTs, the warm SST range is less representative of the current tropical climate but increasingly more representative for the tropics the more the it warms.

### **Sensitivity of These Observed Relationships to a Warmer Climate State**

The El Niño period from May 2015 to April 2016 is extracted as a proxy for a warmer climate scenario. It is observed that the evolutions of opaque and thin liquid and ice cloud covers, as well as the RH profile within the individual regimes in the absence and presence of near-surface precipitation are very similar to the normal climate scenario. It is thus concluded that the relationships between RH, cloud cover and near-surface precipitation describe atmospheric composites that are robust to natural climate variability.

### **About the Intermediate Regime**

The primary focuses of this study are the processes characteristic of the ascending and descending regimes. Although the intermediate regime has been the focus of fewer previous studies, it is here concluded to largely be a mixture of the other two, where the low liquid water cloud cover is slightly wider than in the descending regime, and the high ice cloud cover smaller compared to the ascending regime. The moisture profiles in the intermediate regime also typically align themselves as averages between those of the ascending and descending regimes. The intermediate regime is thus a good representation of the tropics as a whole, as it is subject to processes in both the ascending and descending regimes, but the relationships between the water cycle variables are best studied in the focus regions defined by a more robust sign of vertical pressure velocity.

### 3.1 Introduction

Previous studies (e.g. Ramanathan and Collins 1991, Pierrehumbert 1995, Inamdar and Ramanathan 1998, Fu et al. 2002) have discussed if a self-regulating response to climate change allows the Earth system to modulate the outgoing longwave radiation (OLR) to prevent a runaway greenhouse effect. OLR is a function of surface temperature, atmospheric water vapor and clouds (Roca et al. 2000), intimately studied under clear-sky conditions (Goldblatt et al. 2013), whilst uncertainties remain in cloudy scenes (Stephens et al. 2016). We currently lack a comprehensive observational view of how moisture, clouds and precipitation co-vary with surface warming at the instantaneous time scale, in both the upper and lower troposphere and under different large-scale forcing.

According to the *iris hypothesis* (Lindzen et al. 2001), OLR increases with surface warming due to decreasing high ice cloud cover. Namely, precipitation efficiency increases with surface temperature, which leads to less detrainment and smaller convective anvils. The Lindzen et al. (2001) paper was however disputed on account of their choice of (*i*) study region (Pacific Warm Pool Region), (*ii*) identifying clouds by an infrared brightness temperature  $< 260$  K and (*iii*) representing sea surface temperature (SST) as a cloud-weighted parameter. These limitations were identified in the papers by Hartmann and Michelsen (2002), Lin et al. (2002) and Rapp et al. (2005).

Since then, it seems that model studies support an intensified hydrological cycle with more vigorous convective systems of greater precipitation efficiency (Allan and Soden 2008, Allan et al. 2014, Mauritsen and Stevens 2015, Bony et al. 2016), whilst *observational* work diverge. Li et al. (2019) found a positive IRIS feedback in the CESM model due to larger convective precipitation efficiency, less anvil detrainment, and thus thinner anvils. In the ascending branch of the tropical hydrological cycle some observational studies concluded on weak positive correlations between both upper tropospheric cloudiness and SST, as well as precipitation efficiency and SST (e.g. Lin et al. 2006, Su et al. 2008), whilst other observed a narrowing and strengthening of the Hadley cell with smaller average cloud cover (Su et al. 2017). Low liquid water clouds in subsidence regions are another key uncertainty for climate sensitivity prediction (Bony et al. 2004, Bony and Dufresne 2005, Zhai et al. 2015, Kamae et al. 2016, Ceppi et al. 2017, Klein et al. 2017). This study quantifies the cloud cover evolution with SST under both strong ascent and strong descent in instantaneous observations.

Previous observational studies usually either 1) only observed one or two of the three key variables (humidity, clouds, precipitation) and only ever discussed the third; 2) lacked the instantaneous covariation between them; 3) lacked the detailed vertical structure (e.g. Dewey and Goldblatt 2018) by focusing only on the upper (Gettelman et al. 2006, Buehler et al. 2008) or lower troposphere (Ross et al. 2002, Läderach and Raible 2013); or 4) provided detailed observations but lacked the large scale context by under-sampling the tropical ocean (e.g. Rapp et al. 2005, Su et al. 2008).

In the present study, we build an observational-based understanding of how water vapor profiles, cloud properties (cover, phase, opacity) and near-surface precipitation (480-960 m) vary together with tropical ( $30^{\circ}\text{S}$  to  $30^{\circ}\text{N}$ ) SST at the instantaneous time scale. It uses four years (May 2012 to April 2016) of instantaneous observations, that accounts for natural variability, collected by advanced satellites and subsequently analyzed together here for the first time. Relative humidity (RH) profiles are provided by the microwave radiometer SAPHIR

(Sounder for Atmospheric Profiling of Humidity in the Intertropics by Radiometry) onboard the Megha-Tropiques satellite, cloud characteristics by the CALIPSO (Cloud-Aerosol Lidar and Infrared Pathfinder Satellite Observation) lidar CALIOP (Cloud-Aerosol Lidar with Orthogonal Polarization), and near-surface precipitation by the CloudSat Cloud Profiling Radar (CPR).

We first present the individual satellite datasets (Section 3.2) and build the collocated composite dataset of the atmospheric water cycle at the instantaneous time scale and  $1^\circ \times 1^\circ$  spatial resolution (Section 3.3) which we refer to as the MTCC (Megha-Tropiques-CALIPSO-CloudSat) dataset. With the MTCC dataset, we perform statistical analyses of satellite data, based on instantaneous global scale statistics of the key tropical atmospheric water cycle variables. We observe and analyze how the key tropical atmospheric water cycle variables covary instantaneously with each other and SST, under atmospheric large-scale ascent and descent separately (Section 3.4). In Section 3.5 we show that the above-mentioned composite results are robust to natural climate variability such as El Niño and discuss the implications as well as limitations of the current work. We also compare our results to the iris hypothesis. Key messages are summarized in Section 3.6.

## 3.2 Data

### 3.2.1 Relative Humidity from SAPHIR

RH data is retrieved from the cross-track scanning, passive microwave radiometer SAPHIR onboard the Indo-French satellite Megha-Tropiques. Megha-Tropiques flies in a low inclination orbit ( $20^\circ$  at the equator) at an altitude of 866 km, which enables greater sampling of the tropical region ( $30^\circ\text{S}$  to  $30^\circ\text{N}$ ) compared to other previous lower observing platforms (Roca et al. 2015). It orbits the entire tropical belt within 100 minutes, yielding 14 to 15 orbits per day and 3 to 5 observations per day in the same location.

The SAPHIR microwave moisture sounder observes with a scan angle of  $\pm 42.96^\circ$  around nadir and a swath of 1700 km. SAPHIR measures the radiation emitted by water vapor in six channels around the 183.31 GHz absorption line, yielding a moisture profile of RH data in six pressure layers. This allows for RH profile estimations from the upper troposphere (upper limit at 100 hPa) down to the boundary layer (lower limit at 950 hPa) under both clear and cloudy conditions, as long as the clouds do not produce large hydrometeors or ice crystals, characterized as deep convection or convective overshoots (Burns et al. 1997, Greenwald and Christopher 2002). SAPHIR is the first microwave sounder to provide direct observations of the moisture profile with six observing channels. Previous satellites typically observed the moisture profile with three (e.g. Advanced Microwave Sounding Unit-B, AMSU-B) or five channels (Advanced Technology Microwave Sounder). Compared to the other 183 GHz radiometers Microwave Humidity Sounder and AMSU-B, RH estimates derived from SAPHIR have a higher accuracy in the upper and lower troposphere, thanks to three additional channels located closer to the center and the wings (Brogniez et al. 2013).

The present study uses the instantaneous  $1^\circ \times 1^\circ$  product L2B, in which each RH pixel within a grid box is averaged and weighted by its uncertainty that is computed within the retrieval scheme (Sivira et al. 2017). Only  $1^\circ \times 1^\circ$  grid boxes filled to more than 75 % by pixels flagged as valid are considered in the gridded SAPHIR product, and in the MTCC dataset.

### 3.2.2 Cloud Properties from GOCCP

In this study, cloud data are taken from the General Circulation Model-Oriented CALIPSO Cloud Product (GOCCP, Chepfer et al. 2010, 2013, Cesana and Chepfer 2012, Cesana et al. 2016), which consists of diagnosed cloud properties of CALIOP that measures the attenuated backscatter at 532 nm with a horizontal resolution of 333 m and a 90 m footprint size at ground level (Winker et al. 2009). CALIPSO flies as part of the near sun-synchronous A-train constellation. It yields 15 orbits per day, each one crossing the equator twice daily at 01:30 am and 01:30 pm local time (LT).

We use the latest version of the GOCCP product (GOCCP v.3.1.2, Guzman et al. 2017) with a spatial resolution of  $1^\circ \times 1^\circ$ . Each grid box contains the clear-sky cover, the opaque cloud cover and the thin cloud cover, the sum of which equals 100 %. Opaque clouds (optical depth  $> 3$  to 5) fully attenuate the laser beam, whilst thin clouds (optical depths  $< 3$  to 5) do not. Most liquid clouds are opaque to the lidar, whilst most ice clouds are transparent to the lidar (Chepfer et al. 2014). In addition, GOCCP v.3.1.2 gives one value of  $Z_{OPAQUE}$ , and one value of  $Z_{THIN}$  in each grid box. The altitude  $Z_{OPAQUE}$  is the center of the 480 m thick altitudinal bin just below the altitude of full attenuation averaged over all the opaque cloud profiles in the grid box, and  $Z_{THIN}$  the altitude half-way between cloud top and cloud base in a thin cloud (Vaillant de Guélis et al. 2017). In the present study *cloudy grid boxes* are defined as grid boxes of total cloudiness (opaque + thin cloud covers within a grid box)  $> 5\%$  and *clear-sky grid boxes* as grid boxes of total cloudiness  $\leq 5\%$ .

We further categorize cloudy objects after phase (liquid or ice). Previous publications have discussed the altitude at which tropical ice clouds form. Typically, it is located above 600 hPa (Li et al. 2012, Cesana et al. 2012, 2016). No further information is provided by the CALIPSO lidar for altitudes below  $Z_{OPAQUE}$ . Therefore, we distinguish between low liquid water clouds where  $Z_{OPAQUE}$  ( $Z_{THIN}$ )  $< 5$  km (labelled “Only Liquid” clouds) and high ice clouds where  $Z_{OPAQUE}$  ( $Z_{THIN}$ )  $> 5$  km (labelled “Ice” clouds). This approximate cloud phase distinction at 5 km altitude is chosen for the present study based on Figure 7 in Cesana and Chepfer (2013) (Fig. C-15, Appendix C) but should not be confused with the cloud masks built for the GOCCP product by them.

### 3.2.3 Near-Surface Precipitation from CloudSat

CloudSat flies as part of the A-train (10 – 15 seconds behind CALIPSO) and carries a 94 GHz cloud profiling radar, designed to profile atmospheric hydrometeors (Haynes et al., 2009). Its vertical resolution is 480 m and the footprint 1.4 km in diameter at the surface with an along-track resolution of 1.8 km and a minimum detection signal of  $-30$  dBZ (Smalley et al., 2014). For the purpose of this work, a  $1^\circ \times 1^\circ$  gridded version of the CloudSat Data Processing Center’s 2C-PRECIP-COLUMN (v. P\_R05, Haynes et al. 2013) product is used for near-surface precipitation detection over tropical oceans. Over open ocean surfaces, the 2C-PRECIP-COLUMN product assesses the likelihood of near-surface precipitation between 480 m and 960 m by applying near-surface reflectivity thresholds as well as estimating the path-integrated attenuation from the surface backscatter (Smalley et al., 2014). In the gridded product, local solar daytime and nighttime granule files are gridded separately using a uniform  $1^\circ \times 1^\circ$  grid

and filtered with respect to the 2C-PRECIP-COLUMN quality flags ( $\text{Status\_flag} < 8$ ). We partition cloudy grid boxes by the presence of near-surface precipitation or not, which in the gridded product are manifested by the flags “clear sky” for no near-surface precipitation and “rain possible”, “rain probable” and “rain certain” for the presence of near-surface precipitation (Haynes et al. 2013). Precipitating grid boxes therefore include all rain rates from drizzle to heavy precipitation. We make no distinction between rainfall rates in the figures we show, but comment on the evolution in heavily precipitating ( $\geq 72$  mm/day in the Tropics, Kay et al. 2018) situations. We then compute the *near-surface precipitation cover within a precipitating grid box* as the accumulated number of precipitating profiles, divided by the total number of profiles.

### 3.2.4 Sea Surface Temperature and Vertical Pressure Velocity from ERA5

We combine the above-mentioned satellite datasets with SST and vertical pressure velocity at the 500 hPa level ( $\omega_{500}$ ) from the 5<sup>th</sup> generation of the European Centre for Medium-Range Weather Forecast’s (ECMWF) reanalyses (ERA5: ECMWF ReAnalysis), where  $\omega_{500}$  is used as a proxy for the large-scale circulation. ERA5 is produced from 4D-Var data assimilations of the ECMWF Integrated Forecast System and is given in hourly values with a horizontal resolution of  $\sim 31$  km ( $0.3^\circ \times 0.3^\circ$ ) in 137 vertical hybrid sigma/pressure levels (Dee et al. 2011, Hoffmann et al. 2018). Since the  $\omega_{500}$  parameter is arguably sensitive to local dynamics and subject to significant biases at the instantaneous scale (Trenberth et al. 2000), we average the hourly ERA5  $\omega_{500}$  reanalyses to monthly mean values. Because SST is a much more homogeneously distributed parameter than  $\omega_{500}$ , and fluctuates on longer time scales, it is deemed reliable on the hourly scale. We take the mean of the 01:00 pm and 02:00 pm SST values as the 01:30 pm value (when the A-train crosses the equator). The full tropical belt ( $30^\circ\text{S}$  to  $30^\circ\text{N}$ ) is considered to avoid local and regional biases but limited to fully oceanic grid boxes to exclude biases that could arise due to land-ocean contrasts or the diurnal cycle over land (Noel et al. 2018).

## 3.3 Methods

### 3.3.1 Collocation

As CALIPSO and CloudSat are both part of the A-train constellation, these satellite data are collocated by design. Only daytime data (01:30 pm) is available for CloudSat since 2011, when a battery failure occurred. Therefore, because Megha-Tropiques was launched in October 2011, the present study only considers daytime observations. When collocating the SAPHIR dataset with the A-train datasets, a 2-hour time window is allowed around 01:30 pm for SAPHIR to scan the same GOCCP  $1^\circ \times 1^\circ$  grid box. We assume that the atmospheric state does not change radically within this 2-hour time frame. Then, validated  $1^\circ \times 1^\circ$  grid boxes from SAPHIR (RH) are collocated with GOCCP (cloud) and CloudSat (near-surface precipitation), in which all grid boxes containing at least one profile are used. These collocated grid boxes are then collocated with the ERA5 datasets of SST (at 01:30 pm) and  $\omega_{500}$  (monthly values).

### 3.3.2 Atmospheric Circulation Regimes

Konsta et al. (2012) characterized clouds and cloud properties using CALIPSO-GOCCP and MODIS (Moderate Resolution Imaging Spectroradiometer) observations in three  $\omega_{500}$  regimes; (1)  $\omega_{500} < -20$  hPa/day, (2)  $-20 < \omega_{500} < 20$  hPa/day, and (3)  $\omega_{500} > 20$  hPa/day. Here we partition the MTCC dataset into the same dynamical regimes. Figure 3-1a shows the climatological mean state of cloud fraction profiles plotted as a function of  $\omega_{500}$ . As in Konsta et al. (2012), two sections of large cloud fractions stand out: (i) high ice clouds for strongly negative  $\omega_{500}$  ( $< -20$  hPa/day) and (ii) low liquid water clouds for strongly positive  $\omega_{500}$  ( $> 20$  hPa/day) (separated by the horizontal grey line in Fig. 3-1a). The respective  $\omega_{500}$  ranges of these two sections overlap in the interval  $-20 < \omega_{500} < 20$  hPa/day, with smaller fractions of both low liquid water clouds and high ice clouds. The ascending regime appears to be dominated by high ice clouds in the MTCC dataset, when in fact, low liquid water clouds likely coexist with these (though not represented in MTCC when they occur below  $Z_{OPAQUE}$ ). Low liquid water clouds dominate the descending regime.

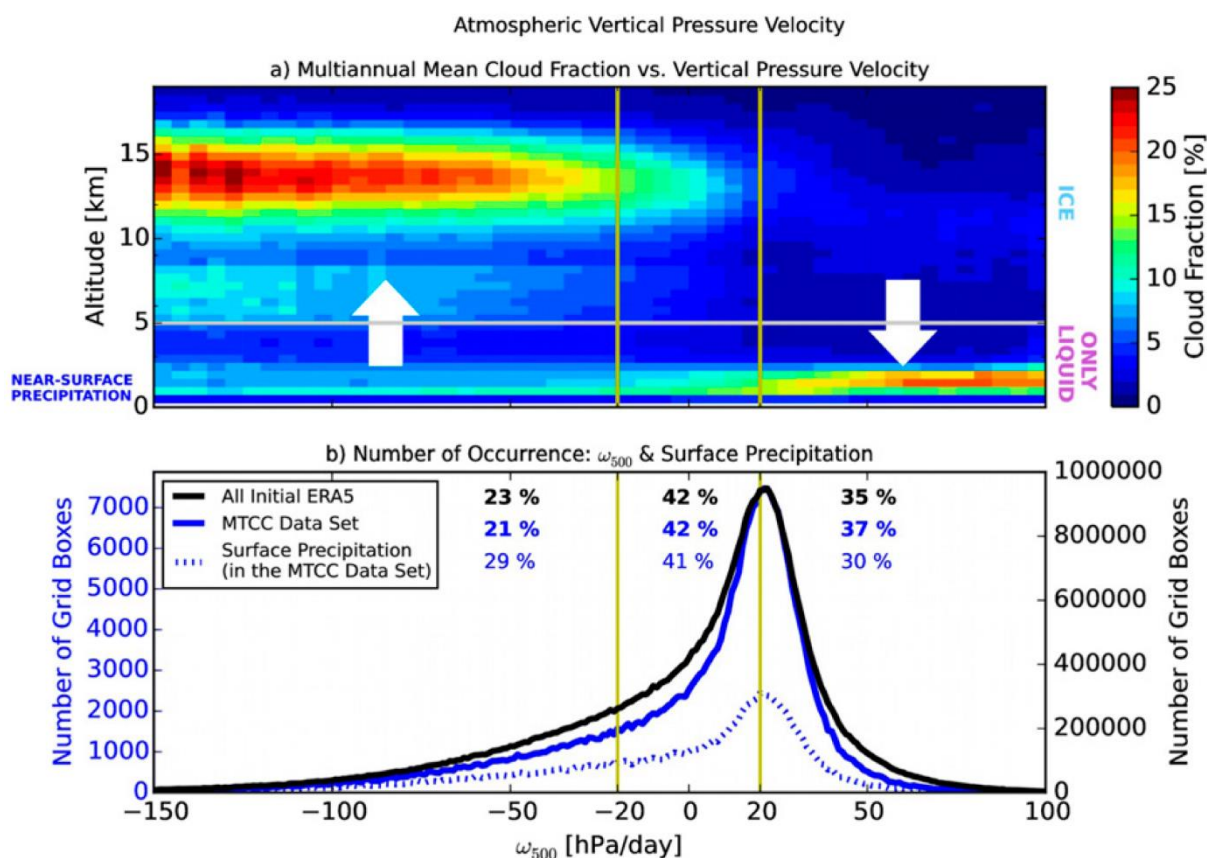


**FIGURE 3-1** (a) Multiannual mean cloud fraction profiles as a function of vertical pressure velocity. The horizontal line represents the  $Z = 5$ -km level, which separates ice and only liquid phase clouds in the present study. The altitude at which “near-surface precipitation” is referred to (480-960 m) is also highlighted. (b) Distributions of grid boxes sorted by monthly mean  $\omega_{500}$  for ERA5 data sampled over the tropical oceans from May 2012 to April 2016 (black), the remaining  $\omega_{500}$  data in the collocated MTCC dataset (solid blue), and the subset of the collocated MTCC data containing near-surface precipitation (dashed blue). Percentages show the contribution of each regime to the total number of grid boxes in the respective distributions. The right y axis belongs to the black curve, while the left y axis belongs to the two blue curves.

Figure 3-1b shows the resemblance between the  $\omega_{500}$  distributions of the under-sampled MTCC dataset (solid blue) and the full time period without regard to satellite overpasses (black). The MTCC dataset samples less than 1 % of the ERA5 grid boxes, but because regime percentages are sampled similarly (differing by 2 %), the MTCC dataset is deemed representative of the tropical oceans. 42 % of the MTCC grid boxes are sampled in the intermediate regime, 37 % in the descending regime and 21 % in the ascending regime. The dataset is dominated by non-precipitating scenes, but when near-surface precipitation occurs (dashed blue), it is most frequent in the intermediate regime (41 %), and about equally frequent in the ascending (29 %) and descending regimes (30 %).

### 3.3.3 Summary of the Synergistic Dataset

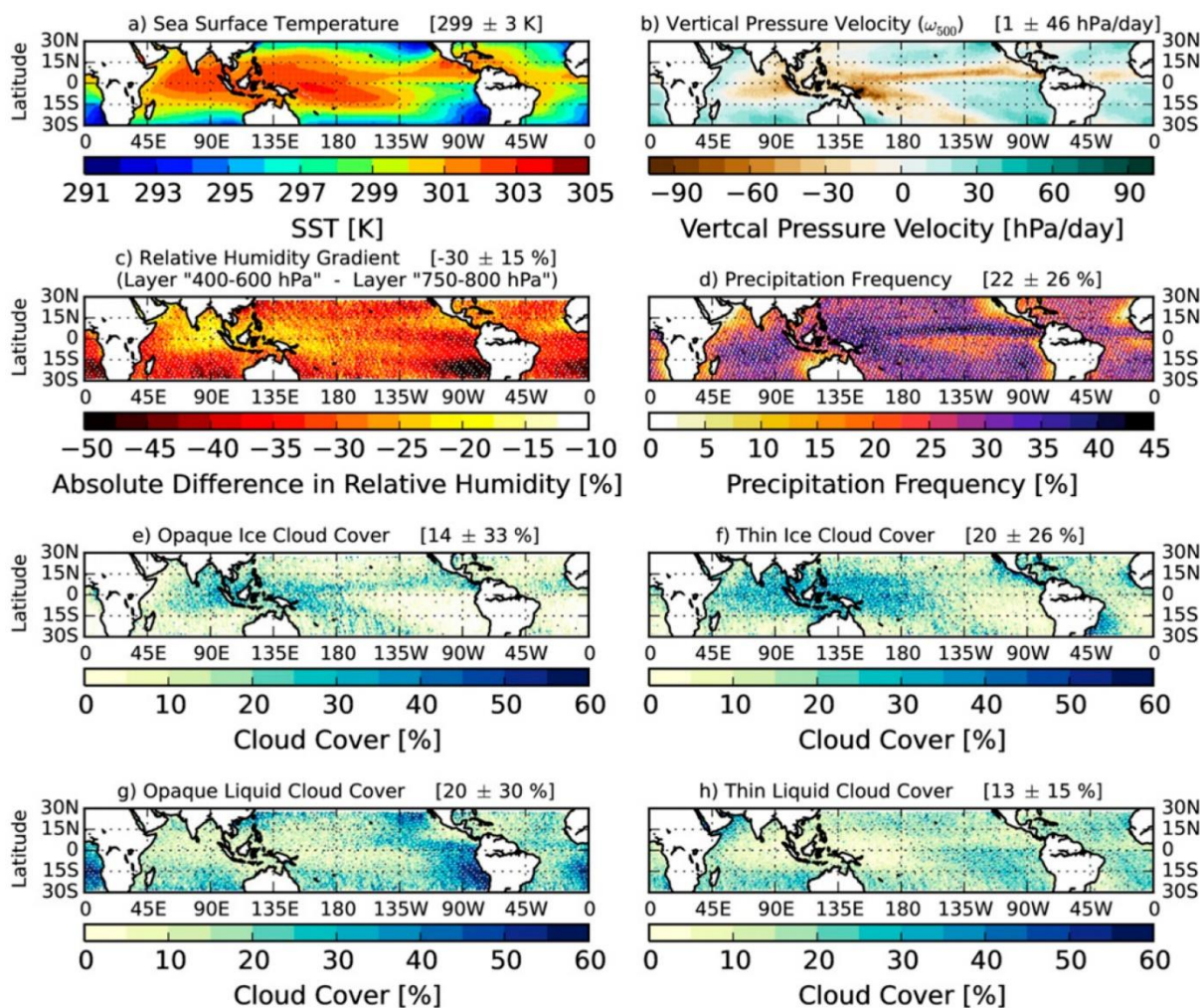
The MTCC dataset is summarized in Table 3-1. It covers the tropical oceanic region (30°S to 30°N) with a spatial resolution of  $1^\circ \times 1^\circ$  and consists of once daily (~01:30 pm) collocated instantaneous observations of RH profiles, cloud cover and SST, within three monthly mean  $\omega_{500}$  regimes. Cloudy grid boxes (cloudiness > 5 %) are further categorized according to phase (high ice/low liquid), opacity (opaque/thin) and the presence of near-surface precipitation. Thus, the entire tropical belt is represented by 27 categories: 3 categories of clear-sky cover  $\geq 95$  % (one for each  $\omega_{500}$  regime) and 24 cloudy categories (3  $\omega_{500}$  regimes  $\times$  2 phases  $\times$  2 opacities  $\times$  2 near-surface precipitation criteria). From this point on, only once daily grid boxes where data for all parameters are available, within each regime and category, are considered in the MTCC dataset.

Figure 3-2 shows the multiannual mean state of the MTCC parameters at 01:30 pm. As expected, the strongest convection is found in a narrow band along the intertropical convergence zone (ITCZ). This is the region of the highest SSTs (a), least negative RH gradient (c), greatest occurrence of near-surface precipitation (d) and widest high ice phase clouds (e, f). High ice and low liquid water clouds cover on average equally much of the tropical oceans (33 % and 34 %, respectively), but represent different regions (the ITCZ and the stratocumulus regions off the west coast of continents, respectively). Whilst thin clouds cover most of the high ice phase regions, opaque clouds cover more of the low liquid water phase regions. The standard deviations of the instantaneous  $\omega_{500}$ , near-surface precipitation frequency of occurrence and cloud covers show large spreads around their respective mean values (indicating wide ranges of local and instantaneous values not captured by the color bars corresponding to the mean values in Figure 3-2).

**TABLE 3-1:** The table summarizes the variables of the synergistic data set used in the present study (left) built from the initial variables (right). Shown here is the first half of the table. The second half follows on the next page.

		Variables in the Study						Initial Variables					
Source	Variable	Unit	Horizontal Resolution	Temporal Resolution	Criteria	Variable	Unit	Horizontal Resolution	Vertical Resolution	Temporal Resolution	Data Availability		
Megha-Tropiques (SAPHIR L2B) Sivira et al. (2015) Brogniez et al. (2016)	Relative Humidity	%	$1^\circ \times 1^\circ$	Once Daily (1.30 pm)	75 % of the pixels must be valid	Relative Humidity	%	10 km <sup>2</sup> at nadir	6 pressure layers	3 to 5 observations per day in the same location.	October 2011 – December 2018		
	Opaque Ice Cloud Cover	%	$1^\circ \times 1^\circ$	Once Daily (1.30 pm)	$Z_{OPAQUE} > 5 \text{ km}$	Opaque Cloud Cover	fraction: 0 – 1	333 m		Once Daily (1.30 pm)	June 2006 – October 2018		
Guzman et al. (2017)	Thin Ice Cloud Cover	%	$1^\circ \times 1^\circ$	Once Daily (1.30 pm)	$Z_{THIN} > 5 \text{ km}$	Opaque Cloud Altitude	km	333 m	480 m	Once Daily (1.30 pm)	June 2006 – October 2018		
	Opaque Liquid Cloud Cover	%	$1^\circ \times 1^\circ$	Once Daily (1.30 pm)	$Z_{OPAQUE} < 5 \text{ km}$	Thin Cloud Cover	fraction: 0 – 1	333 m		Once Daily (1.30 pm)	June 2006 – October 2018		
	Thin Liquid Cloud Cover	%	$1^\circ \times 1^\circ$	Once Daily (1.30 pm)	$Z_{THIN} < 5 \text{ km}$	Thin Cloud Altitude	km	333 m	480 m	Once Daily (1.30 pm)	June 2006 – October 2018		
						Thin Cloud Cover	fraction: 0 – 1	333 m		Once Daily (1.30 pm)	June 2006 – October 2018		

Source	Variable	Unit	Horizontal Resolution	Temporal Resolution	Criteria	Variable	Unit	Horizontal Resolution	Vertical Resolution	Temporal Resolution	Data Availability
CloudSat (2C-PRECIP-COLUMN)	No Near-Surface Precipitation	<i>Unitless</i> Precipitation not present.	$1^\circ \times 1^\circ$	Once Daily (1.30 pm)	dBZ < -15 at 750-1000 m Smalley et al. (2014)	Reflectivity	dBZ	1.4 km	480 m	Once Daily (1.30 pm)	June 2006 – August 2016
	Near-Surface Precipitation <u>Includes:</u> Drizzle, Rain, Heavy Rain	<i>Unitless</i> Precipitation is present.	$1^\circ \times 1^\circ$	Once Daily (1.30 pm)	dBZ > -15 at 750-1000 m Smalley et al. (2014)	Reflectivity	dBZ	1.4 km	480 m	Once Daily (1.30 pm)	June 2006 – August 2016
	Heavy Near-Surface Precipitation	<i>Unitless</i> Heavy precipitation is present.	$1^\circ \times 1^\circ$	Once Daily (1.30 pm)	dBZ > 40 at 750-1000 m Smalley et al. (2014)	Reflectivity	dBZ	1.4 km	480 m	Once Daily (1.30 pm)	June 2006 – August 2016
ERA5 Dee et al. (2011)	Sea Surface Temperature	K	$1^\circ \times 1^\circ$	Once Daily (1.30 pm)	Oceanic Grid Boxes	Sea Surface Temperature	K	$0.3^\circ \times 0.3^\circ$	Surface Level	Hourly	January 2000 – December 2018
	Ascending Regime	hPa/day	$1^\circ \times 1^\circ$	Monthly Means	$\omega_{500} < -20$ hPa/day	Vertical Pressure Velocity	Pa/s	$0.3^\circ \times 0.3^\circ$	137 sigma pressure levels	Hourly	January 2000 – December 2018
	Intermediate Regime	hPa/day	$1^\circ \times 1^\circ$	Monthly Means	$-20 < \omega_{500} < 20$ hPa/day	Vertical Pressure Velocity	Pa/s	$0.3^\circ \times 0.3^\circ$	137 sigma pressure levels	Hourly	January 2000 – December 2018
Hoffman et al. (2018)	Descending Regime	hPa/day	$1^\circ \times 1^\circ$	Monthly Means	$\omega_{500} > 20$ hPa/day	Vertical Pressure Velocity	Pa/s	$0.3^\circ \times 0.3^\circ$	137 sigma pressure levels	Hourly	January 2000 – December 2018



**FIGURE 3-2:** Maps of multiannual gridbox mean (a) sea surface temperature, (b) vertical pressure velocity, (c) relative humidity gradient (from layer “400–600 hPa” to layer “750–800 hPa”), (d) near-surface precipitation frequency, (e) opaque ice cloud cover, (f) thin ice cloud cover, (g) opaque low liquid cloud cover, and (h) thin low liquid cloud cover at 1330 LT. Values in brackets are the tropical oceanic multiannual means over the time period May 2012–April 2016 plus or minus their standard deviations.

### 3.3.4 Statistical Representation of the Collocated Instantaneous Dataset

The results in Section 4 below are presented solely for the instantaneous scale, in order to avoid smoothed averages and certify that the same situations are viewed and compared for moisture, clouds and near-surface precipitation. The median cloud cover and moisture profile evolutions with SST shown in Section 4, are only computed for 0.25 K SST bins that include at least five instantaneous observations. A bootstrapping algorithm is then applied to the data within each 0.25 K SST bin to remove statistically unlikely median values. In addition, evolutions calculated for SST bins containing less than 100 grid boxes are shaded by a gray filter in Figures 3-5, 3-8, C3-3 to acknowledge their weaker significance.

Because OLR increases non-linearly with free tropospheric moisture (Allan et al. 1999, Roca et al. 2000), changes in low humidity have a larger effect on the OLR than changes in high humidity. Therefore, when RH is compared in Figures 3-5, 3-8, C3-3, the relative RH difference is favored over the absolute difference.

### 3.4 Analyses of the Tropical Atmospheric Water Cycle's Variation with SST in Different Regimes

#### 3.4.1 Cloud Cover Variations with SST

Figure 3-3a shows the distributions of the three  $\omega_{500}$  regimes with SST. The descending regime dominates the cold SST range ( $< 299.25$  K) and the ascending regime the warm ( $> 301.75$  K). Both regimes have significant impact on the moderate SST range ( $299.25 < \text{SST} < 301.75$  K) as well, otherwise dominated by the intermediate regime. Figure 3-3b shows that the middle troposphere is driest in the descending regime and moistest in the ascending regime (more than twice as moist as the descending), and that there is little difference between the regimes in the boundary layer and at the top of the troposphere.

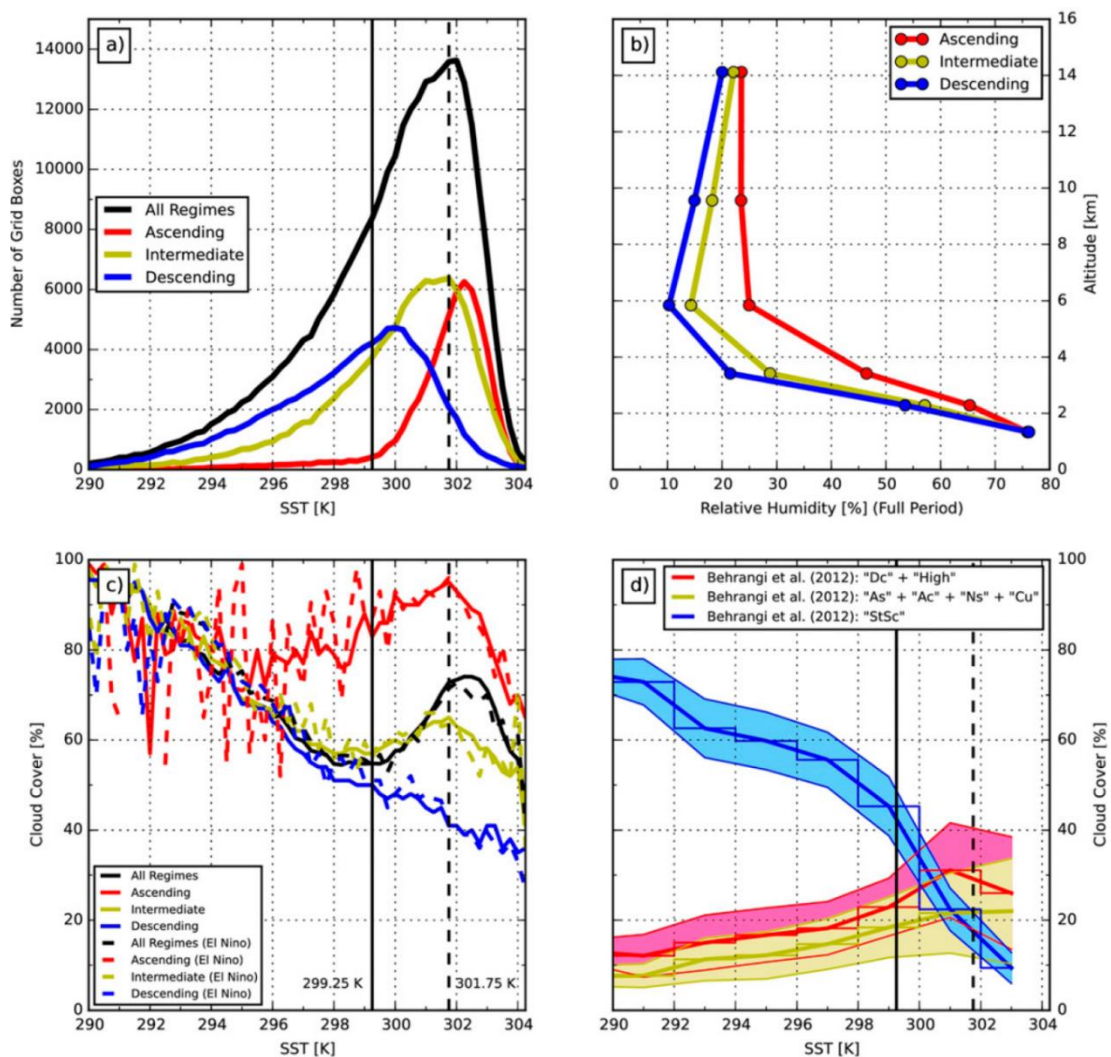


**FIGURE 3-3:** (a) Number distribution (gridbox sampling) with SST of the full MTCC dataset (black) as well as within the three  $\omega_{500}$  regimes. (b) Mean RH profiles over the full SST range for the three  $\omega_{500}$  regimes. (c) Median cloud cover for the individual  $\omega_{500}$  regimes as well as without regime consideration (black). Solid lines are for the full period (May 2012–April 2016) and dashed lines are for the El Niño period (May 2015–April 2016). (d) Evolutions of regime-accumulated cloud type cover from Table 1 in Behrangi et al. (2012). The central line for each regime is the sum over the single cloud types in Table 1 in Behrangi et al. (2012), in the present paper deemed to belong to the respective regime. The shading illustrates the uncertainty around the central line, taken as the sum of the two distinct cloud type values in Table 1 in Behrangi et al. (2012). Vertical lines are the SST thresholds at 299.25 (solid) and 301.75K (dashed).

After examining how the atmospheric circulation is tied to SST (Fig. 3-3a), we now examine how the cloud cover *within a grid box* varies with SST (Fig. 3-3c). Figure 3-3c shows the median grid box cloud cover evolution within each  $\omega_{500}$  regime, as well as over the whole tropics (“All Regimes”, solid black curve). In the descending regime, the cloud cover decreases almost monotonically with SST. In contrast, the cloud cover evolution in the intermediate regime shows a transition that can be defined by a local minimum at 299.25 K and the evolutions in both the ascending and intermediate regimes show transitions defined by local maxima at 301.75 K. Throughout the rest of the paper, we refer to these transitions as the *cold* and *warm* SST thresholds. Our *cold SST threshold* (299.25 K, Fig. 3-3) is consistent with the SST range (298 to 301 K) previously discussed as the onset of tropical deep convection, (Johnson and Xie 2010, Evans and Webster 2014, Aumann et al. 2017) and our *warm SST threshold* (301.75 K, Fig. 3) with where the frequency distribution of deep convective systems typically peaks (Waliser et al. 1993, Sabin et al. 2013, Houze et al. 2015).

Over the warm SST range, cloud cover decreases in all three regimes (3-3c), an observation we have not seen before. Each regime likely includes dynamical as well as thermodynamical components. For example, the descending (ascending) regime is sampled over a narrow  $\omega_{500}$  (SST) range whilst a wide range of SSTs (negative  $\omega_{500}$  values). The regime cloud cover decreases in all regimes over the four-year time period, fluctuating on annual time scales (~12 months) in the descending and intermediate regimes, whilst on shorter time scales (~6 months) in the ascending regime (Fig. C-12, Appendix C).

For comparison with previous work, Figure 3-3d shows the cloud cover evolutions with SST of the cloud types identified by the CloudSat 2B-CLDCLASS product in Behrangi et al. (2012). The colors represent the regimes where these cloud types are likely sampled. The cloud cover variations with SST in 3-3c and 3-3d agree to a first order in the ascending and descending regimes, but discrepancies are expected when comparing regime-median cloud cover variations to cloud type variations. Also, CALIOP (present study) captures thin clouds unresolved by CPR (Behrangi et al. 2012), which could partly explain the overall smaller cloud covers in 3d compare to 3-3c. Supplementary Figure C3-1 shows comparisons with previous observational studies that identified clouds by brightness temperature and assumed linear relationships between high ice cloud cover and cloud-weighted SST (Table 3-2). The cloud-weighting flattens the fluctuations in the instantaneous cloud cover evolutions, which could explain why previous studies plotted linear regressions and missed the non-linearity over the moderate and warm SST ranges.

Because Figure 3-3c shows that the cloud cover varies differently with SST in different regimes, we now examine each of them independently and characterize how RH, clouds and near-surface precipitation co-vary with SST. For this purpose, we make use of the full MTCC dataset (relying on the cloud types defined in Section 3.3) and discuss their variations within each SST range; *cold* ( $< 299.25$  K), *moderate* ( $299.25 < \text{SST} < 301.75$  K) and *warm* ( $> 301.75$  K).

**TABLE 3-2:** Study set-up in some previous work dedicated to the tropical cloud cover evolution with SST.

Author	Study Set-Up
Lindzen et al. (2001)	Data Source: Japanese Meteorological Geostationary Satellite Area: 30°S-30°N & 130°E-170°W (Pacific Warm Pool Region) Time Period: 1 January 1998 – 31 August 1999 SST Range: 298 – 303 K (cloud-weighted SST) Separated clouds with brightness temperature $BT_{11\mu m} < 220$ K and $BT_{11\mu m} < 260$ K.
Rapp et al. (2005)	Data Source: TRMM (VIRS) Area: 30°S-30°N & 130°E-170°W (Pacific Warm Pool Region) Time Period: 1 January 1998 – 31 August 1999 SST Range: 294 – 304 K Cloud size normalized by rainfall amount. Separated single and multi-core convective systems. Separated systems with brightness temperature $BT_{11\mu m} < 250$ K, $< 260$ K, $< 270$ K.
Lin et al. (2006)	Data Source: TRMM (CERES, TMI, VIRS) Area: 30°S – 30°N. $1^\circ \times 1^\circ$ . Oceanic grid boxes. Time Period: 1 January 1998 – 31 August 1998 SST Range: 290 – 305 K Evolution of deep convective system's areal cover with SST.
Su et al. (2008)	Data Source: AIRS (cloud fraction at pressure $< 300$ hPa) Area: 15°S – 15°N, tropical oceanic region Time Period: 1 September 2002 – 30 September 2006 SST Range: 300.8 – 302.6 K (cloud-weighted SST)
Behrangi et al. (2012)	Data Source: CALIPSO (2B-GEOPROF) and CloudSat (2B-CLDCLASS) Area: 30°S-30°N. Resolution: $3^\circ \times 3^\circ$ . Oceanic grid boxes. Time Period: 1 January 2007 – 31 December 2008 SST Range: 291 – 304 K Separated clouds into 9 classes with CloudSat (2B-CLDCLASS). Resolution: $3^\circ \times 3^\circ$ .

### 3.4.2 Co-Variation of RH, Clouds and Near-Surface Precipitation with SST in the Descending Regime

We first examine the horizontal extent of clouds in the descending regime ( $\omega_{500} > 20$  hPa/day), by counting the number of cloudy grid boxes (Fig. 3-4). This regime covers 36.8 % of the full tropical belt, where the area containing clouds accounts for 36.1 %. Low liquid water clouds without near-surface precipitation is the dominant category in the descending regime (18.0 %) and low liquid water clouds with near-surface precipitation contribute the second most (9.9 %). Most of the clouds are located over the moderate SST range, and the number distributions peak around 300 K (Fig. 3-4).

Next, we examine how the low liquid water cloud cover *within a grid box* varies with SST (Fig. 3-5a,b,c). The low liquid water cloud cover is decomposed into *opaque* and *thin* low liquid water clouds with/without near-surface precipitation. Regardless of near-surface precipitation category, the *opaque* low liquid water cloud grid box cover decreases monotonically with warming over the whole SST range, whilst the *thin* low water liquid cloud grid box cover is largely constant.

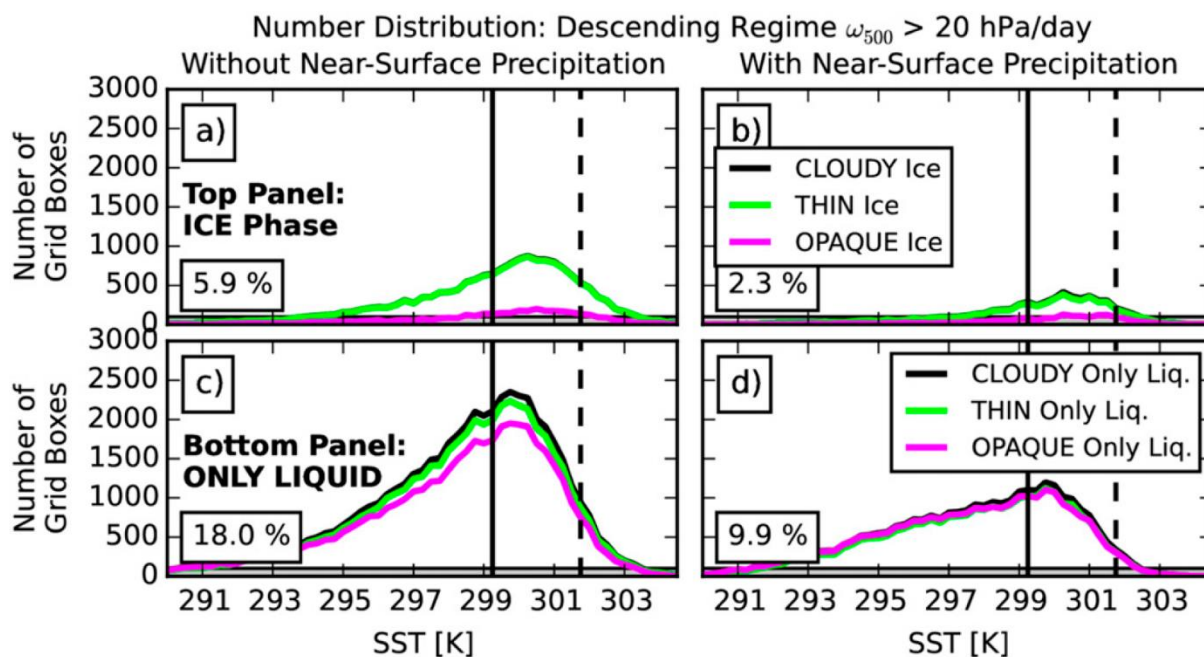


**FIGURE 3-4:** Gridbox number distributions with SST for the descending regime:  $\omega_{500} > 20$  hPa day<sup>-1</sup>. Occurrence of grid boxes containing (a) ice clouds but no near-surface precipitation, (b) ice clouds and near-surface precipitation, (c) only liquid clouds but no near-surface precipitation, and (d) only liquid clouds and near-surface precipitation. Vertical lines are for the same SST thresholds as identified in Fig. 3-3.

We finally describe how the RH profile *within a grid box* varies with SST (Fig. 3-5d,e,f). In the descending regime, only the lower troposphere is moist and the moistest ( $> 75\%$ ) for the coldest SSTs. RH is higher in the free troposphere over the cold SST range and in the presence of non-precipitating low liquid water clouds, whilst moister when these clouds precipitate over the moderate and warm ranges (3-5f).

Figure 3-6 shows how the tropical atmosphere changes when SST warms 1 K. The individual bullets in the top panel are weighted by their number contribution to the whole descending regime. Because low liquid water clouds without near-surface precipitation dominate the descending regime, we first analyze the influence of 1 K SST increase on this cloud population (pink circles in Fig. 3-6a,b,c). Overall SST ranges, an increase of 1 K SST is associated with a boundary layer drying (Fig. 3-6d,e) and decreasing opaque low liquid water cloud grid box cover (Fig. 3-6a,b,c). Over the cold SST range, we simultaneously observe a boundary layer drying ( $-2\% \text{ K}^{-1}$ ) and the greatest decrease in opaque low liquid water cloud cover ( $-8\% \text{ K}^{-1}$ ). Meanwhile, the overall tropical area containing these clouds increases slightly (the number of grid boxes increases  $+0.1\% \text{ K}^{-1}$ , not shown), suggesting that the condensed water is distributed over a larger portion of the tropical belt. Similarly, over the moderate SST range, an increase of 1 K SST is associated with a slightly drier boundary layer ( $-1\%$ ), a moistening of the middle troposphere ( $+2\%$ ) and decreasing non-precipitating low liquid water grid box cloud cover ( $-1\% \text{ K}^{-1}$ ). The overall area containing these clouds decreases as well ( $-0.2\% \text{ K}^{-1}$ , not shown), leading to a possible decrease in the amount of non-precipitating condensed water.

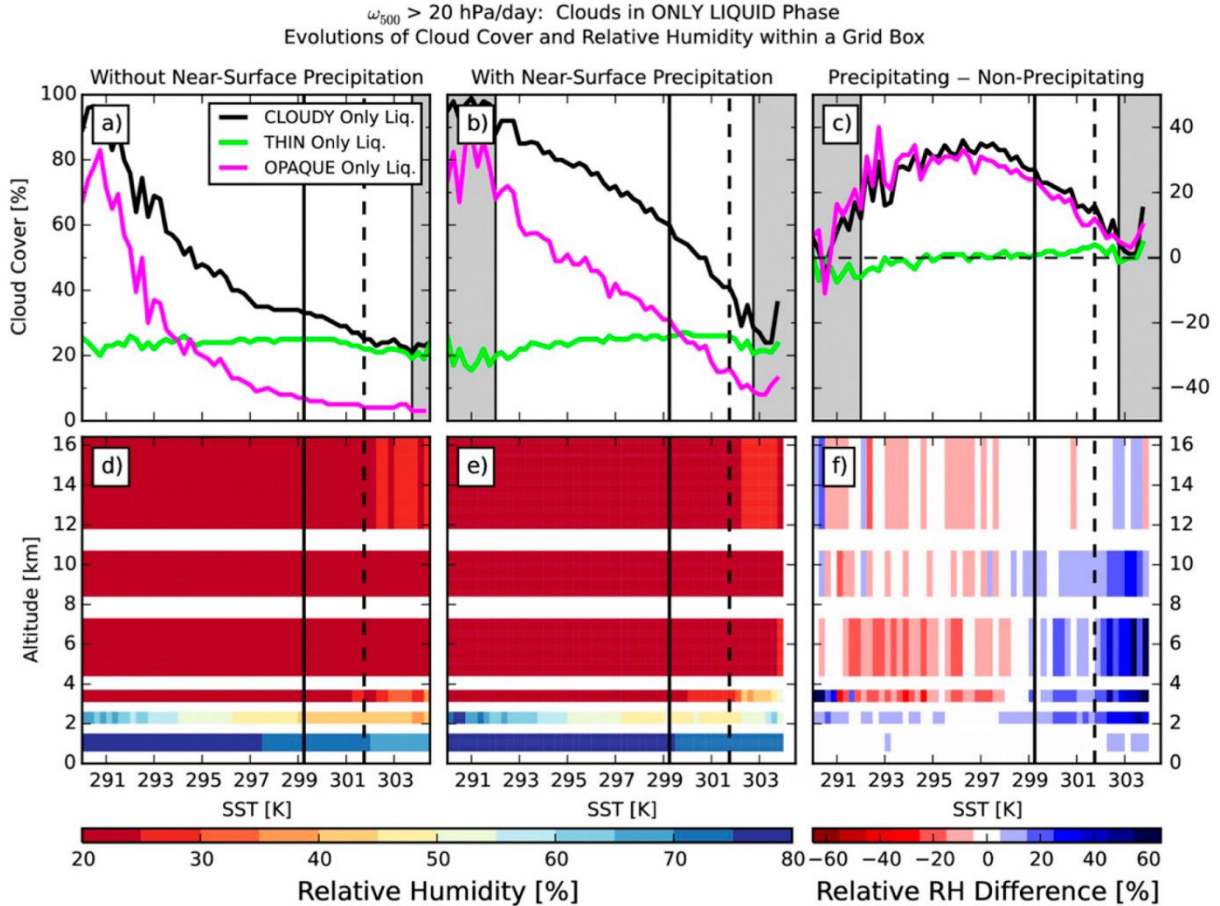


**FIGURE 3-5:** Evolution of the observed cloud cover and relative humidity with SST within grid boxes in the descending regime ( $\omega_{500} > 20$  hPa day<sup>-1</sup>), identified as containing only liquid clouds. **(top)** Median thin and opaque low liquid cloud covers in grid boxes **(a)** without near-surface precipitation and **(b)** with near-surface precipitation, as well as **(c)** their absolute difference. Note that addition of the green and magenta lines does not equal the black as both opaque and thin clouds are not present in all grid boxes (as evident from their differing number distributions in Fig. 3-4). Shaded gray areas cover SST bins where the median cloud cover or RH values in the present category were calculated for less than 100 grid boxes. **(bottom)** Median relative humidity profiles for grid boxes containing only liquid clouds **(d)** without near-surface precipitation and **(e)** with near-surface precipitation, as well as **(f)** their relative difference. Vertical lines are for the same SST thresholds as identified in Fig. 3-3.

The second most important cloud population is precipitating low liquid water clouds (red circles in Fig. 3-6a,b,c), whose responses in RH and cloud cover to a 1 K SST warming are of the same signs as the non-precipitating situations (pink circles). The opaque cloud amplitude response is however stronger in non-precipitating situations over the cold SST range ( $-8\% \text{ K}^{-1}$ ), whilst in the presence of near-surface precipitation ( $-6\% \text{ K}^{-1}$ ) over the moderate SST range.

Decreasing marine boundary layer cloud cover with warming has been shown in previous observational studies (Eastman et al. 2011, Behrangi et al. 2012, Zhai et al. 2015). Behrangi et al. (2012) found decreasing stratus and stratocumulus cloud cover with SST (Fig. 3-3d) and Zhai et al. (2015) observed decreasing monthly mean marine boundary layer cloud fractions in the merged CloudSat and CALIPSO cloud product over the SST range 291 to 299 K in the subsidence regions (20°NS – 40°NS). The largely constant thin low liquid water cloud cover with warming (Fig. 3-5a,b) clarifies that the decreasing low liquid water cloud cover is due to decreasing opaque low liquid water cloud cover with warming, whose evolution appears consistent with these previous publications and which we expect represents the transition from stratus clouds to stratocumulus.

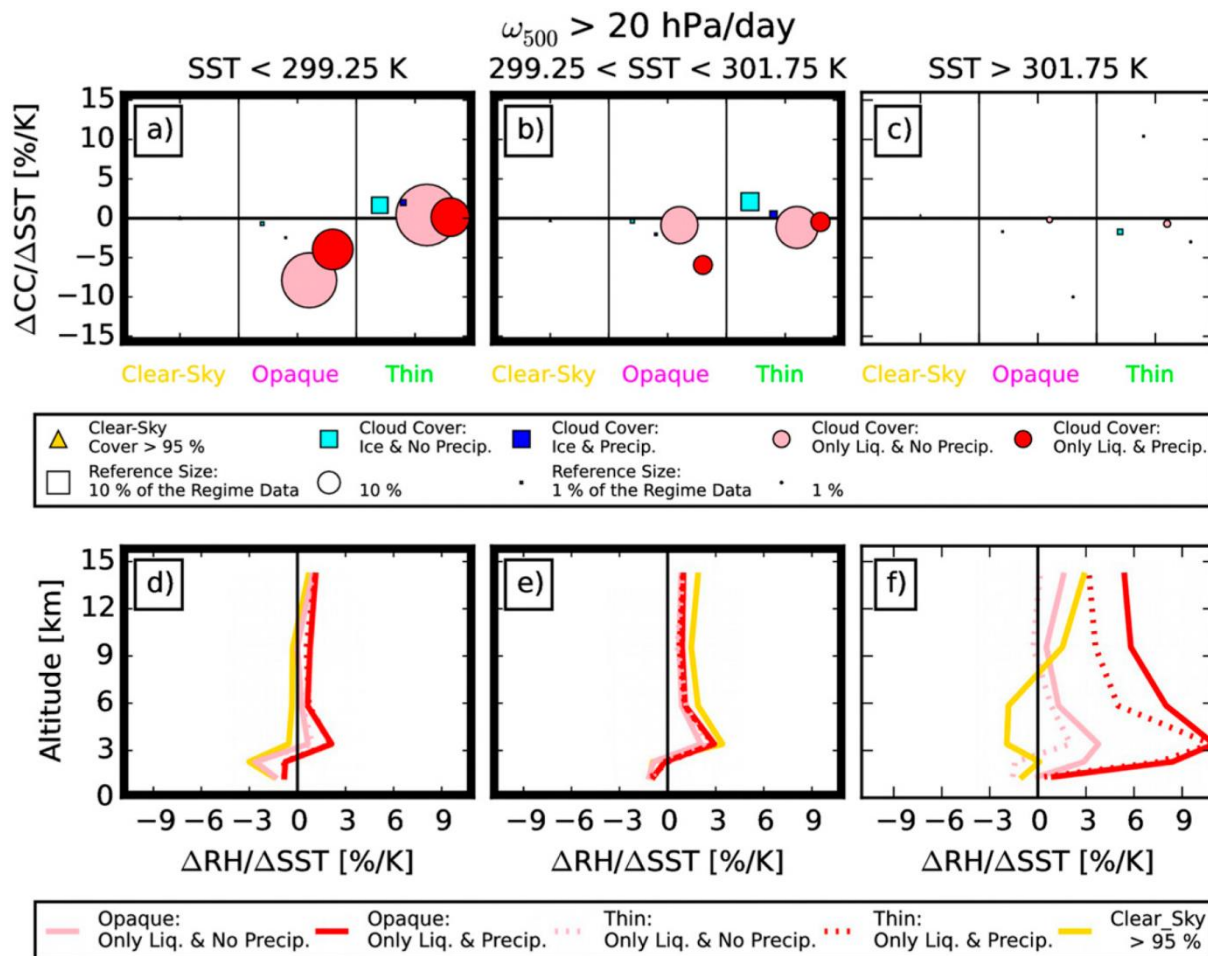


**FIGURE 3-6: (top)** Change of cloud cover associated with 1-K SST warming. Circles indicate only liquid cloud phase, squares ice phase, and golden pyramids clear-sky cover > 95% (these are almost invisible as their magnitudes are  $< 0.5\% \text{ K}^{-1}$ ). Bullet sizes are weighted by their number contribution to the descending regime:  $\omega_{500} > 20 \text{ hPa day}^{-1}$ . **(bottom)** Change of RH profiles associated with 1-K SST warming. Values of rate of change are given within the three SST ranges: **(a),(d)** SST < 299.25 K, **(b),(e)** 299.25 < SST < 301.75 K, and **(c),(f)** SST > 301.75 K. The trend values in the top and bottom panels are calculated from the respective top and bottom panels in Fig. 5.

### 3.4.3 Co-Variation of RH, Clouds and Near-Surface Precipitation with SST in the Ascending Regime

Figure 3-7 displays the grid box sampling of the ascending regime ( $\omega_{500} < -20 \text{ hPa/day}$ ) with SST. This regime covers 21.1 % of the overall tropical belt and is dominated by high ice clouds (14.5 %). Low liquid water clouds cover only 6.6 %. Most of these clouds occur over the moderate and warm SST ranges with a maximum occurrence at 302.25 K (Figures 3-7 and 3-3a).

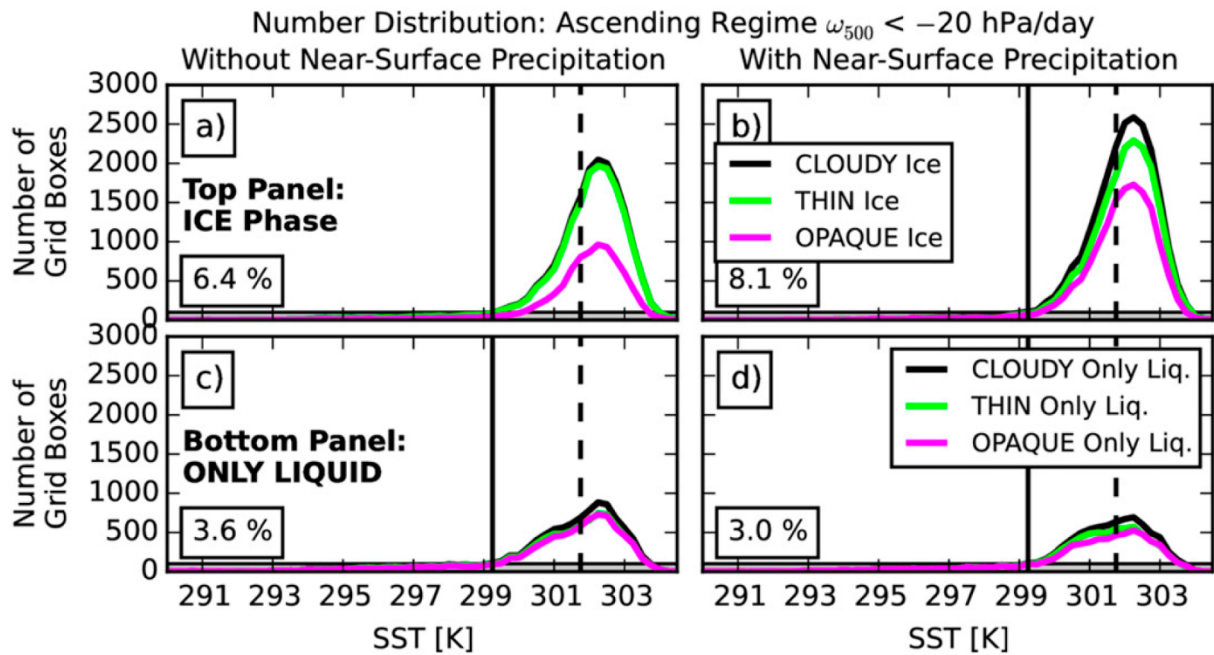


**FIGURE 3-7:** Gridbox number distributions with SST for the ascending regime:  $\omega_{500} < -20$  hPa day<sup>-1</sup>. Occurrence of grid boxes containing (a) ice clouds but no near-surface precipitation, (b) ice clouds and near-surface precipitation, (c) only liquid clouds but no near-surface precipitation, and (d) only liquid clouds and near-surface precipitation. Vertical lines are for the same SST thresholds as identified in Fig. 3.

Figures 3-8a,b show how opaque and thin high ice cloud cover *within a grid box* vary with SST. Over the moderate SST range, the grid boxes containing opaque high ice clouds are almost fully overcast (> 80 %), whilst over the warmest SST range, the opaque high ice cloud cover decreases with SST, possibly in favor of increasing thin high ice cloud cover. Moreover, the presence of near-surface precipitation is associated to larger opaque high ice cloud grid box cover (+40 %).

Figures 3-8d and 3-8e show that the boundary layer and the middle troposphere are moist (> 60 %) in the presence of high ice clouds, but the RH profile varies with SST. Hatched areas in Fig. 3-8 indicate where the interquartile range (IQR) of RH is greater than 35 % (Figure C3-7, Supplementary Material). In these areas we recall the potentially dry bias in SAPHIR where deep convective profiles are discarded on account of the scattering by their large ice crystals (Brogniez et al. 2013). Over the moderate SST range, humidity increases with SST in the lower free troposphere and peaks around the warm SST threshold (301.75 K), indicative of rising altitude of convective mixing and cloud development. The free tropospheric RH (FTRH) is greater in precipitating compared to non-precipitating scenes (up to 40 %) over the full SST range. In fact, in the presence of heavy near-surface precipitation (Fig. C-13, Appendix C), RH > 65 % in all free-tropospheric layers, whilst the boundary layer is dry (~45 %).

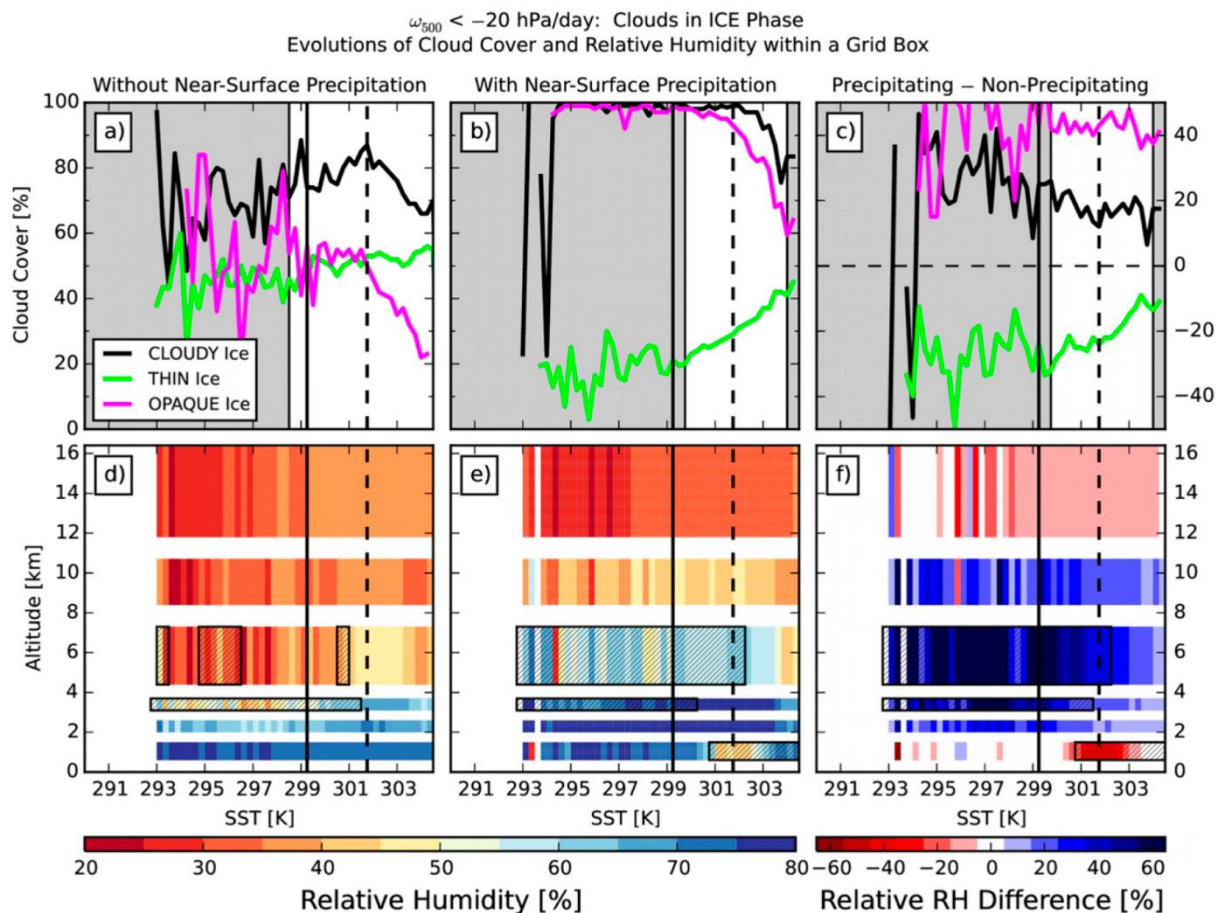


**FIGURE 3-8:** Evolution of the observed cloud cover and relative humidity with SST within grid boxes in the ascending regime ( $\omega_{500} < -20$  hPa day<sup>-1</sup>), identified as containing ice clouds. **(top)** Median thin and opaque ice cloud covers in grid boxes **(a)** without near-surface precipitation and **(b)** with near-surface precipitation, as well as **(c)** their absolute difference. Note that addition of the green and magenta lines does not equal the black as both opaque and thin clouds are not present in all grid boxes (as evident from their differing number distributions in Fig. 3-7). Shaded gray areas cover SST bins where the median cloud cover or RH values in the present category were calculated for less than 100 grid boxes. **(bottom)** Median relative humidity profiles for grid boxes containing ice clouds **(d)** without near-surface precipitation and **(e)** with near-surface precipitation, as well as **(f)** their relative difference. Black squared and hatched areas indicate layer sections where the interquartile range is greater than 35%, and as such are deemed nonsignificant (supplemental Fig. C3-11). Vertical lines are for the same SST thresholds as identified in Fig. 3-3.

Figure 3-9 shows the rate of change of cloud covers and RH associated to 1 K SST increase in the ascending regime. As scenes containing high ice clouds with near-surface precipitation dominate this regime, we first analyze the changes in this population (dark blue squares and profiles in Fig. 3-9, middle and right columns). Over the moderate SSTs, the free troposphere moistens (Fig. 3-9e) in the presence of thin clouds (+1.5 % K<sup>-1</sup>, dotted dark blue line) and in clear-sky grid boxes (+5 % K<sup>-1</sup>, yellow). The horizontal extent of high ice clouds increases (+0.1 to +0.2 % K<sup>-1</sup>, not shown) and so does the thin high ice cloud grid box cover (+3 % K<sup>-1</sup>), whilst the opaque high ice cloud grid box cover decreases slightly (-2 % K<sup>-1</sup>). In contrast, when SST warms 1 K over the warm SST range, the boundary layer moistens, and the free troposphere dries substantially (-4 to -8 % K<sup>-1</sup>). The horizontal extent of high ice clouds decreases (-0.2 to -0.3 %) (not shown), as does the opaque high ice cloud cover (-13 % K<sup>-1</sup>), whilst the thin high ice cloud cover increases (+6 % K<sup>-1</sup>).

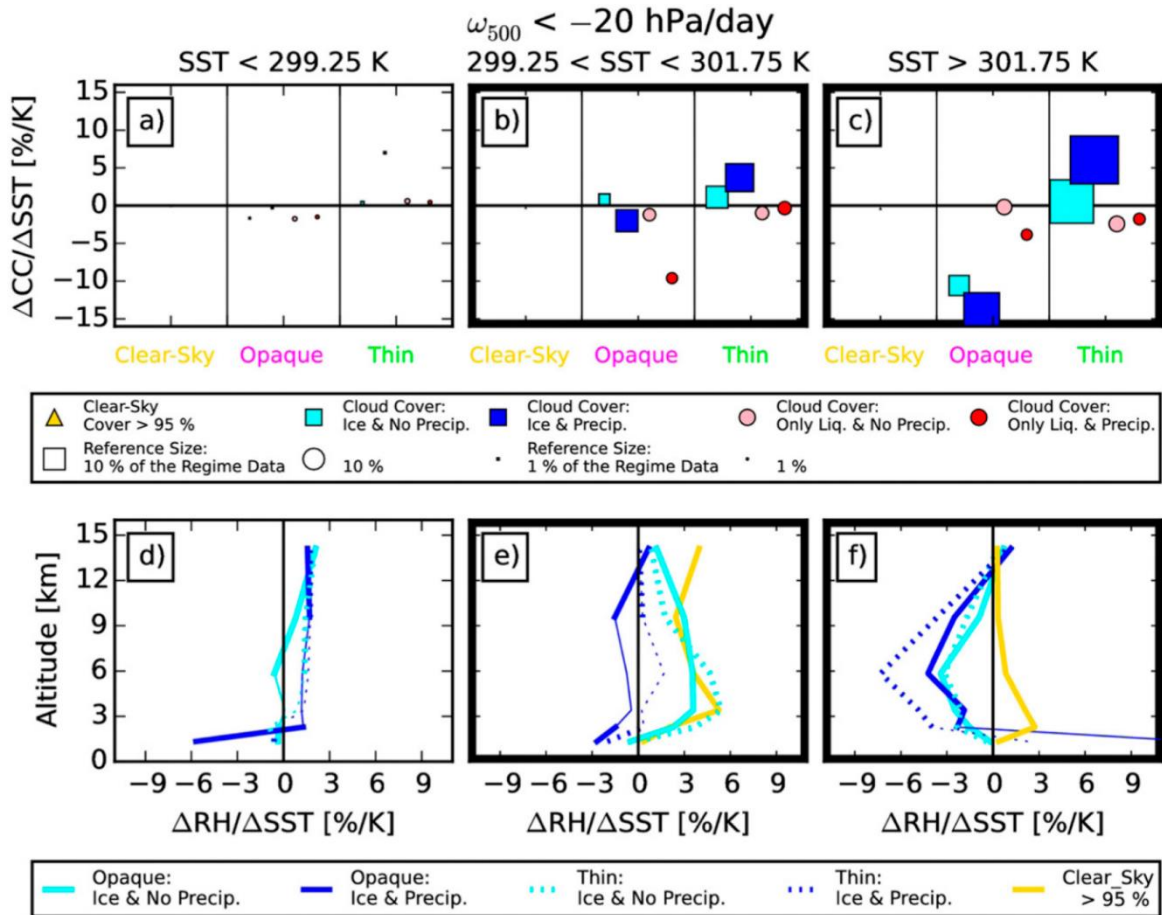


**FIGURE 3-9: (top)** Change of cloud cover associated with 1-K SST warming. Circles indicate only liquid cloud phase, squares ice phase, and golden pyramids clear-sky cover > 95% (these are almost invisible as their magnitudes are  $< 0.5\% \text{ K}^{-1}$ ). Bullet sizes are weighted by their number contribution to the ascending regime:  $\omega_{500} < -20$  hPa day<sup>-1</sup>. **(bottom)** Change of RH profiles associated with 1-K SST warming. Thick lines in the bottom row show significant values (corresponding to nonhatched areas in Fig. 3-8), while thin lines show all rates of change. Values of rate of change are given within the three SST ranges: **(a),(d)** SST < 299.25 K, **(b),(e)** 299.25 < SST < 301.75 K, and **(c),(f)** SST > 301.75 K. The trend values in the top and bottom panels are calculated from the respective top and bottom panels in Fig. 3-8.

The second most important population is high ice clouds without near-surface precipitation (light blue squares and profiles in Fig. 9). Here when SST warms 1 K, the high ice cloud changes (Fig. 3-9b,c) are like the precipitating category (dark blue squares), suggesting that high ice clouds and near-surface precipitation are poorly coupled. Precipitating high ice clouds (both opaque and thin) dry the free troposphere more than the non-precipitating counterparts.

We now compare our results in the ascending regime to previous observational work:

- That opaque high ice cloud cover decreases with SST in the ascending regime over the warm SST range ( $> 301.75$  K), established in this study, is consistent with Igel et al. (2014), who found anvils (the glaciated part of a deep convective system) to grow smaller and thicker with SST based on CloudSat observations. The CloudSat radar is insensitive to thin clouds, so these were likely poorly represented in the Igel et al. (2014) study. The CALIPSO lidar does however effectively distinguish between opaque and thin clouds in the present study, and thus, the increase in thin high ice cloud cover with SST, established in this study, adds new information about the high ice clouds' variation with SST.

- The increase in FTRH around the warm SST threshold (301.75 K) is consistent with the peak value in column water vapor (CWV) in Dewey and Goldblatt (2018) – although their study was conducted over a wider region than ours (60°S to 60°N) and over both land and ocean surfaces.
- The higher FTRH in the ascending regime (Figure 3-8) compared to the descending regime (Figure 5) seems consistent with the results in Masunaga (2014) who showed with AIRS (NASA’s Atmospheric Infrared Sounder) observations that the large-scale updraft in organized systems is generally supplied by moisture through low and middle tropospheric convergence, whilst in contrast, free tropospheric moisture is diverging above shallow cumulus clouds (expected in the descending regime).
- The higher FTRH associated to near-surface precipitation is consistent with Peters and Neelin (2006) and Holloway and Neelin (2009). The latter observed in radiosonde and precipitation gauge measurements (from the Nauru Island, western equatorial Pacific), that the transition to deep convection and increased precipitation rates is governed by the CWV above the 850 hPa pressure level, whilst largely independent of the boundary layer integrated CWV content. Our satellite-based results suggest that these previous local and punctual observations might be representative of tropical ascending regions.

## 3.5 Discussion

### 3.5.1 Sensitivity of the Results to the Natural Climate Variability

Section 3.4 establishes new observed relationships between RH, clouds and near-surface precipitations. Here we examine the sensitivity of these relationships to natural climate variability. For this purpose, we extracted the El Niño period (May 2015 to April 2016) and compared it to the full period (May 2012 to April 2016) with and without the El Niño period.

There is no notable difference in the  $\omega_{500}$  distributions between the three time periods (not shown). Moreover, Figures 3-10a,b,c suggests that there are overall little differences in the individual frequency of occurrence of each atmospheric category between the three time periods. Yet, the relative contribution of grid boxes containing high ice clouds is greater during the El Niño period, at the expense of slightly fewer grid boxes containing low liquid water clouds. Consistently, Figure 3-10d,e,f show that the mean RH profiles are drier (–2 to –5%) in the lower troposphere during El Niño, whilst the mid-troposphere is up to 9 % moister.

We also compared the detailed RH, cloud and near-surface precipitation analysis within each  $\omega_{500}$  regime (Figures 3-5 and 3-8 for the full period) to the El Niño period and found no noticeable differences (Figures C3-6 to C3-8, Supplementary Material). That comparison suggests that the relationship between RH, clouds and near-surface precipitation shown in Section 3.4 describes atmospheric composites that are robust to natural climate variability, as it is only the frequency of occurrence of each atmospheric category that changes (Fig. 3-10a,b,c), and not the relationship between RH, clouds and precipitation.

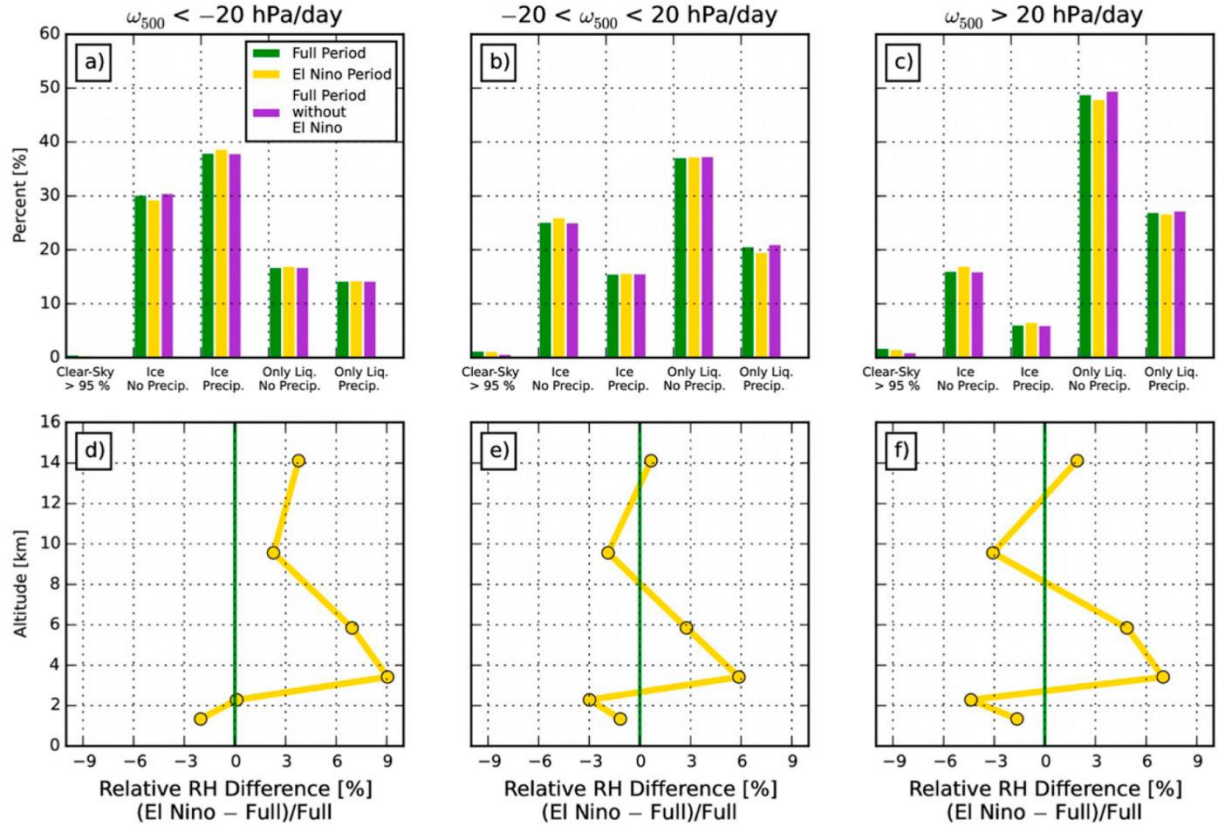


**FIGURE 3-10: (top)** Frequency of occurrence of grid boxes within each subcategory, normalized by the total number of grid boxes within the respective vertical pressure velocity regime: **(a)**  $\omega_{500} < -20$  hPa day<sup>-1</sup>, **(b)**  $-20 < \omega_{500} < 20$  hPa day<sup>-1</sup>, and **(c)**  $\omega_{500} > 20$  hPa day<sup>-1</sup>. **(bottom)** Vertical profiles of mean relative RH difference for the El Niño period minus full period, normalized by the profile of the full period in the same three vertical pressure velocity regimes: **(d)**  $\omega_{500} < -20$  hPa day<sup>-1</sup>, **(e)**  $-20 < \omega_{500} < 20$  hPa day<sup>-1</sup>, and **(f)**  $\omega_{500} > 20$  hPa day<sup>-1</sup>.

### 3.5.2 About the Intermediate Circulation Regime

Section 3.4 establishes the relationship between RH, clouds and near-surface precipitation within the descending and ascending regimes, but 42 % of the tropical oceans is sampled within the intermediate regime ( $-20 < \omega_{500} < 20$  hPa/day). Supplementary Figure S3 shows that this regime is largely a mixture of the other two. It resembles the descending regime in number distributions of low liquid water clouds (Fig. C3-3d,e compared to Fig. 3-4c,d) and the ascending regime for high ice clouds (Fig. C3-3a,b compared to Fig. 3-8a,b).

The intermediate regime's SST variations of low liquid water cloud cover and high ice cloud cover *within a grid box* (C3-3j,k and C3-3g,h, respectively) are comparable to those in the descending (Fig. 3-5a,b) and ascending regimes (Fig. 3-8a,b), respectively. Although, opaque high ice cloud cover is smaller ( $-20$  %) and thin high ice cloud cover larger ( $+5$  %) in the intermediate regime.

The moisture profiles for the high ice (Fig. C3-3m,n) and low liquid water (Fig. C3-3p,q) phase clouds also resemble those of the ascending (Fig. 3-8c,d) and descending (Fig. 3-5c,d) regimes, respectively, though the FTRH in the intermediate regime is slightly higher in the low liquid water phase compared to the descending regime, whilst slightly drier than the ascending regime's high ice phase.

### 3.5.3 Limits of the Study

Heavily precipitating pixels are not represented in the SAPHIR L2B product (Brogniez et al. 2013). Instead the moisture profile in such grid boxes are represented by the average of the surrounding pixels in the rest of the  $1^\circ \times 1^\circ$  grid box, so long as at least 75 % of them are filled with valid pixels. We deem this representation to be statistically meaningful but are aware of the potentially dry bias in these grid boxes.

Because CloudSat only provide daytime observations since 2011, the MTCC dataset observes the tropical atmospheric water cycle once daily at one instantaneous moment (~01:30 pm) and cannot be used to observe the diurnal cycle, or any time scale less than 24 hours. Thus, the present study is a statistical representation of the atmospheric water cycle's evolution with SST at 01:30 pm.

We define our large-scale regimes by monthly mean  $\omega_{500}$  values because we do not trust them on shorter time scales. In doing so however, we ignore fluctuations that occur on shorter time scales, where small scale convection is probably the most important physical process. Also, monthly mean vertical motion is potentially ambiguous since a single value could equally represent days of strong upward and moderate downward vertical motion during the month or more constant weak upward motion.

The time period in this paper covered only one El Niño event, when in fact, they are not all identical. For example, Su and Jiang (2013) showed largely opposite cloud fraction anomalies in the 2007/08 and 2009/10 El Niño events, with larger cloud fractions in the boundary layer and above 14 km during the 2009/10 El Niño, whilst smaller fractions from 2 to 14 km. During the 2007/08 event, there was instead increased cloud fractions from 2 to 17 km and little change outside of this range. Takahashi et al. (2013) found similar results using measurements from AIRS and MLS (Microwave Limb Sounder onboard Aura), as well as higher than normal specific humidities above 300 hPa. Therefore, the comparisons made between the El Niño period and the full period are only valid for this El Niño event and should not be taken as proxies for any given event.

### 3.5.4 The Super Greenhouse Effect

The super greenhouse effect (Focus Box 2, Ch. 1) discusses the positive feedback loop on SST induced by reduced OLR due to increasing atmospheric opacity with evaporation rate. It has previously been observed under clear-sky conditions (Hallberg and Inamdar 1993, Allan et al. 1999, Stephens et al. 2016), but uncertainties remain for cloudy scenes.

Dewey and Goldblatt (2018) observed that the clear-sky OLR (from Clouds and the Earths Radiant Energy System observations) increases linearly with surface temperature up to 298 K and decreases for higher surface temperatures, whilst the clear-sky column water vapor (AIRS observations) increases non-linearly with surface temperature past this value. In all-sky conditions, they observed that inclusion of clouds decreased the OLR for any given temperature, as well as shifted the peak OLR value towards lower surface temperatures, effectively amplifying the super greenhouse effect compared to clear-sky conditions. They concluded that above some surface temperature threshold, evaporation rates are high enough for the boundary layer to be essentially opaque to the thermally emitted surface radiation. There, the rate of near-surface absorption exceeds that of OLR emission at the top of the atmosphere

and the reabsorption drives the rapid surface warming initiating deep convection (Dewey and Goldblatt 2018).

In the present study, we add the simultaneous observations of clouds and moisture with SST to this discussion and observe a boundary layer drying over the warm SST range where deep convection is expected in all regimes (Figures 3-5, 3-8, C3-3). We therefore suggest a modification of Dewey and Goldblatt’s (2018) conclusion; the increase in column water vapor makes the column integrated atmosphere opaque to the terrestrial emitted surface radiation, but not the boundary layer alone. In Figure 3-8 the transition to deep convection rather appears to be the increasing FTRH above 850 hPa, as discussed in Holloway and Neelin (2009).

### 3.5.5 Implications of the Study

Figure 3-11 presents the conceptual evolution of the atmospheric water cycle with SST warming, based on the joint evolutions observed in Figures 3-4 to 3-9. Under strong descent (top panel: A and B), the warming causes a marked decrease in opaque low liquid water cloud cover and an increase in clear-sky cover, slightly compensated by a moister free troposphere. Together, these two evolutions should lead to increased OLR over the cold SST range (as SST < 298 K according to Dewey and Goldblatt 2018). However, because these are low clouds confined to the lower troposphere, the decreasing cloudiness might not lead to much higher OLR.

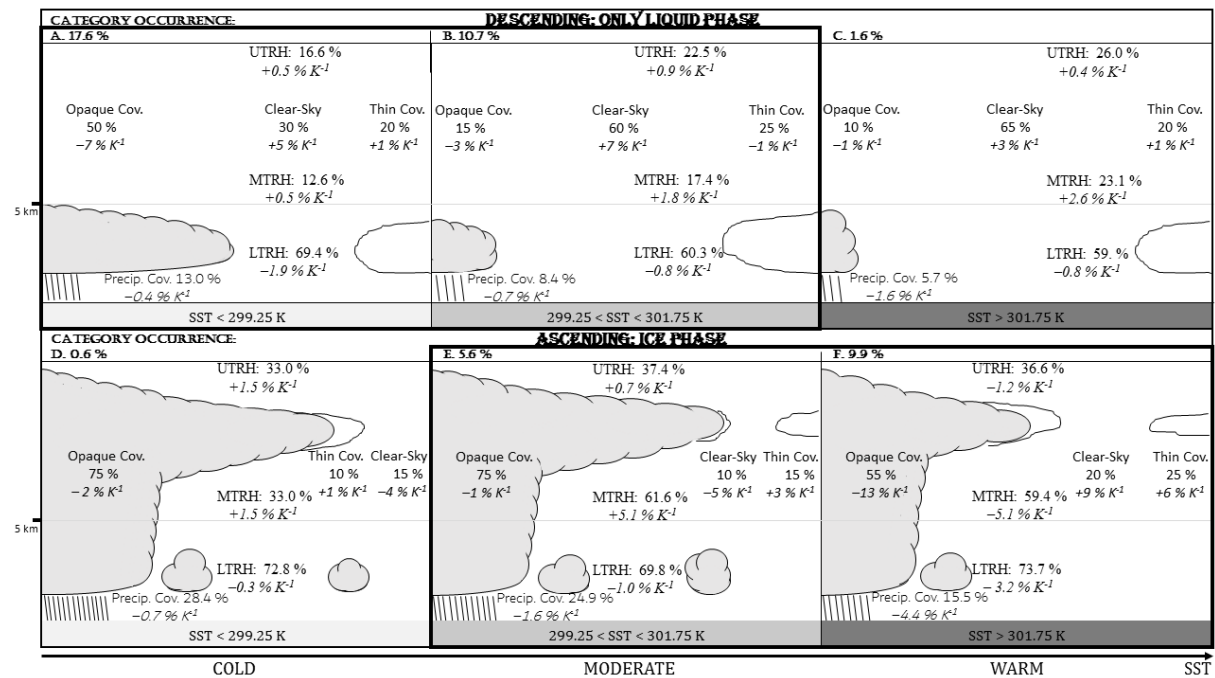


**FIGURE 3-11:** Schematic illustrating the tropical atmospheric water cycle’s evolution with SST. **(top)** Low liquid clouds in the descending regime ( $\omega_{500} > 20$  hPa day<sup>-1</sup>). **(bottom)** High ice clouds in the ascending regime ( $\omega_{500} < -20$  hPa day<sup>-1</sup>). Mean values and illustrations are approximated from Fig. 3-5 for the top row and Fig. 3-8 for the bottom row, while trend values from Fig. 3-6 for the top row and Fig. 3-9 for the bottom row. Mean values are given in normal font and the rate of change of each parameter with 1-K warming is given in italics. Values of category occurrence indicate how much of the tropical ocean is covered by that category and SST range in the MTCC dataset. Abbreviations: UTRH, MTRH, and LTRH stand for upper-, middle-, and lower-tropospheric RH, respectively; “Precip.” stands for near-surface precipitation and “Cov.” for cover within a grid box.

Under strong ascent (bottom panel: E and F), the analysis suggests that over the moderate and warm SST ranges, opaque high ice cloud cover is smaller for warmer SSTs. This decrease is accompanied by an increase in thin high ice cloud cover. In fact, if only grid boxes guaranteed to contain opaque high ice clouds are considered, the increase in thin high ice cloud cover equals the decrease in opaque high ice cloud cover, so that the total high ice cloud cover is always 100 % (Fig. C-14, Appendix C). This observation could be a valuable constraint for climate models. The near-surface precipitation cover decreases acceleratingly with warming. The OLR should increase in accordance with both decreasing cloudiness and increasing FTRH for SSTs < 298 K (Dewey and Goldblatt 2018), but over the moderate and warm SST ranges the evolution of OLR is less ambiguous. In heavily precipitating scenes (Fig. C-13, Appendix C), FTRH  $\geq$  65 %, the opaque high ice cloud cover is 100 % over the cold and moderate SST ranges and  $\geq$  80 % over the warm. In these situations, the total high ice cloud cover is always 100 %, so OLR must be substantially reduced.

Together, the decreasing opaque high ice cloud cover ( $-13 \text{ \% K}^{-1}$ ) and drying mid-troposphere ( $-5 \text{ \% K}^{-1}$ ) over the warm SST range (10F), support the iris hypothesis (Lindzen et al. 2001). However, the increasing thin high ice cloud cover ( $+6 \text{ \% K}^{-1}$ ) and decreasing near-surface precipitation cover ( $-4.4 \text{ \% K}^{-1}$ ) suggest that the decreasing opaque high ice cloud cover is not compensated by increased precipitation (as suggested in the iris hypothesis), but rather by increasing thin high ice cloud cover.

### 3.6 Conclusion

We build a composite synergistic dataset (MTCC) of instantaneous observations (once daily at 01:30 pm) of RH (Megha-Tropiques), clouds (CALIPSO) and near-surface precipitation (CloudSat) to analyze SST variations of the tropical atmospheric water cycle at the instantaneous scale. We only consider fully oceanic grid boxes of  $1^\circ \times 1^\circ$  horizontal resolution and partition the tropical atmosphere into three vertical pressure velocity regimes (descending, ascending, intermediate), with cloudy grid boxes categorized after phase (high ice/low liquid), opacity (opaque/thin) and the presence of near-surface precipitation.

Cloudy grid boxes without near-surface precipitation dominate the descending and intermediate regimes, whilst precipitating grid boxes dominate the ascending regime. Clear-sky grid boxes ( $< 5 \text{ \%}$  cloudiness) are extremely rare, meaning that clouds are almost always present. We identify two SST thresholds, based on the median cloud cover evolutions, with local minima and maxima at the cold (299.25 K) and warm (301.75 K) thresholds. These thresholds fall within the SST ranges where previous studies have located the onset of deep convection and the peak frequency of occurrence of deep convection, respectively. Over the warm SST range (SST  $> 301.75\text{K}$ ), the total cloud cover decreases with SST in all three regimes.

The descending regime with low liquid water clouds dominates the cold SST range ( $< 299.25 \text{ K}$ ) where the free troposphere is always dry ( $\sim 20 \text{ \%}$ ). The low liquid water cloud cover variations are governed by the opaque low liquid water cloud cover ( $-8 \text{ \% K}^{-1}$ ), as the thin liquid cloud cover stays largely constant ( $\sim 20 \text{ \%}$ ). In the presence of near-surface precipitation, the opaque and total low liquid water cloud covers are wider and the FTRH moister over the moderate and warm SSTs, whilst drier over the cold SSTs.

The ascending regime with high ice clouds dominates the warm SST range, though low liquid water clouds are frequently present below. By the onset of deep convection, humidity increases with increasing SST in the lower free troposphere and peaks around the warm SST threshold. The present study confirms the decrease in opaque high ice cloud cover over the warm SST range, identified in previous studies, but shows that this decrease is compensated by increasing thin high ice cloud cover and perhaps not by increasing precipitation (as suggested in the iris hypothesis). Over the whole SST range, the free troposphere is moister and the opaque high ice cloud cover larger in the presence of near-surface precipitation (at the expense of smaller thin high ice clouds).

The intermediate regime has been the focus of fewer previous publications. We conclude that this regime is largely a mixture of the ascending and descending regimes, where the low liquid water cloud cover is slightly wider, and the high ice cloud cover smaller, compared to the descending and ascending regimes, respectively. The moisture profiles also typically align themselves as an average between the other two regimes.

The clear-sky cover increases in all regimes over the warm SST range, but the free troposphere moistens when low liquid water clouds are present and dries in the presence of high ice clouds. The evolution of OLR with warming is therefore not unambiguous from our results but requires a quantification.



## Chapter 4

# 4 Covariations on Different Temporal and Spatial Scales

4	Covariations on Different Temporal and Spatial Scales.....	94
4.1	Introduction.....	95
4.1.1	State of the Art.....	95
4.1.2	Science Questions.....	97
4.2	Method.....	98
4.2.1	Building a Dedicated Dataset.....	98
4.2.1.1	Observational Data Used in This Chapter.....	98
4.2.1.2	Data Processing.....	99
4.2.1.2.1	Grid Box Dataset Obtained From Data Collocated on the Instantaneous Timescale (Method A).....	99
4.2.1.2.2	Grid Box Dataset Obtained From Data Collocated on Longer Timescales (Method B).....	99
4.2.1.2.3	Tropical Mean Values.....	101
4.2.1.3	Summary of the Different Datasets.....	101
4.2.2	Regression Computation Amongst Different Variables and Assessment of Regression Robustness.....	101
4.2.2.1	Orthogonal Distance Regression.....	101
4.2.2.2	Kendall Rank Coefficient: $\tau$ -B.....	102
4.2.3	Comparing Covariations Obtained with the Different Datasets.....	102
4.3	Analysis of Observed Water Cycle Variable Covariations on Different Timescales.....	104
4.3.1	How Do RH, Cloud Cover, Altitude and Temperature Vary with SST on Different Timescales?.....	104
4.3.1.1	Variations of RH on the Global Scale?.....	105
4.3.1.2	Variations of Cloud Characteristics on the Global Scale?.....	107
4.3.2	How Does the Low Liquid Cloud Cover Vary with SST on Different Timescales? ...	108
4.3.3	How Do Cold Ice Cloud Characteristics Vary with SST Over the Warmest Waters on Different Timescales?.....	110
4.3.3.1	High Ice Cloud Cover.....	110
4.3.3.2	High Ice Cloud Altitudes and Temperatures.....	113
4.3.4	How Do Cloud Characteristics Covary and How Do They Vary with RH on Different Timescales?.....	114
4.3.4.1	How Do Clouds and RH Covary on the Grid Box and Global Scales?.....	114
4.3.4.2	How Do Clouds Covary on the Grid Box and Global Scales?.....	118
4.4	Discussion of These Results.....	119

4.4.1	Limits of the Study .....	119
4.4.2	Sensitivity of the Results to the Choice of Data Analysis Method (Comparing A and B) 120	
4.4.3	Assuming Linear Covariation.....	122
4.4.4	Discussion on a 4 K Warmer Climate Scenario .....	122
4.5	Summary and Conclusions.....	125

## 4.1 Introduction

### 4.1.1 State of the Art

From a global perspective, the Earth system can be considered as an isolated system, where the climate and climate variations are constrained by the net radiative flux at the top of the atmosphere. The IPCC AR5 (2013) concluded that the Earth system is warming due to a *radiative forcing*  $F$  (a perturbation to the Earth system) induced by an anthropogenic increase in atmospheric greenhouse gases that causes an imbalance and net downward flux  $\Delta R$  at TOA. The present annual net imbalance is 0.6 to 0.7  $\text{Wm}^{-2}$  (Stephens et al. 2012, Loeb et al. 2018). In time,  $\Delta R$  goes to zero and the Earth system will adjust to this forcing by establishing a new equilibrium surface temperature  $T_s$ . The equilibrium climate change  $\Delta T_s$  can then be characterized by (e.g. Rose and Rayborn 2016, Goosse et al. 2018):

$$F = \lambda \Delta T_s \quad (\text{E4-1})$$

The feedback formalism (discussed in Ch. 1) deals with the responses and impacts of all Earth system variables as individual additive terms. It assumes that changes in radiative flux are proportional to changes in surface temperature, and that the total feedback parameter  $\lambda$  can be expressed as a sum of individual parameters  $\lambda_j$ :

$$\lambda = \sum_j \lambda_j \quad (\text{E4-2})$$

How will this new temperature impact the individual atmospheric water cycle variables (water vapor, clouds, etc.)? And how will the modified water cycle variables influence the new temperature? Expanding E4-1 and E4-2, we can express the sensitivity of the change in the TOA net radiative flux to a change in surface temperature as (Eq. 4-3):

$$\frac{dF}{dT_s} = \frac{\partial F}{\partial T_s} + \sum_j \frac{\partial F}{\partial Y_j} \frac{dY_j}{dT_s} \quad (\text{E4-3})$$

Where the water cycle variables  $Y$  may be dependent on each other (E4-4):

$$\frac{dY_j}{dT_s} = \frac{\partial Y_j}{\partial T_s} + \sum_k \frac{\partial Y_j}{\partial Y_k} \frac{dY_k}{dT_s} \quad (\text{E4-4})$$

Changes in TOA radiative fluxes with atmospheric moisture and cloud variables ( $\frac{\partial F}{\partial Y_j}$ , E4-3) can be reliably estimated from radiative transfer computations (e.g. Liou 2002), but changes in RH and cloud variables with SST ( $\frac{dY_j}{dT_s}$ , E4-3) are more uncertain, as previously reported magnitudes of rates of change vary considerably, with significant implications for their resulting feedbacks (Vial et al. 2013, Ceppi and Gregory 2017, Zelinka et al. 2016, 2020). The

marine boundary layer cloud cover and middle-tropospheric RH are of particular interest as they have previously been discussed as emergent constraints (Focus Box 1, Ch. 1) for climate predictions (Fasullo and Trenberth 2012, Qu et al. 2014, Klein and Hall 2015). Second order uncertain terms concern how one atmospheric water cycle variable changes with another, e.g. how cloud characteristics change with the humidity profile or the covariation of cloud properties ( $\frac{\partial Y_j}{\partial Y_k}$ , E4-4).

How does cloud cover change with sea surface temperature (SST)? This question concerns both the change in low liquid cloud cover and the change in high ice cloud cover. The rate of change of marine boundary layer cloud cover with SST is central to the shortwave (SW) feedback, but also the term associated with the most uncertainty in the feedback equation (e.g. Bony and Dufresne 2005, Clement et al. 2009, Brient and Bony 2013, Myers and Norris 2015, Qu et al. 2015, Zhai et al. 2015, Klein et al. 2017). These warm low liquid clouds are radiatively relevant as effective reflectors of SW radiation (e.g. Henderson et al. 2012).

In contrast to warm low liquid clouds, the outgoing longwave radiation (OLR) emitted from the top of high ice clouds is considerably lower than that emitted from the surface, so these clouds induce a considerable warming effect (e.g. Matus and L'Ecuyer 2017). According to the *iris hypothesis* (first postulated by Lindzen et al. in 2001 and later reassessed in several papers like Fu et al. 2002, Hartmann and Michelsen 2002, Lin et al. 2004, 2006, Su et al. 2008), high ice cloud cover (convective anvils) decreases with SST due to increasing convective precipitation efficiency that leads to smaller convective anvils as fewer hydrometeors are left to build them. To a first approximation, this hypothesis compares the horizontal extent of the tropical moist and dry regions.

How do cloud altitudes and emission temperatures change with SST? The *Fixed-Anvil Temperature hypothesis* (first presented by Hartmann and Larson in 2002 and subsequently assessed in e.g. Zelinka and Hartmann 2010, 2011, Seeley et al. 2019) says that cloud altitudes will rise in response to surface temperature increase. They will rise in such a way that they stay at the same temperatures as before the warming, which means that the temperature at the anvil detrainment level will remain constant, making the anvil emission temperatures (and the outgoing longwave radiation OLR, emitted by them to space) independent of surface temperature. The altitude of anvil detrainment (convective outflow) occurs at the altitude where radiative cooling decreases most rapidly with height, which is where the saturation vapor pressure of water vapor becomes so low that water vapor no longer has a significant effect on the emitted radiation.

The feedback parameter for global net energy flux at TOA with surface temperature is often determined by a linear regression fit, under the assumption that the feedback parameter is constant in time (Gregory et al. 2004). In reality, the global radiation is sensitive to patterns of temporally varying surface warming (“pattern-effects”) (Stevens et al. 2016, Zhou et al. 2016, Ceppi and Gregory 2017), manifested by local and regional dynamics on the grid box scale. For example, in Ch. 3 we observed nonlinear responses in opaque ice cloud cover and free-tropospheric RH with SST on the instantaneous grid box scale for SSTs > 299 K (Höjgård-Olsen et al. 2020). Such nonlinear dynamics complicate the feedback formalism as they imply that linearity is not a valid assumption for  $\frac{dY_j}{dT_s}$  in E4-3 (Klein et al. 2017, Loeb et al. 2020).

The answer to how the energy balance at the top of the atmosphere (TOA) and the atmospheric variables (humidity, clouds, precipitation, etc.) will respond to the radiative forcing induced by increasing greenhouse gases is sensitive to the spatial and temporal scale under consideration. It is therefore interesting to characterize how the tropical atmospheric water cycle variables covary on different scales.

Spatial and temporal scales are not independent of each other, as the larger the atmospheric system/phenomenon, the longer its expected lifespan or the adjustment time to changes for the components and variables it interacts with (e.g. Orlanski 1975, Steyn et al. 1981). Scales range from microscale turbulence (meters and seconds), to thunderstorms (kilometers, hours), to tropical cyclones (100 km, days), to seasonal monsoons (1000 km, months), to global circulation and climate change (> 10,000 km, years to decades). Process-oriented studies about local and regional dynamics are best observed on the grid box scale (or even smaller point observations, e.g. radiosondes, buoys, aircrafts) and instantaneous to daily timescales. In contrast, from a climatological perspective, long-term trends are most relevant on the global scale, as climate change is constrained by the global energy budget and the net radiative flux at the top of the atmosphere.

Time-varying climate predictions have previously been made with models (e.g. Armour et al. 2013, Gregory and Andrews 2016), where timescales can easily be separated. But models are constrained by observations and to my knowledge, there are no observational studies that deal with questions across timescales. Today, we have a long enough record of highly resolved observations of tropical coverage to capture variabilities on different timescales, so that we could seek answers to such questions.

#### 4.1.2 Science Questions

As in the previous chapter, this study focuses on the responses of the tropical atmospheric water cycle variables ( $Y$  in E4-3 and E4-4) to different SST. Namely, the changes in tropical relative humidity (RH) and cloud characteristics (cover, altitude, temperature) with SST, as well as the responses of cloud characteristics with RH in the lower, middle, and upper troposphere. But where the previous chapter observed variations with SST on the instantaneous grid box scale, this study assesses the variations on different temporal (daily, monthly, seasonal, annual) and spatial scales (global and grid box):

**Question 1:** How do RH, cloud cover, altitude and temperature vary with SST on different timescales? These are the first order feedbacks ( $\frac{dY_j}{dT_s}$ , E4-3), which I will answer from the perspective of both grid box and global values. The computation of these “global values” are explained in Sect. 4.2.1.2.3.

- What are the rates of change on different timescales?
- Are the signs and rates of covariations robust across timescales from daily to annual?

**Question 2:** How does the low liquid cloud cover vary with SST on different timescales? The change of low liquid cloud cover is central to the SW feedback, and part of the answer to the iris hypothesis.

- What are the rates of change on different timescales?
- Are the signs and rates of covariations robust across timescales from daily to annual?

**Question 3:** How do cold ice clouds (cover, altitude, temperature) vary with SST over the warmest waters ( $SST > 299$  K) on different time scales? The change in ice cloud cover with SST is central to the iris hypothesis, whilst changes in ice cloud altitude and temperature with SST are central to the FAT.

- What are the rates of change on different timescales?
- Are the signs and rates of covariations robust across timescales from daily to annual?

**Question 4:** How do cloud cover, altitude and temperature vary with RH on different timescales? These are the second order feedbacks ( $\frac{\partial Y_j}{\partial Y_k}$ , E4-4).

- What are the rates of change on different timescales?
- Are the signs and rates of covariations robust across timescales from daily to annual?

I start this chapter by presenting the data methods that I have used to analyze the covariations (Sect. 4.2), followed by a presentation of the results of these analyses, answers to the science questions asked above, and comparisons of these answers to previously published results (Sect. 4.3). Then I will discuss limitations of this study along with the implications of my results and the limitations (Sect. 4.4), and end with my conclusions of this study (Sect. 4.5).

## 4.2 Method

### 4.2.1 Building a Dedicated Dataset

#### 4.2.1.1 Observational Data Used in This Chapter

The variables used in this study to answer the science questions asked above are listed in Table 4-1. They include observations of the RH profile (SAPHIR, Ch. 2), cloud characteristics (GOCCP, Ch. 2) and reanalysis of SST (ERA5, Ch. 2). These are the same variables as in the previous chapter, except cloud altitudes and temperatures that were not used previously.

**TABLE 4-1:** List of variables used in this study. All variables are two-dimensional and of  $1^\circ \times 1^\circ$  spatial resolution. These variables are described in detail in Chapter 2.

Variable	Abbreviation	Unit	Source	Time Period
Upper-Tropospheric RH (100-200 hPa)	UTRH	%	SAPHIR	2012 - 2018
Middle-Tropospheric RH (400-600 hPa)	MTRH	%	SAPHIR	2012 - 2018
Lower-Tropospheric RH (850-950 hPa)	LTRH	%	SAPHIR	2012 - 2018
Opaque Cloud Cover	$C_{OPAQUE}$	%	CALIPSO GOCCP	2008 - 2019
Thin Cloud Cover	$C_{THIN}$	%	CALIPSO GOCCP	2008 - 2019
Opaque Cloud Altitude	$Z_{OPAQUE}$	km	CALIPSO GOCCP	2008 - 2019
Thin Cloud Altitude	$Z_{THIN}$	km	CALIPSO GOCCP	2008 - 2019
Opaque Cloud Temperature	$T_{OPAQUE}$	K	CALIPSO GOCCP	2008 - 2019
Thin Cloud Temperature	$T_{THIN}$	K	CALIPSO GOCCP	2008 - 2019
Sea Surface Temperature	SST	K	ERA5	2008 - 2019

#### 4.2.1.2 Data Processing

To characterize how cloud properties, RH and SST covary on different timescales (daily, monthly, seasonal, annual), we must consider sampling differences in the observations of cloud properties and RH. I do this by first collocating the water cycle variables and then select only the grid boxes that are filled with values of them all. I use two different methods (A and B) to collocate the data. The flowchart in Fig. 4-1 shows the computational steps following methods A and B.

##### 4.2.1.2.1 Grid Box Dataset Obtained From Data Collocated on the Instantaneous Timescale (Method A)

In *Method A*, I use GOCCP orbit files regridded to  $1^\circ \times 1^\circ$  resolution (Ch. 2) and SAPHIR orbit files regridded to  $1^\circ \times 1^\circ$  resolution (Ch. 2). The collocation on the instantaneous timescale is the same as in the previous chapter (Ch. 3). It consists of keeping only the grid boxes observed by both CALIPSO (01:30 pm) and SAPHIR within the same 2-hour time window (00:30 – 02:30 pm). All grid boxes that do not meet this criterion are rejected from the dataset. Then, this “instantaneous SAPHIR-and-CALIPSO-collocated dataset” is completed with  $1^\circ \times 1^\circ$  gridded products of surface skin temperature reanalysis from ERA5 (Ch. 2) at 01:30 pm in fully oceanic grid boxes (grid boxes containing land are rejected).

From these instantaneously observed grid boxes I perform a temporal upscaling, where I compute maps of grid box mean values on the daily, monthly, seasonal, and annual timescales. That is, for each variable and every grid box, I compute one timescale mean value.

##### 4.2.1.2.2 Grid Box Dataset Obtained From Data Collocated on Longer Timescales (Method B)

In *Method B*, I start from the same GOCCP and SAPHIR files as in Method A, but here I first compute timescale mean maps independently for each variable before I perform the grid box-by-grid box collocation.

For example, when I collocate UTRH and opaque cloud cover on the annual scale, over one year, I first compute one annual mean map of UTRH and one annual mean map of *COPAQUE* independently of each other. Then, I collocate the grid boxes in these two maps by rejecting all grid boxes that do not contain an annual mean value for both UTRH and *COPAQUE*, effectively keeping only the grid boxes that are filled by annual mean values in both maps. The daily, monthly, and seasonal datasets are computed following the same steps.

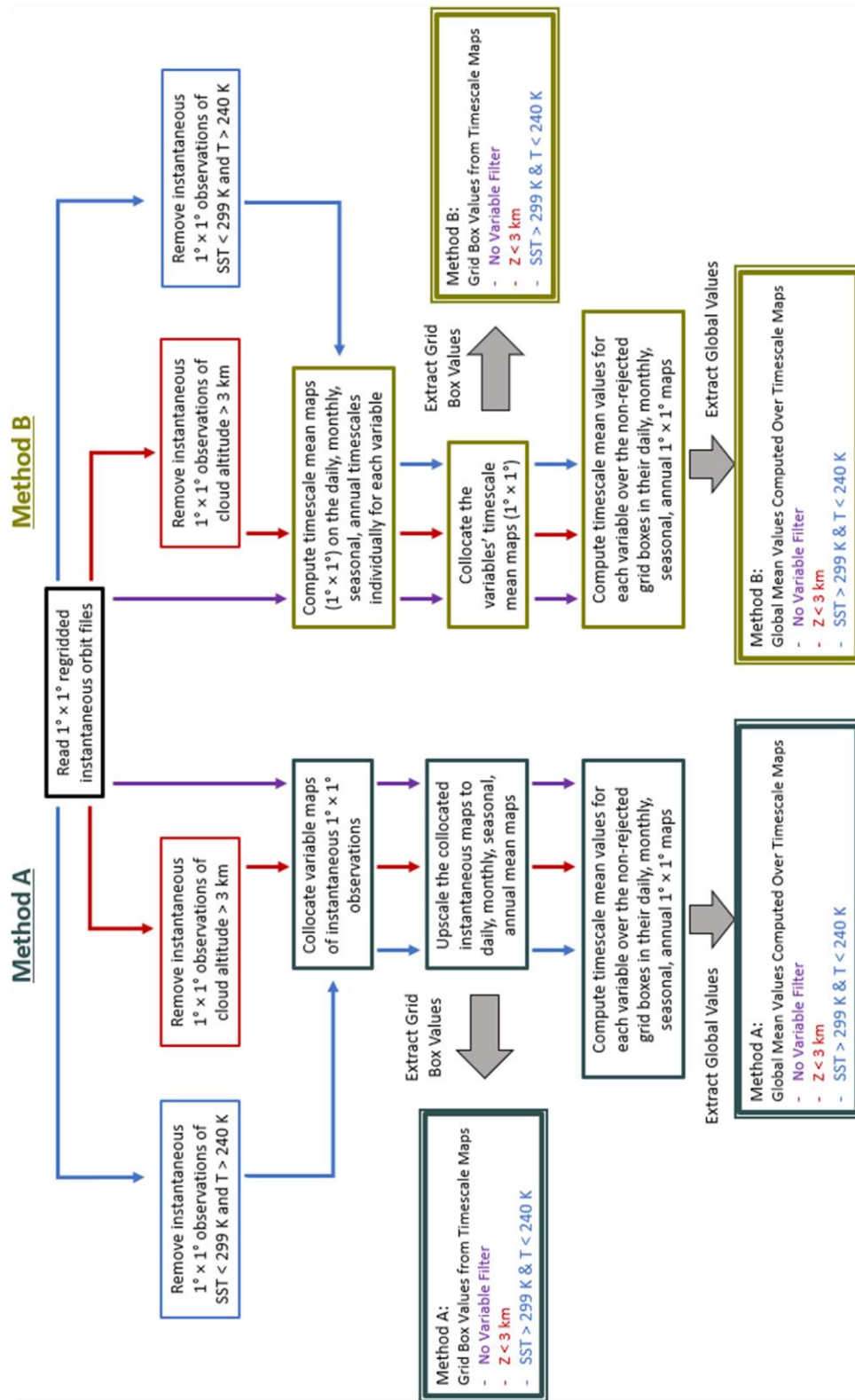


**FIGURE 4-1:** Flowchart summarizing the steps in the data processing to compute grid box values and global values from the data analysis methods A and B. Dark gray boxes (left column) show the processing steps for Method A, whilst brown boxes (right column) show processing steps for Method B. Big light gray arrows show the extracted data (four double-edged boxes). Horizontal big light gray arrows in the fourth row show the extraction of grid box data from the timescale maps, and downward pointing big light gray arrows in the bottom row show the extraction of global data computed as averages over the timescale maps. The processing is done for three types of variable filters: purple) all variables are considered, red) only grid boxes of cloud altitudes < 3 km are considered, blue) only grid boxes where SST > 299 K and cloud temperatures < 240 K are considered. The extracted data are listed in the four double-edged boxes.

#### 4.2.1.2.3 Tropical Mean Values

For each variable, I take its timescale map computed by Method A, and compute one average value over all non-rejected grid boxes. Throughout the rest of this manuscript, I refer to such a value as a *global value*, even though they are only computed over oceanic grid boxes in the tropical belt (30°N to 30°S).

Similarly, I compute one global value for each timescale map computed by Method B as well, resulting in four categories of data analysis.

Because one global value is an average value over all grid box observations, it includes all local and regional dynamics. Comparisons between global values on e.g. the annual scale, thus show how the annual average of a variable has changed from one year to the next. Rates of changes computed from global values of some pair of variables are therefore interpreted as representing the variability on the present timescale, the temporal variability.

To evaluate the iris and FAT hypotheses that concern anvil clouds, I extract a subsample of the data. Following the results of the previous chapter (Höjgård-Olsen et al. 2020), I only consider grid boxes where SST > 299 K, but I also add the requirement that cloud temperatures must be less than 240 K ( $T_{OPAQUE}, T_{THIN} < 240$  K), which is a reasonable approximation for the bottom of the anvil detrainment region (Kuang and Hartmann, 2007). Then I extract a second subset of the data to study the marine boundary layer clouds. For these data I only consider clouds measured at altitudes less than 3 km ( $Z_{OPAQUE}, Z_{THIN} < 3$  km). Lastly, I compute grid box and global values from both Method A and B for these two subsampled datasets as well.

#### 4.2.1.3 Summary of the Different Datasets

Table 4-2 summarizes the twelve datasets (3 variable filters  $\times$  2 types of values  $\times$  2 collocation *methods*) built to answer the science questions.

**TABLE 4-2:** List of the twelve datasets built to answer the science questions asked in this study. 3 variable filters  $\times$  2 types of values  $\times$  2 collocation methods.

	Full Tropical Oceanic Belt (no filter)	Low Liquid Clouds $Z < 3$ km	High Ice Clouds Over Warm Waters: SST > 299 K and T < 240 K
Grid Box Values	Computed by Method A	Computed by Method A	Computed by Method A
	Computed by Method B	Computed by Method B	Computed by Method B
Global Values	Computed by Method A	Computed by Method A	Computed by Method A
	Computed by Method B	Computed by Method B	Computed by Method B

## 4.2.2 Regression Computation Amongst Different Variables and Assessment of Regression Robustness

### 4.2.2.1 Orthogonal Distance Regression

In Sect. 3, I characterize how pairs of variables covary over tropical oceans on each timescale (annual, seasonal, monthly, daily). I use the orthogonal distance regression (ODR, e.g. Boggs et al. 1988) to fit linear regressions instead of ordinary least squares fit (OLS). OLS assumes that there is one independent variable and one dependent variable and that the former is measured without error. Because I cannot be sure that one variable is measured without error when I observe snapshots of the atmospheric state, this assumption is not defensible (Leng et al. 2007, Lolli and Gasparini 2012). In contrast, the ODR accounts for measurement errors in both variables as it treats them both as random.

#### 4.2.2.2 Kendall Rank Coefficient: $\tau$ -B

I assess the significance of the linear regressions with the Kendall rank coefficient ( $-1 < \tau < 1$ ), which measures the similarity of the orderings of data (Kendall 1945). More specifically, I use the  $\tau$ -B coefficient that accounts for ties when measuring the correspondence between rankings. I choose the Kendall rank correlation as it makes no assumptions of either the shape of the data distributions or linearity. I choose the significance level 0.05 to determine if a regression is statistically significant ( $p < 0.05$ ) or not ( $p > 0.05$ ) following Fisher (1926, 1956). Effectively, if  $p < 0.05$ , then I can reject the null hypothesis that there is no trend with 95 % confidence. These results are reported in Figs. 4,6,8,10,12.

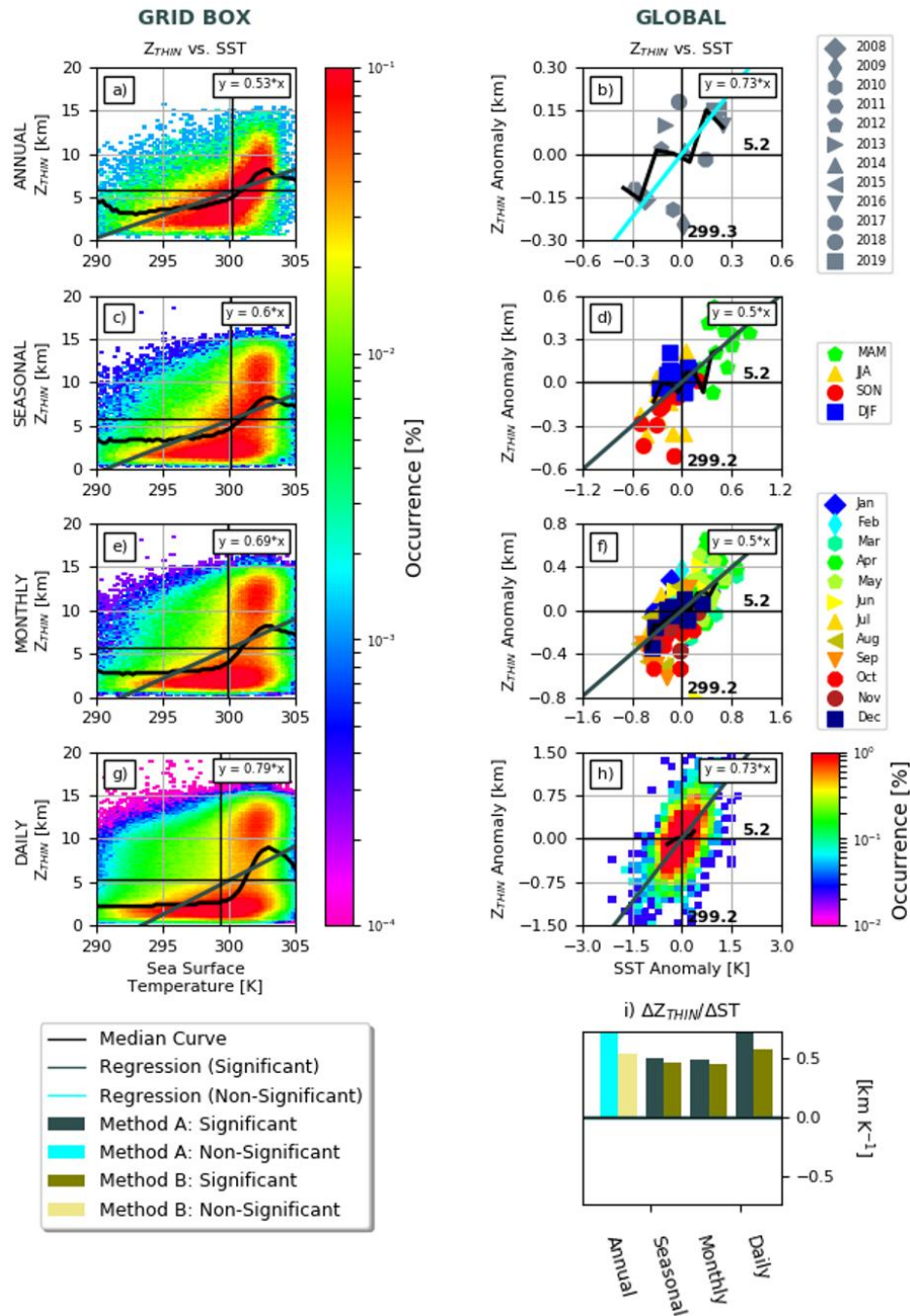
#### 4.2.3 Comparing Covariations Obtained with the Different Datasets

Figure 4-2 shows an example of the covariation between one pair of variables. It shows how daytime (01:30 pm) thin cloud altitude varies with SST on the four timescales, using data collocated with Method A. It compares the local and regional dynamics observed in the grid box values (left column) to the temporal variability in the global values (right column).

In the left column, the black curve shows the median thin cloud altitude value for each 0.25 K SST bin. The same bootstrapping algorithm and number of data requirements as in the previous chapter are applied (Sect. 3.3.4). A linear fit (dark green line) is also fitted directly to the scatter distribution. In this figure, the sign is the same for the regressions fitted to the grid box scatter distributions (left) and the global value scatter distributions (right), so the right column confirms that thin cloud altitude increases with SST on all time scales and in both grid box values and global values.

As Fig. 4-2 shows, global values are typically aligned so that a linear regression could be reliably fitted to represent the rate of change of one atmospheric water cycle variable with another. The regressions are significant (solid lines) based on the Kendall test (previous subsection) on the daily, monthly and seasonal scales, whilst nonsignificant (dashed line) on the annual scale. This is an observation I make for most rates of changes presented in Sect. 4.3 for the annual scale and is likely due to too few years on record in this dataset.

The nonlinear dynamics on the grid box scale are poorly represented by one linear fit. Thus, when I present results for different pairs of variables in Sect. 4.3, I choose to show the dynamics on the grid box scale as median curves (black curve, left column), whilst values of rates of changes computed from global values separately in barcharts.



**FIGURE 4-2:** Change in thin cloud altitude with SST on the (a, b) annual, (c, d) seasonal, (e, f) monthly, and (g, h) daily timescale over the years 2008-2019 computed with Method A. **Left column:** Density scatter plot of grid box values. **Right column:** Scatter plots of tropical global values. Black curves show median thin cloud altitude value for each SST bin and linear lines regressions fitted with ODR to the scatter distributions. Gray (light blue) line means that the regression is significant (nonsignificant) with respect to a  $p$  value = 0.05. The linear regressions in subplots b,d,f,h are also reported in subplot i) and again in the synthesized figure 4-3(f). Light blue and gray bars are from the regressions in subplots b, d, f, h, whilst yellow and brown bars from rates of changes of global values computed from Method B (supplementary figure D-1).

### 4.3 Analysis of Observed Water Cycle Variable Covariations on Different Timescales

In this section, I analyze the results and answers to the science questions asked in Sect. 1.2, starting with (Sect. 4.3.1) the first order uncertain terms in the feedback equation (changes in RH and cloud variables with SST). Then I analyze the change in low liquid cloud cover with SST (Sect. 4.3.2), followed by the changes in high ice clouds (cover, altitude, temperature) with SST (Sect. 4.3.3) and their implications for the FAT and iris hypotheses. I end (Sect. 4.3.4) with the covariations between cloud variables and RH (second order uncertain terms).

#### 4.3.1 How Do RH, Cloud Cover, Altitude and Temperature Vary with SST on Different Timescales?

Figure 4-3 shows how daytime RH and cloud variables change with SST on the grid box scale. A similar picture as in the previous chapter emerges, with more or less constant evolutions with SST prior to the onset of deep convection ( $SST < 299\text{ K}$ ), and a strong nonlinear signal over SSTs  $> 299\text{ K}$ , characterized by a considerable pick-up in UTRH and MTRH (a,d), increasing opaque cloud cover (b) and rising cloud altitudes (e,f), peaking around  $302\text{ K}$ . What is new in Fig. 4-3 from the previous chapter are the evolutions with SST on four different timescales, as well as the evolutions of the additional variables opaque and thin cloud altitudes and temperatures that are about constant for SSTs  $< 299\text{ K}$  and follow a similar nonlinear dynamic as the MTRH and opaque cloud cover for SSTs  $> 299\text{ K}$ .

The observation that the same atmospheric water cycle variable varies similarly with SST on all timescales in Fig. 4-3, suggests that these dynamical features are robust with respect to timescale.

However, for opaque clouds (central column) the curves representing the monthly, seasonal and annual timescales are clustered together, and the daily scale curve detached from them, which implies that the dynamical evolutions of opaque cloud characteristics observed on the daily scale are less representative of the monthly, seasonal and annual scales (and vice versa) than dynamics of RH and thin clouds. This difference between timescale dynamics is in fact an artifact of the averaging of instantaneous observations, namely a result of the sensitivity to the number of data over which the timescale average is calculated, where the impact of an extreme value is increasingly greater for the average value the fewer the observations. An indication of this is supplementary figure D-2 (Appendix D), which is the same as Fig. 4-3 but for grid box values computed with Method B, and in which the monthly, seasonal and annual curves in subplots b,e,h are much closer to the daily curve. As the grid box collocation is performed on the present timescale (daily, monthly, seasonal, annual) in Method B (compared to on the instantaneous timescale in Method A), and each grid box value is independently computed for each variable before the collocation, these grid box values better represent their variables' timescale mean states. The downside to Method B, however, is that the timescale averages are not computed over the same situations for all variables.

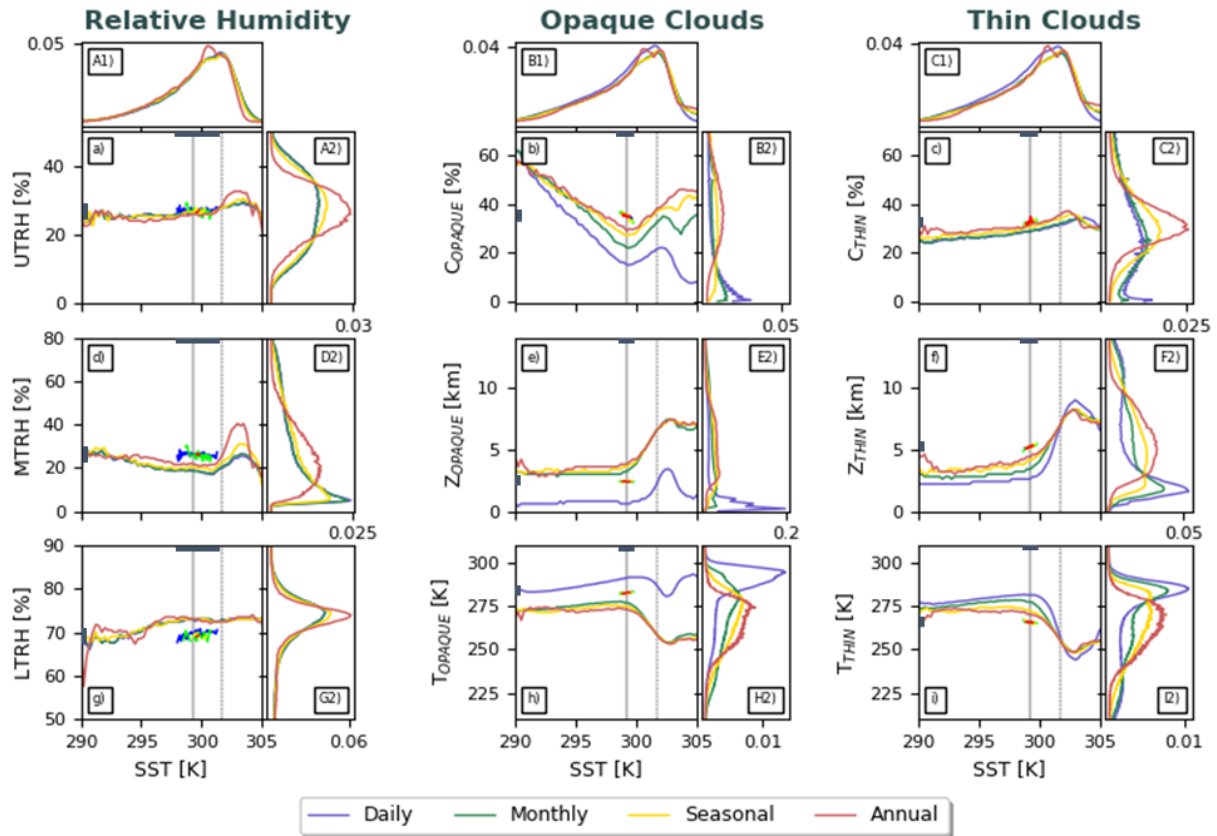


**FIGURE 4-3:** Change in RH and cloud characteristics with SST for grid box values on the (red) annual, (yellow) seasonal, (green) monthly, and (blue) daily timescale. a) upper-tropospheric RH, b) opaque cloud cover, c) thin cloud cover, d) middle-tropospheric RH, e) opaque cloud altitude, f) thin cloud altitude, g) lower-tropospheric RH, h) opaque cloud temperature, i) thin cloud temperature. Subplots A1, B1, C1 show the PDFs of SST, whilst subplots A2-I2 show the PDFs of the RH and cloud variables in a-i. Changes in RH with SST (left column) are computed over the years 2012-2018, whilst changes in cloud with SST (central and right columns) are computed over the years 2008-2019. The curves are fitted to grid box value distributions computed by Method A as illustrated in Fig. 4-2 (left column black line). The global curves show the range of locations of the median curves fitted to global values as illustrated in Fig. 4-2 (right column black line, seen here in subplot f). These ranges are also highlighted by the thick gray lines on the inside of the frames in subplots a-i. The rates of changes computed from global values are reported as histograms in Fig. 4-2.

#### 4.3.1.1 Variations of RH on the Global Scale?

The ranges of the global values are also plotted in Fig. 4-3 (thick gray lines on the inside of subplot frames) to facilitate the comparison between timescales, and the rates of changes computed from these are reported in histogram form in Fig. 4-4. Starting with the change in RH with SST (a-c), we can see that the signs are mostly consistent across all timescales, with decreasing LTRH and MTRH, whilst increasing UTRH with SST (up to  $+2\% \text{ K}^{-1}$ ).

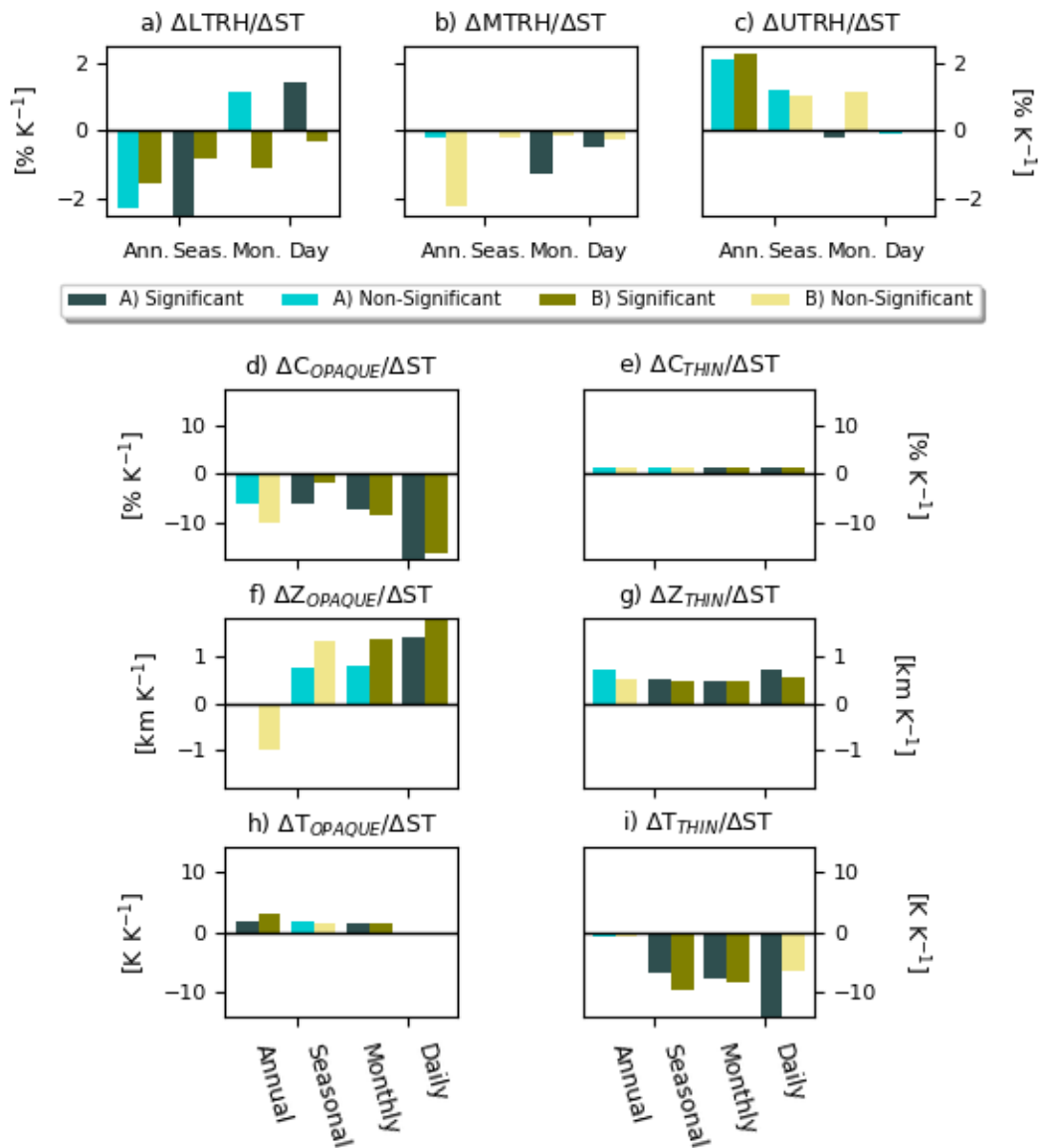


**FIGURE 4-4:** Histograms of rates of change computed from global values of daytime relative humidity (RH: lower, middle, upper troposphere), cloud cover (C), cloud altitude (Z) and cloud temperature (T) (separated into opaque and thin clouds) with sea surface temperature (ST) on the annual, seasonal, monthly, and daily time scales. Bars in cyan/teal are computed for Method A, whilst bars in yellow/brown for Method B. Dark and light coloring respectively indicate statistically significant and non-significant rates of change with respect to  $p$  value = 0.05. Percental (%) values of cloud cover and relative humidity are in absolute (not relative) values.

How do these observations compare to previous work? Numerous previous observational studies have focused on the change in specific humidity with surface temperature, but fewer have focused on RH. Willett et al.<sup>16</sup> (2008) found decreasing decadal tropical lower-tropospheric RH in all seasons from 1973 to 2003 ( $-0.11\%$ , from  $-0.04\%$  in DJF to  $-0.13\%$  in SON). Meanwhile, the tropical clear-sky upper troposphere has moistened slightly since 1979 ( $+0.008\%$  in Bates and Jackson<sup>17</sup> 2001, and  $+0.005\%$  in Shi and Bates<sup>18</sup> 2011), primarily in

<sup>16</sup> Willett et al. (2008): HadCRUH,  $5^\circ \times 5^\circ$  gridded monthly data,  $20^\circ\text{N}$ - $20^\circ\text{S}$ , 1973-2003

<sup>17</sup> Bates and Jackson (2001): HIRS (clear-sky), 200-500 hPa,  $2.5^\circ \times 2.5^\circ$  gridded monthly data, 1979-1998

<sup>18</sup> Shi and Bates (2011): HIRS (clear-sky), 200-500 hPa,  $2.5^\circ \times 2.5^\circ$  gridded monthly data, 1979-2009

the equatorial band 10°N-10°S (+0.084 % in and +0.025 %, respectively in the same publications). The smaller magnitudes in the more recent study by Shi and Bates (2011), covering one more recent decade, are consistent with John et al.<sup>19</sup> (2011) who found a negative decadal trend in UTRH (−1.1 %) over the period 1999-2009.

A straightforward comparison to the rates of changes with SST reported in Fig. 4-4 cannot be made from these previously published temporal trends. But considering that the tropical SST has warmed by approximately +0.05 K yr<sup>-1</sup> since 1950 (Kumar et al. 2010), we can conclude that the signs of the rates of change in Fig. 4-4 are consistent with the signs in these previous studies. Moreover, the IPCC AR5 (2013) actually concluded that, whilst the specific humidity at large scales over oceans has increased with surface warming since the 1970s at a rate expected from the Clausius-Clapeyron equation (+7 % K<sup>-1</sup>), no significant trends in large-scale oceanic RH has been observed. This observation is perhaps consistent with the lack of significant rates of changes in the middle and upper troposphere and varying signs and magnitudes in the lower in Fig. 4-4.

#### 4.3.1.2 Variations of Cloud Characteristics on the Global Scale?

In the previous chapter we established that on the instantaneous grid box scale, the decrease in tropical opaque cloud cover with SST is due to decreasing opaque liquid cloud cover with SST in the subsidence regions and decreasing opaque ice cloud cover for SSTs > 302 K. These nonlinear dynamics were also observed by e.g. Behrangi et al.<sup>20</sup> (2012) and confirmed here in Fig. 4-3.

On the global scale, the signs of the rates of change for all cloud variables with SST in Fig. 4-4 (d-i) are more robust across timescales than those for RH and the signs are consistent with the overall evolutions of the median curves in Fig. 4-3.

Opaque cloud cover decreases with SST by −6 to −10 % K<sup>-1</sup> on the annual, seasonal and monthly scales (4-4d). The negative sign of opaque cloud cover with SST in Fig. 4-4 is consistent with Zelinka and Hartmann<sup>21</sup> (2011) who employed a suite of satellite observations and found tropical-mean cloud fractions to decrease with SST by −0.02 to −0.06 % K<sup>-1</sup> at altitude levels below 200 hPa.

Positive rates of change are observed for both opaque cloud altitude and temperature in Fig. 4-4 (up to +0.8 km K<sup>-1</sup> and +3 K K<sup>-1</sup>, respectively). When cloud altitudes rise, we expect cloud temperatures to drop, but Fig. 4-4h shows that it is not the case in these rates of change computed from global values. The reason for this is explained by the different rates of changes in the low liquid and high ice clouds with SST outlined in Sect. 4.3.3.2.

For rates of changes of thin clouds with SST, all cloud variables (cover, altitude, temperature) are robust in both sign and magnitude on all timescales (about +1.4 % K<sup>-1</sup>, +0.5 km K<sup>-1</sup> and −6.5 to −16.7 K K<sup>-1</sup>, respectively).

---

<sup>19</sup> John et al. (2011): AMSU-B, 200-500 hPa, 1° × 1° gridded daily data, 30°N-30°S, 1999-2009

<sup>20</sup> Behrangi et al. (2012): CALIPSO, CloudSat, 30°S-30°N, 3° × 3°, 2007-2008

<sup>21</sup> Zelinka and Hartmann (2011): CloudSat, AIRS, MODIS, interannual tropical mean cloud fraction, 30°N-30°S

The implications of the results in Fig. 4-4d-g for the LW cloud feedback, are consistent with the signs of the observed LW cloud feedbacks in Vaillant de Guéllis et al.<sup>22</sup> (2018), except for the thin cloud altitude, which is positive in their work (implying lower thin cloud altitudes with SST). I am however confident in the positive rates of change reported in Fig. 4-4g as the fitted regressions are visualized in Figs. 4-2 and D-1 (Appendix D, right column) and because the positive sign is consistent with decreasing emission temperatures in 4-4i. In addition, the present study includes five additional years of observations, and is restricted to tropical oceans only, so the results are not directly comparable between our two studies.

#### 4.3.2 How Does the Low Liquid Cloud Cover Vary with SST on Different Timescales?

Next, I look at the change in cloud characteristics with SST in the two subsampled datasets extracted to focus on just the low liquid clouds ( $Z < 3$  km, Figs. 5,6) and the highest ice clouds ( $SST > 290$  K and  $T < 240$  K, Figs. 7,8) separately, the answers to which target the iris and FAT hypotheses.

Figure 4-5b shows that opaque liquid cloud cover decreases with SST on the grid box scale on all timescales (by  $-3$  to  $-5$  %  $K^{-1}$ ) which is to be compared to  $-4$  to  $-8$  %  $K^{-1}$  on the instantaneous timescale in the descending regime in the previous chapter. Both the sign and magnitude of these rates of change are consistent with the rates of changes of this same pair of variables from the global values presented in Fig. 4-6 ( $-2$  to  $-5$  %  $K^{-1}$ ). This is a useful result due to the community's lack of consensus in the exact rate of change of marine boundary layer clouds with SST.

In simulations of the tropical climate over the 21st century with CMIP3 and CMIP5 models, Qu et al.<sup>23</sup> (2015) found SST to induce a decrease in tropical mean low cloud cover in subsidence regions by  $-1$  to  $-2$  %  $K^{-1}$ .

In tropical subsidence regions, both Zhai et al.<sup>24</sup> (2015) and Myers and Norris<sup>25</sup> (2015) observed decreasing low cloud cover with SST ( $-1.5$  %  $K^{-1}$ ), and in the subsidence region off the southwest coast of Africa, Eastman et al.<sup>26</sup> (2011) found regional seasonal mean daytime stratocumulus clouds to decrease by  $-12$  %  $K^{-1}$ . In Fig. 4-6, opaque liquid cloud cover decreases by  $-2$  to  $-5$  %  $K^{-1}$ , but the different magnitudes could perhaps be explained by different definitions of the observed cloud diagnostics in our studies.

---

<sup>22</sup> Vaillant de Guéllis et al. (2018): CALIPSO, monthly global means over ocean surfaces, 2008-2014

<sup>23</sup> Qu et al. (2015): 21st century simulations in CMIP3 and CMIP5 models

<sup>24</sup> Zhai et al. (2015): CALIPSO-CloudSat (RL-GEOPROF-LIDAR, v.R04), 20°N/S-40°N/S, monthly, 2006-2010

<sup>25</sup> Myers and Norris (2015): CALIPSO cloud fraction at 850 hPa in the subtropics,  $2.5^\circ \times 2.5^\circ$ , 2006-2012

<sup>26</sup> Eastman et al. (2011): EECRA ship track observations computed to regional seasonal mean cloud amounts, 1954-2008

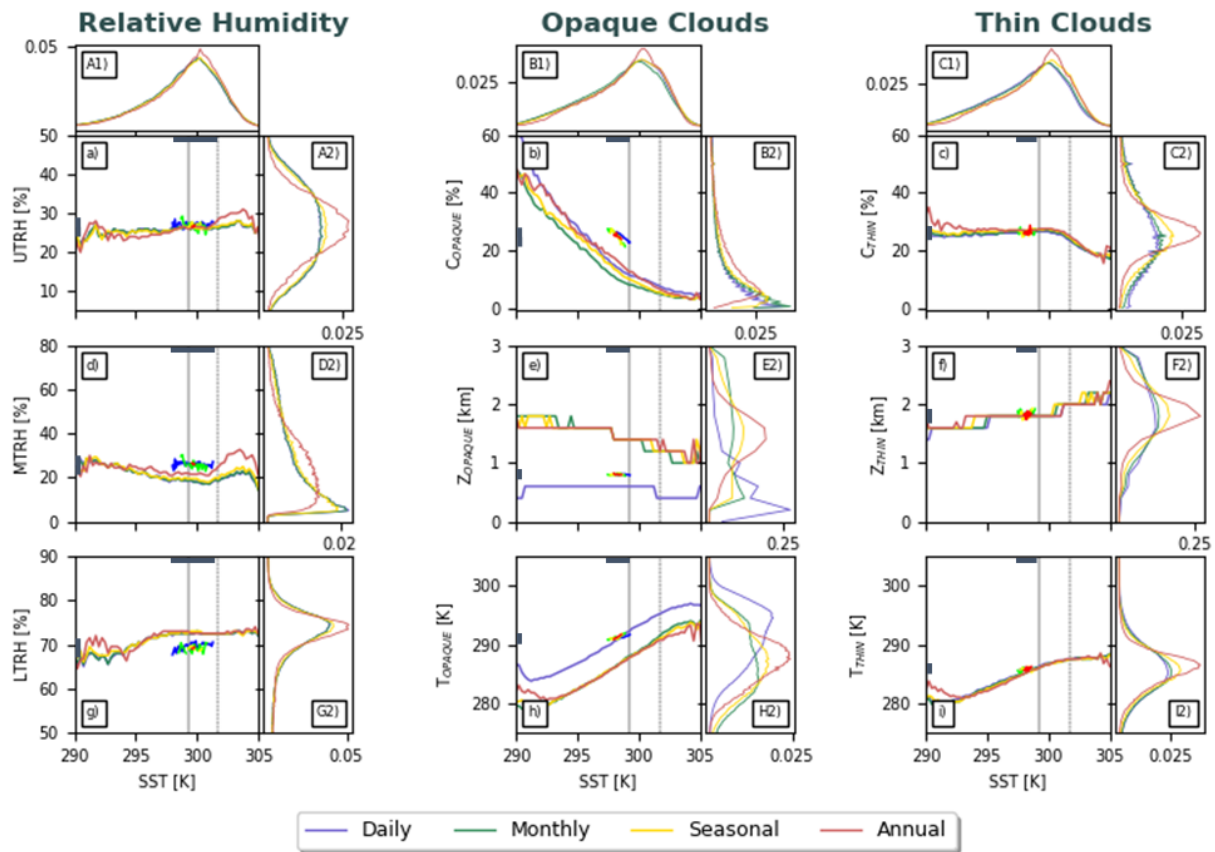


**FIGURE 4-5:** Change in RH and cloud characteristics with SST for grid box values in the subsampled dataset where cloud altitude  $< 3$  km on the (red) annual, (yellow) seasonal, (green) monthly, and (blue) daily timescale. a) upper-tropospheric RH, b) opaque cloud cover, c) thin cloud cover, d) middle-tropospheric RH, e) opaque cloud altitude, f) thin cloud altitude, g) lower-tropospheric RH, h) opaque cloud temperature, i) thin cloud temperature. Subplots A1, B1, C1 show the PDFs of SST, whilst subplots A2-I2 show the PDFs of the RH and cloud variables in a-i. Changes in RH with SST (left column) are computed over the years 2012-2018, whilst changes in cloud with SST (central and right columns) are computed over the years 2008-2019. The curves are fitted to grid box value distributions computed by Method A as illustrated in Fig. 4-2 (left column). The global curves show the range of locations of the median curves fitted to global values. These ranges are also highlighted by the thick gray lines on the inside of the frames in subplots a-i. The rates of change of these are reported in Fig. 4-6.

Chepfer et al.<sup>27</sup> (2018) observed decreasing opaque cloud volume (the vertically integrated cloud fraction between the surface and 4 km of altitude) with SST ( $-0.42\% \text{ K}^{-1}$ ) in tropical oceanic subsidence regions ( $\omega_{500} > 0$ ). That decrease in opaque cloud volume with SST is consistent with both decreasing opaque cloud cover and altitude in Figs. 4-5 (b and e), as well as decreasing cover whilst largely constant altitudes of opaque liquid clouds in Fig. 4-6 (d and f).

<sup>27</sup> Chepfer et al. (2018): CALIPSO, 30°S-30°S,  $2^\circ \times 2^\circ$ , monthly, 2008-2014

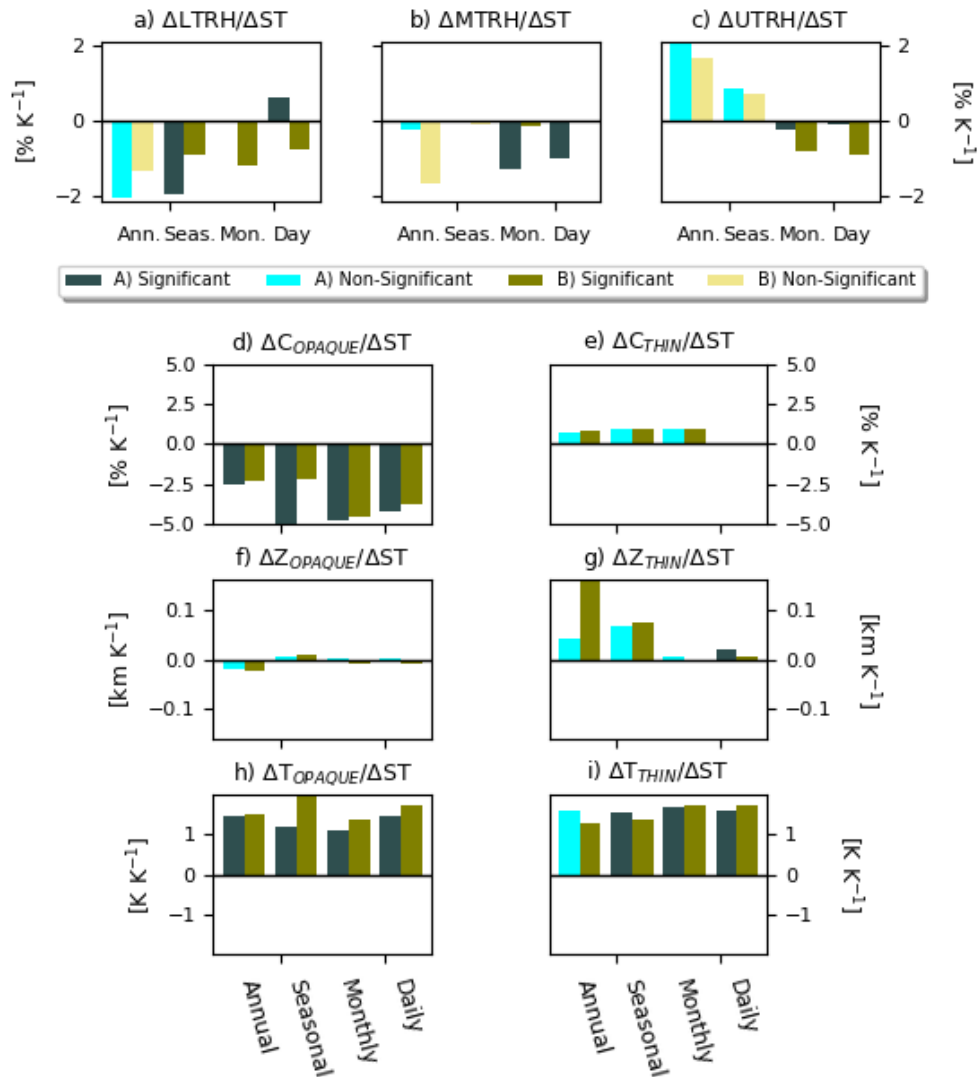


**FIGURE 4-6:** Histograms of rates of change computed from global values in the subsampled dataset where  $Z < 3$  km. Rates of change of daytime relative humidity (RH: lower, middle, upper troposphere), cloud cover (C), cloud altitude (Z) and cloud temperature (T) (separated into opaque and thin clouds) with sea surface temperature (ST) on the annual, seasonal, monthly, and daily time scales. Bars in cyan/teal are computed for Method A, whilst bars in yellow/brown for Method B. Dark and light coloring respectively indicate statistically significant and non-significant rates of change with respect to  $p$  value = 0.05. Percental (%) values of cloud cover and relative humidity are in absolute (not relative) values.

### 4.3.3 How Do Cold Ice Cloud Characteristics Vary with SST Over the Warmest Waters on Different Timescales?

#### 4.3.3.1 High Ice Cloud Cover

Over SSTs  $> 299$  K, Figure 4-7b shows that opaque ice cloud cover decreases with SST on the grid box scale on all timescales by  $-2$  to  $-8$  %  $K^{-1}$ , albeit with a strong nonlinear signal on the daily scale which we recognize from the instantaneous scale in the previous chapter. Both the sign and magnitude of these rates of change are consistent with the rates of changes of this same pair of variables from the global values presented in Fig. 4-8d ( $-2$  to  $-8$  %  $K^{-1}$ ).

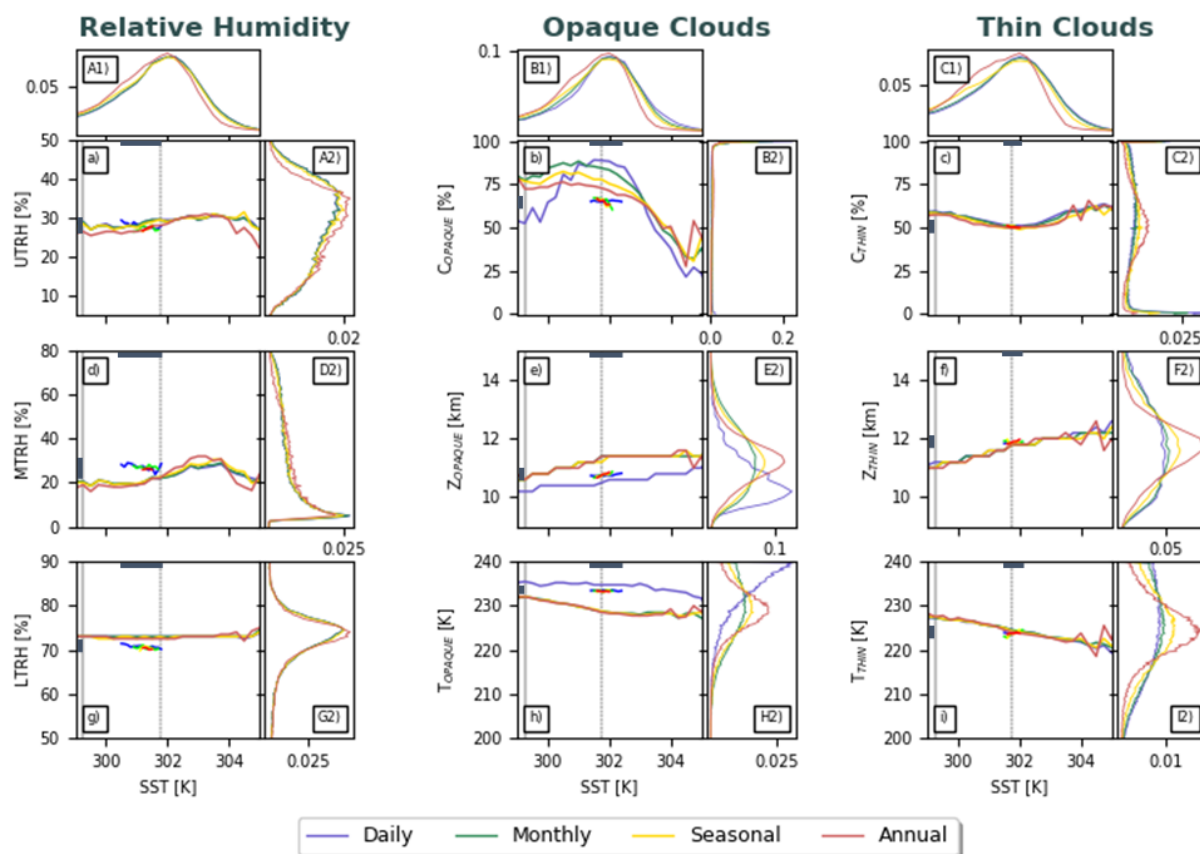


**FIGURE 4-7:** Change in RH and cloud characteristics with SST for grid box values in the subsampled dataset where  $SST > 299$  K and  $T < 240$  K on the (red) annual, (yellow) seasonal, (green) monthly, and (blue) daily timescale. a) upper-tropospheric RH, b) opaque cloud cover, c) thin cloud cover, d) middle-tropospheric RH, e) opaque cloud altitude, f) thin cloud altitude, g) lower-tropospheric RH, h) opaque cloud temperature, i) thin cloud temperature. Subplots A1, B1, C1 show the PDFs of SST, whilst subplots A2-I2 show the PDFs of the RH and cloud variables in a-i. Changes in RH with SST (left column) are computed over the years 2012-2018, whilst changes in cloud with SST (central and right columns) are computed over the years 2008-2019. The curves are fitted to grid box value distributions computed by Method A as illustrated in Fig. 4-2 (left column). The global curves show the range of locations of the median curves fitted to global values. These ranges are also highlighted by the thick gray lines on the inside of the frames in subplots a-i. The rates of change of these are reported in Fig. 4-8.

The decreasing opaque ice cloud cover in Fig. 4-7b is consistent with Igel et al.<sup>28</sup> (2014) who found anvil width to decrease with SST by about  $-35$  km  $K^{-1}$  in CloudSat observations.

Over the Pacific Warm Pool Region, Lindzen et al.<sup>29</sup> (2001) found cumulus cloud coverage colder than 260 K to decrease with cloud-weighted SST by  $-2.2$  %  $K^{-1}$ , whilst a slight increase ( $+0.2$  %  $K^{-1}$ ) in the cover of very cold high clouds ( $T < 220$  K).

<sup>28</sup> Igel et al. (2014): CloudSat,  $1^\circ \times 1^\circ$  regridded instantaneous data (granule files),  $30^\circ N$ - $30^\circ S$

<sup>29</sup> Lindzen et al. (2001): Japanese Geostationary Meteorological Satellite-5,  $30^\circ N$ - $30^\circ S$  &  $130^\circ E$ - $170^\circ W$ , regional daily averages, Jan. 1998 - Aug. 1999

Su et al.<sup>30</sup> (2008) found upper-tropospheric cloud fraction to increase with cloud-weighted SST in three tropical regions (15°N-15°S: +13 % K<sup>-1</sup>, 30°N-30°S: +6 % K<sup>-1</sup>, Pacific Warm Pool Region: +6 % K<sup>-1</sup>). The results of Su et al. (2008) measured with the Atmospheric Infrared Sounder (AIRS), are consistent with the observations of increasing thin ice cloud cover made on the grid box scale in both the previous chapter and in Figs. 4-3 and 4-7 here.

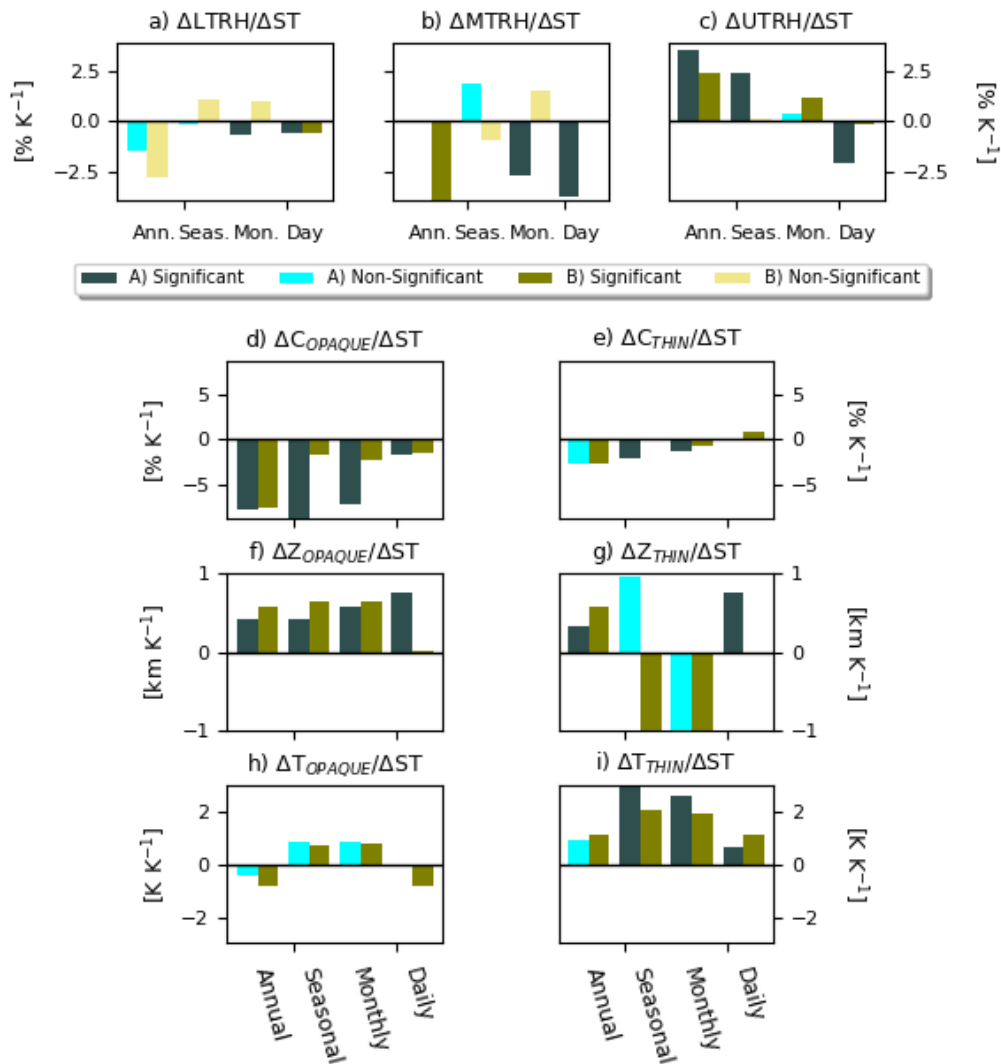


**FIGURE 4-8:** Histograms of rates of change computed from global values in the subsampled dataset where SST > 299 K and T < 240 K. Rates of change of daytime relative humidity (RH: lower, middle, upper troposphere), cloud cover (C), cloud altitude (Z) and cloud temperature (T) (separated into opaque and thin clouds) with sea surface temperature (ST) on the annual, seasonal, monthly, and daily time scales. Bars in cyan/teal are computed for Method A, whilst bars in yellow/brown for Method B. Dark and light coloring respectively indicate statistically significant and non-significant rates of change with respect to p value = 0.05. Percental (%) values of cloud cover and relative humidity are in absolute (not relative) values.

<sup>30</sup> Su et al. (2008): AIRS, p > 300 hPa, 1° × 1°, Sept. 2002 to Sept. 2006

### **Contribution to the Iris Discussion**

As shown already on the instantaneous scale in the previous chapter, this dataset holds some observational support for the iris hypothesis on the grid box scale: (1) Marine boundary layer cloud cover decreases with SST, which leads to greater clear-sky cover in subsidence regions. (2) Over the warmest SSTs (SST > 303 K), opaque ice cloud cover decreases, as does RH in the middle and upper troposphere, which implies a cooling due to an increase in OLR there. Taken together, the greater clear-sky coverage observed due to both decreasing opaque low liquid cloud cover and opaque high ice cloud cover, suggests an increase in emitted OLR with SST in these regions.

In the global values, there are significant negative rates of change of opaque ice cloud cover with SST on all timescales (Fig. 4-8d). These are of the same sign as the trend found by Bony et al.<sup>31</sup> (2016) in the IPSL GCM (about  $-0.75\% \text{ K}^{-1}$ ), but up to one order of magnitude larger.

In the global values, the thin ice cloud cover also decreases with SST on all timescales (Fig. 4-8e). These results contrast the observed increasing thin ice cloud cover with SST over these the warmest SSTs on the grid box scale, in both the present chapter and the previous, and suggest again that the perspectives are different for the global values indicative of temporal variability and the more process-oriented grid box scale values.

#### 4.3.3.2 High Ice Cloud Altitudes and Temperatures

### **Contribution to the FAT Discussion**

In Fig. 4-3e,h for SSTs > 303, both opaque cloud altitudes and temperatures appear about constant with SST on the seasonal and annual time scales. The subsampled dataset over warm SSTs (> 299 K) (Fig. 4-7) shows that ice cloud altitudes actually increase and temperatures decrease seemingly linearly with SST (Opaque:  $+0.13 \text{ km K}^{-1}$  and  $-0.7 \text{ K K}^{-1}$ ; Thin:  $+0.21 \text{ km K}^{-1}$  and  $-1.15 \text{ K K}^{-1}$ ). When ice cloud temperatures are plotted with altitudes in this subsample these are observed to decrease linearly with altitudes ( $-6.5 \text{ K km}^{-1}$ , not shown).

From these observations on the grid box scale, I do not see any clear evidence for the FAT hypothesis. Rather, it appears as if cloud temperatures decrease with altitudes. This conclusion is supported by Igel et al. (2014) who found both anvil base-height and anvil depth to increase with SST (by about  $+0.2$  and  $+0.15 \text{ km K}^{-1}$ ), whilst both lower-anvil temperature and cloud-top temperature to decrease with SST (by about  $-0.35$  and  $-1.5 \text{ K K}^{-1}$ ).

However, there is support for the FAT hypothesis in the global values in Fig. 4-8 (f and h), where significant rise-ups in opaque ice cloud altitudes are observed on all timescales (about  $+0.5 \text{ km K}^{-1}$ ), whilst no consistent temperature change in 4-8h where the sign varies across the timescales ( $-0.84$  to  $+0.87 \text{ K K}^{-1}$ ), and all rates of changes are nonsignificant for Method A.

That there is support for the FAT in spatially global values, whilst not in the grid box values, is supported by previous work dealing with global or tropical mean values (Kuang and Hartmann 2007, Zelinka and Hartmann 2010, 2011), over long timescales (e.g. decadal scales in Zelinka and Hartmann 2010). It suggests that on long timescales, cloud altitudes rise with surface warming with little change in emission temperature ( $< 0.25 \text{ K K}^{-1}$  in Kuang and

---

<sup>31</sup> Bony et al. (2016): IPSL GCM model, annual mean tropical anvil cloud amount, 30°N-30°S, 1979-2005

Hartmann 2007), whilst on short and local scales, cloud temperature varies with SST as expected from changes in cloud altitudes with SST. The nonsignificant trends in ice cloud temperature with SST in Fig. 4-8 could be suggestive of the absence of a trend, but a considerably longer observational record than the 12 years employed in this study, is needed to be confident in this conclusion.

### **Why Are the Rates of Changes Computed from Tropics-Wide Global Values for Both Opaque Cloud Altitudes and Temperatures with SST Positive?**

The positive signs of the rates of changes of both opaque cloud altitude and temperature with SST in Fig. 4-4f,h might be explained by the two subsampled datasets. The results reported for the rates of change of the global values in Figs. 4-6 and 4-8 show that (i) there is little change in opaque liquid cloud altitude with SST (4-6f), so the change in cloud altitude is governed by the change in opaque ice clouds with significant positive rates of changes (about  $+0.5 \text{ km K}^{-1}$  in 4-8f), and that (ii) the rates of change of cloud temperatures are robustly positive for opaque liquid clouds (about  $+1$  to  $+2 \text{ K K}^{-1}$  in 4-6h), whilst of varying sign as well as smaller magnitudes for opaque ice clouds in 4-8h. Hence, the overall rise-up of tropical opaque cloud altitudes is explained by rising opaque ice cloud altitudes, and the warming of the overall tropical opaque clouds by a warming of the low liquid clouds.

A similar implication emerges from the grid box values in Figs. 4-5 and 4-7. Fig. 4-5 shows that, on the grid box scale, the opaque liquid clouds decrease in altitude with SST by  $-0.05 \text{ km K}^{-1}$  and simultaneously warm by  $+1 \text{ K K}^{-1}$ , whilst Fig. 4-7 shows that the opaque ice clouds rise by  $+0.13 \text{ km K}^{-1}$  and simultaneously cool by  $-0.7 \text{ K K}^{-1}$ . In these subsampled datasets, the signs are always opposite for changes in cloud altitude and temperature with SST. The implication of these observations for the rates of change on the global scale in Fig. 4-4 are thus that (i) the rates of change in cloud altitude with SST are positive because the magnitude of the rise of ice clouds is almost three times that of the decrease in liquid cloud altitude and (ii) the rates of change in cloud temperature with SST are also positive because the magnitude of change is greater for the low liquid clouds than the ice clouds, and because grid boxes containing low liquid clouds are more abundant than grid boxes containing high ice clouds.

Rising opaque ice cloud altitudes ( $+0.12$  and  $+0.45 \text{ km K}^{-1}$  in the monthly grid box and global values, respectively) are consistent with the  $+0.24 \text{ km K}^{-1}$  rise in monthly mean opaque cloud altitude with SST in tropical ascending regions ( $\omega_{500} < 0$ ) observed by Chepfer et al. (2018).

#### **4.3.4 How Do Cloud Characteristics Covary and How Do They Vary with RH on Different Timescales?**

##### **4.3.4.1 How Do Clouds and RH Covary on the Grid Box and Global Scales?**

In accordance with the observations made in Fig. 4-3, Fig. 4-9 shows that opaque and thin cloud altitudes rise and temperatures drop with RH in the middle (e, h, n, q) and upper troposphere (f, i, o, r), which is understandable from an expected increase in buoyancy in a moister state.

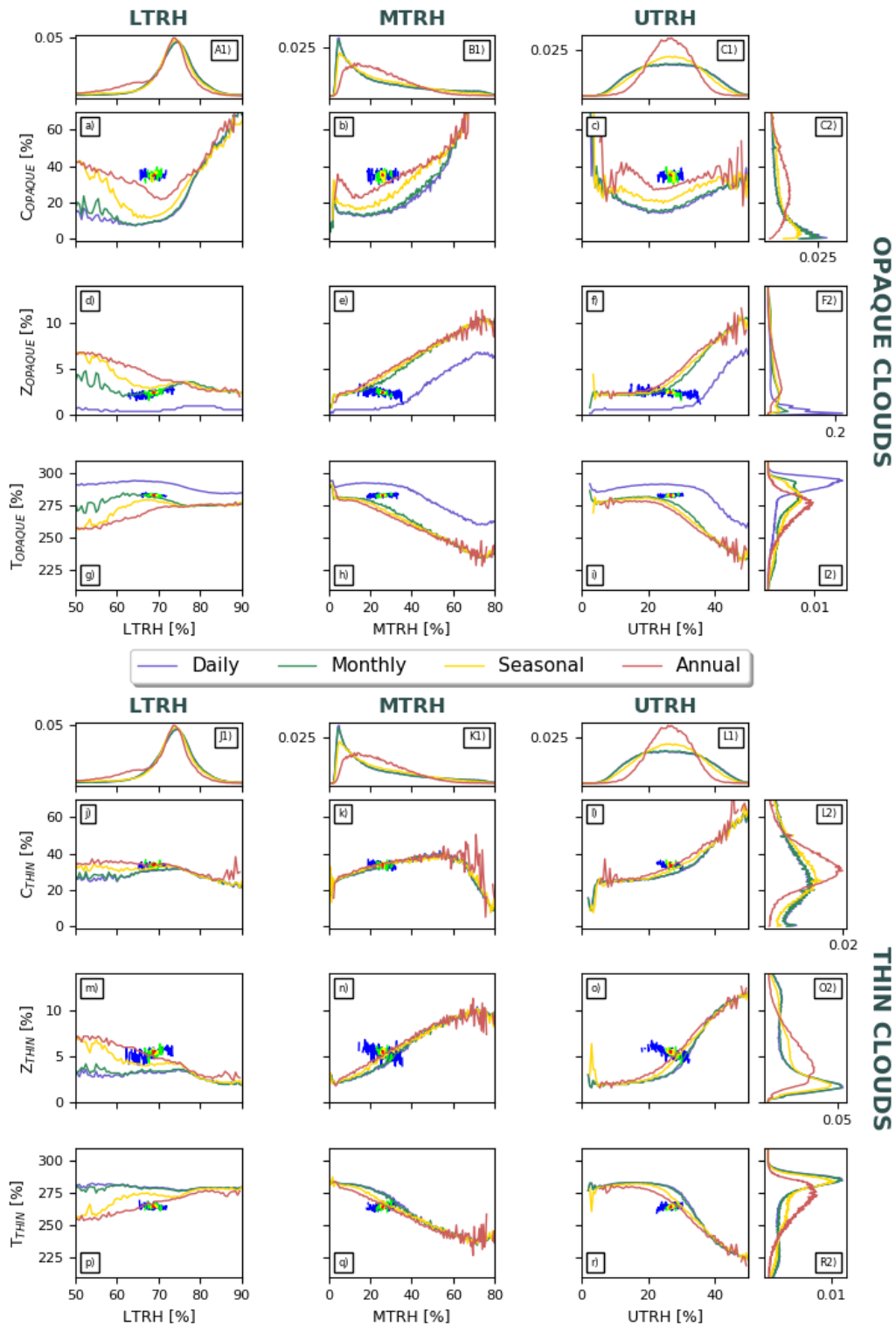


**FIGURE 4-9:** Change in (a-i) opaque and (j-r) thin cloud characteristics with (left column) lower-, (central column) middle-, and (right column) upper-tropospheric RH. Changes with RH are for grid box values on the (red) annual, (yellow) seasonal, (green) monthly, and (blue) daily timescale over the years 2012-2018. Subplots A1, B1, C1 (J1, K1, L1) show the PDFs of LTRH, MTRH, UTRH in grid boxes containing opaque (thin) clouds. Subplots C2, F2, I2 (L2, O2, R2) show the PDFs of opaque (thin) cloud cover, altitude, temperature respectively. The curves are fitted to grid box value distributions computed by Method A as illustrated in Fig. 4-2 (left column). The global curves show the range of locations of the median curves fitted to global values. These ranges are also highlighted by the thick gray lines on the inside of the frames in subplots a-r. The rates of change of these are reported in Fig. 4-12.

But opaque and thin cloud covers respond differently to changes in the RH profile. Thin cloud cover seems insensitive to LTRH (j), but increases with MTRH and UTRH (k, l). Höjgård-Olsen et al. (2020) (Ch. 3) showed that thin liquid cloud cover is largely constant with SST, so that all changes in thin cloud cover can be derived to the free troposphere. The observation made here that thin liquid cloud cover is also insensitive to changes in LTRH, suggests that the thin liquid cloud cover is always about 25 %. The seemingly exponential increase in opaque cloud cover with LTRH and MTRH (a,b) suggests that moisture convergence in the lower free troposphere is key for the extent of opaque ice cloud cover. This observation is consistent with the role of lower-tropospheric moisture convergence for convection (e.g. Peters and Neelin 2006, Neelin et al. 2009, Stevens et al. 2017). The covariation between MTRH and opaque cloud cover is also consistent with the theory surrounding the iris hypothesis that discusses both a drying of the middle troposphere as well as decreasing anvil cloud cover over the warmest SSTs (e.g. Mauritsen and Stevens 2015), which is an observation that we also make in Figs. 3, 4, 7.

The rates of change computed from the global values in Method A and reported in Fig. 4-10 show that the sign and magnitudes are largely consistent across the timescales for changes in cloud variable with RH. The same cannot be said for values computed from Method B, where cloud characteristics appear much less sensitive to changes in the RH profile (as discussed in Sect. 4.4.2). For Method A, the signs of the rates of changes of opaque cloud altitude and temperature with LTRH, MTRH, UTRH are robust across all timescales (LTRH: about  $+0.04 \text{ km } \%^{-1}$  and  $-1.5 \text{ K } \%^{-1}$ , MTRH: about  $-0.04 \text{ km } \%^{-1}$  and  $+0.7 \text{ K } \%^{-1}$ , UTRH: about  $-0.04 \text{ km } \%^{-1}$  and  $+0.6 \text{ K } \%^{-1}$ ). The signs of the rates of changes of thin cloud altitude and temperature with MTRH and UTRH are also robust across all timescales (MTRH: about  $-0.1 \text{ km } \%^{-1}$  and  $+0.8 \text{ K } \%^{-1}$ , UTRH: about  $-0.1 \text{ km } \%^{-1}$  and  $+0.7 \text{ K } \%^{-1}$ ). These rates of changes are of opposite sign to the overall sign of the dynamical changes seen in Fig. 4-9, which suggests that what the global values actually show is the temporal covariability of a pair of variable, rather than physical processes.

I would expect from basic cloud physics that cloud occurrence is positively correlated with RH. In the upper troposphere, Luo and Rossow<sup>32</sup> (2004) found cirrus clouds to be associated with greater humidity. On the instantaneous scale, following the diurnal cycle, Chepfer et al.<sup>33</sup> (2019) observed that vertical profiles of RH (SAPHIR) and thin cloud fraction (CATS lidar) vary together. These observations that RH and thin clouds vary together seem consistent with the results reported in Fig. 4-9l,o and could perhaps explain why there are negligible differences between timescale curves showing the change in both RH (left column) and thin cloud characteristics (right column) with SST in Figs. 3,5,7.

---

<sup>32</sup> Luo and Rossow (2004): ISCCP, TIROS-TOVS, Lagrangian trajectory analysis, 50°N-50°S

<sup>33</sup> Chepfer et al. (2019): SAPHIR, CATS lidar,  $2^\circ \times 2^\circ$ , 30°N-30°S, monthly mean, June-August 2015-2017

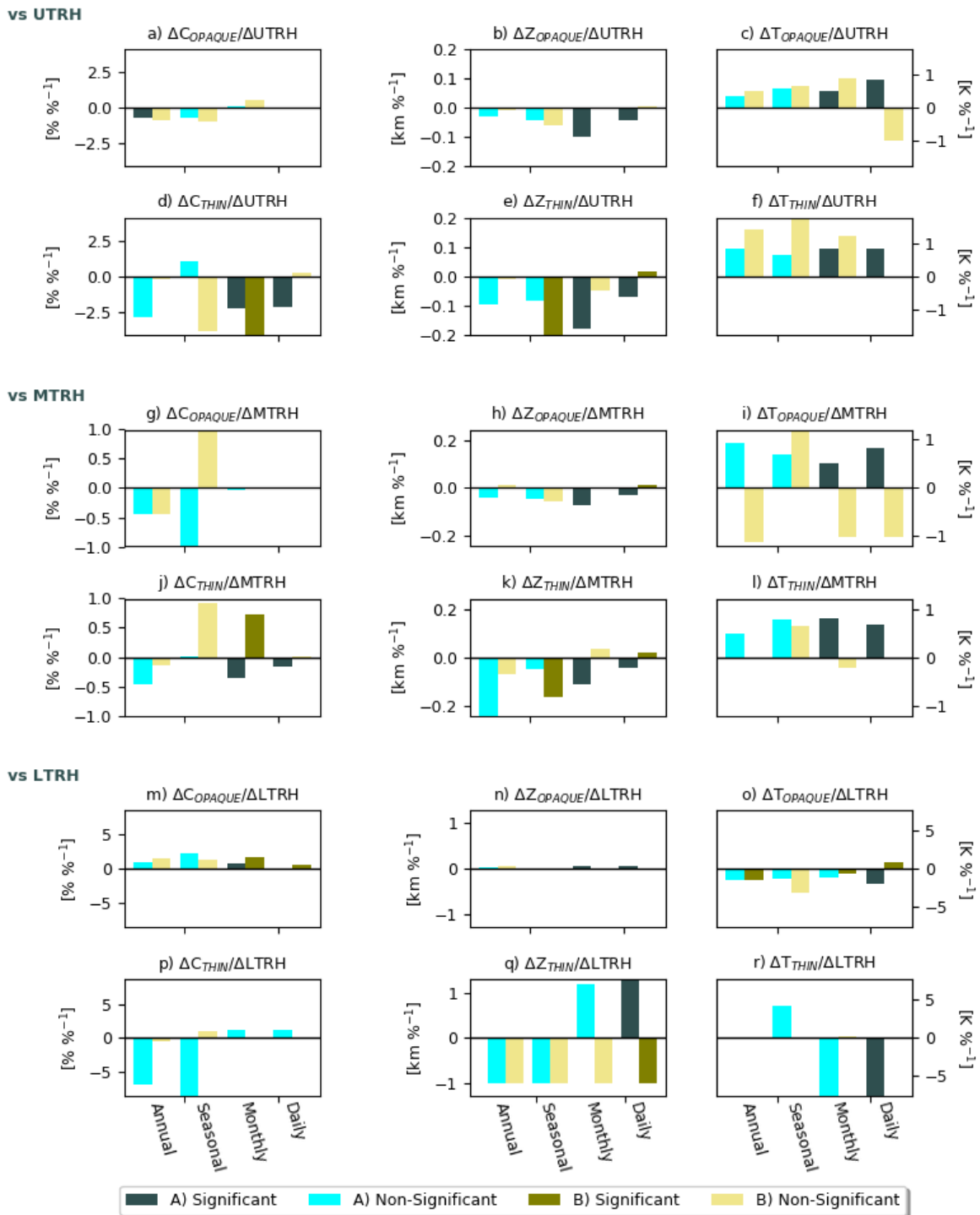


**FIGURE 4-10:** Rates of change of cloud cover (C), cloud altitude (Z) and cloud temperature (T) (separated into opaque and thin clouds) with (a-f) upper, (g-l) middle and (m-r) lower relative humidity on the annual, seasonal, monthly, daily and instantaneous time scales. Bars in cyan/teal are computed for Method A, whilst bars in yellow/brown for Method B. Dark and light coloring respectively indicate statistically significant and non-significant rates of change with respect to a  $p$  value = 0.05. Percental (%) values of cloud cover and relative humidity are in absolute (not relative) values.

#### 4.3.4.2 How Do Clouds Covary on the Grid Box and Global Scales?

Figure 4-11 shows the covariation between cloud variables. It shows that as the cloud cover increases, the altitude increases as well (a,b), whilst the cloud temperature decreases (c,d). This observation holds for both opaque (left column) and thin clouds (right column), although the evolution of these median curves appear linear for opaque clouds, whilst thin clouds show more nonlinear dynamics. As expected, the changes in cloud temperature (c,d) mirrors the changes in cloud altitude (a,b), which is evident from the linear change in cloud temperature with altitude seen in subplots e,f.

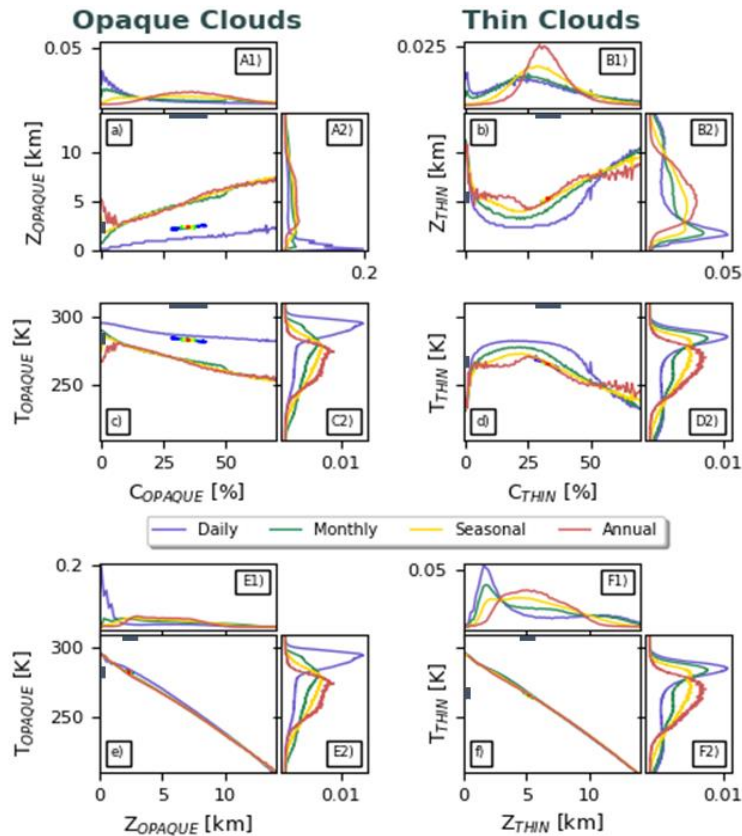


**FIGURE 4-11:** Change in cloud (a, b) altitude with cover (c, d) temperature with cover, and (e, f) temperature with altitude on the (red) annual, (yellow) seasonal, (green) monthly, and (blue) daily timescale over the years 2008-2019. **Left column:** Opaque clouds. **Right column:** Thin clouds. Subplots A1, B1 (E1, F1) show the PDFs of opaque and thin cloud cover (altitude). Subplots A2-F2 show the PDFs of the y variables in subplots a-f. The curves are fitted to grid box value distributions computed by Method A as illustrated in Fig. 4-2 (left column). The global curves show the range of locations of the median curves fitted to global values. These ranges are also highlighted by the thick gray lines on the inside of the frames in subplots a-f. The rates of change of these are reported in Fig. 4-10.

From Fig. 4-11a, one might deduce that opaque cloud altitude increases linearly with opaque cloud cover, but there is a complication to this image: Namely, on the instantaneous scale (where we make our observations), opaque clouds are sampled at either small coverage (0 to 10 %) or large coverage (100 %), albeit with a gap from about 60 to 90 % where much fewer opaque clouds are sampled. This is best seen in supplementary figure D-4 (Appendix D). At the same time, low liquid clouds are sampled for the full range of possible covers (0 to 100 %), whilst high ice clouds are only sampled at close to 100 % cover. A result of the opaque cloud cover distribution with one peak at low cover (close to 0 %) and a second peak at high cover (close to 100 %), is that an unrealistic population of 50 % cover arises as an artifact of

the upscaling to longer timescales (regardless of Method A or B). This population is best seen on the monthly scale, where CALIPSO typically observes the same  $1^\circ \times 1^\circ$  grid box twice. If this grid box is located in the transition region between ascending and subsiding vertical motion (what we would consider the intermediate regime in the previous chapter), one cloud cover observation might be 0 % and the next 100 % – the mean of which is 50 %.

In the corresponding rates of changes computed from the global values (Fig. 4-12), the sign is robust as well as of comparable magnitudes across the four timescales for all these pairs of variables, except for opaque cloud altitude with cover, for which there is little change.

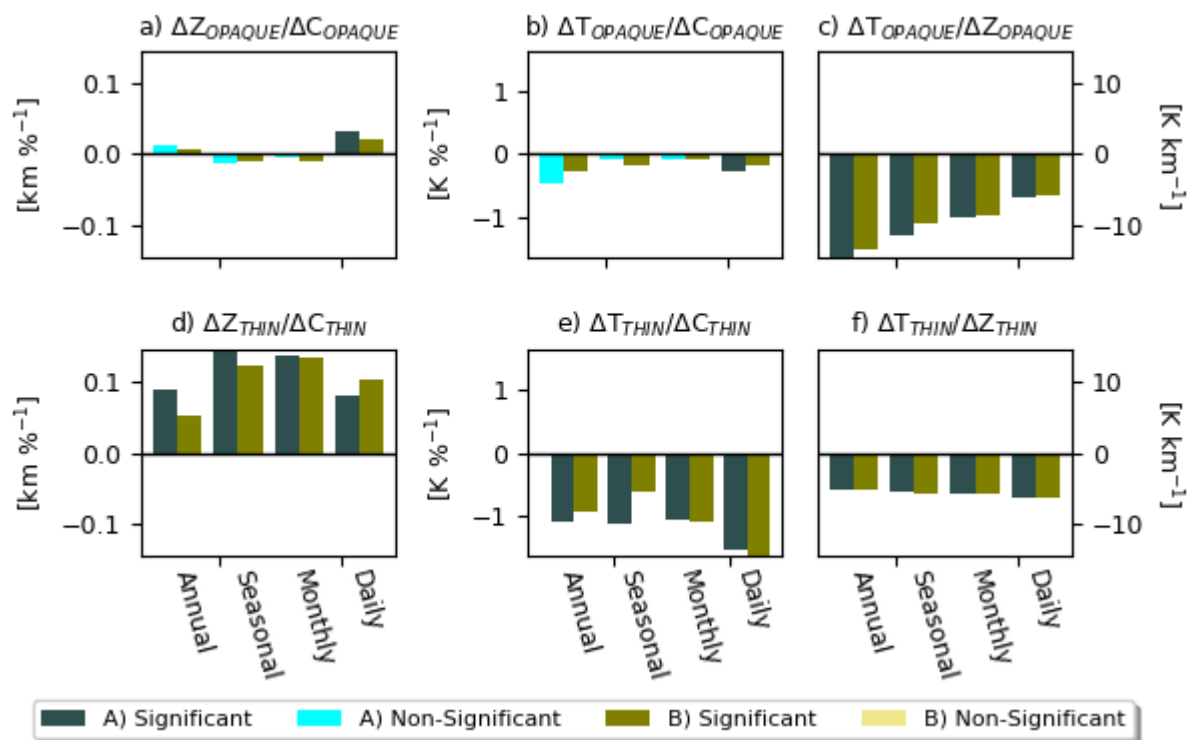


**FIGURE 4-12:** Rates of changes computed from global values of daytime covariations between tropical cloud variables. Rates of change of cloud cover (C), cloud altitude (Z) and cloud temperature (T) (separated into opaque and thin clouds) with each other on the annual, seasonal, monthly, daily and instantaneous time scales. **Top panel:** Opaque clouds. **Bottom panel:** Thin clouds. Bars in cyan/teal are computed for Method A, whilst bars in yellow/brown for Method B. Dark and light coloring respectively indicate statistically significant and non-significant rates of change with respect to a  $p$  value = 0.05. Percental (%) values of cloud cover and relative humidity are in absolute (not relative) values.

## 4.4 Discussion of These Results

### 4.4.1 Limits of the Study

As was the case in the previous chapter, this study only used daytime (01:30 pm) observations over fully oceanic grid boxes in the tropics. As such, the results of this study are statistical representations of pairs of water cycle variable covariations in the daytime oceanic tropics and ignore continental observations as well as features of the diurnal cycle (discussed in e.g. Stubenrauch et al. 2006, Bouniol et al. 2016, Noel et al. 2018, Chepfer et al. 2019).

Most linear regressions fitted to the annual global values do not meet the significance requirement ( $p$  value  $< 0.05$ ). This is likely due to too few years on record in the observational dataset used here. An indication of this conclusion is the fact that more regressions are significant when clouds and SST are compared over the period 2008 to 2019 in Figs. 4,6,8, compared to the number of significant regressions on the annual scale for RH versus SST over the period 2012 to 2018. This could of course also be the result of the lack of statistically significant trends obtained by previous work between RH and SST over large-scale oceanic surfaces as concluded in IPCC AR5 (2013).

#### 4.4.2 Sensitivity of the Results to the Choice of Data Analysis Method (Comparing A and B)

As it turns out, similar results were obtained by both data analysis methods (A and B) for both grid box covariations and rates of changes computed from global values (Figs. 4-3 to 4-11). For that purpose, I deemed results computed from Method A on the grid box scale to be enough to answer the science questions on that spatial scale. Results computed from Method B on the grid box scale for cloud vs. SST and cloud vs. cloud are therefore reported in supplementary figures D-2 and D-3 (Appendix D).

However, Fig. 4-13 below shows considerable differences in the cloud variable evolutions with RH computed for data analysis Method B compared to those computed from Method A in Fig. 4-9, due to cloud characteristics being much less sensitive to changes in the RH profile in Fig. 4-13. This comparison suggests that the thermodynamic relationships between clouds and RH is best observed when the variables are collocated on the instantaneous scale (Method A). The rates of changes computed for these pairs of variables and reported in Fig. 4-10 also show considerable differences between results computed for the two methods, especially for changes with MTRH and UTRH.

If both methods had always given the same results, it would not matter on which timescale the collocation is made, which would suggest that we can compare two variables whose timescale mean values are computed/sampled differently because the geographical climatology or mean state of the variables is robust enough so that the sampling does not matter. This is also likely true the longer the timescale and does evidently often seem to be the case when RH and cloud variables are compared to SST on the timescales considered in the present study.

However, here it is not true when cloud variables are compared to RH. Different results thus imply that the outcome is sensitive to the timescale on which the collocation is performed. In the past, when observational coverage was more limited, studies had to accept to work with the observations available at the time and that these were not always sampled on the same scales. But different results obtained by Methods A and B for the same pairs of variables might question the validity of such studies. For this work, and the observational dataset used herein, it means that we should not compare RH from SAPHIR and CALIPSO cloud observations that are sampled on different timescales.

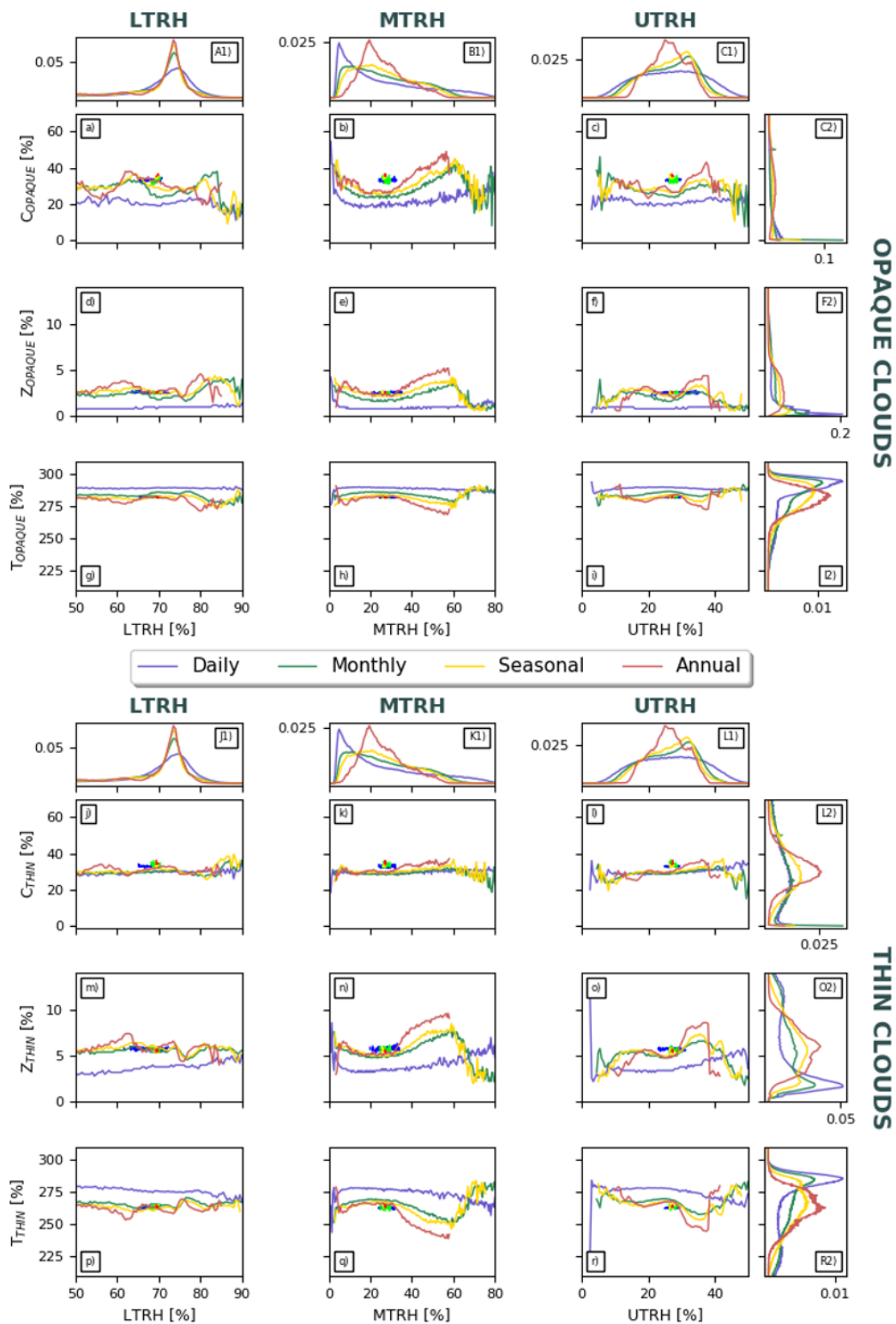


**FIGURE 4-13:** Change in (a-i) opaque and (j-r) thin cloud characteristics with (left column) lower-, (central column) middle-, and (right column) upper-tropospheric RH. Changes with RH are for grid box values on the (red) annual, (yellow) seasonal, (green) monthly, and (blue) daily timescale over the years 2012-2018. Subplots A1, B1, C1 (J1, K1, L1) show the PDFs of LTRH, MTRH, UTRH in grid boxes containing opaque (thin) clouds. Subplots C2, F2, I2 (L2, O2, R2) show the PDFs of opaque (thin) cloud cover, altitude, temperature respectively. The curves are fitted to grid box value distributions computed by Method B as illustrated in Fig. 4-2 (left column). The global curves show the range of locations of the median curves fitted to global values. These ranges are also highlighted by the thick gray lines on the inside of the frames in subplots a-r. The rates of change of these are reported in Fig. 4-12.

#### 4.4.3 Assuming Linear Covariation

As indicated in the introduction, the community is aware that assuming linear covariation is an inaccurate representation of the feedback terms. Had the overall trends in the median curves (Figs. 3,5,7,9,11) always been of the same sign as the rates of changes computed from the global values (reported in Figs. 4,6,8,10,12), the latter could directly have been implemented to solve the feedback equation, but the present study shows that this is a problem on both temporal and spatial scales, which implies that it is very important to work in the right kind of framework for the question that is asked.

On the grid box scale (Figs. 3,5,7,9,11), we observe similar nonlinear dynamics on all timescales. The fact that these dynamics are nonlinear implies however that they change differently over different x-variable ranges (SST or RH), a feature which linear regressions do not capture. Hence, conclusions drawn from local experiments can explain relationships and dynamics in the present location, but cannot be applied to different locations. For example, conclusions drawn from observations made in the subsidence (convective) regions for an increase in 1 K SST, say nothing about changes in convective (subsidence) regions for a change in 1 K SST, nor anything about the change in the tropics as a whole for a uniform 1 K SST increase.

The feedback formalism (E4-1) assumes that the feedback parameters are constant in time. Here we demonstrate that this is not true, as significant rates of changes computed for global values in Figs. 4,6,8,10,12 vary in magnitude across timescales. On accounts of these results, we cannot assume linearity across timescales. It is however possible that magnitude differences between significant rates of changes on different timescales will be smaller if computed over a longer time period. If these satellite instruments employed here will be allowed to operate for years to come, it would be interesting to revisit these statistics from a decadal perspective (as e.g. Dessler 2010, Zhou et al. 2016).

#### 4.4.4 Discussion on a 4 K Warmer Climate Scenario

What will the climate be like in the future? This is the ultimate prediction our community wants to make and a number of possible scenarios resulting from different forcings<sup>34</sup> have been investigated. One of them is the Atmospheric Model Intercomparison Project (AMIP) climate scenario forced by a rise in global mean surface temperature of +4 K (“AMIP+4K”).

In the previous and present chapters, the upper limit of the SST range was set to 305 K. Above 305 K, there are so few observations in this collocated dataset that the median values do not meet the significance requirements set up for the computation of the median curves (i.e. the bootstrapping algorithm and the minimum number of data within one SST bin in Ch. 3, Sect. 3.3.4).

A uniform +4 K warming (as assumed in the AMIP+4K scenario) shifts the distribution of tropical SST values and the peak occurrence +4 K. From this shift we can make an observationally based estimation of the tropical climate after such a forcing, assuming that the atmosphere will respond in the same way as now. Fig. 4-14 below is the same as Fig. 4-3, but shows a shift of the SST range by +4 K and the *cumulative distribution functions* (CDF) of SST

---

<sup>34</sup> [http://www.ipcc-data.org/sim/gcm\\_monthly/AR5/CMIP5-Experiments.html](http://www.ipcc-data.org/sim/gcm_monthly/AR5/CMIP5-Experiments.html), accessed 2020-08-18

for the current climate (+0 K: solid) and a 4 K warmer climate scenario (+4 K: dashed) in subplots A1, B1, C1 instead of the PDFs in Fig. 4-3.

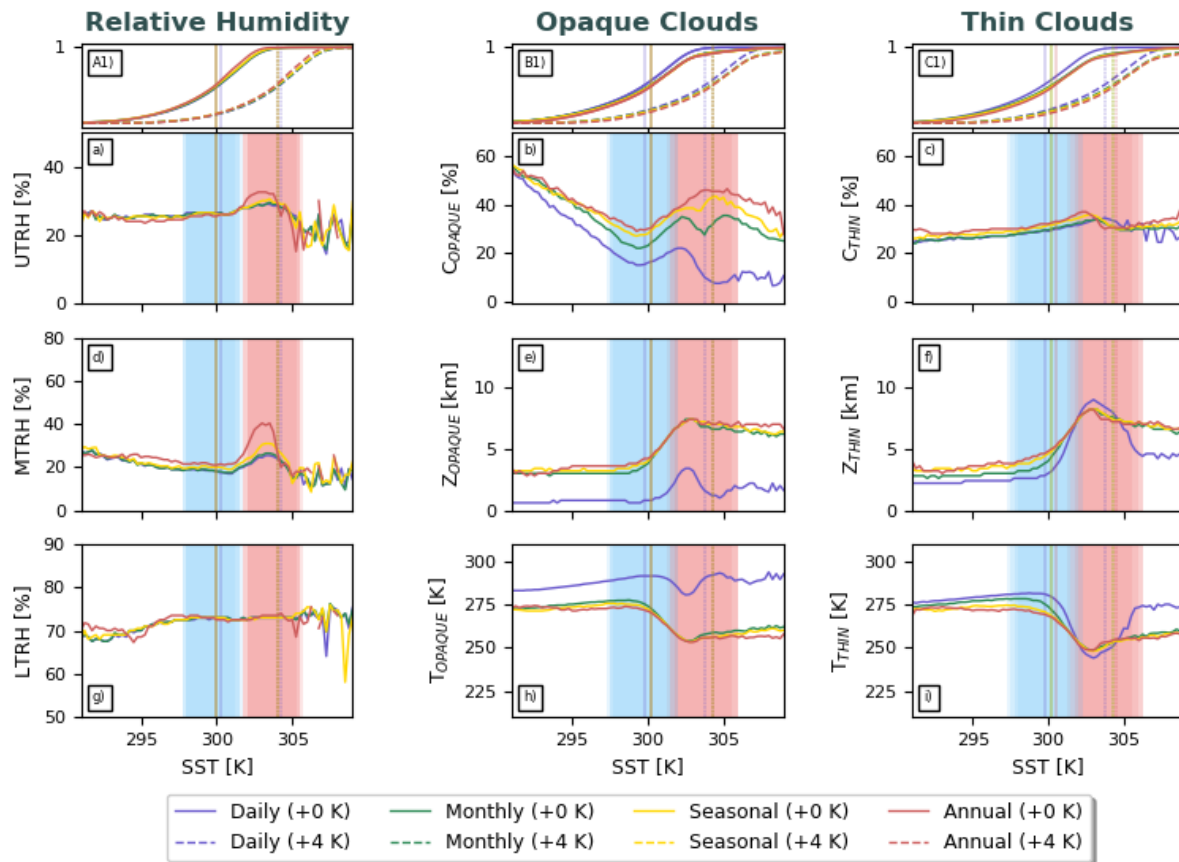


**FIGURE 4-14:** Change in RH and cloud characteristics with SST for grid box values on the (red) annual, (yellow) seasonal, (green) monthly, and (blue) daily timescale. a) upper-tropospheric RH, b) opaque cloud cover, c) thin cloud cover, d) middle-tropospheric RH, e) opaque cloud altitude, f) thin cloud altitude, g) lower-tropospheric RH, h) opaque cloud temperature, i) thin cloud temperature. Subplots A1, B1, C1 show the CDFs of SST for the current climate (solid lines) and +4 K climate scenario (dashed lines). Blue and pink shadings in subplots a-i show the interquartile range (25th to 75th percentile) of the SST distributions in the current and a +4 K climate scenario. Changes in RH with SST (left column) are computed over the years 2012-2018, whilst changes in cloud with SST (central and right columns) are computed over the years 2008-2019. The timescale curves are fitted to grid box value distributions computed by Method A as illustrated in Fig. 4-2 (left column).

The CDF is the integral of the probability density function (PDF). Effectively it gives the probability of obtaining an x-value (here: SST) lower than or equal to the present x-value. For the purpose of the discussion about Fig. 4-14, the CDF is a useful and illustrative alternative to the PDF, as it is easy to see the median x-value and visualize the range of its interquartile range (IQR).

Figure 4-14 shows that there is apparently no notable change in RH with SSTs > 305 K, as all levels of the RH profile seem to converge towards plateau values there. Thin clouds seem to follow similar changes with SST as MTRH and UTRH, which speaks for the covariation between the thin cloud and RH profiles observed by Chepfer et al. (2019). Opaque cloud cover (14b) continues to decrease with SST also for SSTs > 305 K. A slight decrease (increase) in opaque cloud altitude (temperature) with SST is also observed for SSTs > 305 K.

As the SST distribution is shifted +4 K, there will be a shift in the weight of the different regions and dynamical regimes, as indicated by the blue and pink shadings showing the IQR of the SST distributions in the current and a +4 K climate scenario. The weight of the colder SST range dominated by decreasing marine boundary layer cloud cover (SST  $\lesssim$  299 K) will diminish in favor of convective regions. This observation motivates the importance of better understanding of the tropical convective regions. For example, Chepfer et al.<sup>35</sup> (2014) found the shape of tropical opaque and thin cloud fraction profiles to stay the same, but rise by up to 1.7 km in an AMIP+4K scenario simulated by the HadGEM2-A model. Such evolutions of tropical mean cloud altitudes seem very plausible if convective regions become more dominant.

In the current climate, the IQR ranges from 297.25 to 301 K (median SST value: 299.75 K), and covers the transition region between subsidence and convective regions, whilst in the +4 K climate scenario, the IQR is shifted to range between 301.25 and 305 K (median SST value: 303.75 K), i.e. it covers the convective regions characterized by decreasing opaque ice cloud cover and free-tropospheric RH with SST.

As discussed in Fig. 4-3, opaque clouds change differently with SST on the annual, seasonal and monthly timescales compared to the daily: (4-14b), the cover is larger the longer the timescale, peaking twice on both the monthly and seasonal scales, (4-14e), the altitude is higher and decreases only slightly (about -1 km) from its peak notation, and (4-14h), the temperature is correspondingly lower and increases slightly (about +3 K) after its peak notation. The same observations can be made for thin cloud altitude and temperature (4-14f,i). Still, I would make the same argument as above (when discussing Fig. 4-3) that this is likely a result of the number of observations over which the timescale average grid box values are computed. For that reason, I will make two estimations of the change from the current tropical climate state to a +4 K tropical climate based on the dynamics observed over their respective IQR ranges on the (I) daily and (II) annual scale in Fig. 4-14:

#### **I) Discussion of +4 K Warmer Tropical Climate Based on the Daily Scale Dynamics in Fig. 4-14**

On the daily scale, going from the variable means over the present-day SST IQR range (blue shading) to a +4 K IQR range (pink shading), the middle and upper troposphere moisten from 18.3 to 21.9 % RH and from 26.3 to 28.1 % RH respectively, whilst there is no change in LTRH (+0.1 %). Simultaneously, opaque clouds rise by +1.3 km (emission temperature drops by 3 K), but decrease in cover by -2.5 %. Thin clouds grow larger, as the cover increases by +2.7 % (comparable to the decrease in opaque cloud cover), and rise substantially from 2.9 to 7.8 km, with a corresponding drop in temperature from 280.0 to 252.2 K.

Taken together, these observations suggest that as the tropical SSTs warm uniformly by 4 K, slightly more OLR could be emitted due to decreasing opaque cloud cover (-2.5 %). This potential increase in OLR should however be off-set by simultaneously more SW absorption, increasing thin cloud cover (+2.7 %) and free-tropospheric RH (+2 to 3 %). In addition, the lower emission temperatures (opaque: -3 K, thin: -27.8 K) due to rising cloud altitudes (opaque: +1.3 km, thin: +4.9 km), suggest a decrease in OLR that could not be compensated

---

<sup>35</sup> Chepfer et al. (2014): HadGEM2-A model, COSP/lidar, 1 year (2008)

for by a small decrease in opaque cloud cover. My conclusion is thus an accumulation of energy in the tropics when surface emissions corresponding to +4 K warmer surface temperatures cannot be radiated away at a comparable rate - indicative of a super-greenhouse scenario (Focus Box 2, Ch. 1). This conclusion is however based on the unrealistic assumption of the tropical belt as an isolated system and thus ignores heat exchanges between the tropics and extra-tropics.

## **II) Discussion of +4 K Warmer Tropical Climate Based on Annual Scale Dynamics in Fig. 4-14**

On the annual scale, going from the variable means over the present-day SST IQR range (blue shading) to a +4 K IQR range (pink shading), the middle and upper troposphere moisten roughly twice as much as on the daily scale (MTRH: from 21.7 to 29.6 %, UTRH: from 25.5 to 29.4 %), with no change at all in LTRH. Simultaneously, opaque clouds rise by +2.9 km (emission temperature drops by  $-6.5$  K), and their cover increases by +10.2 %. Thin cloud cover increases by +2 %, and altitudes rise by +2.9 km, with temperatures dropping  $-16.4$  K.

Taken together, these observations suggest a noteworthy increase in opacity as MTRH and UTRH increase by 8 and 4 %, respectively. In addition, increasing cloud cover and dropping emission temperatures will lead to even less OLR. Increasing opaque ice cloud cover (+10.2 %) results in both less OLR and SW absorption in these scenes. I do however not expect the cooling effect of the latter to be able to fully compensate for the decreasing OLR due to increasing free-tropospheric RH and rising cloud altitudes. Hence, my conclusion must be the same as for the daily scale above.

### 4.5 Summary and Conclusions

In this study, we analyze the covariations of RH (SAPHIR) and cloud characteristics (CALIPSO) with tropical SST (ERA5) on annual, seasonal, monthly and daily timescales, as well as on both the process-oriented grid box scale and in rates of changes of global values. The work is motivated by these terms being associated with the most uncertainty in the feedback equation.

The results on the grid box scale show similar nonlinear dynamics in the changes of the RH profile and cloud characteristics with SST on all timescales. This result implies that these statistical relationships are robust with respect to timescale and effectively that the dynamical changes of the RH profile and cloud characteristics and SST, can be studied on all timescales.

On the grid box scale, I observe the following dynamical changes of the tropical atmospheric water cycle with SST: For SSTs  $< 299$  K, RH decreases with SST in the middle troposphere, as does the opaque liquid cloud cover. By the onset of deep convection (around 299 K), there is a pick-up in RH in the middle and upper troposphere that likely fuels deep convection, causing cloud altitudes to rise and ice cloud cover to increase with SST until their peaks around SST = 302 K. For SSTs  $> 302$  K, RH decreases again in the middle and upper troposphere with further warming, as does the opaque ice cloud cover, whilst opaque cloud altitudes and temperatures settle at plateau values close to their peak values.

On the global scale, the sign of significant rates of change of RH with SST are not always robust across timescales, but they seem largely negative in the lower and middle troposphere (about  $-2$  and  $-0.1$  %  $K^{-1}$ , respectively). UTRH increases with SST (up to  $+2$  %  $K^{-1}$ ), but these regressions are nonsignificant. In contrast, the signs of the rates of change for cloud variables with SST are more robust across timescales, and their signs are consistent with the overall changes with SST observed on the grid box scale. For rates of changes of thin clouds with SST, all cloud variables (cover, altitude, temperature) are robust in both sign and magnitude on all timescales ( $+1.4$  %  $K^{-1}$ ,  $+0.5$  km  $K^{-1}$  and  $-6$  to  $-14$  K  $K^{-1}$ , respectively). Opaque cloud cover decreases with SST by  $-6$  to  $-10$  %  $K^{-1}$  on the annual, seasonal and monthly scales and positive rates of changes are observed for both opaque cloud altitude and temperature (about  $+0.5$  to  $+0.8$  km  $K^{-1}$  and  $+1.4$  to  $+3$  K  $K^{-1}$ , respectively). The reason for the positive sign in both opaque cloud altitude and temperature with SST is derived to rising cloud altitudes in deep convective clouds (about  $+0.5$  km  $K^{-1}$ ) whilst little change in low liquid clouds, and a warming of the low liquid clouds with SST (about  $+1$  to  $+2$  K  $K^{-1}$ ) that are more abundant than the high ice clouds (for which there are no notable significant changes).

The cover of opaque liquid clouds ( $Z_{OPAQUE} < 3$  km) decreases with SST at similar rates on all timescales in both the grid box values for SSTs  $< 299$  K ( $-3$  to  $-5$  %  $K^{-1}$ , which is compared to  $-4$  to  $-8$  %  $K^{-1}$  on the instantaneous timescale in the previous chapter), and in the rates of changes computed from the global values ( $-2$  to  $-5$  %  $K^{-1}$ ). That the signs and magnitudes of these rates of change are consistent both across timescales and between grid box and global values is a useful result that should help to constrain the rate of change of marine boundary layer clouds with SST.

There is evidence for the iris hypothesis in our results: On the grid box scale, marine boundary layer cloud cover decreases with SST, which leads to greater clear-sky cover in the subsidence regions. And, over the warmest SSTs (SST  $> 303$  K), opaque ice cloud cover decreases, as does RH in the middle and upper troposphere. In the global values, there are significant negative rates of change of opaque ice cloud cover with SST on all timescales ( $-7$  %  $K^{-1}$  on longer whilst  $-2$  %  $K^{-1}$  on shorter).

There is evidence for the FAT hypothesis in the rates of changes computed from the global values in the subsampled dataset centered around the coldest ice clouds over the warmest waters ( $T < 240$  K and SST  $> 299$  K), where opaque cloud altitudes rise by  $+0.5$  km  $K^{-1}$ , whilst there is no apparent change in their emission temperatures. In the grid box values however, cloud altitudes increase and temperatures decrease seemingly linearly with SST (Opaque:  $+0.13$  km  $K^{-1}$  and  $-0.7$  K  $K^{-1}$ ; Thin:  $+0.21$  km  $K^{-1}$  and  $-1.15$  K  $K^{-1}$ ), without any apparent support for the FAT hypothesis, as when these cloud temperatures are plotted with altitudes, they are observed to decrease linearly with altitudes ( $-6.5$  K  $km^{-1}$ ).

I end this study by a discussion of a warmer tropical state as a result of a uniform increase in SST by  $+4$  K (following the AMIP+4K scenario). In my idealized scenario that unrealistically assumes absence of heat transport into or out of the tropics (!), the tropics would move towards a super-greenhouse state, where increasingly more OLR is emitted at the surface than can be radiated away by the atmosphere due to a general increase in opacity (greater free-tropospheric RH) and colder cloud emission temperatures.

When individual rates of changes computed for some specific timescale and pair of variables are compared to previously reported values, the sign is most often consistent, but magnitudes may vary, which is likely partly explained by differences in the considered study region, time period, or precise definition of water cycle variable diagnostics.

This work however studies observed rates of changes of the same pair of variables across timescales, and may as such very well be one of the first observational studies of this kind. Although we find significant rates of changes with SST to often be of the same sign, as well as of comparable magnitude, for all timescales, the linear regressions rarely show a general tendency of gradually increasing or decreasing magnitudes going from the daily to annual timescales. The fact that magnitudes of significant rates of changes vary between timescales leads to the conclusion that feedback factors cannot be assumed to be timescale-invariant.



## Conclusions and Perspectives

In this chapter, I summarize the main conclusions drawn from the answers to the principal science questions asked in my PhD thesis, as well as future outlooks and perspectives building on these answers. The objective of this thesis was to better our understanding of the processes linking water vapor, clouds, precipitation and surface temperature in the tropics. The study is motivated by the covariation of the water cycle variables with surface warming being associated with the most uncertainty in the climate feedback mechanisms. Previous observational work typically did not observe the detailed vertical structure of the tropical atmospheric water cycle and the covariations between its principal variables, or if they did, they under sampled the tropical region and therefore missed the large-scale context. In this work I simultaneously study the relative humidity (RH) profile, cloud characteristics and near-surface precipitation, and their variations with sea surface temperature (SST). I build a collocated observational dataset of these variables retrieved from satellite instruments of high vertical resolution (SAPHIR, CALIOP, CPR, described in Ch. 2).

During this work, I have addressed several science questions. The principal two are restated here and their main results summarized below:

### ***Question 1: How Do RH and Cloud Characteristics Vary with SST on the Instantaneous Grid Box Scale, Under the Influence of the Large-Scale Circulation, and in the Absence or Presence of Near-Surface Precipitation?***

In Ch. 3 I study simultaneous variations of the RH profile and cloud cover with SST on the instantaneous grid box scale and under the influence of the large-scale atmospheric circulation. Clouds are separated by phase, opacity and the presence of near-surface precipitation. The instantaneous variations of water cycle variables with SST are observed to be robust to natural variability.

Distinctively different characteristics are observed for the ascending and descending large-scale regimes. Cloud cover decreases monotonically with SST in the descending regime, whilst the variations in the ascending and intermediate regimes are nonlinear and characterized by two transitions; a local minimum at  $SST = 299.25$  K, and a local maximum at  $SST = 301.75$  K, referred to here as the cold and warm SST thresholds respectively.

The descending regime is the most important regime for  $SSTs < 299.25$  K, and is characterized by a dry free troposphere and low clouds in the liquid phase in the absence of near-surface precipitation. The cover of thin liquid clouds is constant and insensitive to changes in SST, whilst opaque liquid cloud cover decreases with SST.

The ascending regime is characterized by high clouds in the ice phase and greater free tropospheric RH in the presence of near-surface precipitation. By the onset of deep convection ( $SST = 299.25$  K), RH increases with increasing SST in the lower free troposphere and peaks around the warm SST threshold. Over  $SSTs > 301.75$  K, opaque ice cloud cover decreases with SST, but the decrease is compensated for by increasing thin ice cloud cover.

Three observations are made to hold for all regimes: (i) the total cloud cover decreases with SST over SSTs  $> 301.75$  K, (ii) opaque cloud cover is observed to always be larger in the presence of near-surface precipitation, and (iii) the precipitation cover (i.e. the horizontal extent of near-surface precipitation) within a grid box decreases with warming and the magnitude of the decrease increases with warming.

That the decrease in opaque ice cloud cover is compensated for by increasing thin ice cloud cover, and not by increased precipitation cover, has implications for the iris hypothesis. The theory surrounding the iris hypothesis says that the increase in OLR due to smaller convective anvils is radiatively balanced by an increase in latent heat release due to greater precipitation efficiency. In Ch. 3 however, we observed that the precipitation cover decreases with SST and that the magnitude of the decrease increases moving through the cold, moderate and warm SST ranges.

### **Question 2: How Do RH and Cloud Characteristics Covary with SST on Different Temporal and Spatial Scales?**

The first question (Question 1) was restricted to one temporal scale and one spatial scale. This question assesses the dependence of the water cycle variables' covariations and responses to surface warming on the choice of temporal and spatial scale by observing them on four different timescales (daily, monthly, seasonal, annual), as well as in both global values (computed over oceanic grid boxes between  $30^{\circ}$ N to  $30^{\circ}$ S) and more process-oriented grid box values.

On the grid box scale, I observe similar dynamical changes of the tropical atmospheric water cycle with SST on all timescales and consistent with those observed on the instantaneous timescale (Question 1). For SSTs  $< 299$  K, RH decreases with SST in the middle troposphere, as does the opaque liquid cloud cover. By the onset of deep convection (around 299 K), there is a pick-up in RH in the middle and upper troposphere that fuels deep convection, causing cloud altitudes to rise and ice cloud cover to increase with SST. For SSTs  $> 302$  K, RH decreases again in the middle and upper troposphere with further warming, as does the opaque ice cloud cover, whilst opaque cloud altitudes and temperatures settle at plateau values close to their peak values.

On the global scale, the sign of the rates of change of RH with SST are largely negative in the lower and middle troposphere, whilst positive in the upper troposphere. However, these regressions vary somewhat in sign across timescales and are predominantly nonsignificant in the middle and upper troposphere. In contrast, the signs of the rates of change for cloud variables with SST are more robust across timescales, and their signs are consistent with the overall changes with SST observed on the grid box scale. For rates of changes of thin clouds with SST, all cloud variables (cover, altitude, temperature) are robust in both sign and magnitude on all timescales. Opaque cloud cover decreases with SST on the annual, seasonal and monthly scales and positive rates of changes are observed for both opaque cloud altitude and temperature. The reason for the positive sign in both opaque cloud altitude and temperature with SST is derived to rising cloud altitudes in deep convective clouds whilst little change in low liquid clouds, and a warming of the low liquid clouds with SST that are more abundant than the high ice clouds (for which there are no notable significant changes).

The change in low opaque cloud cover with SST is central to the SW cloud feedback. It is found that the cover of opaque liquid clouds decreases with SST at similar rates on all timescales in both the global and grid box values ( $-3$  to  $-5$  %  $K^{-1}$ ). That the signs and magnitudes of the rates of changes computed for opaque liquid clouds with SST are consistent both across timescales and between grid box and global values is a useful result for constraining the rate of change of marine boundary layer clouds with SST.

Over SSTs  $> 299$  K, the opaque ice cloud cover decreases with SST on all timescales, and magnitudes of rates of change computed from both global and grid box values are within the same range. The sign of this change is consistent with the instantaneous scale (Question 1) and confirms that opaque ice cloud cover does in fact decrease with SST over the warmest waters – regardless of temporal or spatial scale considered here.

On the grid box scale, ice cloud altitudes increase and temperatures decrease seemingly linearly with SST, and both opaque and thin ice cloud temperatures are observed to decrease linearly with altitudes. From these observations, I see no clear evidence for the FAT hypothesis on the grid box scale. There is however evidence for the FAT in the rates of changes computed from the global values, where opaque ice cloud altitudes rise on all timescales, whilst there is no consistent change in temperature, as the sign varies across the timescales and half of them are nonsignificant. As discussed in Ch. 4, previous work typically assessed the FAT hypothesis in long-term, spatially global values, and the non-significant trends in ice cloud temperature with SST computed from global values in this study could be suggestive of the absence of a trend. A considerably longer observational record than the 12 years employed in this study, is however required to be confident in this conclusion.

## Perspectives

At the end of my thesis, I feel that this work has contributed to our understanding of the tropical atmospheric water cycle's response to surface warming, by establishing physical relationships between water vapor, clouds, precipitation and sea surface temperature. There is a lot of potential in the collocated observational dataset of high vertical resolution of water cycle variables that I employed in my work. As discussed, it needs to be allowed to operate for a longer time to have more robust statistics to draw conclusions from, but there is also room to include additional variables (e.g. other precipitation characteristics and radiative fluxes), as well as observations over land and during nighttime. Thus, there are some unanswered questions that I think would be most interesting to pursue in the future. These topics are outlined in this last section.

The observation that the decrease in opaque ice cloud cover is compensated for by increasing thin ice cloud cover and not by increased precipitation contrasts the theory surrounding the iris hypothesis, although it must be emphasized that we did not observe the same precipitation variable (iris: efficiency; here: cover). Hence, if the iris hypothesis is right to expect greater precipitation efficiency with warming, the greater precipitation rate could be a result of a narrowing of the precipitation area with warming, which is what I observe in Ch. 3. In my work I wanted to be able to distinguish between precipitating and non-precipitating cloudy objects at the near-surface level, for which task the CPR onboard CloudSat excels. Answering this question of how the precipitation rate changes with SST would however require

an instrument that could measure intense rain rates as well, which is a problem for the CPR signal that becomes completely attenuated in heavily precipitating situations. Thus, how the precipitation rate changes with SST is a question that I never got around to answer, but a question which I nevertheless find very interesting to pursue in the future. For this purpose, observations made by the 13.8 GHz precipitation radar (PR) carried by the Tropical Rainfall Measuring Mission (TRMM) satellite could serve as a useful complement to CloudSat where its signal is attenuated by heavy precipitation. The near-surface precipitation level of PR is at a slightly higher but comparable altitude than CloudSat's (0.5 to 2 km, depending on surface terrain, Liu and Zipser 2014), and the synergy between the two radars is welcome as noted by Haynes et al. (2009). However, TRMM stopped collecting data on April 15, 2015, so inclusion of TRMM observations to the MTCC dataset employed here would only be possible from October 2012 (launch of Megha-Tropiques) to April 2015, and thus only yield 2.5 years of collocated observations. A second complement to consider could be the newly released Frequent Rainfall Observations on GridS (FROGS, Roca et al. 2019) dataset. It consists of  $1^\circ \times 1^\circ$  gridded daily precipitation retrieved from satellite observations, ground-based observations and reanalysis up until 2017. It could be a useful complement to CloudSat observations, but being available as daily values it lacks the instantaneous observation. Any complementary dataset to aid CloudSat observations would however first require a comparison of their retrievals to robustly establish their similarities, strengths, weaknesses and complementary abilities.

In Ch. 3 and Ch. 4 I discuss the impacts on the net radiative flux at the top of the atmosphere (TOA) that I expect from the observed changes in RH and clouds with SST. What this discussion is missing is however a conclusive observational tool of the TOA radiative fluxes. The ambition was to add instantaneous observations of the SW and LW radiative fluxes at TOA, measured for example by the CERES instrument onboard NASA's Aqua satellite, but including radiation will have to be a future step. The Aqua satellite flies as part of the A-train constellation, and as such, it flew in formation with CALIPSO and CloudSat prior to the formation of the C-train. Its observations before February 2018 are thus collocated by design with CALIPSO and CloudSat, which means that CERES observations could easily be added to the collocated dataset.

The dataset employed here only considers daytime (01:30 pm LT) observations, meaning that the statistics derived from it cannot be taken as representative of other times of the day. This particular time of the day is in between the times of peak cloud occurrence in the early morning hours and late afternoon and coincides with a daily minimum of free-tropospheric RH (Chepfer et al. 2019). Including observations at 01:30 am would not make an observational dataset of the diurnal cycle, but at least it would add nighttime statistics to the discussions. To build statistics over the diurnal cycle, it would be better to employ a collocated observational dataset between e.g. Megha-Tropiques (RH and TOA radiative fluxes) and the CATS lidar (cloud characteristics) as in Chepfer et al. 2019, or between Megha-Tropiques and a suite of geostationary satellites as in Brogniez and Kirstetter (2020).

Additionally, my studies are performed over fully oceanic grid boxes only. This is not due to lack of data over land, as the collocated satellite dataset includes them too. Rather I wanted to first establish observed physical relationships of the tropical atmospheric water cycle over a homogeneous surface. Then, subsequently, I want to include land surfaces to account for the full tropical belt, as well as study land-ocean contrasts and interactions. It is well-understood

from model studies that the formation and dissipation of convective clouds over land are thermodynamic results of the strong diurnal cycle of surface temperature. Recent observational studies (e.g. Bouniol et al. 2016, Chepfer et al. 2019) have established useful satellite-based characteristics of the diurnal cycle of water vapor, clouds, precipitation and radiation, but their temporal record is still short. We are thus lacking robust satellite-based climatologies over land, derived from simultaneous observations of both the low and free troposphere.

To quantify how characteristics of water vapor, clouds and precipitation covary under the influence of surface warming, and understand why they change the way they do, we need a long record of observations with high resolution. In the end, the observational record of 12 years (2008 to 2019) that I employed in Ch. 4, was not enough to detect significant trends on the annual scale. Even longer records of these highly resolved observations are thus needed to detect trends on the annual scale and to make long-term climate predictions. Fortunately, the satellites employed here are still in operation, i.e. the record continues to grow. A promising future launch that can add to this observational is the EarthCARE<sup>36</sup> (Earth Clouds, Aerosols, and Radiation Explorer, Lefebvre et al. 2017) mission, whose launch is planned for 2021. Its science objectives are similar to CALIPSO and CloudSat; namely to investigate the interactions between aerosols, cloud characteristics, precipitation and radiation. It will carry both an atmospheric lidar (355 nm) to observe vertical profiles of aerosols and thin clouds, as well as a cloud profiling radar like the one carried by CloudSat (94 GHz) to profile the vertical structure of clouds. Additional instruments to be carried by EarthCARE are a multi-spectral imager to observe clouds and aerosols in visible, near-infrared, shortwave and thermal infrared channels, and a broadband radiometer to observe TOA radiative fluxes in one SW and one LW channel.

---

<sup>36</sup> More information about the EarthCARE mission can be found here (last accessed September 10, 2020): <https://earth.esa.int/web/guest/missions/esa-future-missions/earthcare>



# Appendices

Appendices .....	135
A Basic Radiative Transfer Equations .....	136
B Supporting Data Information .....	138
Cloud Detection by the OPAQ Algorithm.....	138
Comparing Precipitation Detection by the CPR and TRMM .....	139
C Supplementary Figures of Höjgård-Olsen et al. (2020).....	140
Cloud-Weighted Cloud Cover Evolutions.....	140
Evolutions of Cloud Cover and Relative Humidity .....	141
Descending Regime.....	141
Intermediate Regime .....	142
Ascending Regime .....	143
Changes in Cloud Cover and Relative Humidity when SST Warms 1 K in the Intermediate Regime .....	144
Differences: El Niño vs. Full Time Period .....	145
Descending Regime.....	145
Intermediate Regime .....	146
Ascending Regime .....	147
Interquartile Ranges of Cloud Cover and Relative Humidity.....	148
Descending Regime.....	148
Intermediate Regime .....	149
Ascending Regime .....	150
Timeseries of Tropical Monthly Mean Cloud Cover .....	151
Heavily Precipitating Grid Boxes vs. Non-Precipitating: Ascending Regime .....	152
Opaque Ice Cloud Grid Boxes in the Ascending Regime .....	153
Figure 7 in Cesana and Chepfer (2013).....	154
D Supplementary Figures of Chapter 4.....	155
Change in Thin Cloud Altitude with SST: Method B .....	155
Change in Relative Humidity and Cloud Characteristics with SST for Grid Box Values: Method B.....	156
Change in Cloud Characteristics for Grid Box Values: Method B .....	157
Change in Opaque Cloud Altitude with Cover on the Grid Box Scale .....	158
E Résumé de thèse en français .....	159

## A Basic Radiative Transfer Equations

This appendix contains some of the most fundamental relationships and equations of radiative transfer. These are relevant for understanding the physical theory surrounding my work, but seeing as they are neither new information, nor equations that I have used in my work, I have collected them here in the appendix. I have consulted Wallace and Hobbs 2006 and Seinfeld and Pandis 2006 when I wrote these equations and their formulations.

Blackbodies are materials that absorb and emit all radiation. The monochromatic intensity of radiation emitted from a blackbody  $B_\lambda$  emitted at temperature  $T$  is given by the *Planck function*:

$$B_\lambda(T) = \frac{c_1 \lambda^{-5}}{\pi(e^{c_2/\lambda T} - 1)} \quad (\text{EA-1})$$

where  $\lambda$  is the wavelength,  $c_1 = 3.74 \times 10^{-16} \text{ W m}^2$  and  $c_2 = 1.45 \times 10^{-2} \text{ m K}$ .

However, not all materials behave as black bodies. The monochromatic emissivity, absorptivity, reflectivity and transmissivity of a non-blackbody are the ratios of emitted, absorbed, reflected and transmitted monochromatic intensities with respect to the incident:

$$\begin{aligned} \varepsilon_\lambda &= \frac{I_\lambda(\text{emitted})}{B_\lambda(T)} & \alpha_\lambda &= \frac{I_\lambda(\text{absorbed})}{I_\lambda(\text{incident})} \\ R_\lambda &= \frac{I_\lambda(\text{reflected})}{I_\lambda(\text{incident})} & T_\lambda &= \frac{I_\lambda(\text{transmitted})}{I_\lambda(\text{incident})} \end{aligned} \quad (\text{EA-2})$$

As a beam of radiation passes through an atmospheric layer and encounters new molecules, its monochromatic intensity decreases by

$$dI_\lambda = -I_\lambda K_\lambda N \sigma ds \quad (\text{EA-3})$$

where  $K_\lambda$  is the scattering or absorption efficiency, and  $N$  the number of particles per unit volume  $\sigma ds$ . The *extinction coefficient* is the added effects of absorption and scattering on reducing the monochromatic intensity of the beam:

$$K_\lambda(\text{extinction}) = K_\lambda(\text{absorption}) + K_\lambda(\text{scattering}) \quad (\text{EA-4})$$

For spherical particles, these coefficients can be evaluated by the dimensionless size parameter  $x$ :

$$x = \frac{2\pi r}{\lambda} \quad (\text{EA-5})$$

When  $x \ll 1$  (*Rayleigh scattering*), the particles are ineffective at scattering the present wavelength radiation and it occurs in both the forward and backward directions. When  $x \gtrsim 1$ , the present wavelength radiation is primarily scattered in the forward direction.

The layer transmissivity also decreases with atmospheric depth as

$$T_\lambda = e^{-\tau_\lambda \sec \theta} \quad (\text{EA-6})$$

where,

$$\tau_\lambda = \int_z^\infty k_\lambda \rho r dz \quad (\text{EA-7})$$

Here,  $\rho$  is the density of the air,  $r$  the mass of absorbing gas per molecule and  $k_\lambda$  the mass absorption coefficient. Conservation of energy requires that the sum of the flux absorptivity, reflectivity and transmissivity of a layer equals unity:

$$\alpha_\lambda^f + R_\lambda^f + T_\lambda^f = 1 \quad (\text{EA-8})$$

When radiation passes through an isothermal layer, its monochromatic intensity exponentially approaches that of a black body of the same temperature as the layer. The intensity emitted to space is emitted from atmospheric levels near the level of unit optical depth. Where the optical depth is much less than 1, the emissivity is so small that emission is negligible, and where the optical depth is much greater than 1, the transmissivity of the overlying is so low that only a fraction of the intensity emitted from the present layer makes it out to space. This level of optical depth is a function of wavelength. Water vapor (the most abundant atmospheric greenhouse gas), is an efficient absorber of infrared radiation, and the level of unit optical depth for infrared radiation is around 300 hPa. Hence, this is the top of the layer where water vapor still exists in enough quantities for the atmosphere to be opaque to IR emissions.

Radiation interacts with matter through absorption, emission and scattering in discrete quanta *photons* of energy

$$E = h\tilde{\nu} \quad (\text{EA-9})$$

The internal energy of a gas molecule is the sum of its orbital, vibrational, rotational and translational energy levels

$$E = E_o + E_v + E_r + E_t \quad (\text{EA-10})$$

Each element has its own unique set of possible electron orbits, vibrational frequencies and rotational rates and each possible energy level is characterized by its unique combination of these energies. Orbital transitions correspond to absorption lines in the UV spectrum, vibrational transitions to the near-infrared and infrared and rotational transitions to lines in the infrared and microwave spectrum.

The *Clausius-Clapeyron equation* (below) describes how the saturation vapor pressure ( $e_s$ ) increases with temperature ( $T$ ):

$$\frac{1}{e_s} \frac{de_s}{dT} = \frac{L_v}{R_v T^2} \quad (\text{EA-11})$$

where  $L_v$  is the latent heat of vaporization ( $2.5 \times 10^6 \text{ J kg}^{-1}$ ) and  $R_v$  the gas constant for water vapor ( $461.5 \text{ J K}^{-1} \text{ kg}^{-1}$ ).

## B Supporting Data Information

### Cloud Detection by the OPAQ Algorithm

Cloud detection is done by the *OPAQ algorithm*. It is explained in detail in Guzman et al. (2017), but an illustration of how it distinguishes between clear-sky, thin and opaque cloud profiles is given in Fig. B-1 below.

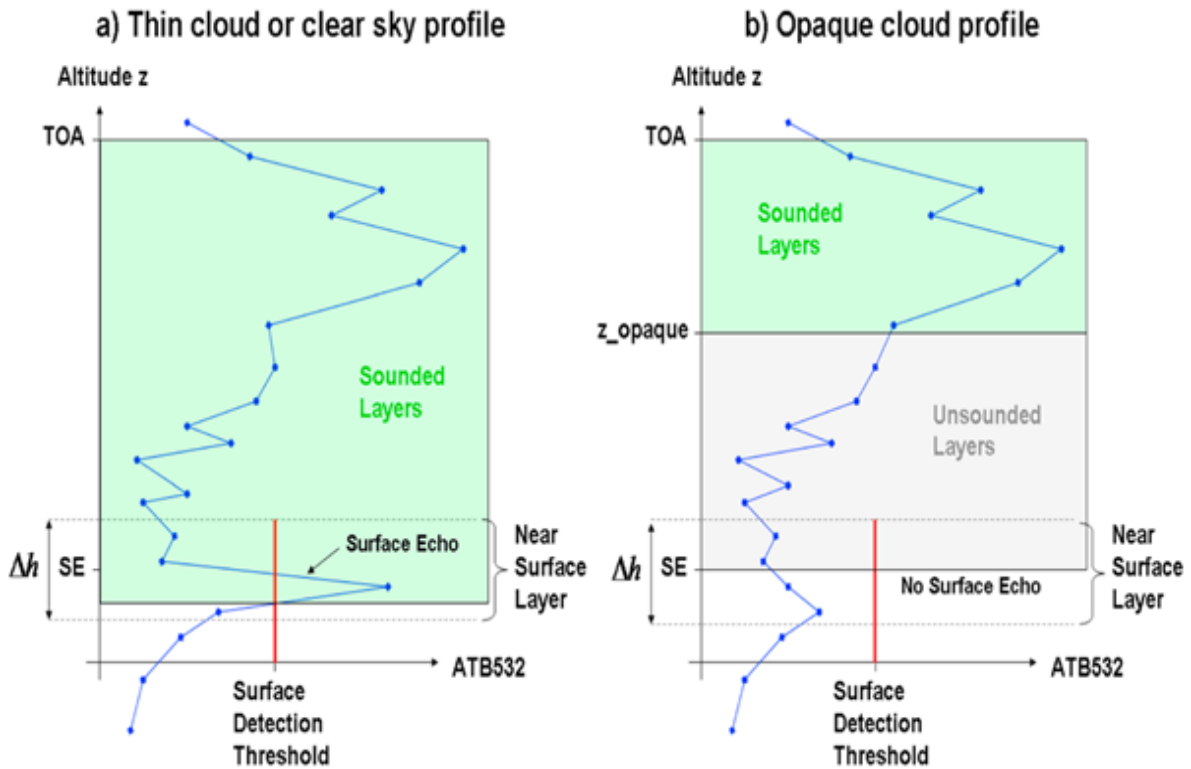
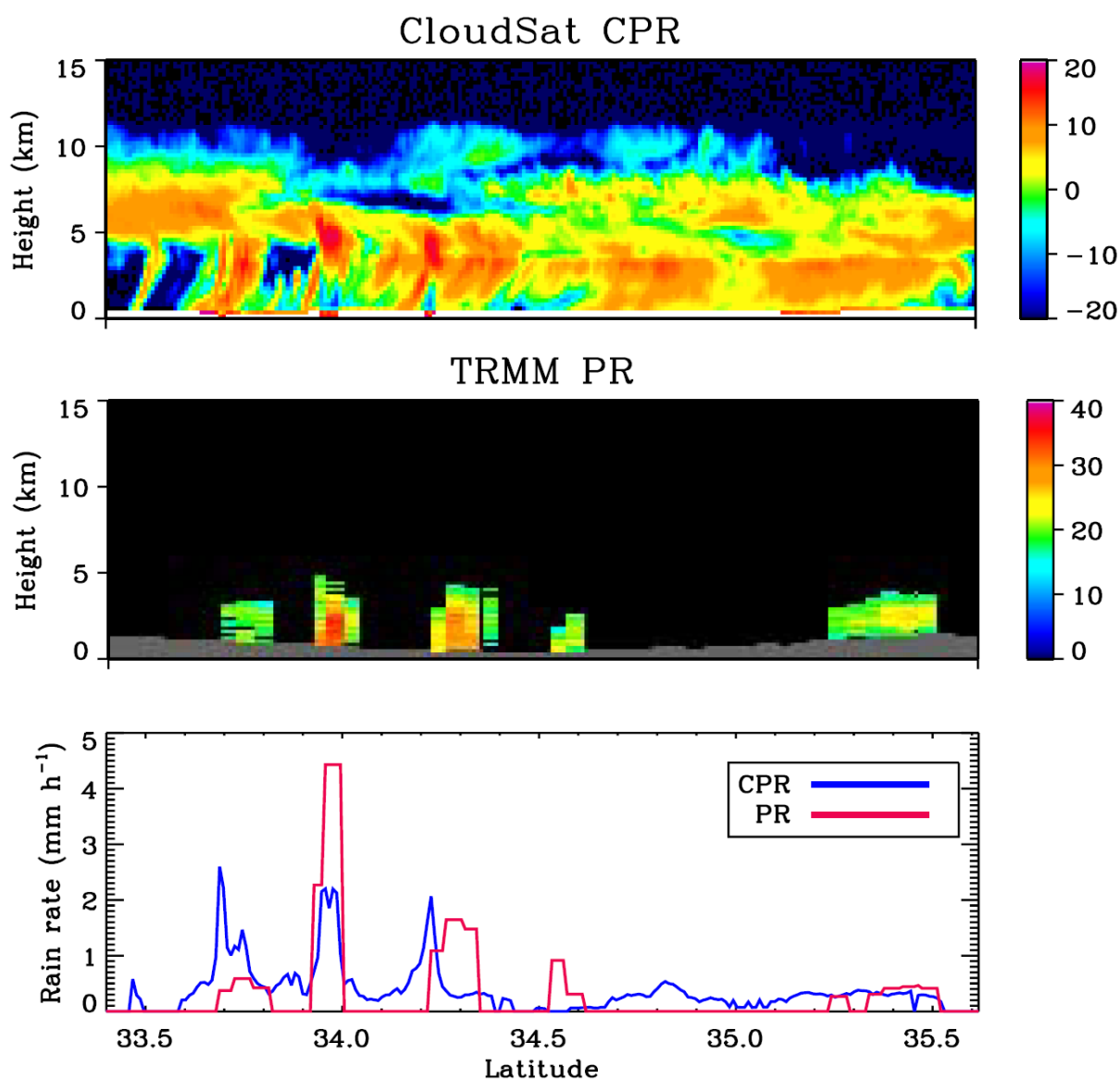


**FIGURE B-1:** Surface echo detection scheme: ATB surface detection threshold applied in a near-surface layer of thickness  $\Delta h$  with respect to the surface elevation (SE) for a) a thin cloud or clear-sky profile case where the surface is detected and b) an opaque cloud profile where the surface is not detected. The figure is extracted from Guzman et al. (2017).

The algorithm takes individual profiles of total attenuated backscatter from CALIOP and seeks a “surface echo” near the surface elevation (i.e. in the “Near Surface Layer” in Fig. B-1). A profile will have a surface echo if a fraction of the lidar pulse reached the surface before it was reflected to its source on the satellite telescope (the “echo”). A profile containing a thin cloud (visible optical depth  $< 3$  to  $5$ ) or no clouds at all (clear sky) will have a surface echo, as is illustrated by the surface echo spike in Fig. B-1a. In contrast, a profile containing an opaque cloud (visible optical depth  $> 3$  to  $5$ ) will not contain a surface echo (Fig. B-1b), for the lidar beam is completely scattered at some altitude before it reaches the surface. The *surface detection threshold* ( $SDT = 0.001 \text{ km}^{-1} \text{ sr}^{-1}$ , vertical red lines in Fig. B-1) represents the minimum ATB value that can be attributed to a surface echo and thus separates opaque cloud profiles ( $ATB < SDT$ ) from thin/clear-sky profiles ( $ATB > SDT$ ) (Guzman et al. 2017).

## Comparing Precipitation Detection by the CPR and TRMM

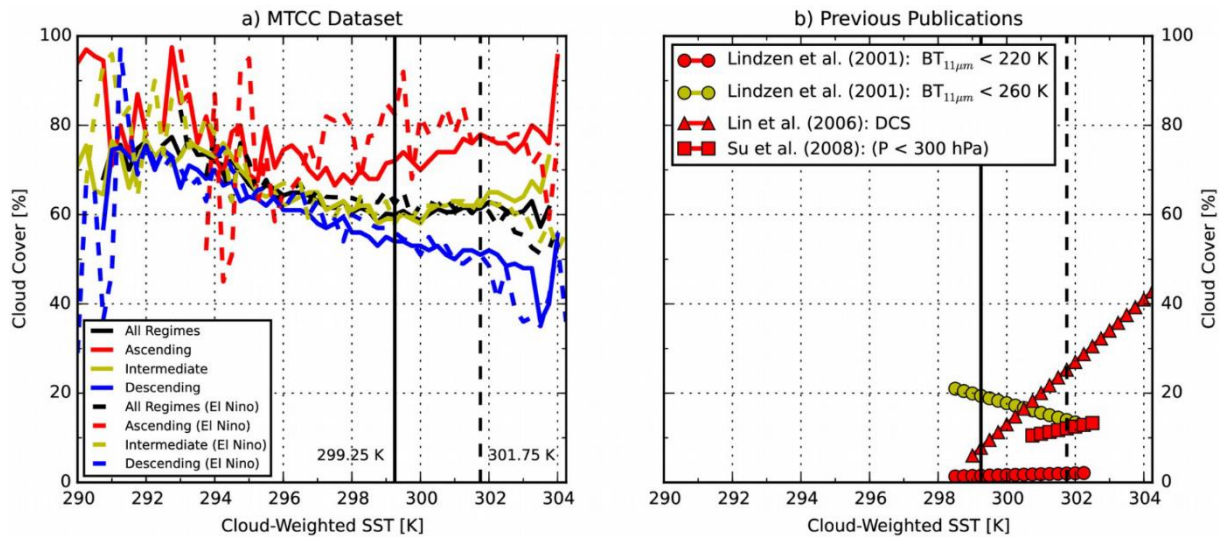
The high sensitivity of the CPR was illustrated in Haynes et al. (2009), who compared the CPR to the 13.8 GHz precipitation radar (PR) carried onboard Tropical Rainfall Measuring Mission (TRMM) satellite (Fig. B-2). They showed a higher sensitivity to low rain rates of CPR, particularly for rain rates less than  $2 \text{ mm hr}^{-1}$ . The higher sensitivity of the CPR is most noticeable in the latitudinal gaps between PR precipitation detection (the longest consecutive one being between  $34.7^\circ$  and  $35.2^\circ$ , middle and bottom figures), where the CPR observes light precipitation falling out of the bright band at around 4.5 km altitude (Haynes et al. 2009). The higher sensitivity of the CPR is to be expected as the CPR is sensitive to both clouds and precipitation, whilst the PR only targets precipitation.



**FIGURE B-2:** (top) CPR reflectivity (dBZ), (middle) PR reflectivity (dBZ), and (bottom) rain rate retrievals for a TRMM-CloudSat crossover on December 1, 2006. The figure is extracted from Haynes et al. (2009).

## C Supplementary Figures of Höjgård-Olsen et al. (2020)

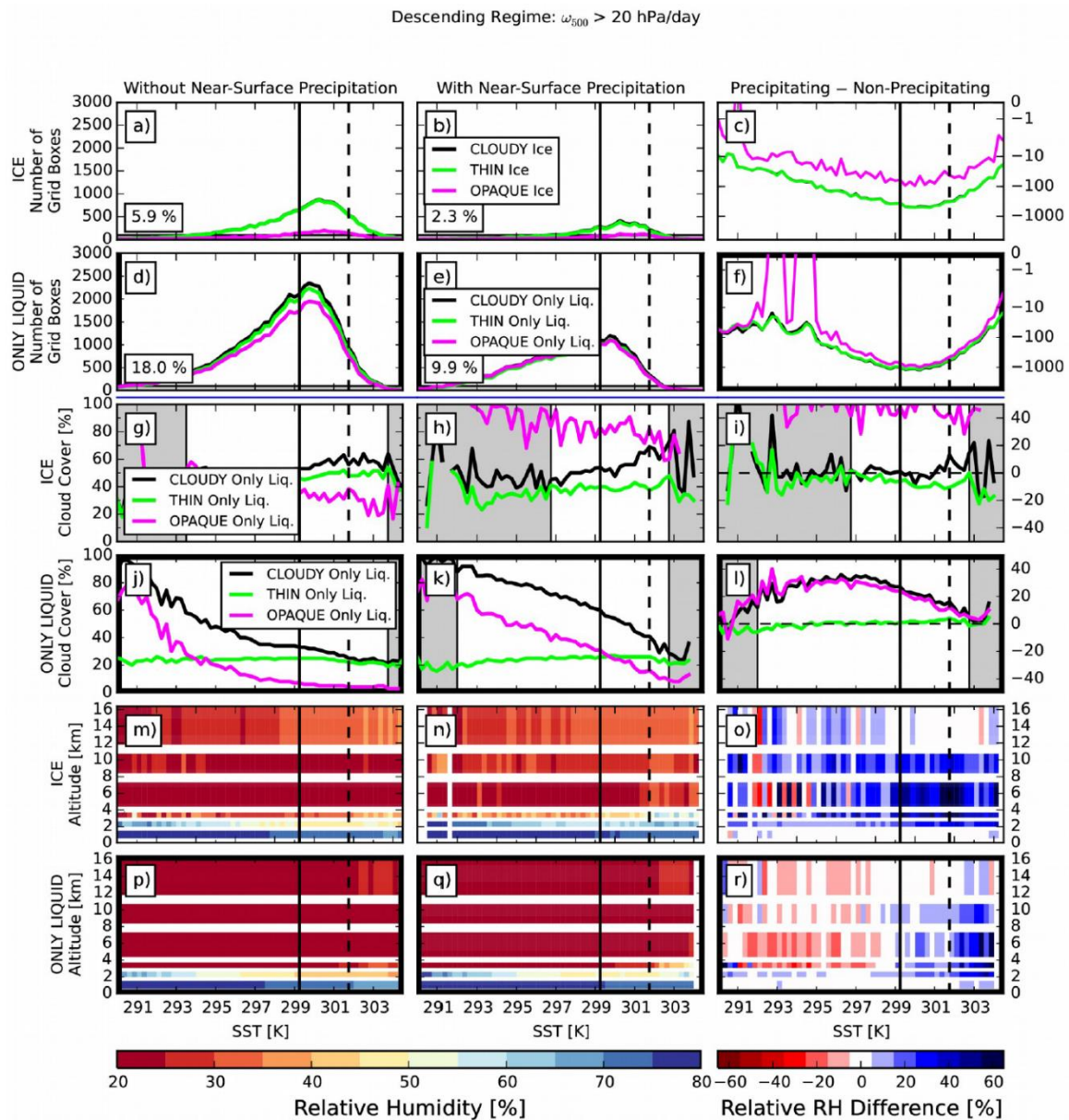
### Cloud-Weighted Cloud Cover Evolutions



**FIGURE C-1:** **a)** Cloud cover evolutions with cloud-weighted SST for the individual  $\omega_{500}$  regimes as well as without regime consideration (black). Solid lines are for the full period (May 2012 to April 2016) and dashed lines for the El Niño period (May 2015 to April 2016). **b)** Cloud cover evolutions with cloud-weighted SST in three previous publications. Colors indicate to which regime the authors of the present study deem these to belong. Vertical lines are the SST thresholds at 299.25 K (solid) and 301.75 K (dashed).

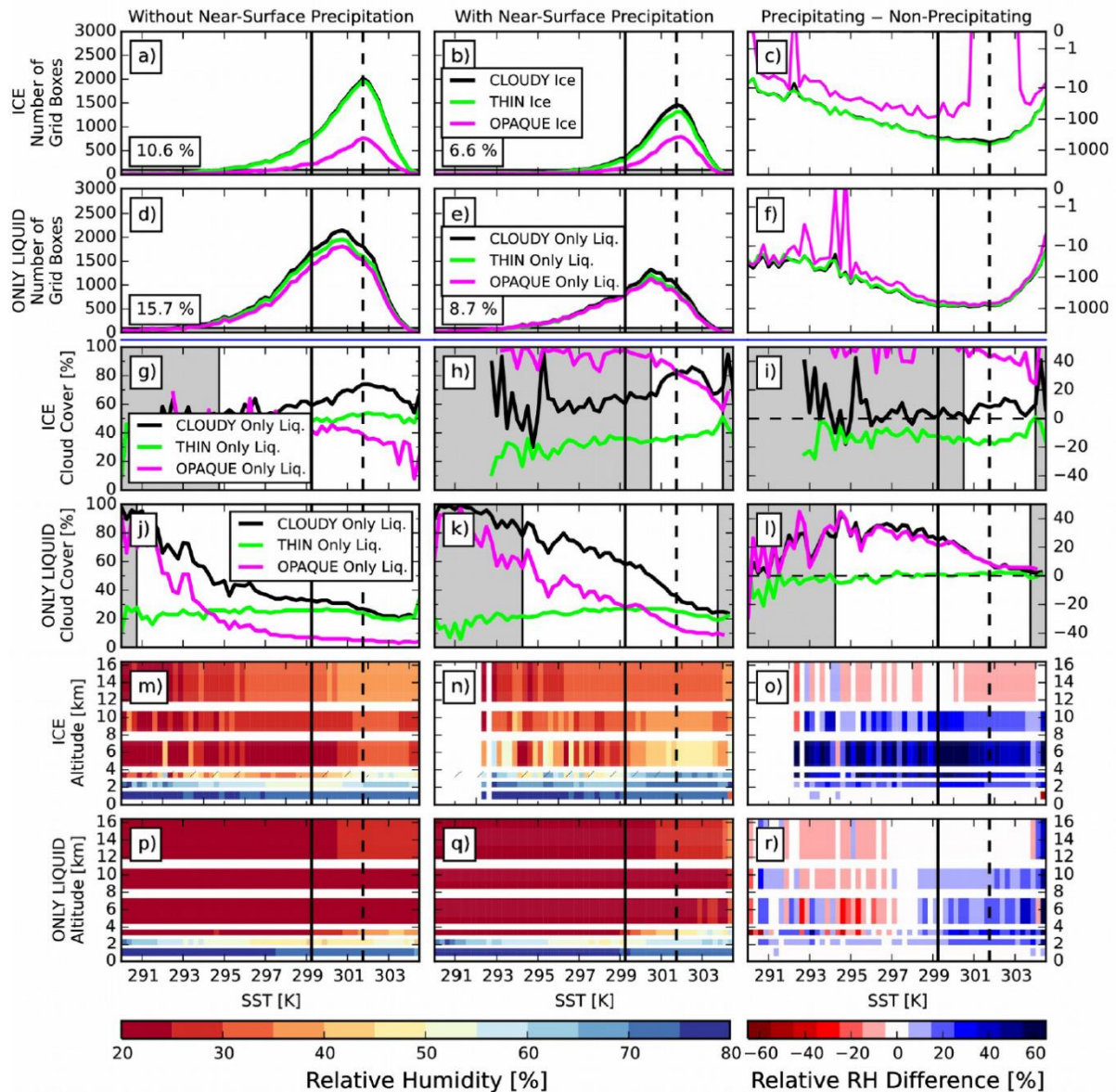
# Evolutions of Cloud Cover and Relative Humidity

## Descending Regime



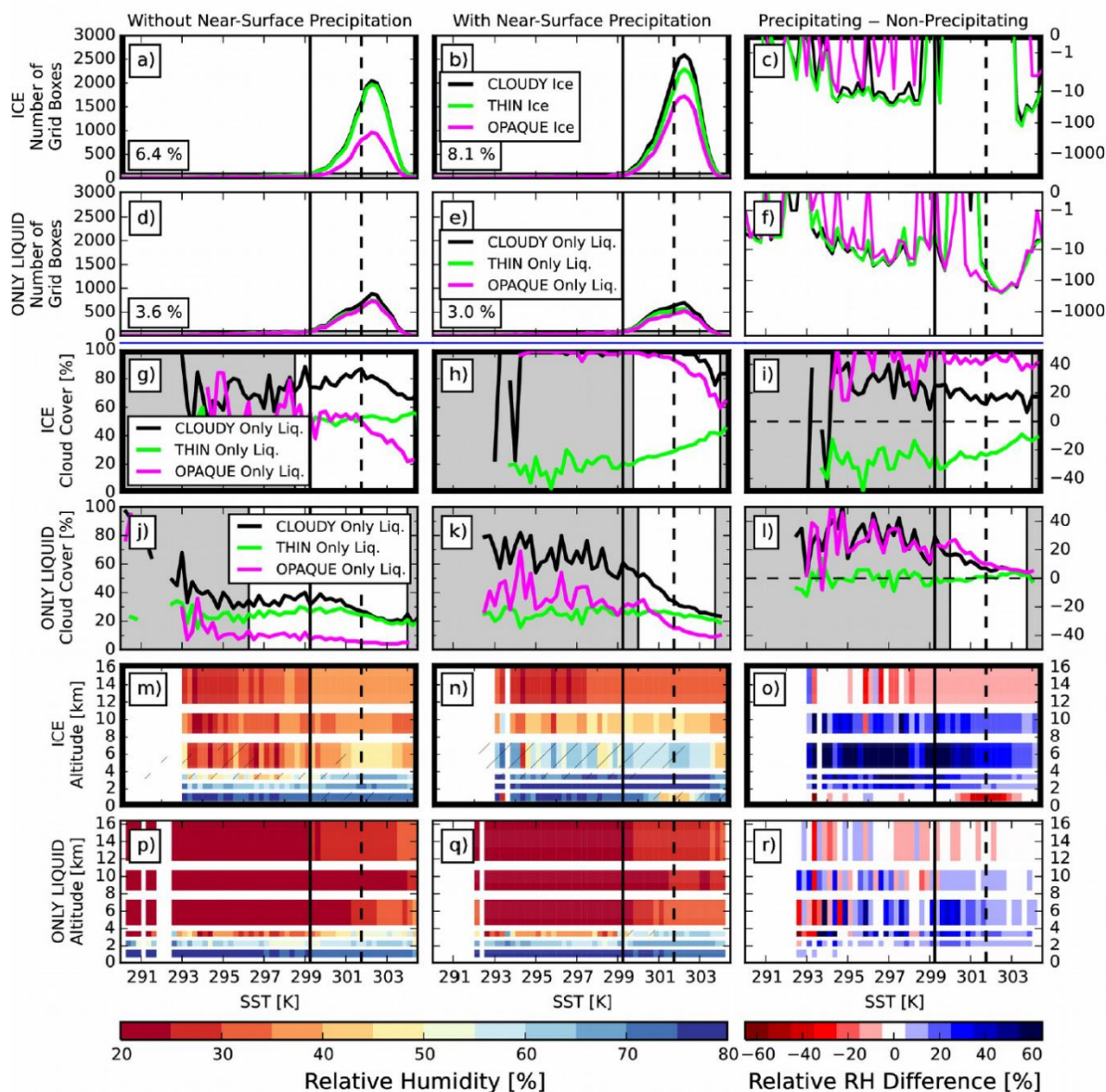
**FIGURE C-2:** Evolution of the observed cloud cover and relative humidity with SST for the descending regime:  $\omega_{500} > 20$  hPa/day. **Top two panels:** Occurrence of grid boxes containing ice (a – c) and liquid clouds (d – f) for non-precipitating and precipitating scenes, as well as their absolute difference. Notice the logarithmic y scale in subplots c and f. The percentages represent the contribution of that category to the entire MTCC data set. Grid boxes of clear-sky > 95 % in the descending regime represent 0.67 % of the data set. Shaded grey areas cover SST bins where the median cloud cover or RH value in the present category was calculated for less than 100 grid boxes. The blue horizontal line separates the number distributions from the evolution within a grid box. **Middle two panels:** Median thin and opaque ice (g – i) and liquid (j – l) cloud covers within non-precipitating and precipitating grid boxes, as well as their absolute difference. Note that addition of the green and magenta lines does not equal the black as both opaque and thin clouds are not present in each grid box (as evident from their differing number distributions). Shaded areas cover SST bins where the median cloud cover or RH value in the present category was calculated for less than 100 grid boxes. **Lower panels:** Median relative humidity profiles for grid boxes containing ice (m – o) and liquid (p – r) clouds for non-precipitating and precipitating scenes, as well as their relative difference. Vertical lines are for the same SST thresholds as identified in Figure 3-3. Subplots highlighted in black squares show dominating cloud phase in the descending regime.

## Intermediate Regime

Intermediate Regime:  $-20 < \omega_{500} < 20$  hPa/day

**FIGURE C-3:** Evolution of the observed cloud cover and relative humidity with SST for the intermediate regime:  $-20 < \omega_{500} < 20$  hPa/day. **Top two panels:** Occurrence of grid boxes containing ice (*a – c*) and liquid clouds (*d – f*) for nonprecipitating and precipitating scenes, as well as the absolute difference between these. Notice the logarithmic y scale in subplots *c* and *f*. The percentages represent the contribution of that category to the entire MTCC data set. Grid boxes of clear-sky  $> 95\%$  in the intermediate regime represent  $0.55\%$  of the data set. Shaded areas cover SST bins where the median cloud cover or RH value in the present category was calculated for less than 100 grid boxes. The blue horizontal line separates the number distributions from the evolution within a grid box. **Middle two panels:** Lines of median thin and opaque ice (*g – i*) and liquid (*j – l*) cloud covers for nonprecipitating and precipitating scenes, as well as their absolute difference. Note that addition of the green and magenta lines does not equal the black as both opaque and thin clouds are not present in each grid box (as evident from their differing number distributions). Shaded areas cover SST bins where the median cloud cover or RH value in the present category was calculated for less than 100 grid boxes. **Lower panels:** Median relative humidity profiles for grid boxes containing ice (*m – o*) and liquid (*p – r*) clouds for nonprecipitating and precipitating scenes, as well as their relative difference. Vertical lines are for the same SST thresholds as identified in Figure 3-3. Hatched areas cover SST bins where the interquartile range of RH is greater than  $35\%$  (Fig. C-10). Subplots highlighted in black squares show dominating cloud phase in the intermediate regime.

## Ascending Regime

Ascending Regime:  $\omega_{500} < -20$  hPa/day

**FIGURE C-4:** Evolution of the observed cloud cover and relative humidity with SST for the ascending regime:  $\omega_{500} < -20$  hPa/day. **Top two panels:** Occurrence of grid boxes containing ice (*a – c*) and liquid clouds (*d – f*) for non-precipitating and precipitating scenes, as well as the absolute difference between these. Notice the logarithmic y scale in subplots *c* and *f*. The percentages represent the contribution of that category to the entire MTCC data set. Grid boxes of clear-sky  $> 95\%$  in the ascending regime represent 0.13 % of the data set. Shaded areas cover SST bins where the median cloud cover or RH value in the present category was calculated for less than 100 grid boxes. The blue horizontal line separates the number distributions from the evolution within a grid box. **Middle two panels:** Lines of median thin and opaque ice (*g – i*) and liquid (*j – l*) cloud covers for non-precipitating and precipitating scenes, as well as their absolute difference. Note that addition of the green and magenta lines does not equal the black as both opaque and thin clouds are not present in each grid box (as evident from their differing number distributions). Shaded areas cover SST bins where the median cloud cover or RH value in the present category was calculated for less than 100 grid boxes. **Lower panels:** Median relative humidity profiles for grid boxes containing ice (*m – o*) and liquid (*p – r*) clouds for non-precipitating and precipitating scenes, as well as their relative difference. Vertical lines are for the same SST thresholds as identified in Figure 3-3. Hatched areas cover SST bins where the interquartile range of RH is greater than 35 % (Fig. C-11). Subplots highlighted in black squares show dominating cloud phase in the ascending regime.

### Changes in Cloud Cover and Relative Humidity when SST Warms 1 K in the Intermediate Regime

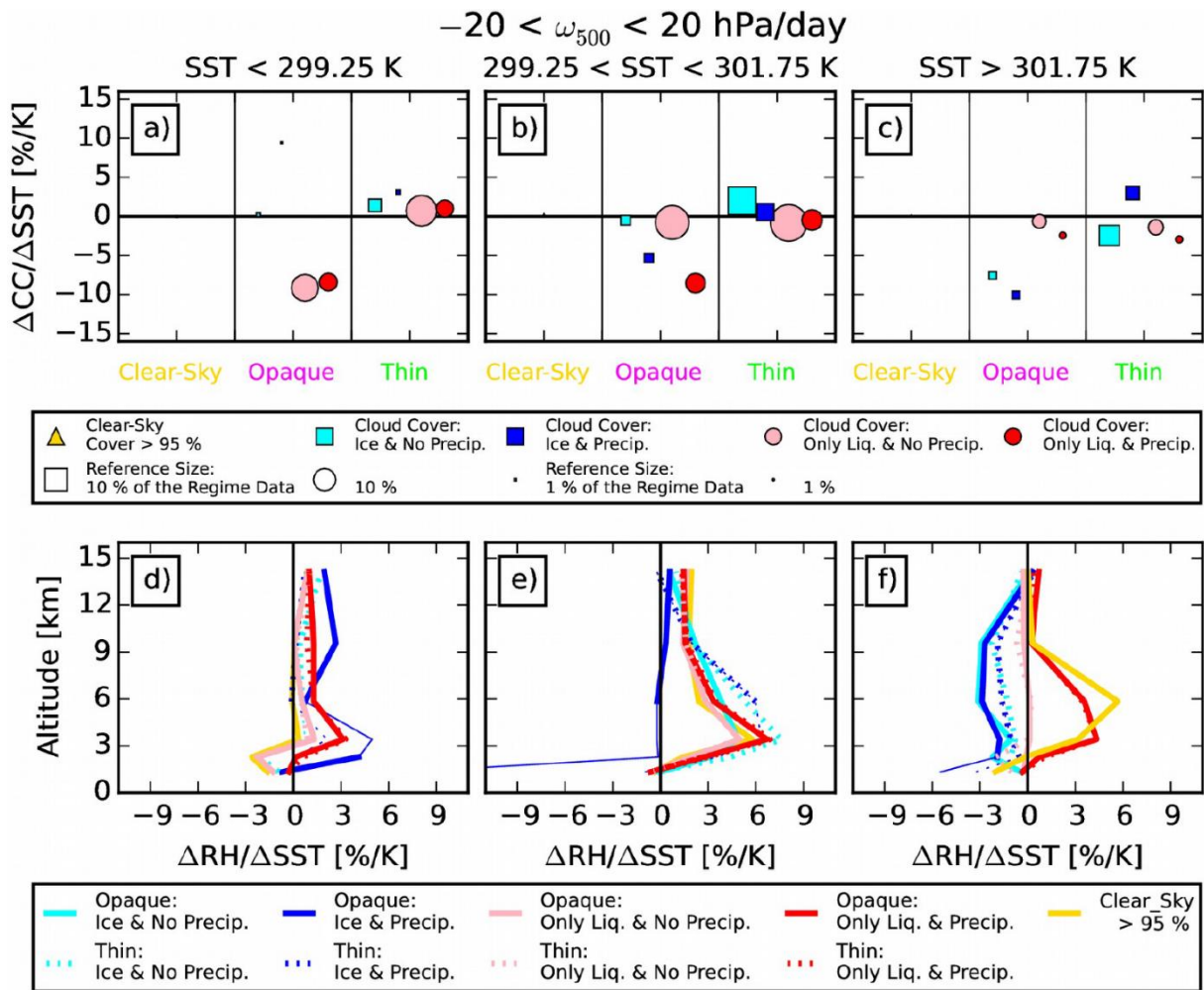


**FIGURE C-5: Top panel:** Change of cover associated to 1 K SST warming. Circles indicate only liquid cloud phase, squares ice phase and golden pyramids clear-sky cover > 95 % (these are almost invisible as their magnitudes are < 0.5 % K<sup>-1</sup>). Bullet sizes are weighted by their number contribution to the **intermediate regime**:  $-20 < \omega_{500} < 20$  hPa/day. **Bottom panel:** Change of RH profiles associated to 1 K SST warming. Thick lines in the bottom panel show significant values, whilst thin lines show all rates of change. Values of rate of change are given within the three SST ranges (a & d: SST < 299.25 K, b & e: 299.25 < SST < 301.75 K, c & f: SST > 301.75 K). The trend values in the top and bottom panels are calculated from the subplots *g, h, j, k* and *m, n, p, q* in Figure C3, respectively.

## Differences: El Niño vs. Full Time Period

## Descending Regime

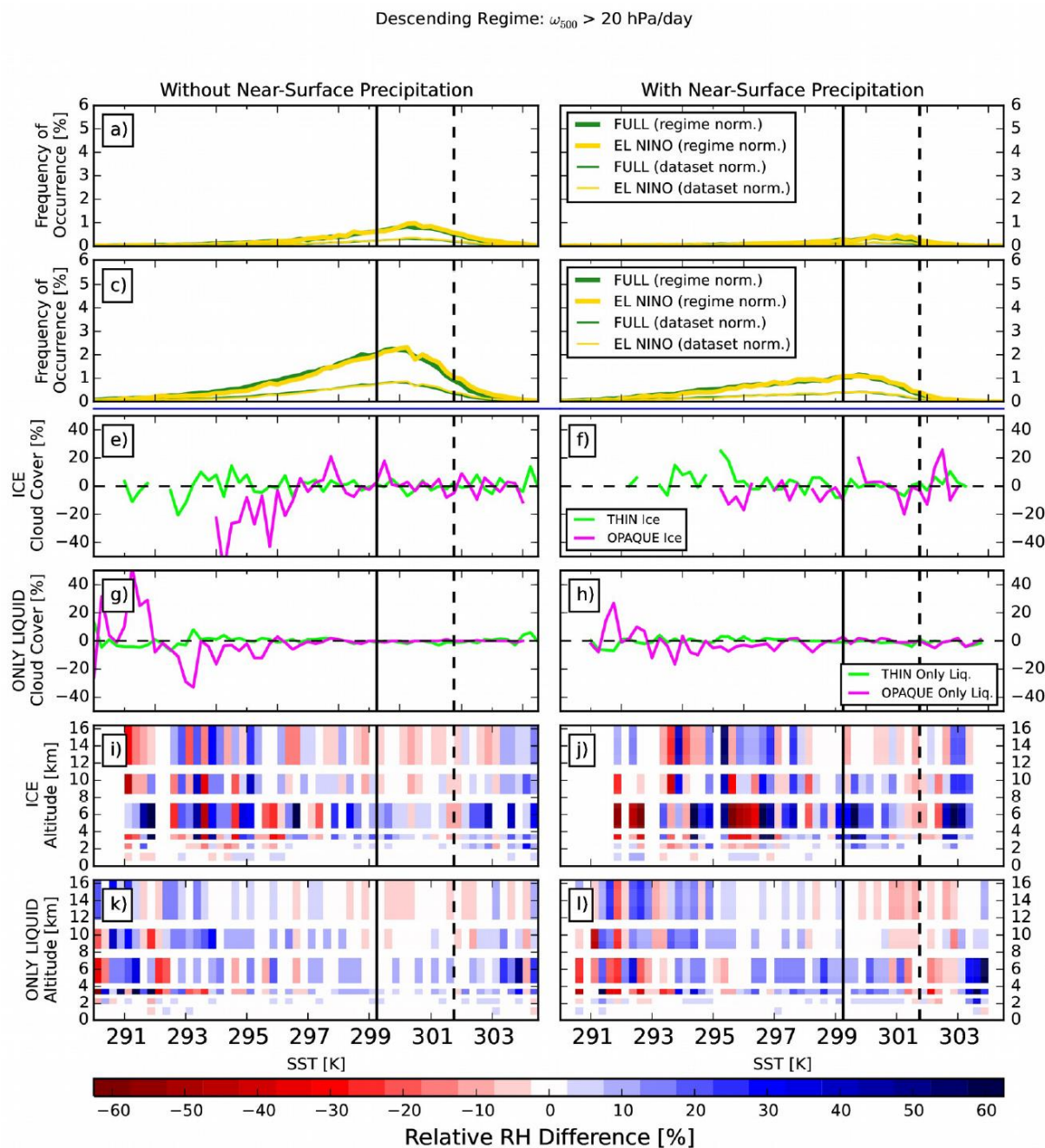


**FIGURE C-6:** Descending regime:  $\omega_{500} > 20$  hPa/day. **Top two panels:** Probability distributions of grid boxes containing ice (*a* – *b*) and only liquid clouds (*c* – *d*) without/with near-surface precipitation (left/right column) in only the ascending regime (thick lines) and over all the regimes (thin lines). The blue horizontal line separates the number distributions from the evolution within a grid box. **Middle two panels:** Absolute difference of median thin and opaque ice (*e* – *f*) and only liquid (*g* – *h*) cloud cover without/with near-surface precipitation (left/right column). **Lower panels:** Profiles of relative RH difference for grid boxes containing ice (*i* – *j*) and only liquid (*k* – *l*) clouds without/with near-surface precipitation (left/right column). Vertical lines are for the same SST thresholds as identified in Figure 3-3.

## Intermediate Regime

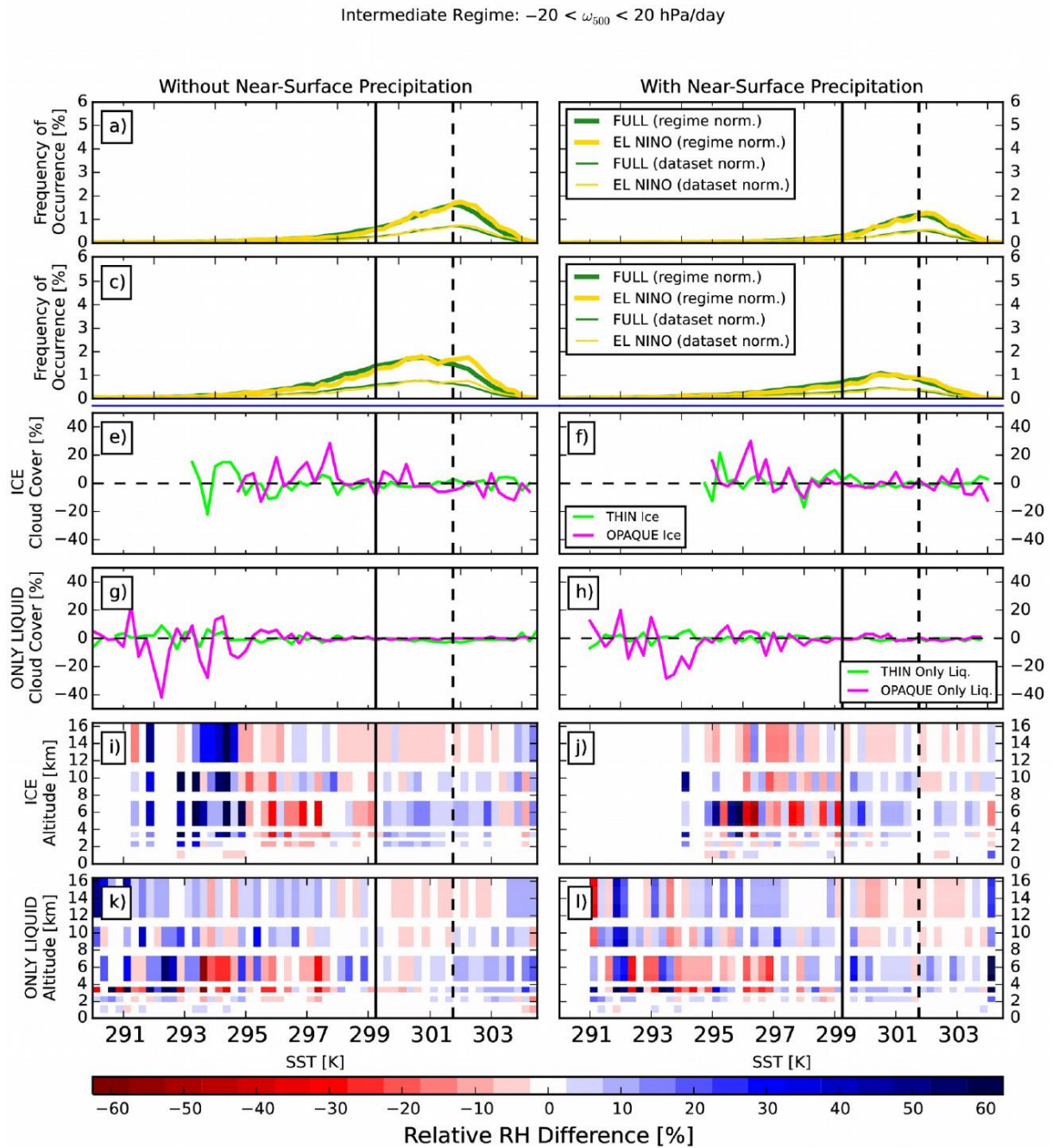


**FIGURE C-7:** Intermediate regime:  $-20 < \omega_{500} < 20$  hPa/day. **Top two panels:** Probability distributions of grid boxes containing ice (*a* – *b*) and only liquid clouds (*c* – *d*) without/with near-surface precipitation (left/right column) in only the ascending regime (thick lines) and over all the regimes (thin lines). The blue horizontal line separates the number distributions from the evolution within a grid box. **Middle two panels:** Absolute difference of median thin and opaque ice (*e* – *f*) and only liquid (*g* – *h*) cloud cover without/with near-surface precipitation (left/right column). **Lower panels:** Profiles of relative RH difference for grid boxes containing ice (*i* – *j*) and only liquid (*k* – *l*) clouds without/with near-surface precipitation (left/right column). Vertical lines are for the same SST thresholds as identified in Figure 3-3.

## Ascending Regime

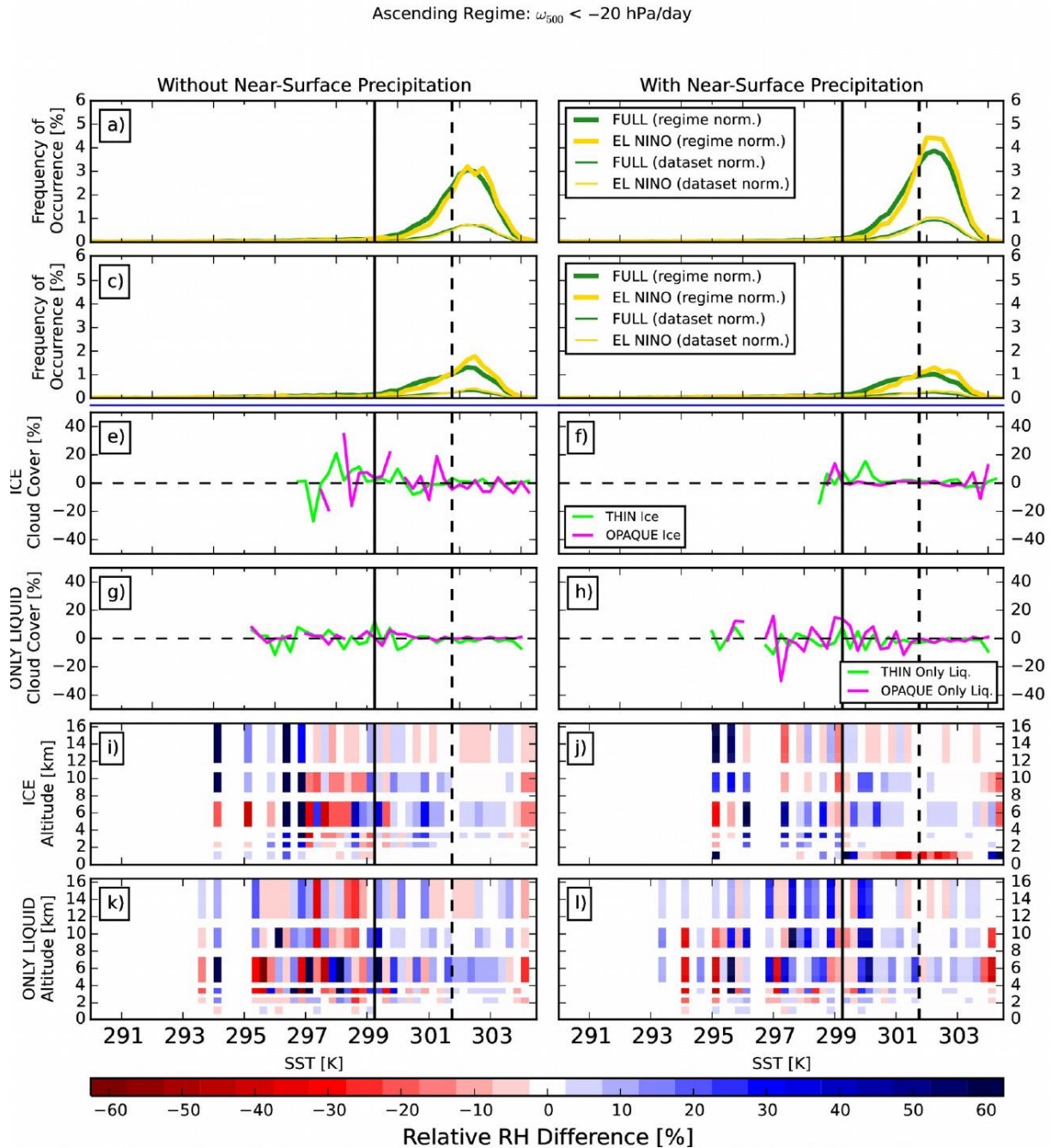


**FIGURE C-8:** Ascending regime:  $\omega_{500} < -20$  hPa/day. **Top two panels:** Probability distributions of grid boxes containing ice (*a* – *b*) and only liquid clouds (*c* – *d*) without/with near-surface precipitation (left/right column) in only the ascending regime (thick lines) and over all the regimes (thin lines). The blue horizontal line separates the number distributions from the evolution within a grid box. **Middle two panels:** Absolute difference of median thin and opaque ice (*e* – *f*) and only liquid (*g* – *h*) cloud cover without/with near-surface precipitation (left/right column). **Lower panels:** Profiles of relative RH difference for grid boxes containing ice (*i* – *j*) and only liquid (*k* – *l*) clouds without/with near-surface precipitation (left/right column). Vertical lines are for the same SST thresholds as identified in Figure 3-3.

## Interquartile Ranges of Cloud Cover and Relative Humidity

## Descending Regime

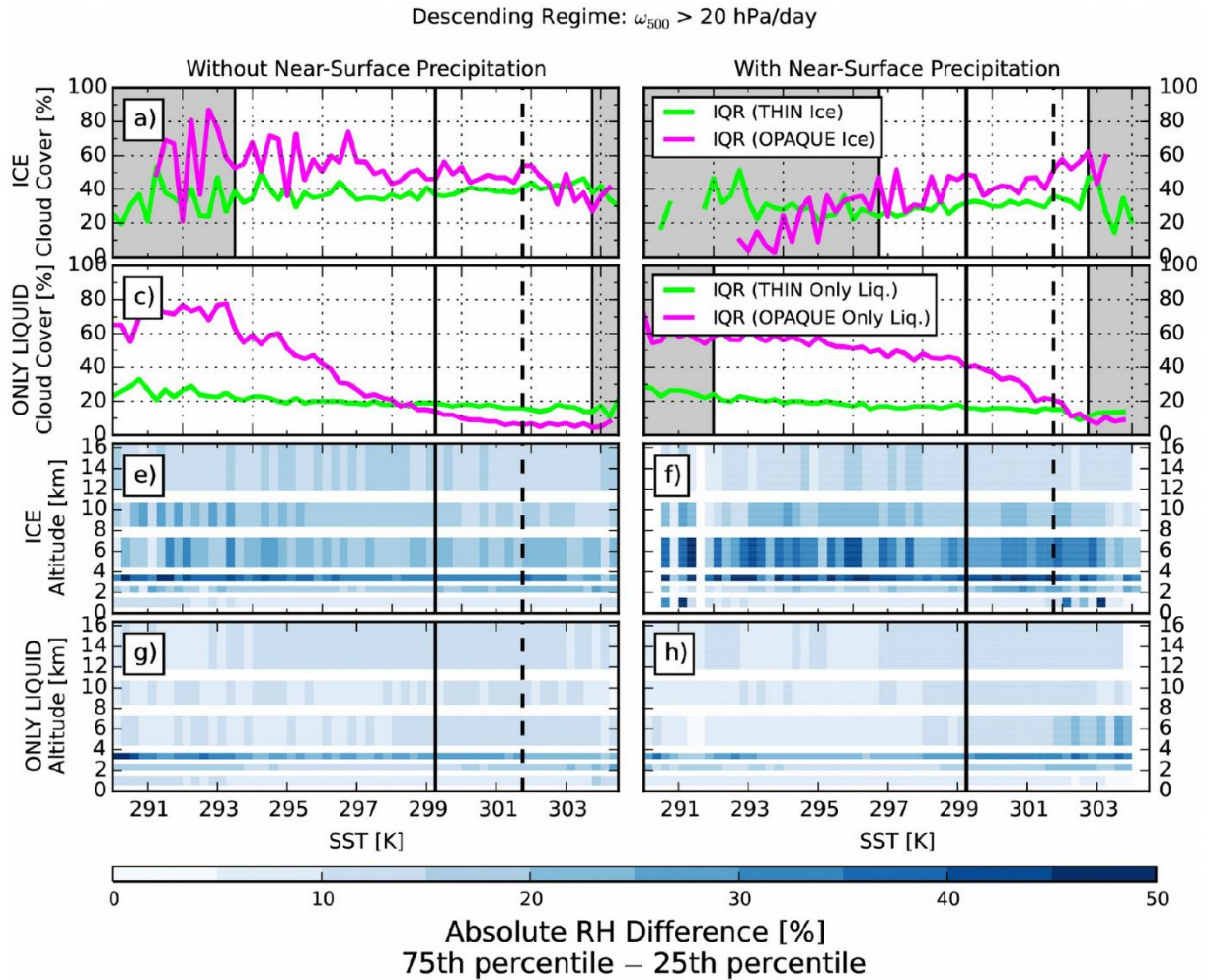


**FIGURE C-9:** Evolution of the interquartile range (IQR) of the median cloud covers and relative humidity profiles (in Figure 3-5) with SST for the descending regime:  $\omega_{500} > 20$  hPa/day. **Top two panels:** IQR of the median thin and opaque ice (*a* – *b*) and only liquid (*c* – *d*) cloud covers for non-precipitating and precipitating scenes. **Lower panels:** IQR of the median relative humidity profiles for grid boxes containing ice (*e* – *f*) and only liquid (*g* – *h*) clouds for nonprecipitating and precipitating scenes. Vertical lines are for the same SST thresholds as identified in Figure 3-3. Shaded gray areas cover SST bins where the median cloud cover or RH values in the present category were calculated for less than 100 grid boxes.

## Intermediate Regime

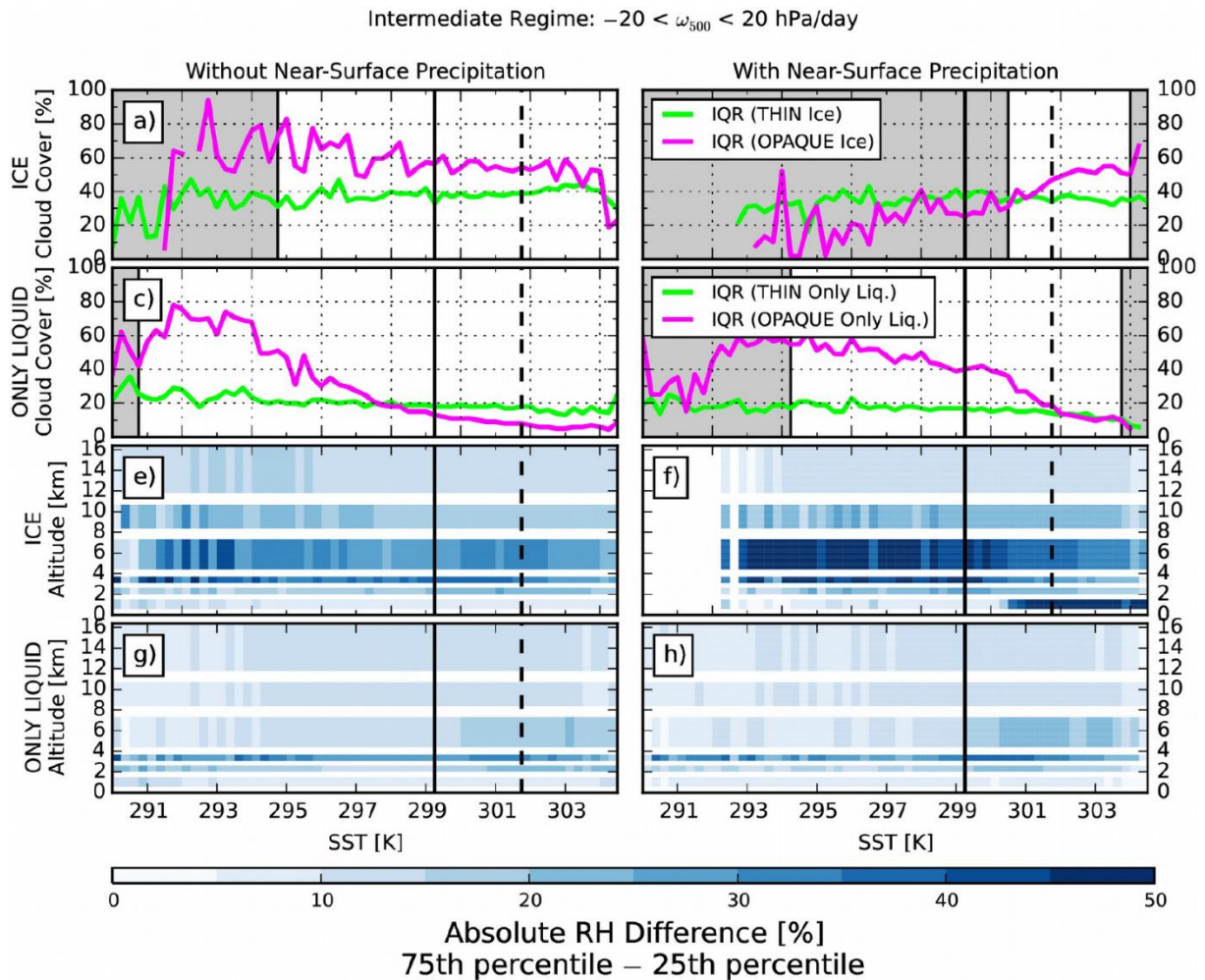


**FIGURE C-10:** Evolution of the interquartile range (IQR) of the median cloud covers and relative humidity profiles (in Fig. C3) with SST for the intermediate regime:  $-20 < \omega_{500} < 20$  hPa/day. **Top two panels:** IQR of the median thin and opaque ice (*a – b*) and only liquid (*c – d*) cloud covers for non-precipitating and precipitating scenes. **Lower panels:** IQR of the median relative humidity profiles for grid boxes containing ice (*e – f*) and only liquid (*g – h*) clouds for non-precipitating and precipitating scenes. Vertical lines are for the same SST thresholds as identified in Figure 3-3. Shaded gray areas cover SST bins where the median cloud cover or RH values in the present category were calculated for less than 100 grid boxes.

## Ascending Regime

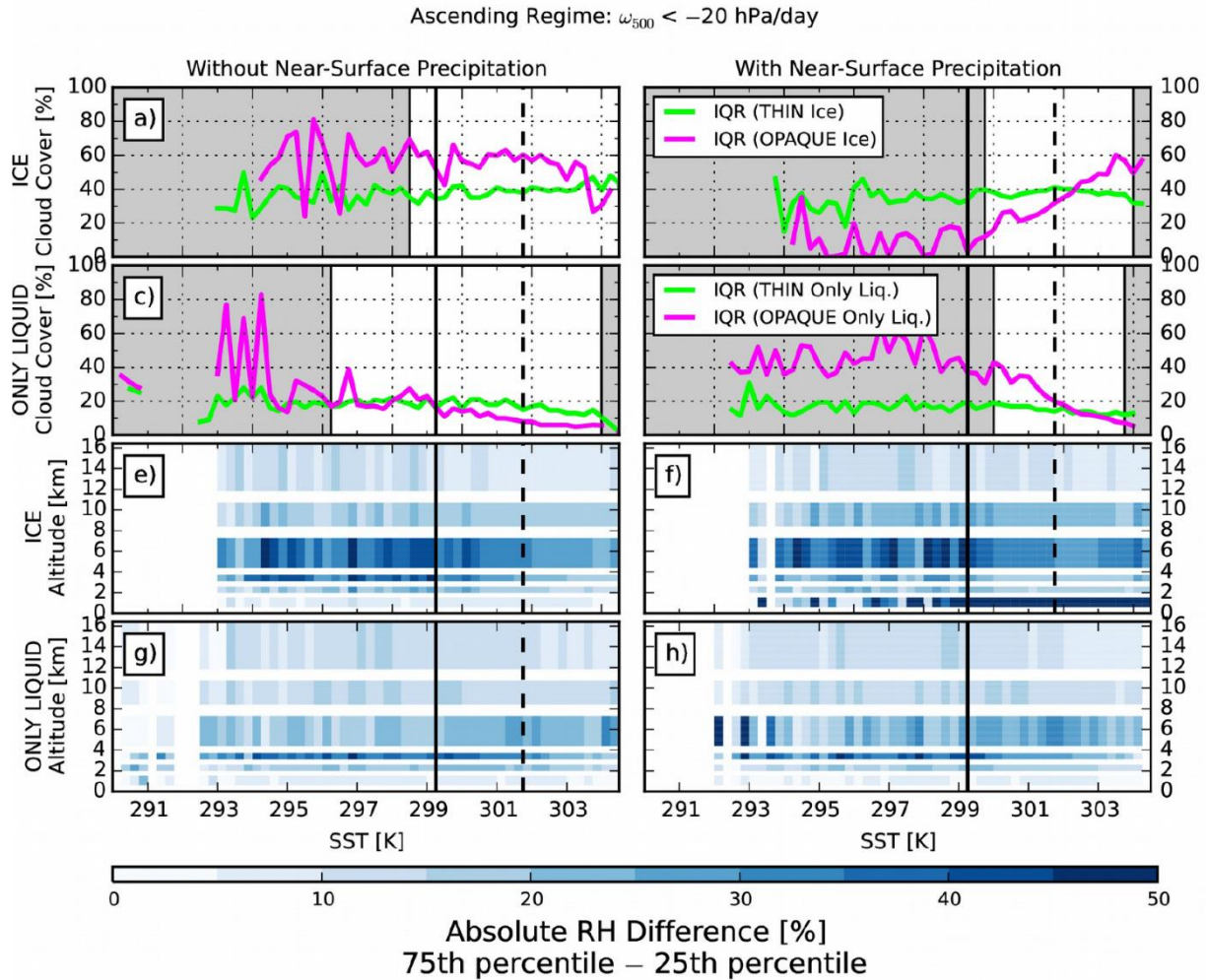


**FIGURE C-11:** Evolution of the interquartile range (IQR) of the median cloud covers and relative humidity profiles (in Fig. 3-8) with SST for the ascending regime:  $\omega_{500} < -20$  hPa/day. **Top two panels:** IQR of the median thin and opaque ice (*a – b*) and only liquid (*c – d*) cloud covers for non-precipitating and precipitating scenes. **Lower panels:** IQR of the median relative humidity profiles for grid boxes containing ice (*e – f*) and only liquid (*g – h*) clouds for nonprecipitating and precipitating scenes. Vertical lines are for the same SST thresholds as identified in Figure 3-3. Shaded gray areas cover SST bins where the median cloud cover or RH values in the present category were calculated for less than 100 grid boxes.

## Timeseries of Tropical Monthly Mean Cloud Cover

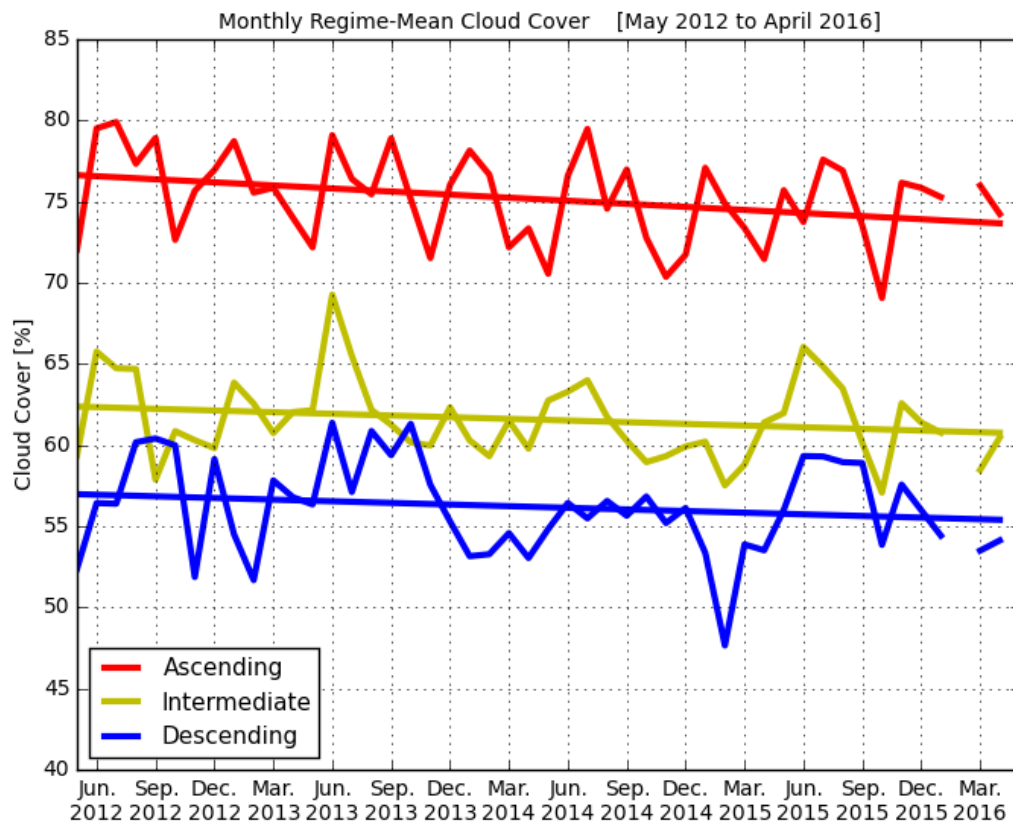


**FIGURE C-12:** Monthly mean cloud cover over the time period May 2012 to April 2016 in the (red) ascending regime, (yellow) intermediate regime, and (blue) descending regime.

## Heavily Precipitating Grid Boxes vs. Non-Precipitating: Ascending Regime

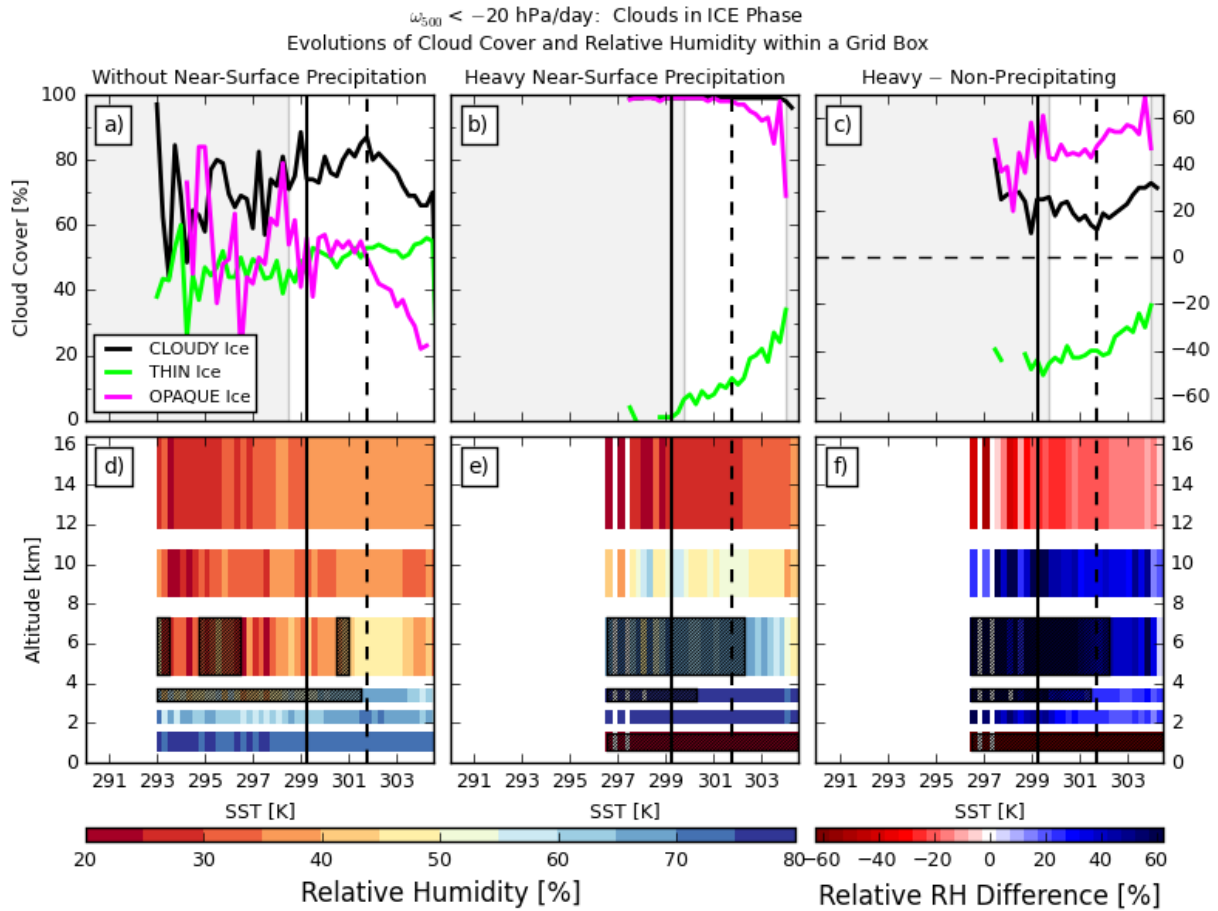


**FIGURE C-13:** Evolution of the observed cloud cover and relative humidity with SST within grid boxes in the ascending regime ( $\omega_{500} < -20$  hPa day<sup>-1</sup>), identified as containing ice clouds. **(top)** Median thin and opaque ice cloud covers in grid boxes **(a)** without near-surface precipitation and **(b)** with heavy near-surface precipitation, as well as **(c)** their absolute difference. Note that addition of the green and magenta lines does not equal the black as both opaque and thin clouds are not present in all grid boxes. Shaded gray areas cover SST bins where the median cloud cover or RH values in the present category were calculated for less than 100 grid boxes. **(bottom)** Median relative humidity profiles for grid boxes containing ice clouds **(d)** without near-surface precipitation and **(e)** with heavy near-surface precipitation, as well as **(f)** their relative difference. Black squared and hatched areas indicate layer sections where the interquartile range is greater than 35%, and as such are deemed nonsignificant. Vertical lines are for the same SST thresholds as identified in Fig. 3-3.

## Opaque Ice Cloud Grid Boxes in the Ascending Regime

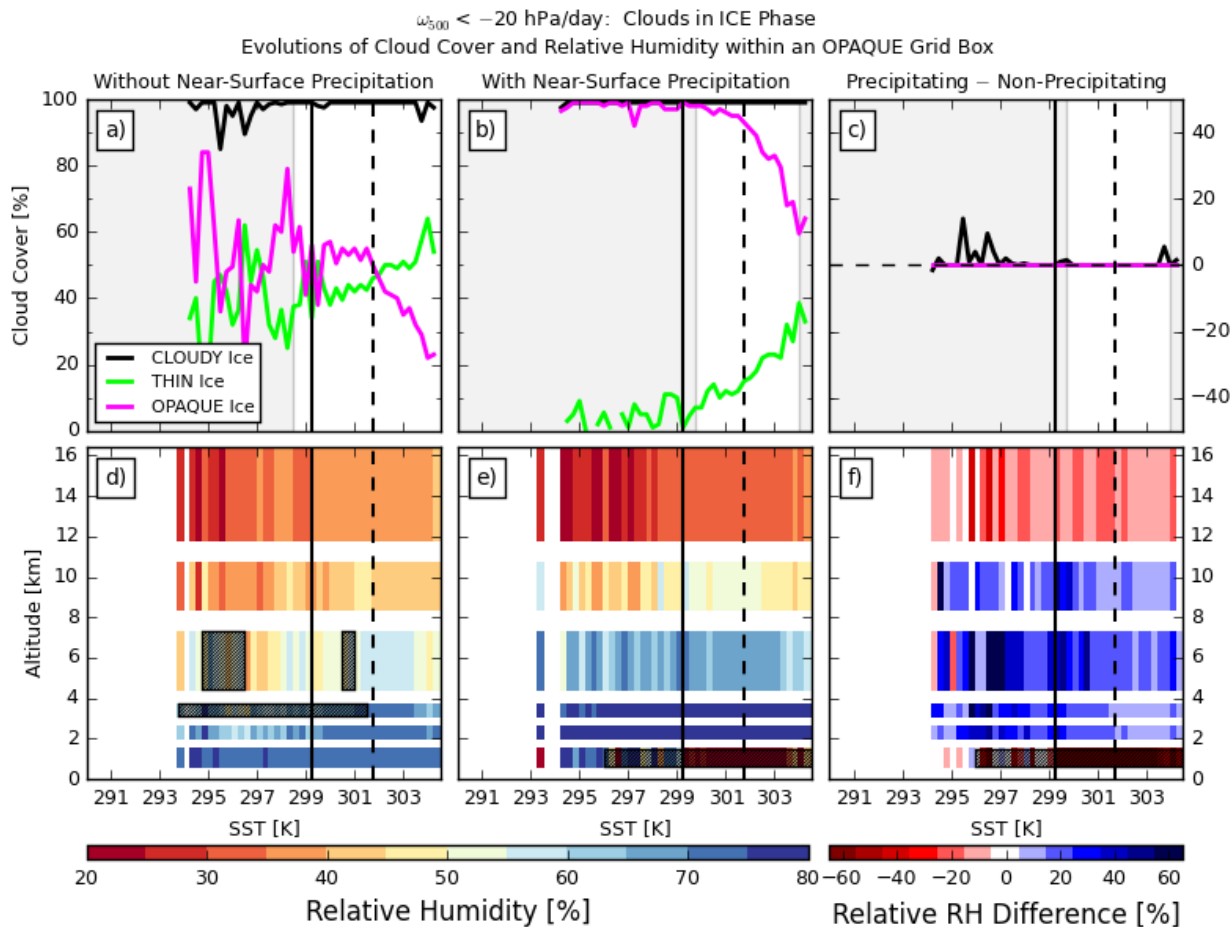


**FIGURE C-14:** Evolution of the observed cloud cover and relative humidity with SST within grid boxes guaranteed to contain opaque clouds in the ascending regime ( $\omega_{500} < -20$  hPa day<sup>-1</sup>), identified as containing ice clouds. **(top)** Median thin and opaque ice cloud covers in grid boxes **(a)** without near-surface precipitation and **(b)** with near-surface precipitation, as well as **(c)** their absolute difference. Shaded gray areas cover SST bins where the median cloud cover or RH values in the present category were calculated for less than 100 grid boxes. **(bottom)** Median relative humidity profiles for grid boxes containing ice clouds **(d)** without near-surface precipitation and **(e)** with near-surface precipitation, as well as **(f)** their relative difference. Black squared and hatched areas indicate layer sections where the interquartile range is greater than 35%, and as such are deemed nonsignificant. Vertical lines are for the same SST thresholds as identified in Fig. 3-3.

Figure 7 in Cesana and Chepfer (2013)

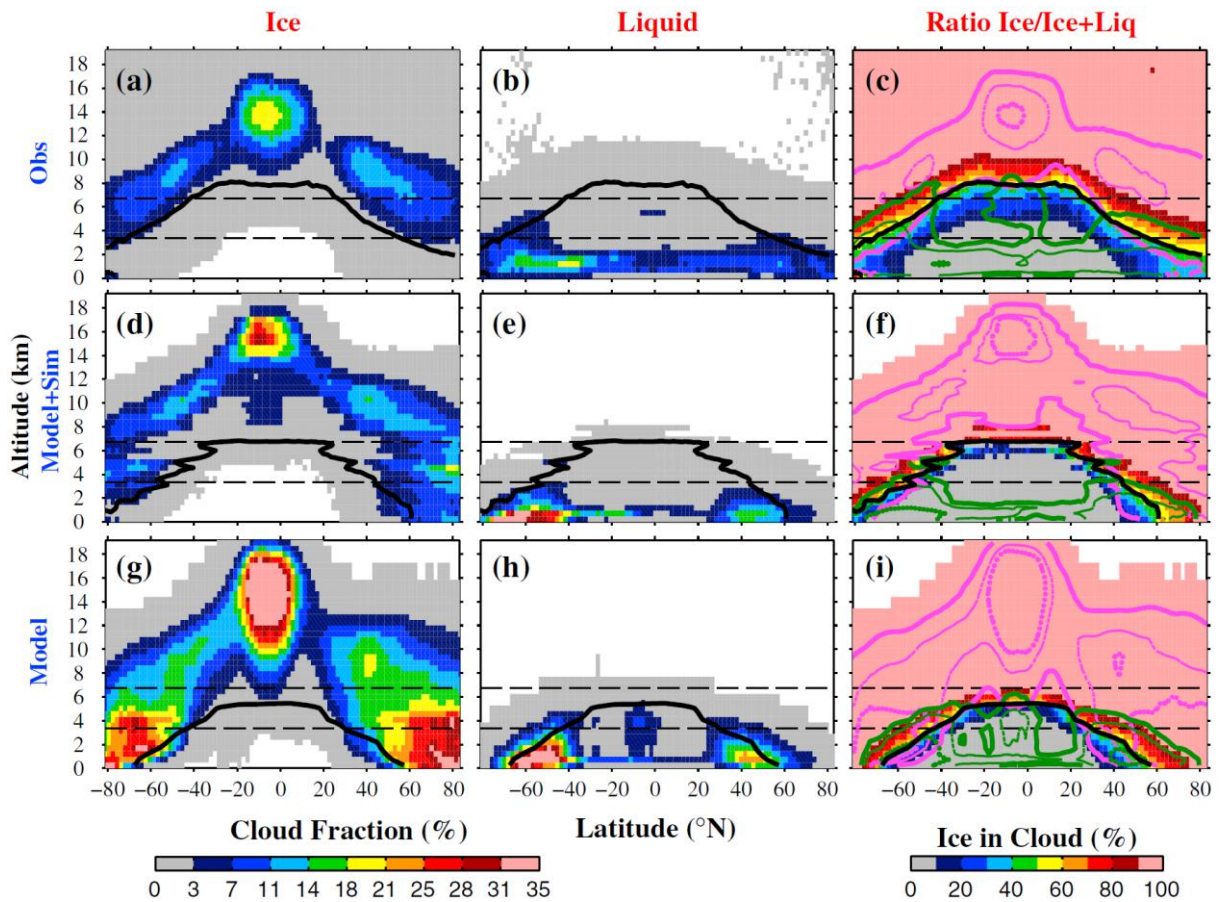


**FIGURE C-15:** Cloud phase vertical distribution observed and simulated in JFM. **(left column)** Ice cloud fraction, **(center)** liquid cloud fraction, and **(right)** ice fraction with respect to the total condensate, **(top row)** for observations from CALIPSO-GOCCP, **(middle row)** for simulations by the “LMDZ GCM+COSP lidar simulator,” and **(bottom row)** for simulations by LMDZ GCM alone, at a vertical resolution of  $\Delta z = 480$  m. The black line corresponds to the equiprobability between liquid and ice (50%). The solid and dashed pink and green isolines show the ice (respectively 2%, 10%, and 18%) and liquid (respectively 2% and 6%) cloud fractions. The horizontal black dashed lines separate the low- and middle-level clouds (3.36 km) and the middle- and high-level clouds (6.72 km). The figure is extracted from Cesana and Chepfer (2013).

## D Supplementary Figures of Chapter 4

### Change in Thin Cloud Altitude with SST: Method B

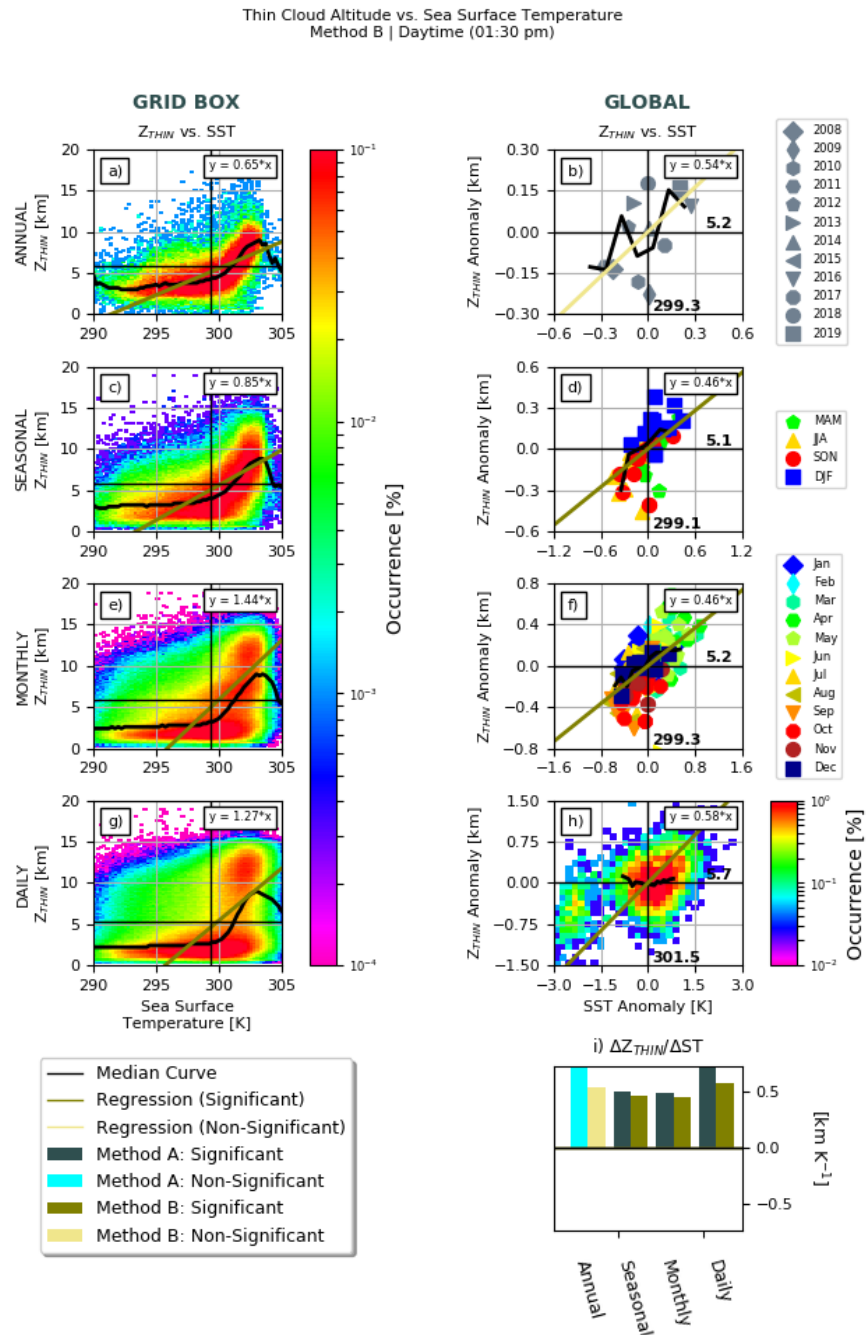


**FIGURE D-1:** Change in thin cloud altitude with SST on the (a, b) annual, (c, d) seasonal, (e, f) monthly, and (g, h) daily timescale over the years 2008-2019 computed with Method B. **Left column:** Density scatter plot of grid box values. **Right column:** Scatter plots of tropical global values. Black curves show median thin cloud altitude value for each SST bin and linear lines regressions fitted with ODR to the scatter distributions. Brown (yellow) line means that the regression is significant (nonsignificant) with respect to a  $p$  value = 0.05. Subplot i) shows rates of change of thin cloud altitude with SST computed from global values. Yellow and brown bars are from the regressions in subplots b, d, f, h, whilst light blue and gray bars from rates of changes of global values computed from Method A (Fig. 4-1).

## Change in Relative Humidity and Cloud Characteristics with SST for Grid Box Values: Method B

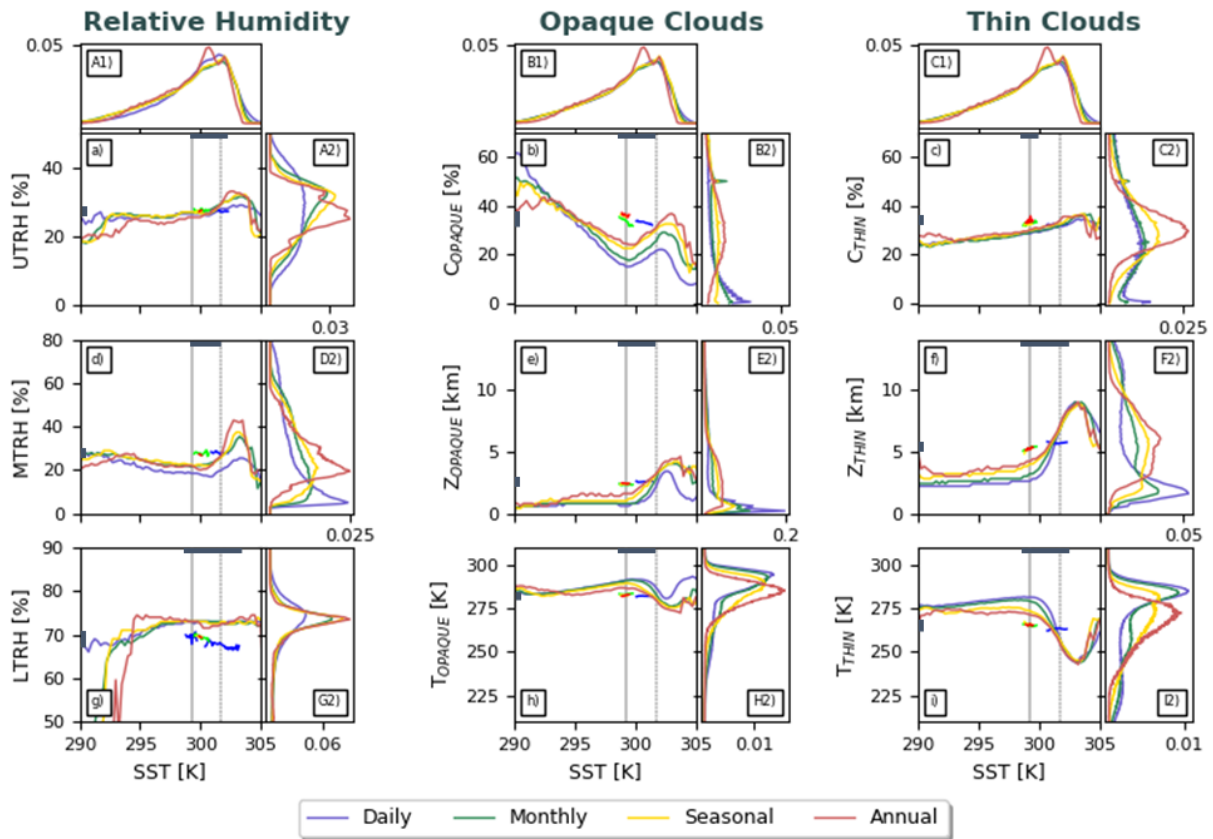


**FIGURE D-2:** Change in RH and cloud characteristics with SST for grid box values on the (red) annual, (yellow) seasonal, (green) monthly, and (blue) daily timescale. a) upper-tropospheric RH, b) opaque cloud cover, c) thin cloud cover, d) middle-tropospheric RH, e) opaque cloud altitude, f) thin cloud altitude, g) lower-tropospheric RH, h) opaque cloud temperature, i) thin cloud temperature. Subplots A1, B1, C1 show the PDFs of SST, whilst subplots A2-I2 show the PDFs of the RH and cloud variables in a-i. Changes in RH with SST (left column) are computed over the years 2012-2018, whilst changes in cloud with SST (central and right columns) are computed over the years 2008-2019. The curves are fitted to grid box value distributions computed by Method B as illustrated in Fig. 4-2 (left column). The global curves show the range of locations of the global values presented in Fig. 4-3. These ranges are also highlighted by the thick gray lines on the inside of the frames in subplots a-i.

## Change in Cloud Characteristics for Grid Box Values: Method B

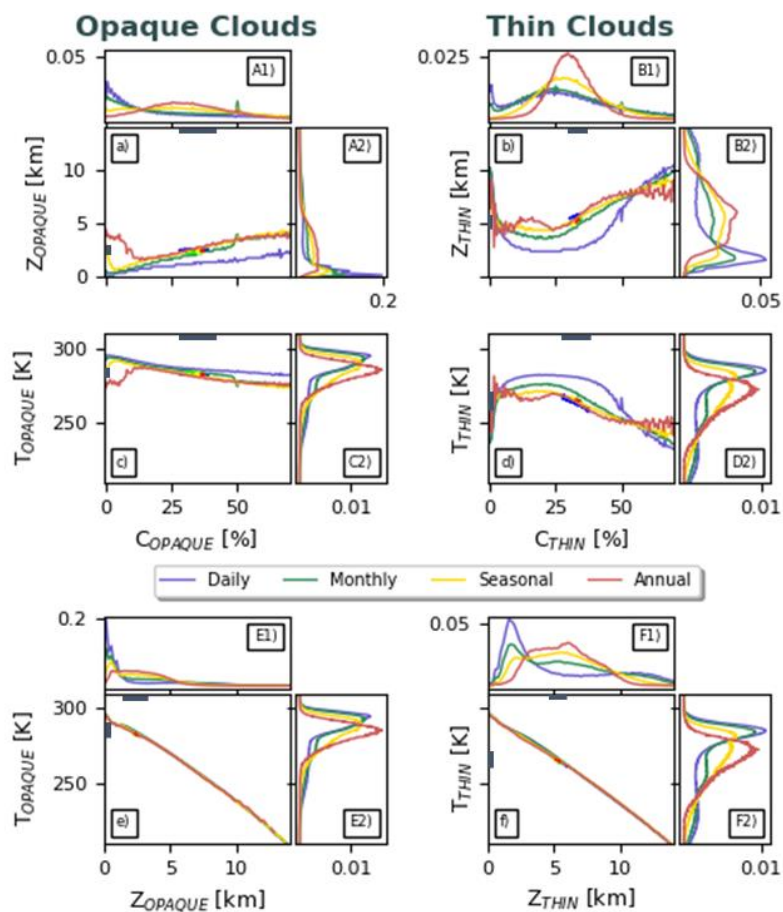


**FIGURE D-3:** Change in cloud (a, b) altitude with cover (c, d) temperature with cover, and (e, f) temperature with altitude on the (red) annual, (yellow) seasonal, (green) monthly, and (blue) daily timescale over the years 2008-2019. **Left column:** Opaque clouds. **Right column:** Thin clouds. Subplots A1, B1 (E1, F1) show the PDFs of opaque and thin cloud cover (altitude). Subplots A2-F2 show the PDFs of the y variables subplots a-f. The curves are fitted to grid box value distributions computed by Method B as illustrated in Fig. 4-2 (left column). The global curves show the range of locations of the global values presented in Fig. 4-12. These ranges are also highlighted by the thick gray lines on the inside of the frames in subplots a-f.

## Change in Opaque Cloud Altitude with Cover on the Grid Box Scale

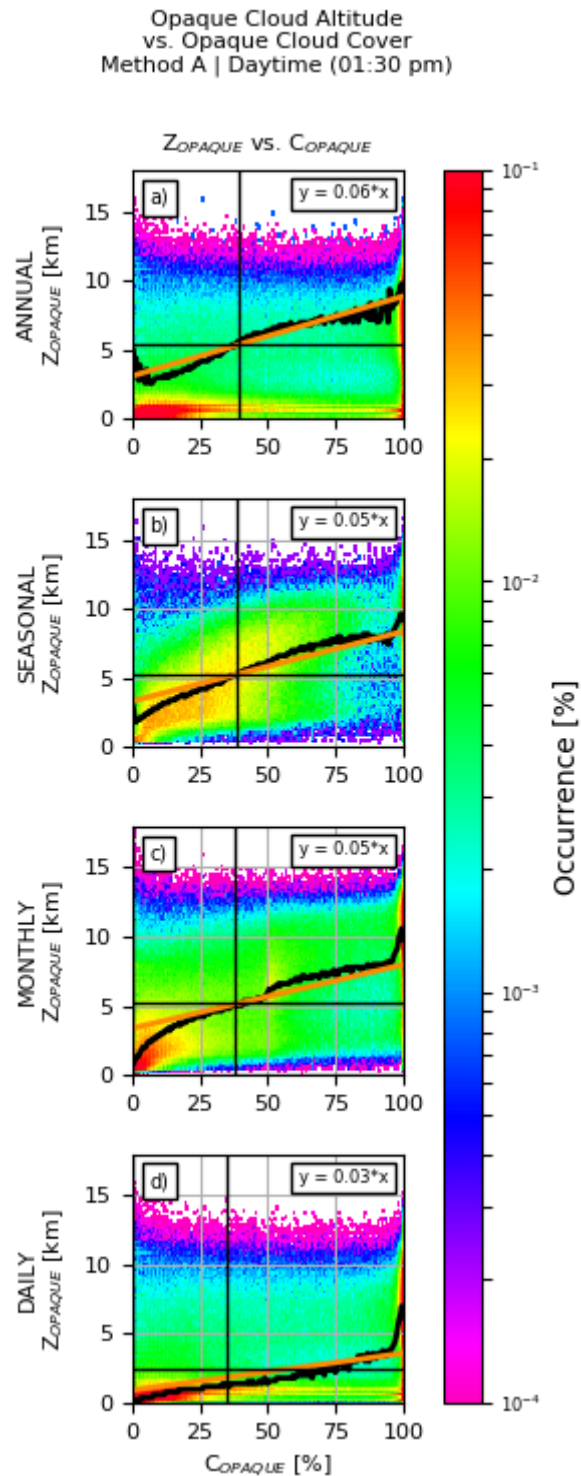


**FIGURE D-4:** Change in opaque cloud altitude with opaque cloud cover on the (a) annual, (b) seasonal, (c) monthly, and (d) daily timescale over the years 2008-2019. Density scatter plot of grid box values. Black curve shows median opaque cloud altitude value for each 1 % cloud cover bin. Orange line shows linear regression fitted with ODR to the scatter distribution. Solid line means that the regression is significant with respect to a p value = 0.05.

## E Résumé de thèse en français

L'atmosphère tropicale est un système complexe de processus dynamiques et thermodynamiques. A cela, s'ajoute un forçage radiatif dû aux gaz à effet de serre anthropiques et au réchauffement climatique qui en résulte. Les projections climatiques supposent souvent que le paramètre de rétroaction est constant dans le temps, de sorte que les changements de flux radiatif sont proportionnels aux changements de température de surface.

En fait, les incertitudes de projections sont associées à la réponse du cycle de l'eau atmosphérique au réchauffement de la surface et motivent ainsi la nécessité de mieux comprendre les processus liant les nuages, la circulation de l'eau atmosphérique et le climat.

Ce travail vise à améliorer notre compréhension de la co-variabilité des températures de surface de la mer, humidité relative, nuages et précipitations, à différentes échelles temporelles et spatiales dans la ceinture tropicale (30°N à 30°S). Il repose sur un ensemble unique de mesures de journée (13h30) de haute résolution verticale qui regroupe le profil d'humidité relative, les caractéristiques des nuages et les précipitations près de la surface fournis par le radiomètre microonde SAPHIR embarqué sur le satellite Megha-Tropiques, le lidar CALIOP embarqué sur le satellite CALIPSO, et le radar CPR embarqué sur le satellite CloudSat. Ces données ont une résolution horizontale de 1° par 1° et couvrent la période de 2012 à 2018. Elles sont associées aux champs de température de surface de la mer et de vitesse verticale de l'atmosphère des ré-analyses ERA5.

- ❖ Le premier axe était focalisé sur la coévolution des profils de humidité relative, de la couverture nuageuse et de la température de surface de la mer, sous contrainte de circulation à grande échelle en exploitant l'échelle instantanée de variation. À ma connaissance, il s'agit d'une première analyse intégrant entièrement des observations de la réponse du cycle de l'eau atmosphérique tropicale à la température de surface de la mer à cette échelle. Des relations physiques sont établies pour les différents régimes de circulation de grande échelle, et leurs caractéristiques se maintiennent avec la variabilité naturelle du climat (comme El Niño-Southern Oscillation). Ainsi, le régime subsident est caractérisé par une troposphère libre sèche et une décroissance, avec l'augmentation de la température de surface de la mer, de la fraction de nuages opaque de phase liquide, et un refroidissement prévu par ciel clair avec température de surface de la mer. Le régime ascendant est caractérisé par des variations non linéaires de la fraction de nuages de phase glacée et d'humidité relative de la troposphère avec un maximum autour d'une température de surface de la mer de 302 K, ce qui implique des impacts non linéaires sur les flux radiatifs.
- ❖ Le deuxième axe qui a été considéré portait sur l'hypothèse de facteurs de rétroaction invariants dans le temps aux échelles journalière, mensuelle, saisonnière et annuelle. Les taux de changement de l'humidité relative et des caractéristiques des nuages avec la température de surface de la mer définis à l'échelle globale (océans tropicaux) sont comparés aux taux de changement calculés localement, sur chaque point de la grille. À l'échelle globale, les changements en profil d'humidité relative et en température des nuages de glace sont peu significatifs, tandis que la couverture de nuages opaques diminue et que l'altitude des nuages de glace augmentent. Ces résultats suggèrent un renforcement du refroidissement radiatif de ciel clair avec la température de surface de la mer, alors que la température d'émission des nuages est invariante, ce qui est à la base de certaines hypothèses sur le fonctionnement de l'atmosphère tropicale.

Cet ensemble de données a été exploré selon deux axes : Ces résultats mettent en évidence des différences significatives en fonction de l'échelle de temps considérée, et qui peuvent ainsi être utilisés comme diagnostic pertinent pour l'évaluation des modèles climatiques.

# List of Abbreviations and Notations

## Abbreviations

A-train	Afternoon-train
AIRS	Atmospheric InfraRed Sounder
AMIP	Atmospheric Model Intercomparison Project
AMSR-E	Advanced Microwave Scanning Radiometer for EOS
AMSU	Advanced Microwave Sounding Unit
AR5	Fifth Assessment Report of the IPCC
ARPIA intervals	Atmospheric Relative humidity Profiles Including Analysis of confidence intervals
ATB	ATtenuated Backscatter
ATMS	Advanced Technology Microwave Sounder
BT	Brightness Temperature
C-train	C for CALIPSO and CloudSat - train
CA	Cloud Altitude
CC	Cloud Cover
CDF	Cumulative Distribution Function
CT	Cloud Temperature
CERES	Clouds and the Earth's Radiant Energy Budget
CALIOP	Cloud-Aerosol Lidar with Orthogonal Polarization
CALIPSO	Cloud-Aerosol Lidar and Infrared Pathfinder Satellite Observations
CESM	Community Earth System Model
CFMIP	Cloud Feedback Model Intercomparison Project
CMIP	Coupled Model Intercomparison Project
CNES	Centre National d'Etudes Spatiales)
COSP	CFMIP Observation Simulator Package
CPR	Cloud Profiling Radar
CRE	Cloud Radiative Effect
CTP	Cloud Top Pressure
DJF	December, January, February
EarthCARE	Earth Clouds, Aerosols, and Radiation Explorer
ECMWF	European Centre for Medium-range Weather Forecasts
ENSO	El Niño Southern Oscillation
ERA5	ECMWF ReAnalysis 5
ERB	Earth Radiation Budget
ERBE	Earth Radiation Budget Experiment
FROGS	Frequent Rainfall Observations on GridS
FTRH	Free-Tropospheric Relative Humidity
GAM	General Additive Model
GCM	General Circulation Model
GEWEX	Global Energy and Water Cycle Experiment
GMAO	Global Modelling and Assimilation Office
GOCCP	GCM-Oriented CALIPSO Cloud Product
GPCP	Global Precipitation Climatology Project

HadISST	Hadley Centre Ice and SST
IPCC	Intergovernmental Panel on Climate Change
IPSL	Institut Pierre-Simon-Laplace
ISCCP	International Satellite Cloud Climatology Project
ISRO	Indian Space Research Organization
ITCZ	InterTropical Convergence Zone
JJA	June, July, August
JPL	Jet Propulsion Laboratory
LATMOS	Laboratoire Atmosphères, Milieux, Observations spatiales
Lidar	Light Detection And Ranging
LMD	Laboratoire de Météorologie Dynamique
LT	Local Time
LTRH	Lower-Tropospheric Relative Humidity
LW	LongWave
MHS	Microwave Humidity Sounder
MODIS	Moderate Resolution Imaging Spectrometer
MTCC	Megha-Tropiques, Calipso, Cloudsat
MTRH	Middle-Tropospheric Relative Humidity
NASA	National Aeronautics and Space Administration
NARVAL	Next-Generation Airborne Remote Sensing Research for Validation studies
NCEP-	National Centers for Environmental Prediction –
NCAR	National Center for Atmospheric Research
OAGCM	Ocean-Atmosphere General Circulation Model
OLR	Outgoing Longwave Radiation
PDF	Probability Density Function
PR	Precipitation Radar
RH	Relative Humidity
SAPHIR	Sounder for Atmospheric Profiling of Humidity in the Intertropics by
Radiometry	
ScaRaB	Scanner for Radiation Budget
SR	Scattering Ratio
SSM/I	Special Sensor Microwave Imager
SST	Sea Surface Temperature
SW	ShortWave
TMI	TRMM Microwave Imager
TRMM	Tropical Rainfall Measuring Mission
UTRH	Upper-Tropospheric Relative Humidity

## Notations

$C_{OPAQUE}$	Opaque cloud cover
$C_{THIN}$	Thin cloud cover
$T_{OPAQUE}$	Opaque cloud temperature
$T_{THIN}$	Thin cloud temperature
$Z_{OPAQUE}$	Opaque cloud altitude
$Z_{THIN}$	Thin cloud
$\omega_{500}$	Vertical pressure velocity at 500 hPa

## Bibliography

- Ahrens, D. C. (2013). *Meteorology Today: An Introduction to Weather, Climate, and the Environment*, 10<sup>th</sup> Edition, Brooks/Cole, Cengage Learning
- Aires, F., Bernardo, F., Prigent, C. (2013). Atmospheric water-vapour profiling from passive microwave sounders over ocean and land. Part I: Methodology for the Megha-Tropiques Mission, *Q. J. R. Meteorol. Soc.* 139, pp. 852-864.
- Allan, R. P. (2012). The Role of Water Vapour in Earth's Energy Flows. *Surv. Geophys.*, Springer, DOI 10.1007/s10712-011-9157-8
- Allan, R. P., Liu, C., Zahn, M., Lavers, D. A., Koukouvagias, E., Bodas-Salcedo, A. (2014). Physically Consistent Responses of the Global Atmospheric Hydrological Cycle in Models and Observations. *Surveys in Geophysics*, DOI 10.1007/s10712-012-9213-z
- Allan, R. P., Shine, K. P., Slingo, A., Pamment, J. A. (1999). The dependence of clear-sky outgoing long-wave radiation on surface temperature and relative humidity. *Quarterly Journal of the Royal Meteorological Society*, 125, pp. 2103-2126.
- Allan, R. P., Soden, B. J. (2008). Atmospheric Warming and the Amplification of Precipitation Extremes. *Science*, 321, pp. 1481-1484.
- Andrews, T., Gregory, J. M., Webb, M. J., Taylor, K. E. (2012). Forcing, feedbacks and climate sensitivity in CMIP5 coupled atmosphere-ocean climate models. *Geophysical Research Letters*, 39, doi:10.1029/2012GL051607
- Armour, K. C., Bitz, C. M., Roe, G. H. (2013). Time-Varying Climate Sensitivity from Regional Feedbacks. *Journal of Climate*, 26, DOI: 10.1175/JCLI-D-12-00544.1
- Aumann, H. H., Ruzmaikin, A., Behrangi, A. (2017). Increase in the Frequency of Tropical Deep Convective Clouds with Global Warming. *Atmos. Chem. Phys.*, doi: 10.5194/acp-2017-135.
- Bates, J. J., Jackson, D. L. (2001). Trends in upper-tropospheric humidity. *Geophysical Research Letters*, 28, pp. 1695-1698.
- Behrangi, A., Kubar, T., Lambriksen, B. (2012). Phenomological Description of Tropical Clouds Using *CloudSat* Cloud Classification. *Monthly Weather Review*, 140, pp. 3235-3249.
- Behrangi, A., Richardson, M. (2018). Observed High-Latitude Precipitation Amount and Pattern and CMIP5 Model Projections. *Remote Sensing*, 10, doi:10.3390/rs10101583
- Berg, W., L'Ecuyer, T. Haynes, J. M. (2010). The Distribution of Rainfall over Oceans from Spaceborne Radars. *Journal of Applied Meteorology and Climatology*, 49, pp. 535-543, DOI: 10.1175/2009JAMC2330.1
- Bergeron, T. (1935). On the physics of clouds and precipitation. *Proces Verbaux l'Association Météorologie*, International Union of Geodesy and Geophysics, pp. 156-178.
- Boggs, P. T., Spiegelman, C. H., Donaldson, J. R., Schnabel, R. B. (1988). A Computational Examination of Orthogonal Distance Regression. *Journal of Econometrics*, 38, pp. 169-201.

- Bony, S., Dufresne, J.-L. (2005). Marine boundary layer clouds at the heart of tropical cloud feedback uncertainties in climate models. *Geophysical Research Letters*, 32, doi: 10.1029/2005GL023851.
- Bony, S., Dufresne, J.-L., Le Treut, H., Morcrette, J.-J., Senior, C. (2004). On dynamic and thermodynamic components of cloud changes. *Climate Dynamics*, 22, pp. 71-86, DOI 10.1007/s00382-003-0369-6
- Bony, S., Stevens, B., Coppin, D., Becker, T., Reed, K. A., Voigt, A., Medeiros, B. (2016). Thermodynamic control of anvil cloud amount. *PNAS*, 113, pp. 8927-8932.
- Bony, S., Stevens, B., Frierson, D. M. W., Jakob, C., Kageyama, M., Pincus, R., Sheperd, T. G., Sherwood, S. C., Siebesma, A. P., Sobel, A. H., Watanabe, M., Webb, M. J. (2015). Clouds, circulation and climate sensitivity. *Nature Geoscience*, 8, DOI: 10.1038/NGEO2398
- Bouniol, D., Roca, R., Fiolleau, T., Poan, D. E. (2016). Macrophysical, Microphysical, and Radiative Properties of Tropical Mesoscale Convective Systems over Their Life Cycle. *Journal of Climate*, DOI: 10.1175/JCLI-D-15-0551.1
- Brient, F., Bony, S. (2013). Interpretation of the positive low-cloud feedback predicted by a climate model under global warming. *Climate Dynamics*, 40, 2415-2431, DOI 10.1007/s00382-011-1279-7
- Brogniez, H., Clain, G., Roca, R. (2015). Validation of Upper-Tropospheric Humidity from SAPHIR on board *Megha-Tropiques* Using Tropical Soundings. *Journal of Applied Meteorology and Climatology*, 54, pp. 896-908.
- Brogniez, H., Fallourd, R., Mallet, C., Sivira, R., Dufour, C. (2016) Estimating Confidence Intervals around Relative Humidity Profiles from Satellite Observations: Applications to the SAPHIR Sounder. *Journal of Atmospheric and Oceanic Technology*, 33, pp. 1005-1022.
- Brogniez, H., Kirstetter, P.-E. (2020). Coupling of Clouds and Tropospheric Relative Humidity in the Tropical Western Atlantic: Insights from Multisatellite Observations. *Geophysical Research Letters*, 47, <https://doi.org/10.1029/2020GL087466>
- Brogniez, H., Kirstetter, P.-E., Eymard, L. (2013). Expected improvements in the atmospheric humidity profile retrieval using the Megha-Tropiques microwave payload. *Q. J. R. Meteorol. Soc.*, 139, pp. 842-851.
- Buehler, S. A., Kuvatov, M., John, V. O., Milz, M., Soden, B. J., Jackson, D. L., Notholt, J. (2008). An upper tropospheric humidity data set from operational satellite microwave data. *Journal of Geophysical Research*, 113, doi: 10.1029/2007JD009314
- Burns, B. A., Wu, X., Diak, G. R. (1997). Effects of Precipitation and Cloud Ice on Brightness Temperatures in AMSU Moisture Channels. *IEEE Transactions on Geoscience and Remote Sensing*, 35, pp. 1429-1437.
- Byrne, M. P., Pendergrass, A. G., Rapp, A. D., Wodzicki, K. R. (2018). Response of the Intertropical Convergence Zone to Climate Change: Location, Width, and Strength. *Current Climate Change Reports*, 4, pp. 355-370, <https://doi.org/10.1007/s40641-018-0110-5>

Caldwell, P. M., Zelinka, M. D., Taylor, K. E., Marvel, K. (2016). Quantifying the Sources of Intermodel Spread in Equilibrium Climate Sensitivity. *Journal of Climate*, 29, pp. 513-524, DOI: 10.1175/JCLI-D-15-0352.1

Capderou, M. (2009). *Sampling: Comparison with other Meteorological Satellites*. Megha-Tropiques Technical Memorandum #1. Available online at:

<http://meghatropiques.ipsl.polytechnique.fr/available-documents/mttm/index.html>

Capderou, M. (2014). *Handbook of Satellite Orbits From Kepler to GPS*, Springer.

Ceppi, P., Briant, F., Zelinka, M. D., Hartmann, D. L. (2017). Cloud feedback mechanisms and their representation in global climate models. WIREs Clim Change 2017, e465. doi: 10.1002/wcc.465

Ceppi, P., Gregory, J. M. (2017). Relationship of tropospheric stability to climate sensitivity and Earth's observed radiation budget. *PNAS*, 14, pp. 13126-13131,

doi/10.1073/pnas.1714308114  
Cesana, G., Chepfer, H. (2013). Evaluation of the cloud thermodynamic phase in a climate model using CALIPSO-GOCCP. *Journal of Geophysical Research: Atmospheres*, 118, pp.7922-7937.

Cesana, G., Chepfer, H. (2012). How well do climate models simulate cloud vertical structure? A comparison between CALIPSO-GOCCP satellite observations and CMIP5 models. *Geophysical Research Letters*, 39, doi:10.1029/2012GL053153.

Cesana, G., Chepfer, H. (2013). Evaluation of the cloud thermodynamic phase in a climate model using CALIPSO-GOCCP. *Journal of Geophysical Research: Atmospheres*, 118, pp.7922-7937.

Cesana, G., Chepfer, H., Winker, D., Getzewich, B., Cai, X., Jourdan, O., Mioche, G., Okamoto, H., Hagihara, Y., Noel, V. (2016). Using in-situ airborne measurements to evaluate three cloud phase products derived from CALIPSO. *Journal of Geophysical Research: Atmospheres*, 121, pp. 1-21

Cesana, G., Kay, J. E., Chepfer, H., English, J. M., de Boer, G. (2012). Ubiquitous low-level liquid-containing Arctic clouds: New observations and climate model constraints from CALIPSO-GOCCP. *Geophysical Research Letters*, 39, doi: 10.1029/2012GL053385

Charney, J. G., Arakawa, A., Baker, D. J., Bolin, B., Dickinson, R. E., Goody, R. M., Leith, C. E., Stommel, H. M., Wunsch, C. I. (1979). Carbon dioxide and climate: A scientific assessment. Report of an Ad-Hoc Group on Carbon Dioxide and Climate, National Academy of Sciences, Washington D.C., USA.

Chepfer, H., Bony, S., Winker, D., Cesana, G., Dufresne, J. L., Minnis, P., Stubenrauch, C. J., Zeng, S. (2010). The GCM-Oriented CALIPSO Cloud Product (CALIPSO-GOCCP). *Journal of Geophysical Research*, 115, pp. 1-13.

Chepfer, H., Bony, S., Winker, D., Chiriaco, M., Dufresne, J.-L., Sèze, G. (2008). Use of CALIPSO lidar observations to evaluate the cloudiness simulated by a climate model. *Geophysical Research Letters*, 35, doi:10.1029/2008GL034207

Chepfer, H., Brogniez, H., Noel, V. (2019). Diurnal variations of cloud and relative humidity profiles across the tropics. *Nature Scientific Reports*, doi.org/10.1038/s41598-019-52437-6

- Chepfer, H., Cesana, G., Winker, D., Getzewich, B., Vaughan, M., Liu, Z. (2013). Comparison of Two Difference Cloud Climatologies Derived from CALIOP-Attenuated Backscattered Measurements (Level 1): The CALIPSO-ST and the CALIPSO-GOCCP. *Journal of Atmospheric and Oceanic Technology*, 30, pp. 725-744.
- Chepfer, H., Noel, V., Chiriaco, M., Wielicki, B., Winker, D., Loeb, N., & Wood, R. (2018). The potential of a multidecade spaceborne lidar record to constrain cloud feedback. *Journal of Geophysical Research: Atmospheres*, 123, pp. 5433–5454, <https://doi.org/10.1002/2017JD027742>
- Chepfer, H., Noel, V., Winker, D., Chiriaco, M. (2014). Where and when will we observe cloud changes due to climate warming? *Geophysical Research Letters*, 41, pp. 8387–8395, doi:10.1002/2014GL061792.
- Clement, A. C., Burgman, R., Norris, J. R. (2009). Observational and Model Evidence for Positive Low-Level Cloud Feedback. *Science*, 325, pp. 460-464.
- Dee, D. P., Uppala, S. M., Simmons, A. J., Berrisford, P., Poli, P., Kobayashi, S., Andrae, U., Balmaseda, M. A., Balsamo, G., Bauer, P., Bechtold, P., Beljaars, A. C. M., van de Berg, L., Bidlot, J., Bormann, N., Delsol, C., Dragani, R., Fuentes, M., Geer, A. J., Haimberger, L., Healy, S. B., Hersbach, H., Hólm, E. V., Isaksen, L., Kållberg, P., Köhler, M., Matricardi, M., McNally, A. P., Monge-Sanz, B. M., Morcrette, J.-J., Park, B.-K., Peubey, C. de Rosnay, P., Tavolato, C., Thépaut, N.-J., Vitart, F. (2011). The ERA-Interim reanalysis: configuration and performance of the data assimilation system. *Q. J. R. Meteorol. Soc.*, 137, pp. 553-597.
- Dessler, A. E. (2010). A Determination of the Cloud Feedback from Climate Variations over the Past Decade. *Science*, 330, pp. 1523-1527.
- Dessler, A. E. (2013). Observations of Climate Feedbacks over 2000-10 and Comparisons to Climate Models. *Journal of Climate*, 26, pp. 333-342, DOI: 10.1175/JCLI-D-11-00640.1
- Dewey, M., Goldblatt, C. (2018). Evidence for Radiative-Convective Bistability in Tropical Atmospheres. *Geophysical Research Letters*, pp. 1-9., doi: 10.1029/2018GL078903.
- Dufresne, J.-L., Bony, S. (2008). An Assessment of the Primary Sources of Spread of Global Warming Estimates from Coupled Atmosphere-Ocean Models. *Journal of Climate*, 21, pp. 5135-5144, DOI: 10.1175/2008JCLI2239.1
- Eastman, R., Warren, S. G., Hahn, C. J. (2011). Variations in Cloud Cover and Cloud Types over the Ocean from Surface Observations, 1945-2008. *Journal of Climate*, 24, pp. 5914-5934.
- ERA5 online documentation: latest access: May 5, 2020.  
<https://confluence.ecmwf.int/display/CKB/ERA5%3A+data+documentation#ERA5:datadocumentation-Observations>
- Evans, J. L., Webster, C. C. (2014). A variable sea surface temperature threshold for tropical convection. *Australian Meteorological and Oceanographic Journal*, 64, pp. 1-8.

- Eymard, L. Gheudin, M., Laborie, P., Sirou, F. Le Gac, C., Vinson, J. P., Franquet, S. Desbois, M., Karbou, F., Roca, R., Scott, N., Waldteufel, P. (2002). The SAPHIR humidity sounder. *Notes Act. Instrum. de l'IPSL* 24.
- Fasullo, J.T., Trenberth, K.E. (2012). A less cloudy future: the role of subtropical subsidence in climate sensitivity. *Science*, 338, pp. 792–794.
- Findeisen, W. (1938). Kolloid-meteorologische Vorgänge bei Neiderschlags-bildung. *Meteor. Z.*, 55, pp. 121–133
- Fisher, R. A. (1926). The Arrangement of Field Experiments, *Journal of the Ministry of Agriculture of Great Britain*, 33, 503-513
- Fisher, R. A. (1956). *Statistical Methods and Scientific Inference* New York: Hafner
- Fu, Q. Baker, M., Hartmann, D. L. (2002) Tropical cirrus and water vapor: an effective Earth infrared iris feedback?, *Atmospheric Chemistry and Physics*, 2, pp. 31-37.
- Gettelman, A., Collins, W. D., Fetzer, E. J., Eldering, A., Irion, F. W., Duffy, P. B., Bala, G. (2006). Climatology of Upper-Tropospheric Relative Humidity from the Atmospheric Infrared Sounder and Implications for Climate. *Journal of Climate*, 19, pp. 6104-6121.
- GEWEX (2012). GEWEX Plans for 2013 and Beyond, GEWEX Science Questions.
- Goldblatt, C., Robinson, T. D., Zahnle, K. J., Crisp, D. (2013). Low simulated radiation limit for runaway greenhouse climates. *Nature Geoscience*, doi: 10.1038/NNGEO1892.
- Goosse, H., Kay, J. E., Armour, K. C., Bodas-Salcedo, A., Chepfer, H., Docquier, D., Jonko, A., Kushner, P. J., Lecomte, O., Massonnet, F., Park, H.-S., Pithan, F., Svensson, G., Vancoppenolle, M. (2018). Quantifying climate feedbacks in polar regions. *Nature Communications*, 9, DOI: 10.1038/s41467-018-04173-0
- Gordon, N. D., Klein, S. A. (2014). Low-cloud optical depth feedback in climate models. *Journal of Geophysical Research: Atmospheres*, 119, pp. 6052-6065.
- Greenwald, T. J., Christopher, S. A. (2002). Effect of cold clouds on satellite measurements near 183 GHz. *Journal of Geophysical Research*, 107, pp. 4170.
- Gregory, J. M., Andrews, T. (2016). Variation in climate sensitivity and feedback parameters during the historical period, *Geophysical Research Letters*, 43, pp. 3911-3920, doi:10.1002/2016GL068406.
- Gregory, J. M., Ingram, W. J., Palmer, M. A., Jones, G. S., Stott, P. A., Thorpe, R. B., Lowe, J. A., Johns, T. C., Williams, K. D. (2004). A new method for diagnosing radiative forcing and climate sensitivity. *Geophysical Research Letters*, 31, doi:10.1029/2003GL018747
- Guzman, R. Chepfer, H., Noel, V., Vaillant de Guélis, T., Kay, J. E., Raberanto, P., Cesana, G., Vaughan, M. A., Winker, D. M. (2017), Direct atmosphere opacity observations from CALIPSO provide new constraints on cloud-radiation interactions. *Journal of Geophysical Research: Atmospheres*, 122, pp. 1066-1085.
- Hahn, C. J. Warren, S. G., London, J., Chervin, R.M., Jenne, R. (1990). Atlas of simultaneous occurrence of different cloud types over the ocean. NCAR Tech. Note TN-201+STR, 212 pp.

- Hallberg, R., Inamdar, A. K. (1993). Observations of Seasonal Variations in Atmospheric Greenhouse Trapping and Its Enhancement at High Sea Surface Temperature. *Journal of Climate*, 6, pp. 920-931.
- Hang, Y., L'Ecuyer, T., Henderson, D. S., Matus, A. V. (2019). Reassessing the Effect of Cloud Type on Earth's Energy Balance in the Age of Active Spaceborne Observations. Part II: Atmospheric Heating. *Journal of Climate*, 32, pp. 6219-6236, DOI: 10.1175/JCLI-D-18-0754.1
- Hansen, J., Lacis, A., Rind, D., Russell, G., Stone, P., Fung, I., Ruedy, R., Lerner, J. (1984). Climate Sensitivity: Analysis of Feedback Mechanisms. *Climate Processes and Climate Sensitivity*, 5, pp. 130-163.
- Hartmann, D. L., Larson, K. (2002). An important constraint on tropical cloud - climate feedback. *Geophysical Research Letters*, 29, doi:10.1029/2002GL015835
- Hartmann, D. L., Michelsen, M. L. (2002). No Evidence for Iris. *Bulletin of American Meteorological Society*, pp. 249-254.
- Haynes, J. M., L'Ecuyer, T. S., Stephens, G. L., Miller, S. D., Mitrescu, C., Wood, N. B., Tanelli, S. (2009). Rainfall retrieval over the ocean with spaceborne W-band radar., *Journal of Geophysical Research*, 114, pp. 1-18.
- Haynes, J. M., L'Ecuyer, T. S., Vane, D., Stephens, G., Reinke, D. (2013). Level 2C-Precipitation Column Algorithm Product Process Description and Interface Control Document. downloaded at:  
[http://www.cloudsat.cira.colostate.edu/sites/default/files/products/files/2C-PRECIP-COLUMN\\_PDICD.P2\\_R04.20130124.pdf](http://www.cloudsat.cira.colostate.edu/sites/default/files/products/files/2C-PRECIP-COLUMN_PDICD.P2_R04.20130124.pdf)
- Held, I. M., Shell, K. M. (2012). Using Relative Humidity as a State Variable in Climate Feedback Analysis. *Journal of Climate*, 25, pp. 2578-2582. DOI: 10.1175/JCLI-D-11-00721.1
- Held, I. M., Soden, B. (2000). Water Vapor Feedback and Climate Warming. *Annu. Rev. Energy Environ.*, 25, pp. 441-475.
- Henderson, D. S., L'Ecuyer, T., Stephens, G., Partain, P., Sekiguchi, M. (2012). A Multisensor Perspective on the Radiative Impacts of Clouds and Aerosols. *Journal of Applied Meteorology and Climatology*, 52, pp. 853-871, DOI: 10.1175/JAMC-D-12-025.1
- Hersbach, H., Dee, D. (2016). ERA5 reanalysis is in production, *ECMWF Newsletter* No. 147, 7
- Hoffmann, L., Günther, G., Li, D., Stein, O., Wu, X., Griessbach, S., Heng, Y., Konopka, P., Müller, R., Vogel, B., Wright, J. S. (2018). From ERA-Interim to ERA5: considerable impact of ECMWF's next-generation reanalysis on Lagrangian transport simulations. *Atmospheric Chemistry and Physics*, pp. 1-38. <https://doi.org/10.5194/acp-2018-1199>
- Hogan, R. J., Francis, P. N., Flentje, H., Illingworth, A. J., Quante, M., Pelon, J. (2003). Characteristics of mixed-phase clouds. I: Lidar, radar and aircraft observations from CLARE'98. *Quarterly Journal of the Royal Meteorological Society*, 129, pp. 2089–2116, doi: 10.1256/qj.01.208

Holloway, C. E., Neelin, J. D. (2009). Moisture Vertical Structure, Column Water Vapor, and Tropical Deep Convection. *Journal of the Atmospheric Sciences*, 66, pp. 1665-1683.

Holton, J. R., Hakim, G. J. (2013). *An Introduction to Dynamic Meteorology*, 5<sup>th</sup> Edition, Elsevier, Waltham, MA.

Houze, R. A., Rasmussen, K. L., Zuluaga, M. D., Brodzik, S. R. (2015). The variable nature of convection in the tropics and subtropics: A legacy of 16 years of the Tropical Rainfall Measuring Mission satellite. *Reviews of Geophysics*, pp. 994-1021., doi: 10.1002/2015GR000488.

Höjgård-Olsen, E., Brogniez, H., Chepfer, H. (2020). Observed Evolution of the Tropical Atmospheric Water Cycle with Sea Surface Temperature. *Journal of Climate*, 33, pp. 3449-3470, DOI: 10.1175/JCLI-D-19-0468.1

Igel, M. R., Drager, A. J., van den Heever, S. C. (2014). A CloudSat cloud object partitioning technique and assessment and integration of deep convective anvil sensitivities to sea surface temperature. *Journal of Geophysical Research: Atmospheres*, 119, 10,515–10,535, doi:10.1002/2014JD021717.

Im, E., Sadowy, G. (2000). Cloud Profiling Radar (CPR) for the CloudSat Mission, *IEEE Xplore*, DOI: 10.1109/IGARSS.2000.860259

Im, E., Wu, C., Durden, S. L. (2005). Cloud Profiling Radar for the *CloudSat* Mission. *IEEE Aerospace and Electronic Systems Magazine*, DOI: 10.1109/MAES.2005.1581095

Inamdar, A. K., Ramanathan, V. (1998). Tropical and global scale interactions among water vapor, atmospheric greenhouse effect and surface temperature. *Journal of Geophysical Research*, 103, pp. 32177-32194.

Ingram, W. (2013). A new way of quantifying GCM water vapor feedback. *Climate Dynamics*, 40, pp. 913–924, DOI 10.1007/s00382-012-1294-3

IPCC 2013: *Climate Change 2013: The Physical Science Basis. Contribution to Working Group I to the Fifth Assessment Report of the Intergovernmental Panel on Climate Change* [Stocker, T. F., Qin, D., Plattner, G.-K., Tignor, M., Allen, S. K., Borschung, J., Nauels, A., Xia, Y., Bex, V., Midgley, P. M. (eds.)]. Cambridge University Press, Cambridge, United Kingdom and New York, NY, USA, doi: 10.1017/CBO9781107415324.

John, V. O., Holl, G., Allan, R. P., Buehler, S. A., Parker, D. E., Soden, B. J. (2011). Clear-sky biases in satellite infrared estimates of upper tropospheric humidity and its trends. *Journal of Geophysical Research*, 116, doi:10.1029/2010JD015355

Johnson, N. C., Xie, S.-P. (2010). Changes in the sea surface temperature threshold for tropical convection. *Nature Geoscience*, 3, pp. 842-845.

Kamae, Y., Ogura, T., Shiogama, H., Watanabe, H. (2016). Recent progress toward reducing the uncertainty in tropical low cloud feedback and climate sensitivity: review. *Geoscience Letters*, 3, DOI 10.1186/s40562-016-0053-4

- Kay, J. E., L'Ecuyer, T., Pendergrass, A., Chepfer, H., Guzman, R., Yettella, V. (2018). Scale-Aware and Definition-Aware Evaluation of Modeled Near-Surface Precipitation Frequency Using CloudSat Observations. *Journal of Geophysical Research: Atmospheres*, 123, 4294–4309. <https://doi.org/10.1002/2017JD028213>
- Kendall, M. G. (1945). The Treatment of Ties in Ranking Problems, *Biometrika* Vol. 33, No. 3, pp. 239-251.
- Klein, S. A., Hall, A. (2015). Emergent Constraints for Cloud Feedbacks. *Curr. Clim. Change. Rep.*, 1, pp. 276–287, DOI 10.1007/s40641-015-0027-1
- Klein, S. A., Hall, A., Norris, J. R., Pincus, R. (2017). Low-Cloud Feedbacks from Cloud Controlling Factors: A Review. *Survey of Geophysics*, 38, pp. 1307–1329, [doi.org/10.1007/s10712-017-9433-3](https://doi.org/10.1007/s10712-017-9433-3)
- Konsta, D., Chepfer, H., Dufresne, J.-L. (2012). A process oriented characterization of tropical oceanic clouds for climate model evaluation, based on a statistical analysis of daytime A-train observations. *Clim. Dyn.*, 39, pp. 2091-2108.
- Kuang, Z., Hartmann, D. L. (2007). Testing the Fixed Anvil Temperature Hypothesis in a Cloud-Resolving Model. *Journal of Climate*, 20, DOI: 10.1175/JCLI4124.1
- Kumar, A., Jha, B., L'Heureux, M. (2010). Are tropical SST trends changing the global teleconnection during La Niña? *Geophysical Research Letters*, 37, [doi:10.1029/2010GL043394](https://doi.org/10.1029/2010GL043394)
- L'Ecuyer, T., Stephens, G. L. (2002). An Estimation-Based Precipitation Retrieval Algorithm for Attenuating Radars. *Journal of Applied Meteorology*, 41, pp. 272-285.
- Lebsock, M. (2018). Level 2C RAIN-PROFILE Product Process Description and Interface Control Document. downloaded at: [http://www.cloudsat.cira.colostate.edu/sites/default/files/products/files/2C-RAIN-PROFILE\\_PDICD.P1\\_R05.rev0\\_.pdf](http://www.cloudsat.cira.colostate.edu/sites/default/files/products/files/2C-RAIN-PROFILE_PDICD.P1_R05.rev0_.pdf)
- Lebsock, M. D., Kummerow, C. Stephens, G. L. (2010). An Observed Tropical Oceanic Radiative–Convective Cloud Feedback. *Journal of Climate*, 23, pp. 2065-2078, DOI: 10.1175/2009JCLI3091.1
- Lefebvre, A., Hélière, A., Wallace, K., Nakatsuka, H., Tomita, E. (2017). The ESA EarthCARE mission development status. IEEE International Geoscience and Remote Sensing Symposium (IGARSS), Fort Worth, TX, pp. 4234-4237, doi: 10.1109/IGARSS.2017.8127937.
- Leng, L., Zhang, T., Kleinman, L., Zhu, W. (2007). Ordinary Least Square Regression, Orthogonal Distance Regression, Geometric Mean Regression and their Applications in Aerosol Science, *Journal of Physics: Conference Series*, IOP Publishing, 78
- Li, J.-L. F., Waliser, D. E., Chen, W.-T., Guan, B., Kubar, T., Stephens, G., Ma, H.-Y., Deng, M., Donner, L., Seman, C., Horowitz, L. (2012). An observationally based evaluation of cloud ice water in CMIP3 and CMIP5 GCMs and contemporary reanalyses using contemporary satellite data. *Journal of Geophysical Research*, 117, doi: 10.1029/2012/2012JD017640

- Li, R. L., Storelvmo, T., Fedorov, A. V., Choi, Y.-S. (2019). A Positive IRIS Feedback: Insights from Climate Simulations with Temperature-Sensitive Cloud-Rain Conversion. *Journal of Climate*, 32, pp. 5305-5324.
- Lin, B. L., Wielicki, B. A., Chambers, L. H., Hu, Y. Xu, K.-M. (2002). The Iris Hypothesis: A Negative or Positive Cloud Feedback? *Journal of Climate*, 15.
- Lin, B. L., Wielicki, B. A., Minnis, P., Chambers, L., Xu, K.-M., Hu, Y. (2006). The Effect of Environmental Conditions on Tropical Deep Convective Systems Observed from the TRMM Satellite. *Journal of Climate*, 19, pp. 5745-5761.
- Lin, B. L., Wong, T., Wielicki, B. A., Hu, Y. (2004). Examination of the Decadal Tropical Mean ERBS Nonscanner Radiation Data for the Iris Hypothesis. *Journal of Climate*, 17, pp. 1239-1246.
- Lindzen, R. S., Chou, M.-D., Hou, A. Y. (2001). Does the Earth Have an Adaptive Infrared Iris?. *Bulletin of the American Meteorological Society*, 82, pp. 417-432.
- Liou, K. N., (2002). *An Introduction to Atmospheric Radiation*, 2<sup>nd</sup> Edition, Academic Press: San Diego, CA.
- Liu, C., Zipser, E. (2014). Differences between the Surface Precipitation Estimates from the TRMM Precipitation Radar and Passive Microwave Radiometer Version 7 Products. *Journal of Hydrometeorology*, 15, DOI: 10.1175/JHM-D-14-0051.1
- Liu, Z. (2015). Comparison of versions 6 and 7 3-hourly TRMM multi-satellite precipitation analysis (TMPA) research products. *Atmospheric Research*, 163, pp. 91–101.
- Loeb, N. G., Thorsen, T. J., Norris, J. R., Wang, H., Su, W. (2018). Changes in Earth's Energy Budget during and after the "Pause" in Global Warming: An Observational Perspective. *Climate*, 6, 62; doi:10.3390/cli6030062
- Loeb, N. G., Wang, H., Allan, R., Andrews, T., Armour, K., Cole, J. N. S., Dufresne, J.-L., Forster, P., Gettelman, A., Guo, H., Mauritsen, T., Ming, Y., Paynter, D., Proistosescu, C., Stuecker, M. F., Willén, U., Wyser, K. (2020). New Generation of Climate Models Track Recent Unprecedented Changes in Earth's Radiation Budget Observed by CERES. *Geophysical Research Letters*, 47, e2019GL086705. <https://doi.org/10.1029/2019GL086705>
- Lolli, B., Gasperini, P. (2012). A comparison among general orthogonal regression methods applied to earthquake magnitude conversions, *Geophysical Journal International*, 190, 1135-1151, doi: 10.1111/j.1365-246X.2012.05530.x
- Luo, Z., Rossow, W. B. (2004). Characterizing Tropical Cirrus Life Cycle, Evolution, and Interaction with Upper-Tropospheric Water Vapor Using Lagrangian Trajectory Analysis of Satellite Observations. *Journal of Climate*, 17, pp. 4541-4563.
- Läderach, A., Raible, C. C. (2013). Lower-tropospheric humidity: climatology, trends and the relation to the ITCZ. *Tellus A*, 65, <http://dx.doi.org/10.3402/tellusa.v65i0.20413>
- Marshall, J. S., Palmer, W. M. (1948). The distribution of raindrops size. *Journal of Meteorology*, 5, pp. 165-166.

- Masunaga, H. (2014). Free-tropospheric moisture convergence and tropical convective regimes. *Geophysical Research Letters*, pp. 8611-8618., doi: 10.1002/2014GL062301.
- Matus, A. V., L'Ecuyer, T. (2017). The role of cloud phase in Earth's radiation budget. *J. Geophys. Res. Atmos.*, 122, pp. 2559–2578, doi:10.1002/2016JD025951.
- Mauritsen, T., Stevens, B. (2015). Missing iris effect as a possible cause of muted hydrological change and high climate sensitivity in models. *Nature Geoscience*, 8, pp. 346-351.
- McGee, D., Donohoe, A., Marshall, J., Ferreira, D. (2014). Changes in ITCZ location and cross-equatorial heat transport at the Last Glacial Maximum, Heinrich Stadial 1, and the mid-Holocene. *Earth and Planetary Science Letters*, 390, pp. 69-79, <http://dx.doi.org/10.1016/j.epsl.2013.12.043>
- Megha-Tropiques Level 1 Products Handbook (2015). 1<sup>st</sup> Edition. Ref.: TRO-0-NT-2860-CNES, CNES. downloaded at: [http://www.icare.univ-lille1.fr/projects\\_data/mt/docs/megha-tropiques\\_handbook\\_final\\_09\\_2015.pdf](http://www.icare.univ-lille1.fr/projects_data/mt/docs/megha-tropiques_handbook_final_09_2015.pdf)
- Myers, T. A., Norris, J. R. (2013). Observational Evidence That Enhanced Subsidence Reduces Subtropical Marine Boundary Layer Cloudiness. *Journal of Climate*, 26, DOI: 10.1175/JCLI-D-12-00736.1
- Myers, T. A., Norris, J. R. (2015). On the Relationships between Subtropical Clouds and Meteorology in Observations and CMIP3 and CMIP5 Models. *Journal of Climate*, 28, DOI: 10.1175/JCLI-D-14-00475.1
- Neelin, J. D., Peters, O., Hales, K. (2009). The Transition to Strong Convection. *Journal of Atmospheric Sciences*, 66, pp. 2367-2384, DOI: 10.1175/2009JAS2962.1
- Noel, V., Chepfer, H., Chiriaco, M., Yorks, J. (2018). The diurnal cycle of cloud profiles over land and ocean between 51°S and 51°N, seen by the CATS spaceborne lidar from the International Space Station. *Atmospheric Chemistry and Physics*, <https://doi.org/10.5194/acp-2018-214>
- Orlanski, I. (1975). A Rational Subdivision of Scales for Atmospheric Processes. *Bulletin of the American Meteorological Society*, 56, pp. 527-530.
- Peters, O., Neelin, J. D. (2006). Critical phenomena in atmospheric precipitation. *Nature Physics*, 2, pp. 393-396.
- Pierrehumbert, R. T. (1995). Thermostats, Radiator Fins, and the Local Runaway Greenhouse. *Journal of Atmospheric Sciences*, 52, pp. 1784-1806.
- Pithan, F., Mauritsen, T. (2013). Correspondence: Comments on “Current GCMs’ Unrealistic Negative Feedback in the Arctic”. *Journal of Climate*, 26, pp. 7783-7787, DOI: 10.1175/JCLI-D-12-00331.1
- Po-Chedley, S., Armour, K. C., Bitz, C. M., Zelinka, M. D., Santer, B. D., Fu, Q. (2018). Sources of Intermodel Spread in the Lapse Rate and Water Vapor Feedbacks. *Journal of Climate*, pp. 3187-3206, DOI: 10.1175/JCLI-D-17-0674.1

- Qu, X., Hall, A., Klein, S. A., Caldwell, P. M. (2014). On the spread of changes in marine low cloud cover in climate model simulations of the 21st century. *Climate Dynamics*, 42, pp. 2603–2626, DOI 10.1007/s00382-013-1945-z
- Qu, X., Hall, A., Klein, S. A., DeAngelis, A. M. (2015). Positive tropical marine low-cloud cover feedback inferred from cloud-controlling factors. *Geophysical Research Letters*, 42, pp. 7767–7775, doi:10.1002/2015GL065627.
- Ramanathan, V. Collins, W. (1991). Thermodynamic regulation of ocean warming by cirrus clouds deduced from observations of the 1987 El Niño. *Nature*, 351, pp. 27–32.
- Rapp, A. D., Kummerow, C., Berg, W., Griffith, B. (2005). An Evaluation of the Proposed Mechanism of the Adaptive Infrared Iris Hypothesis Using TRMM VIRS and PR Measurements. *Journal of Climate*, 18, pp. 4185–4194.
- Raval, A., Ramanathan, V. (1989). Observational determination of the greenhouse effect. *Nature*, 42, pp. 758–761.
- Roca, R., Alexander, L. V., Potter, G., Bador, M., Jucá, R., Contractor, S., Bosilovich, M. G., and Cloché, S. (2019). FROGS: a daily  $1^\circ \times 1^\circ$  gridded precipitation database of rain gauge, satellite and reanalysis products, *Earth System Science Data*, 11, pp. 1017–1035, <https://doi.org/10.14768/06337394-73A9-407C-9997-0E380DAC5598>
- Roca, R., Brogniez, H., Chambon, P., Chomette, O., Cloché, S., Gosset, M. E., Mahfouf, J.-F., Raberanto, P., Viltard, N. (2015). The Megha-Tropiques Mission: a review after three years in orbit. *Frontiers in Earth Science*, 3, pp. 1–14.
- Roca, R., Viollier, M., Picon, L., Desbois, M. (2000). A multisatellite analysis of deep convection and its moist environment over the Indian Ocean during the winter monsoon. *Journal of Geophysical Research*, 107, doi: 10.1029/2000JD000040.
- Rose, B. E. J., Rayborn, L. (2016). The Effects of Ocean Heat Uptake on Transient Climate Sensitivity. *Curr Clim Change Rep*, 2, pp. 190–201, DOI 10.1007/s40641-016-0048-4
- Ross, R. J., Elliott, W. P., Seidel, D. J. (2002). Lower-Tropospheric Humidity-Temperature Relationships in Radiosonde Observations and Atmospheric General Circulation Models. *Journal of Hydrometeorology*, 3, pp. 26–38.
- Sabin, T. P., Babu, C. A., Joseph, P.V. (2013). SST-convection relation over tropical oceans. *International Journal of Climatology*, 33, pp. 1424–1435.
- Schaerer G, Wilheit T. 1979. A passive microwave technique for profiling of atmospheric water vapor. *Radio Sci.* 14: 371–375.
- Seeley, J. T., Jeevanjee, N., Romps, D. M. (2019). FAT or FiTT: Are anvil clouds or the tropopause temperature invariant?. *Geophysical Research Letters*, 46, pp. 1842–1850., doi.org/10.1029/2018GL080096
- Seinfeld, J. H., Pandis, S. N. (2006). *Atmospheric Chemistry and Physics From Air Pollution to Climate Change*, 2<sup>nd</sup> Edition, Wiley, Hoboken, NJ.
- Sherwood, S. C., Bony, S., Dufresne, J.-L. (2014). Spread in model climate sensitivity traced to atmospheric convective mixing. *Nature*, 505, pp. 37–42.

Shi, L., Bates, J. J. (2011). Three decades of intersatellite-calibrated High-Resolution Infrared Radiation Sounder upper tropospheric water vapor. *Journal of Geophysical Research*, 116, doi:10.1029/2010JD014847

Sivira, R. G., Brogniez, H., Dufour, C., Cloché, S. (2017). Megha-Tropiques Product Definition Document Instantaneous non-precipitating conditions Level 2 products Relative Humidity profile Derived from SAPHIR SAPHIR-L2-RH Version 1 Release 5. downloaded at: <http://meghatropiques.ipsl.polytechnique.fr/download/product-definition-document-instantaneous-level-2-products-rh-derived-from-saphir/>

Sivira, R. G., Brogniez, H., Mallet, C., Oussar, Y. (2015). A layer-average relative humidity profile retrieval for microwave observations: design and results for the Megha-Tropiques payload. *Atmospheric Measurement Techniques*, 8, pp. 1055-1071.

Smalley, M., L'Ecuyer, T., Lebsock, M., Haynes, J. (2014). A Comparison of Precipitation Occurrence from the NCEP Stage IV QPE Product and the *CloudSat* Cloud Profiling Radar. *Journal of Hydrometeorology*, 15, pp. 444-458.

Smith, S. R., Alory, G., Andersson, A. Asher, W., Baker, A., Berry, D. I., Drushka, K., Figureskey, D., Freeman, E., Holthus, P., Jickells, T., Kleta, H., Kent, E. C., Kolodziejczyk, Kramp, M., Loh, Z., Poli, P., Schuster, U., Steventon, E., Swart, S., Tarasova, O., Petit de la Villéon, L., Vinogradova-Shiffer, N. (2019). Ship-Based Contributions to Global Ocean, Weather, and Climate Observing Systems. *Frontiers in Marine Science*, 6, doi: 10.3389/fmars.2019.00434

Soden, B. J., Held, I. M. (2006). An Assessment of Climate Feedbacks in Coupled Ocean–Atmosphere Models. *Journal of Climate*, 19, pp. 3354-3360.

Stephens, G. L. (2005). Cloud Feedbacks in the Climate System: A Critical Review. *Journal of Climate*, 18, pp. 237-273.

Stephens, G. L., Kahn, B. H., Richardson, M. (2016). The Super Greenhouse Effect in a Changing Climate. *Journal of Climate*, 29, pp. 5469-5482.

Stephens, G. L., L'Ecuyer, T., Forbes, R., Gettleman, A., Golaz, J.-C., Bodas-Salcedo, A., Suzuki, K., Gabriel, P., Haynes, J. (2010). Dreary state of precipitation in global models. *Journal of Geophysical Research*, 115, doi:10.1029/2010JD014532

Stephens, G. L., Li, J., Wild, M., Clayson, C. A., Loeb, N., Kato, S., L'Ecuyer, T., Stackhouse Jr., P. W., Lebsock, M., Andrews, T. (2012). An update on Earth's energy balance in light of the latest global observations. *Nature Geoscience*, 5, pp. 691-696, DOI: 10.1038/NGEO1580

Stephens, G. L., O'Brien, D., Webster, P. J., Pilewski, P., Kato, S., Li, J.-I. (2015). The albedo of Earth, *Rev. Geophys.*, 53, DOI: 141–163, doi:10.1002/2014RG000449.

Stephens, G. L., Tsay, S.-C. (1990). On the cloud absorption anomaly. *Quarterly Journal of the Royal Meteorological Society*, pp. 671-704.

Stevens, B., Brogniez, H., Kiemle, C., Lacour, J-L, Crevoisier, C., Kiliani, J. (2017). Structure and Dynamical Influence of Water Vapor in the Lower Tropical Troposphere. *Surv. Geophys.*, 38, pp. 1371-197.

- Stevens, B., Sherwood, S. C., Bony, S., Webb, M. J. (2016). Prospects for narrowing bounds on Earth's equilibrium climate sensitivity, *Earth's Future*, 4, pp. 512-522, doi:10.1002/2016EF000376.
- Steyn, D. G., Oke, T. R., Hay, J. E., Knox, J. L. (1981). On the Scales in Meteorology and Climate.
- Stout, G. E., Mueller, E. A. (1968). Survey of Relationships Between Rainfall Rate and Radar Reflectivity in the Measurement of Precipitation. *Journal of Applied Meteorology*, 7, pp. 465-474.
- Stubenrauch, C. J., Chédin, A., Rädcl, G., Scott, N. A., Serrar, S. (2006). Cloud Properties and Their Seasonal and Diurnal Variability from TOVS Path-B. *Journal of Climate*, 19, pp. 5531-5553.
- Su, H., Jiang, J. H. (2013). Tropical Clouds and Circulation Changes during the 2007/08 and 2009/10 El Niños. *Journal of Climate*, 26, pp. 399-413.
- Su, H., Jiang, J. H., Gu, Y., Neelin, J. D., Kahn, B. H., Feldman, D., Yung, Y. L., Waters, J. W., Livesey, N. J., Santee, M. L., Read, W. G. (2008). Variations of tropical upper tropospheric clouds with sea surface temperature and implications of radiative effects. *Journal of Geophysical Research*, 113, pp. 1-13.
- Su, H., Jiang, J. H., Gu, Y., Neelin, J. D., Shen, T. J., Zhai, C., Yue, Q., Wang, Z., Huang, L., Choi Y.-S., Stephens, G. L., Yung, Y. L. (2017). Tightening of tropical ascent and high clouds key to precipitation change in a warmer climate. *Nature Communications*, pp. 1-9., doi: 10.1038/ncomms15771.
- Su, H., Jiang, J. H., Teixeira, J., Gettelman, A., Huang, X., Stephens, G. L., Vane, D., Perun, V. S. (2011). Comparison of regime-sorted tropical cloud profiles observed by CloudSat with GEOS5 analyses and two general circulation model simulations. *Journal of Geophysical Research*, 116, doi:10.1029/2010JD01497
- Takahashi, H., Su, H., Jiang, J. H., Luo, Z. J., Xie, S.-P., Hafner, J. (2013). Tropical water vapor variations during the 2006-07 and 2009-10 El Niños: Satellite observations and GFDL AM2.1 simulation. *Journal of Atmospheric Research: Atmospheres*, 118, pp. 8910-8920.
- Tanelli, S., Durden, S. L. Im, E., Pak, K. S., Reinke, D. G., Partain, P., Haynes, J. L., Marchand, R. T. (2008). CloudSat's Cloud Profiling Radar After Two Years in Orbit: Performance, Calibration, and Processing. *IEEE Trans. Geosci. Remote Sens.*, 46, 3560–3573.
- Trenberth, K. E., Stepaniak, D.P., Caron, J. M. (2000). The global monsoon as seen through the divergent atmospheric circulation. *Journal of Climate*, 13(22):3969–3993.
- Vaillant de Guélis, T., Chepfer, H., Guzman, R., Bonazzola, M., Winker, D. M., Noel, V. (2018). Space lidar observations constrain longwave cloud feedback. *Nature Scientific Reports*, 8, DOI:10.1038/s41598-018-34943-1
- Vaillant de Guélis, T., Chepfer, H., Noel, V., Guzman, R., Dubuisson, P., Winker, D. M., Kato, S. (2017). The link between outgoing longwave radiation and the altitude at which a spaceborne lidar beam is fully attenuated. *Atmospheric Measurement Techniques*, 10, pp. 4659-4685.

- Vial, J. Dufresne, J.-L., Bony, S. (2013). On the interpretation of inter-model spread in CMIP5 climate sensitivity estimates. *Climate Dynamics*, 41, pp. 3339–3362, DOI 10.1007/s00382-013-1725-9
- Waliser, D. E., Graham, N. E., Gautier, C. (1993). Comparison of the High Reflective Cloud and Outgoing Longwave Radiation Datasets for Use in Estimation Tropical Deep Convection. *Journal of Climate*, 6, pp. 331-353.
- Wallace, J. M., Hobbs, P. V. (2006). *Atmospheric Science An Introductory Survey*, Elsevier, Burlington, MA.
- Wegener, A. (1911). *Thermodynamik der Atmosphäre*. J. A. Barth.
- Wild, M., Folini, D., Schär, C., Loeb, N., Dutton, E. G., König-Langlo, G. (2013). The global energy balance from a surface perspective. *Climate Dynamics*, 40, pp. 3107–3134, DOI 10.1007/s00382-012-1569-8
- Winker, D. M., Vaughan, M. A., Omar, A., Hu, Y., Powell, K. A. (2009). Overview of the CALIPSO Mission and CALIOP Data Processing Algorithms. *Journal of Atmospheric and Oceanic Technology*, 26, pp. 2310-2323.
- Zelinka, M. D., Hartmann, D. L. (2010). Why is longwave cloud feedback positive?. *Journal of Geophysical Research*, 115, doi:10.1029/2010JD013817
- Zelinka, M. D., Hartmann, D. L. (2011). The observed sensitivity of high clouds to mean surface temperature anomalies in the tropics. *Journal of Geophysical Research*, 116, doi:10.1029/2011JD016459
- Zelinka, M. D., Klein, S. A., Hartmann, D. L. (2012). Computing and Partitioning Cloud Feedbacks Using Cloud Property Histograms. Part II: Attribution to Changes in Cloud Amount, Altitude, and Optical Depth. *Journal of Climate*, 25, pp. 3736-3754, DOI: 10.1175/JCLI-D-11-00249.1
- Zelinka, M. D., Klein, S. A., Taylor, K. E., Andrews, T., Webb, M., Gregory, J. M., Forster, P. M. (2013). Contributions of Different Cloud Types to Feedbacks and Rapid Adjustments in CMIP5. *Journal of Climate*, pp. 5007-5027, DOI: 10.1175/JCLI-D-12-00555.1
- Zelinka, M. D., Myers, T. A., McCoy, D. T., Po-Chedley, S., Caldwell, P. M., Ceppi, P., et al. (2020). Causes of higher climate sensitivity in CMIP6 models. *Geophysical Research Letters*, 47, e2019GL085782. <https://doi.org/10.1029/2019GL085782>
- Zelinka, M. D., Zhou, C., Klein, S. A. (2016). Insights from a refined decomposition of cloud feedbacks, *Geophys. Res. Lett.*, 43, pp. 9259–9269, doi:10.1002/2016GL069917.
- Zhai, C., Jiang, J. H., Su, H. (2015). Long-term cloud change imprinted in seasonal cloud variation: More evidence of high climate sensitivity. *Geophysical Research Letters*, 42, 8729–8737, doi:10.1002/2015GL065911
- Zhou, C., Zelinka, M. D., Klein, S. A. (2016). Impact of decadal cloud variations on the Earth's energy budget. *Nature Geoscience*, DOI: 10.1038/NGEO2828



**Titre :** Observations du cycle de l'eau atmosphérique tropicale et de ses variations avec la température de surface de la mer, à l'aide d'une constellation de satellites.

**Mots clés :** Observations, Humidité, Nuages, Température, Satellites, Tropiques

**Résumé :** Une meilleure compréhension de la façon dont le cycle de l'eau atmosphérique tropicale réagit au changement climatique nécessite une vision observationnelle complète de ses principales variables.

Ce travail construit un ensemble de données synergiques d'observations instantanées colocalisées de l'humidité relative (SAPHIR), des caractéristiques des nuages (CALIOP) et des précipitations proches de la surface (CPR) dans la ceinture tropicale (30°N à 30°S) pour évaluer leur covariabilité avec la température de surface de la mer (ERA5), à différentes échelles temporelles et spatiales et sous l'influence de la circulation à grande échelle (ERA5).

Des relations physiques sont établies entre l'humidité relative, les nuages, les précipitations et la température de la surface de la mer. Différentes caractéristiques sont observées à différentes échelles et dans différents régimes à grande échelle. Ces observations peuvent être utilisées comme un diagnostic solide dans l'évaluation des modèles climatiques.

**Title:** Observations of the Tropical Atmospheric Water Cycle and Its Variations, Using a Constellation of Satellites

**Keywords:** Observations, Moisture, Clouds, Temperature, Satellites, Tropics

**Abstract:** Better understanding of how the tropical atmospheric water cycle responds to climate change requires a comprehensive observational view of its principal variables.

This work builds a synergistic dataset of collocated instantaneous observations of relative humidity (SAPHIR), cloud characteristics (CALIOP), and near-surface precipitation (CPR) in the tropical belt (30°N to 30°S) and assesses their covariability with sea surface temperature (ERA5), on different temporal and spatial scales, as well as under the influence of the large-scale circulation (ERA5).

Physical relationships are established between relative humidity, clouds, precipitation and sea surface temperature. Different characteristics are observed on different scales and within different large-scale regimes. These observations can be used as a strong diagnostic in the evaluation of climate models.